frontiers | Research Topics

Recent developments in pancreatic cancer radiotherapy

Edited by
James C. L. Chow and Antonio Pontoriero

Published in
Frontiers in Oncology

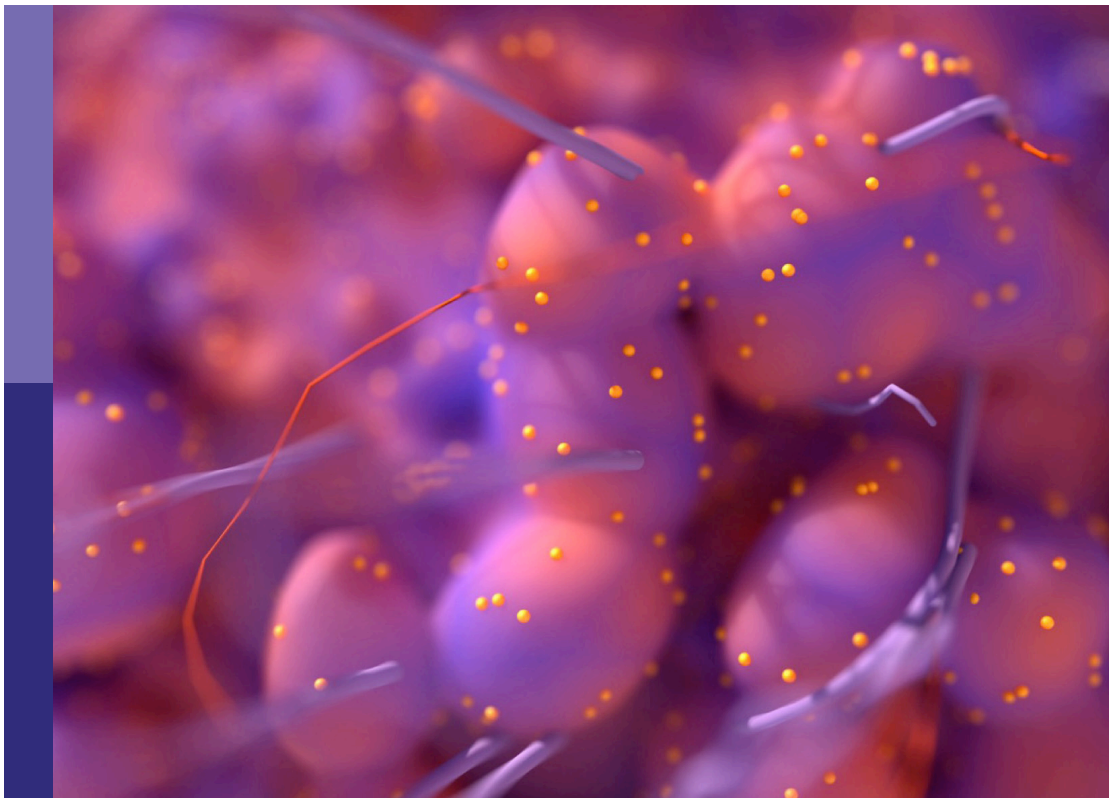

ISSN 1664-8714
ISBN 978-2-83251-991-2
DOI 10.3389/978-2-83251-991-2

About Frontiers

Frontiers is more than just an open access publisher of scholarly articles: it is a pioneering approach to the world of academia, radically improving the way scholarly research is managed. The grand vision of Frontiers is a world where all people have an equal opportunity to seek, share and generate knowledge. Frontiers provides immediate and permanent online open access to all its publications, but this alone is not enough to realize our grand goals.

Frontiers journal series

The Frontiers journal series is a multi-tier and interdisciplinary set of open-access, online journals, promising a paradigm shift from the current review, selection and dissemination processes in academic publishing. All Frontiers journals are driven by researchers for researchers; therefore, they constitute a service to the scholarly community. At the same time, the *Frontiers journal series* operates on a revolutionary invention, the tiered publishing system, initially addressing specific communities of scholars, and gradually climbing up to broader public understanding, thus serving the interests of the lay society, too.

Dedication to quality

Each Frontiers article is a landmark of the highest quality, thanks to genuinely collaborative interactions between authors and review editors, who include some of the world's best academicians. Research must be certified by peers before entering a stream of knowledge that may eventually reach the public - and shape society; therefore, Frontiers only applies the most rigorous and unbiased reviews. Frontiers revolutionizes research publishing by freely delivering the most outstanding research, evaluated with no bias from both the academic and social point of view. By applying the most advanced information technologies, Frontiers is catapulting scholarly publishing into a new generation.

What are Frontiers Research Topics?

Frontiers Research Topics are very popular trademarks of the *Frontiers journals series*: they are collections of at least ten articles, all centered on a particular subject. With their unique mix of varied contributions from Original Research to Review Articles, Frontiers Research Topics unify the most influential researchers, the latest key findings and historical advances in a hot research area.

Find out more on how to host your own Frontiers Research Topic or contribute to one as an author by contacting the Frontiers editorial office: frontiersin.org/about/contact

Recent developments in pancreatic cancer radiotherapy

Topic editors

James C. L. Chow — University of Toronto, Canada

Antonio Pontoriero — University of Messina, Italy

Citation

Chow, J. C. L., Pontoriero, A., eds. (2023). *Recent developments in pancreatic cancer radiotherapy*. Lausanne: Frontiers Media SA.

doi: 10.3389/978-2-83251-991-2

Table of contents

frontiers | Frontiers in Oncology

TYPE Editorial
PUBLISHED 09 March 2023
DOI 10.3389/fonc.2023.1160808

OPEN ACCESS

EDITED AND REVIEWED BY
Rachit Kumar,
Johns Hopkins Medicine, Johns Hopkins University, United States

*CORRESPONDENCE
James C. L. Chow
james.chow@rmp.uhn.ca

SPECIALTY SECTION
This article was submitted to Radiation Oncology, a section of the journal Frontiers in Oncology

RECEIVED 07 February 2023
ACCEPTED 28 February 2023
PUBLISHED 09 March 2023

CITATION
Chow JCL and Pontoriero A (2023) Editorial: Recent developments in pancreatic cancer radiotherapy. *Front. Oncol.* 13:1160808. doi: 10.3389/fonc.2023.1160808

Editorial: Recent developments in pancreatic cancer radiotherapy

James C. L. Chow[1,2*] and Antonio Pontoriero[3]

[1]Radiation Medicine Program, Princess Margaret Cancer Centre, University Health Network, ON, Toronto, Canada, [2]Department of Radiation Oncology , University of Toronto, ON, Toronto, Canada, [3]Radiation Oncology Unit, Department of Biomedical, Dental and Morphological and Functional Imaging Sciences, University of Messina, Messina, Italy

KEYWORDS

pancreatic cancer, radiotherapy, treatment outcome and efficacy, image guidance, retrospective study, stereotactic body radiation therapy, carbon ion therapy, image registration

Editorial on the Research Topic
Recent developments in pancreatic cancer radiotherapy

This book explores the recent advancements in pancreatic cancer radiotherapy, presenting innovative treatment techniques and clinical outcome assessments. Pancreatic cancer is difficult to detect in its early stages as the cancer is usually asymptomatic until it spreads in the patient. So far, no screening tests exist which can detect pancreatic cancer early when it is most curable. Surgery, on its own, is rarely curative in pancreas cancer both due to the anatomic location of the pancreas (at the posterior of the abdomen behind the stomach), and as the disease is generally metastatic at diagnosis. Typically, pancreatic cancer is treated with a combination of surgery, chemotherapy and radiotherapy. Radiotherapy is the most utilized cancer treatment option as over 50% of all cancer patients will receive radiotherapy during their treatment course. With the recent advances of radiation delivery, internal organ motion monitoring, computer calculation, medical image processing, treatment strategy, and treatment planning, encouraging progresses have been made in the pancreatic cancer radiotherapy.

For patients with unresectable pancreatic cancer undergoing definitive radiotherapy, Chen et al. carried out a detailed risk analysis on the treatment outcomes based on potential factors such as overall survival, local progression, distant metastases, carbohydrate antigen, neutrophil-to-lymphocyte ratio and others. They analyzed the biological effective doses in this retrospective study, and found that incorporating new systemic treatments during and after higher biological effective doses from radiotherapy for locally advanced pancreatic cancer is warranted. For novel treatment technique in pancreatic cancer, Feng et al. developed a Haar feature-based method to track the endoscopic ultrasound probe in diagnostic CT and MRI scans for guiding the hydrogel injection in pancreatic cancer radiotherapy. The advantage of this method is that no external tracking hardware is needed when tracking the ultrasound probe. They tested and implemented this method using phantom and patient images, and concluded that their method can find the best matched endoscopic ultrasound image from the dictionary based on simulated images. The pancreas movement was tracked and studied using the synchrony respiratory tracking system in

CyberKnife treatment by Jing et al. The pancreatic displacement was calculated from the patients' x-ray image set and the mean motion amplitudes in the SI, LR and AP directions were determined. They found that the tracking accuracy was affected by the tumour motion amplitude, location and treatment time. Jing et al. therefore concluded that tumours at different locations should be treated differently for the best dose coverage. A retrospective study on stereotactic body radiotherapy combined with chemotherapy was carried out by Lee et al. The overall survival and local progression-free survival were determined for patients with the median follow-up period of 21.1 months. Lee et al. found that stereotactic body radiotherapy followed by chemotherapy was an effective treatment strategy for selected patients with unresectable pancreatic cancer. Moreover, they found that simultaneous integrated protection and the MR-guided adaptive technique were worthwhile to implement in order to minimize the risk of adverse events. Carbon-ion beam has the advantage of a sharp dose distribution due to the characteristic of Bragg peak in pancreatic cancer radiotherapy. In the treatment planning of carbon-ion therapy, Kusano et al. used the CT value replacement method to improve the plan dosimetry due to the influence of the gastrointestinal gas in the patient. They concluded that their method can directly be implemented in clinical practice without additional software and equipment. A retrospective patient study was carried out by Broggi et al. to evaluate patient outcomes for locally advanced pancreatic cancer treated with a combination of chemotherapy and hypofractionated radiotherapy in 15 fractions. Based on the dose-volume results, Broggi et al. found that the risk of duodenal or gastric toxicities was related to the duodenum or stomach dose-volume histogram. The radiation delivery was evaluated by Arumugam et al. using an in-house position monitoring system in pancreas stereotactic body radiotherapy. This in-house system is an online image-based position monitoring system using the radiopaque marker and the Elekta XVI imaging system. In the evaluation, the dosimetric impact due to position deviations and actual delivered dose after position corrections were assessed. From the dosimetric results, Arumugam et al. concluded that their position monitoring system can improve the treatment accuracy using only a general linear accelerator. Another retrospective study was carried out by Cao et al. to investigate the dose in the organs-at-risk and gastrointestinal toxicity, when re-irradiation of stereotactic body radiotherapy was needed for pancreatic cancer patient usually having local recurrence. Using the deformable image registration method, Cao et al. determined various dose-volume variables such as V_{10} of the stomach and D_{mean} of the intestine in the re-irradiation. Jung et al. conducted a clinical outcome evaluation for FOLFIRINOX as a popular systemic regimen followed by stereotactic body radiotherapy in locally advanced pancreatic cancer. In this retrospective study, patient outcome parameters such as overall survival, progression-free survival, resection rate, stereotactic body radiotherapy-related adverse events and prognostic factors were determined. From the result analysis, Jung et al. concluded that the induction of FOLFIRINOX followed by stereotactic body radiotherapy for locally advanced pancreatic cancer can lead to a better survival rate with manageable toxicities. On the radiation delivery, Ma et al. proposed to carry out intensity-modulated electron therapy using mechanical scanning with a robotic arm on a linear accelerator. The beam scan is based on a zigzag pattern generated by an algorithm controlling various delivery parameters such as beam position, beam energy and step-and-shoot discrete scanning. The algorithm was evaluated using CT image set of 10 pancreatic cancer patients and from the result Ma et al. concluded that intensity modulated electron therapy is potentially feasible in pancreatic cancer treatment undergoing intraoperative radiotherapy.

We hope the results and findings in this book can be useful to our colleagues, clinicians and researchers in pancreatic cancer radiotherapy. We would also like to thank and congratulate all authors who contributed their insightful and significant works to this book.

Author contributions

Both JC and AP contributed to manuscript draft, read, and approved the submitted version.

Conflict of interest

The authors declare that the research was conducted in the absence of any commercial or financial relationships that could be construed as a potential conflict of interest.

Publisher's note

frontiers in Oncology

ORIGINAL RESEARCH
published: 04 November 2021
doi: 10.3389/fonc.2021.759811

The Feasibility of Haar Feature-Based Endoscopic Ultrasound Probe Tracking for Implanting Hydrogel Spacer in Radiation Therapy for Pancreatic Cancer

Ziwei Feng[1,2], *Hamed Hooshangnejad*[2,3], *Eun Ji Shin*[4], *Amol Narang*[2], *Muyinatu A. Lediju Bell*[1] *and Kai Ding*[2*]

[1] Department of Electrical and Computer Engineering, Johns Hopkins University, Baltimore, MD, United States, [2] Department of Radiation Oncology and Molecular Radiation Sciences, Johns Hopkins University School of Medicine, Baltimore, MD, United States, [3] Department of Biomedical Engineering, Johns Hopkins University School of Medicine, Baltimore, MD, United States, [4] Department of Gastroenterology, Johns Hopkins University School of Medicine, Baltimore, MD, United States

OPEN ACCESS

Edited by:
Yidong Yang,
University of Science and Technology of China, China

Reviewed by:
Yin Zhang,
Rutgers Cancer Institute of New Jersey, United States
Jing Cai,
Hong Kong Polytechnic University, Hong Kong, SAR China

***Correspondence:**
Kai Ding
kding1@jhmi.edu

Specialty section:
This article was submitted to Radiation Oncology, a section of the journal Frontiers in Oncology

Received: 17 August 2021
Accepted: 11 October 2021
Published: 04 November 2021

Citation:
Feng Z, Hooshangnejad H, Shin EJ, Narang A, Lediju Bell MA and Ding K (2021) The Feasibility of Haar Feature-Based Endoscopic Ultrasound Probe Tracking for Implanting Hydrogel Spacer in Radiation Therapy for Pancreatic Cancer. Front. Oncol. 11:759811. doi: 10.3389/fonc.2021.759811

Purpose: We proposed a Haar feature-based method for tracking endoscopic ultrasound (EUS) probe in diagnostic computed tomography (CT) and Magnetic Resonance Imaging (MRI) scans for guiding hydrogel injection without external tracking hardware. This study aimed to assess the feasibility of implementing our method with phantom and patient images.

Materials and Methods: Our methods included the pre-simulation section and Haar features extraction steps. Firstly, the simulated EUS set was generated based on anatomic information of interpolated CT/MRI images. Secondly, the efficient Haar features were extracted from simulated EUS images to create a Haar feature dictionary. The relative EUS probe position was estimated by searching the best matched Haar feature vector of the dictionary with Haar feature vector of target EUS images. The utilization of this method was validated using EUS phantom and patient CT/MRI images.

Results: In the phantom experiment, we showed that our Haar feature-based EUS probe tracking method can find the best matched simulated EUS image from a simulated EUS dictionary which includes 123 simulated images. The errors of all four target points between the real EUS image and the best matched EUS images were within 1 mm. In the patient CT/MRI scans, the best matched simulated EUS image was selected by our method accurately, thereby confirming the probe location. However, when applying our method in MRI images, our method is not always robust due to the low image resolution.

Conclusions: Our Haar feature-based method is capable to find the best matched simulated EUS image from the dictionary. We demonstrated the feasibility of our method

for tracking EUS probe without external tracking hardware, thereby guiding the hydrogel injection between the head of the pancreas and duodenum.

Keywords: endoscopic ultrasound (EUS), probe tracking, hydrogel spacer, pancreatic cancer, Haar feature, radiation therapy

INTRODUCTION

Pancreatic cancer is the fourth most common cause of cancer death in both sexes in the United States. Perhaps more compelling, it is the most devastating cancer in the United States with the lowest 5-year relative survival rate of 9% (1). Furthermore, only a minority of cases representing resectable diseases have a chance for long-term survival. In contrast, one-third of cases do represent borderline resectable or locally advanced pancreatic cancer (BR/LAPC). Even if an aggressive therapy combining chemotherapy with radiation can be recommended for improving patients' life quality in LAPC cases, the median survival is only extended to 9-15 months (2, 3). Previous autopsy studies proved that 30% of the patients died because of locally destructive diseases (4). Therefore, local control and delaying local progression are important for improving morbidity and extending the survival period for pancreatic cancer patients.

According to a previous study about dose escalation, the outcome with single fractions in 25 Gy or five fractions in 33 Gy were promising for leading a better local tumor control and delaying local progression. Furthermore, some researchers, recently, tested the dosimetric feasibility of implementing dose escalation with intensity-modulated radiation therapy (IMRT) with 67.5 Gy in 15 fractions prescription dose and stereotactic body radiation therapy (SBRT) with 50 Gy in 5 fractions prescription dose (5). Additionally, researchers demonstrated that the overall survival (OS) and local-regional recurrence-free survival (RFS) could be significantly improved after dose escalation during consolidative chemoradiation (6). However, even with the wide implementation of proton therapy and better optimization method (7), the challenge and barriers to implementing these dose escalation strategies involve the proximity and inherent radiosensitivity of the gastrointestinal tract, particularly the duodenum, which is directly adjacent to the head of pancreas (HOP). Plus, the motion of abdominal organs caused by breathing increased the risk of these radiosensitive organs in radiotherapy (8, 9).

In that hydrogel is capable of sparing organs at risk (OARs) from radiation targets, hydrogel injection is a potential solution for reducing the radiation dose received by radiosensitive OARs, thereby sparing them during dose escalation treatments. The utility and outcome of this technique have been evaluated in the treatment of prostate, head and neck, and gynecologic cancers (10–14). By increasing the space between the rectum and the prostate, the radiation dose received by the rectum was reduced, thereby improving the safety of radiation treatment and quality of life (10). Similarly, a previous study in gynecologic malignancy patients proved that hydrogel injection resulted in a significant reduction in the dose delivered to the rectum (13). Furthermore, our previous study has assessed the feasibility of injecting a similar injectable absorbable radiopaque hydrogel spacer (TraceIT, Augmenix, Bedford, MA) between the HOP and the duodenum *via* endoscopic ultrasound (EUS) guidance in human cadaveric specimen experiments (15–18). This TracelT is made up of a hydrogel paste that generates a bleb of particles at the needle tip upon injection. As previous research and the development report showed, the bleb maintains its 3-dimensional structure for three months and is absorbed after seven. We demonstrated the stability, safety, and efficacy of using this hydrogel in pancreatic cancer by creating sufficient space to protect the duodenum and to enhance the potential for dose escalation (16, 19). At present, our group is proceeding with a clinical trial to access the utility of placing a hydrogel spacer between the HOP and the duodenum in BR/LAPC pancreatic cancer cases by EUS guidance without invasion of the duodenum (15).

However, the efficacy of utilizing hydrogel and the accuracy of injecting it can be compromised due to the uncertainty of how much hydrogel is needed and where the optimal hydrogel injected points should be along with the HOP-duodenum interface. For normalizing and perfecting the EUS injection procedure, we proposed an ideal injection workflow in **Figure 1**, including a prediction of separation for anticipating how much hydrogel is injected (20), injection planning, and execution of injection for guiding hydrogel injection in an optimal injected point. As we proposed, before the injection process, injection planning was designed with an optimal injection point based on the anatomical relationship from diagnostic computed tomography or Magnetic Resonance (MR) images. The challenge of executing injection planning centers on how to track the endoscopic probe relative position to the CT (21) or MR images and where to place the probe in the designed injection point. In other words, the challenge is how to align the real-time EUS image with the diagnosed CT or MR images, thereby guiding the injection process to be executed as planned. The present study is mainly aimed to test the feasibility of our method in steps with red frames.

The existing technical solution for ultrasound guidance systems mainly relies on external tracking hardware, such as optical camera, electromagnetic tracking, or mechanical tracking hardware (22–25). These hardware techniques were used to

Abbreviations: BR/LAPC, Borderline resectable or locally advanced pancreatic cancer; IMRT, Intensity modulated radiation therapy; SBRT, Stereotactic body radiation therapy; HOP, Head of pancreas; OAR, Organs at risk; EUS, Endoscopic ultrasound; CT, Computed tomography; MRI, Magnetic resonance imaging; TRUS, Transrectal ultrasound; NCC, Normalized cross correlation; ICT, Interpolated computed tomography; S-MRI, Simulated-magnetic resonance imaging; O-MRI, Original-magnetic resonance imaging.

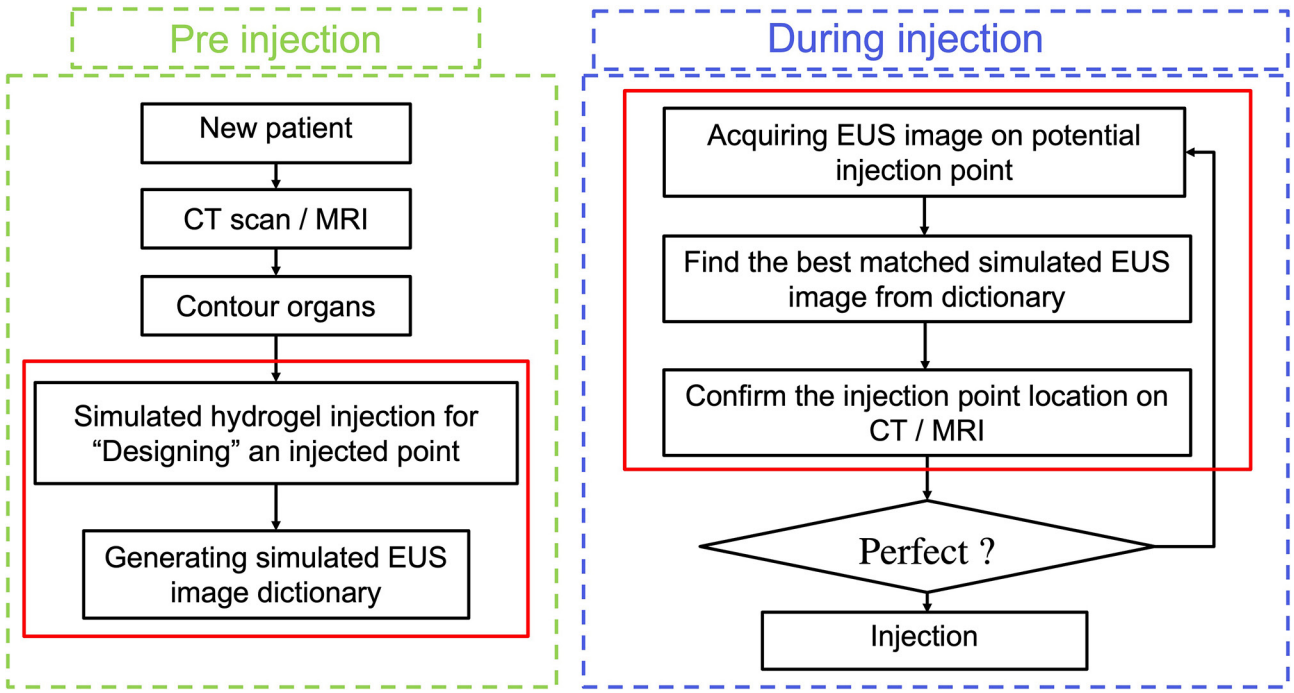

FIGURE 1 | Ideal workflow of injecting hydrogel.

compute consistency between real-time 2D/3D ultrasound images and diagnostic 3D CT or MR images. But owing to the calibration in the clinical procedure, the error caused by internal organs motion was ignored in this tracking method. Therefore, researchers proposed a variety of multi-modalities image registration methods to compensate that tracking errors. For example, Hu et al. (26) developed an automatic non-rigid feature-based registration between magnetic resonance and 3D transrectal ultrasound (TRUS) images (26). They extracted surface normal vectors of 3D US images by using a second-order Gaussian filtering approach, thereby reducing the system sensitivity to noise. In addition, for enhancing the accuracy of EUS navigation in the upper gastrointestinal (GI) system, Bonmati et al. (27) proposed a registration approach to simulate the initialization between pre-obtained CT images to EUS registration by registering landmarks to corresponding segmented anatomical structures (27). By testing different cost-functions (cross correction, mutual information, and gradient methods), Shi et al. (28) optimized the image registration for projecting mucosal disease contours to planning CT datasets by accomplishing rigid registration of optical endoscopy image and CT scans (28). The image registration between EUS and CT images remains a challenging task with low robustness and accuracy. This is owing to: a) the loss of image information of 3D CT data in 2D EUS images; b) the lack of paired anatomical landmarks on EUS/CT; c) the difference of grey level in some structures in CT and EUS images.

One potential candidate to address the challenges is using the Haar feature. Haar features are efficient to represent image information with fast performance. The previous implementations of the Haar feature focused on fingerprint compression, face reorganization (29, 30), and JPEG Image compression (31–33), all of which have promising accuracy for detecting objects. According to previous research, Haar features have a good capacity in distinguishing functions in cascades (29). Silva et al. (31) developed a dictionary-based 3D MR -2D EUS images initialization algorithm by extracting image Haar features to estimate the initialized pose. After initialization, they proposed a fast image-based 3D-2D registration by Powell's method (31, 34). The results proved that these Haar features were an efficient representation for initialized pose utilization for guiding spinal intervention. Thus, these characteristics of Haar features makes it possible to overcome our previous challenges.

In our present study, we develop a Haar feature-based method for tracking EUS probe location on diagnostic CT or MRI without external tracking hardware to facilitate injecting hydrogel in designed injection points. Our methods included the pre-simulation section and Haar features extraction sections. **Figure 1** shows the overview of our proposed method. In the first step, the simulated EUS image set was generated based on anatomic information from CT or MRI images. Secondly, the efficient Haar features are extracted from simulated EUS images set to create a Haar feature dictionary. The probe relative position is estimated by searching the best matched Haar feature vector of the dictionary with Haar feature vectors of real EUS images. The utilization of this method was evaluated in endoscopic phantom, patient CT scan, and patient MR scan.

MATERIALS AND METHODS

Methodology

Field II Simulation and Simulated EUS Dictionary

Field II is a free and open-access Matlab program for simulating ultrasound images by calculating the ultrasound field for both the pulsed and continuous wave case. This method is based on linear systems theory (35–37). When the transducer emits the signal as a Dirac delta function, the corresponding emitted ultrasound field is represented as a time function of a specific point in space according to the spatial impulse response. Thus, this field of different excitations is calculated by convolving the different excitation functions with the spatial impulse response. The detailed explanation and reasoning of this simulation method were published in previous publications (38–40).

In our study, we used two different methods to generate a simulated scatter phantom. As **Figure 2A** row one shows, the first method is used for patient scans. We simulated anatomic scattered phantoms based on the interpolated CT/MR slice of the region of interest. The detail of this method is explained on Field II's official website (http://fieldii.dk//?examples/kidney_example/kidney_example.html). The second method is applied for the phantom experiment. As **Figure 2A (b)** shows, we built a scatter phantom based on our endoscopic training phantom by defining geometric targets directly and assigning proper amplitudes for corresponding scatters. Then, the corresponding simulated EUS images were generated from the top center of the scatter phantom.

Haar Feature Extraction

To accurately and efficiently represent images features, we define eight basic Haar functions shown in **Figure 2B (a)** with scaling (s) and translation (t) parameters as:

$$\varphi_{s,t}(n) = \varphi(2^s n - t) \tag{1}$$

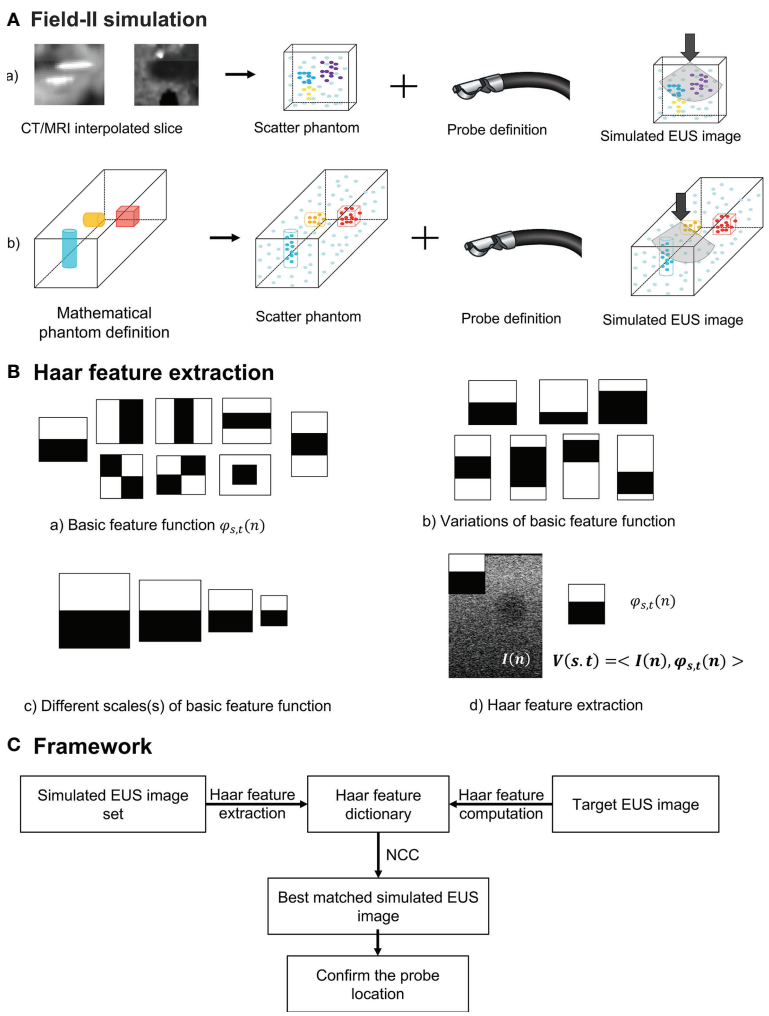

FIGURE 2 | **(A)** The diagram of Field II simulation. **(B) (a)** Basic Haar feature function; **(b)** Two examples of variation of basic feature function; **(c)** Example of different scales of basic feature function; and **(d)** Computation of Haar feature extraction. **(C)** The overview of our proposed framework. NCC, normalized cross-correlation.

Where $n = (n_x, n_y)$ and $t = (t_x, t_y)$ are spatial vectors representing x and y components. The translation parameter t defines the spatial location of the basic Haar feature function. According to previous research, these basic Haar functions are capable of capturing enough intensity patterns of images used for face detection and segmentation (31). Furthermore, the function with the relatively large scaling s is more sensitive to the detection of fine anatomical variation patterns with a large amount of computations. In contrast, by increasing this scaling parameter *s*, the corresponding basic function is able to detect large anatomical variations with fewer coefficients. We varied the scaling parameters in one interval for every basic Haar feature function [**Figure 2B (c)**]. On the other hand, as displayed in **Figure 2B (b)**, the other type of variation for every basic feature function is changing black and white block proportions. To improve the efficiency of computation, the integral image method proposed by Viola and Jones (29) is also implemented as the dot product of the basic Haar function and the image [**Figure 2B (d)**]:

$$V(s,t) = \ < I(n), \varphi_{s,t}(n) > \tag{2}$$

where I(n) is the image intensity, and V is the Haar feature vector. Therefore, the Haar feature vector includes the response of different scales, translations, and variations of basic feature functions, which is enough for encoding images features. The Haar feature dictionary is formed by computing this Haar feature vector of each simulated 2D EUS image.

Overview of the Framework

The overview of our Haar features-based EUS imaging guidance is shown in **Figure 2C**. We tested the feasibility of this method on both the phantom and patient images. Firstly, we generated the simulated EUS image set of phantom or patient which consists of simulated EUS images from Field II. Then, Haar feature vectors of all simulated images were computed and extracted to form a Haar feature dictionary. Similarly, the Haar features vector of the target EUS image was computed as well.

As **Figure 2C** reveals, by calculating normalized cross-correlation (NCC) between the Haar feature vector of target EUS images with every vector within the dictionary, the best matched simulated EUS image was confirmed with the maximum NCC value. The NCC was calculated as follows:

$$I_{match} = \underset{\{I_{sEUS_i}\}}{\arg\max} \frac{1}{N_s} \Sigma_{s=1}^{N_s} NCC(V_{hi}(s), h_{target}(s)) \tag{3}$$

where $V_{hi}(s)$ is the *i*-th Haar feature vector from the dictionary, and $h_{target}(s)$ is the Haar feature vector of the target EUS image. N_s is the number of feature coefficients at every scaling level (31), and I_{match} is the corresponding best matched simulated EUS image. In different experiment, all simulated EUS images are paired with different kinds of 3D image modality, such as CT or MRI. Because we know the location of each simulated EUS image on paired 3D CT or MRI, the probe location is tracked and confirmed in the 3D image data.

Experiments

Phantom Experiments

Simulated EUS Image and Interpolation CT Scans

Figure 3 depicts the interpolated computed tomography (ICT) and corresponding simulated EUS images of our EUS training phantom (ATS Laboratories, Model GIETP). This phantom includes four echogenic sphere targets with a 5-mm radius, which are randomly distributed in a soft rubber-based tissue-mimicking material. A scan channel with a 25-mm radius is in the center of this phantom. This phantom was scanned with a Philips Big Bore 16-slice CT simulator (120 kVp, 1000 mAs/slice, collimation 16 x 1.5-mm, pitch 0.059, rotation time 0.44 s, FOV 600 mm, ultrafast recon kernel, 3-mm slice thickness, 3-mm increment, and standard filter). CT scan datasets were interpolated into a 1-mm slice thickness based on Matlab (Mathwork, Inc, R2020.a). All ICT scans were generated based on these interpolated datasets. Four targets were manually contoured from the CT scan based on Velocity software (Varian Medical Systems, Inc).

One set of real-time EUS images was obtained with a linear endoscopic probe with 128 elements and reconstructed based on the Vantage 128 system (Verasonics Inc., WA, USA). This real-time EUS image was used as the target EUS image, and we generated one corresponding simulated EUS image and interpolated CT scan as ground truth to test our method.

Based on the coordinate data of the targets' contour, an artificial scatter phantom with four identical sphere targets was simulated using Field II. At every target center, as shown in **Figure 3A**, the $I_{0°}^{sEUS}$ represented simulated EUS image set simulated by shifting the image plane along the center of each target axis at 5-mm intervals. Similarly, the $I_{\pm 15°}^{sEUS}$ represented simulated EUS image sets simulated by rotating image direction to ± 15, respectively. Thus, a 2D simulated US image set ($I_{0°}^{sEUS}$ and $I_{\pm 15°}^{sEUS}$) including 30 images was created for every target. The corresponding 2D interpolated CT image ($I_{0°}^{ICT}$ and $I_{\pm 15°}^{ICT}$) sets were created in the same rotated degree and image plane. In the Field II simulation process, we defined the parameters of the endoscopic probe exactly as the endoscopic probe, including a center frequency of 7.5 x 10^6 Hz and a width and height of every element at 0.29 mm and 0.41 mm, respectively. Before computing the Haar feature dictionary, all simulated EUS images are smoothed by a 5 x 5 median filter for removing scattered noise.

Figure 3B shows the workflow of phantom experiments. Each simulated EUS image was registered and paired with a corresponding interpolated CT image in the same location. The simulation of the EUS images process and the interpolation process were performed on the Field II package and our lab software, respectively. The Haar feature vectors of every simulated EUS image consisted of the Haar feature dictionary. By calculating the NCC value between the Haar feature vector of the target EUS image and each vector in the dictionary, the best matched simulated EUS image was found and picked from the simulated EUS set, thereby finding the corresponding paired ICT slice and tracking probe location.

In addition, we tested the matching accuracy and efficiency with a different number of basic Haar feature functions and scale

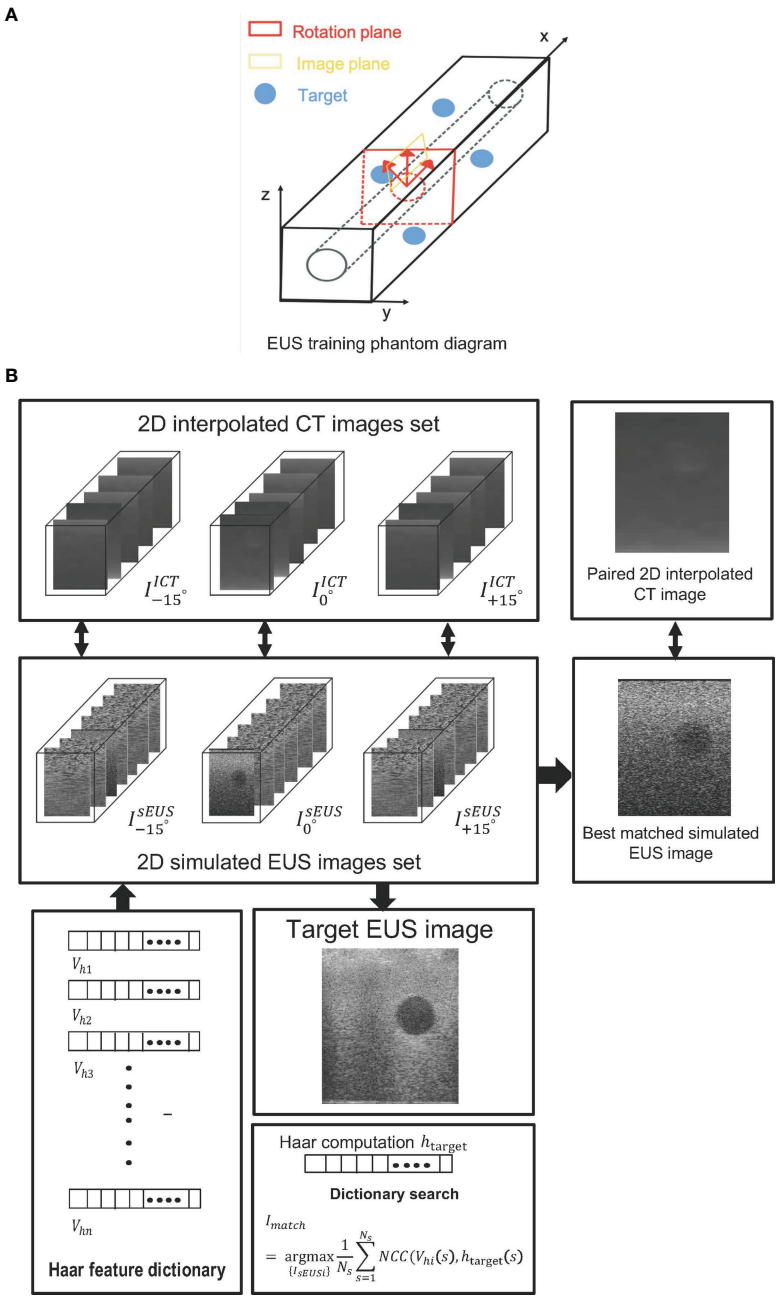

FIGURE 3 | **(A)** The EUS training phantom and CT interpolated plane diagram. **(B)** The workflow of a phantom experiment.

parameters based on phantom experiment data. In this test, the experimental procedure was the same as the previous one but with a different number of basic Haar feature functions or changing the scale parameters.

Patients Experiments

Patient's Experiment Based on CT Scans

For assessing the feasibility of our method on more complicated image data from a real patient, we used our previous patients who were injected with hydrogel spacer at our institution before radiation therapy. Six EUS record videos during the injection process were collected and real EUS image data were generated by extracting frames from these videos. After injection of the hydrogel, CT simulation of this patient (Philips Brilliance Big Bore CT; 3-mm slice thickness, 120 kVp, 200 mA, a 60-cm field of view) was performed. 10 potential injected points located in different slices were selected by the clinician, and corresponding ICT slices of each potential injected point were created. Every

ICT slice has different directions which are different from the traditional CT view (axial, sagittal, and coronal) for mimicking the various views of EUS images. The tumor region was represented as hypoechoic mass whereas no clear edge of the tumor was observed based on CT scans. Thus, according to the tumor contour, we applied a pre-processing step of ICT scans for converting tumor pixels' grey level into black and generated these pre-processing ICT.

A simulated EUS data set was generated by simulating ten EUS images based on pre-processing ICT slices. Specifically speaking, the anatomic phantoms were created by drawing a bitmap image of the scattering strength of the region of interest. In this case, this bitmap determines the factor multiplied with the scattering amplitude generated from the Gaussian distribution, thereby modeling the difference in the density and speed of sound perturbations in the tissue. A curvilinear array with 159 elements in 91.1 mm radius was defined and the simulated EUS images consisted of 128 scanlines. **Figure 4** showed the workflow of the patient's CT experiment. One real EUS image was selected by the clinician as the target EUS image. By extracting Haar feature vectors from simulated EUS images and target EUS images, and computing the NCC value between every simulated EUS image with target one, a best matched simulated EUS image was obtained with a known location on the ICT scan. Therefore, the probe position of the real target EUS image can be confirmed as the location of the best matched simulated EUS image.

Patient Experiment Based on MR Images

Because MR images have a better contrast around the HOP, we further tested the feasibility of our method based on MR image data. We defined the MR images of our previous patients acquired before hydrogel injection at our institution as original pre-MR images (O-MRI). Patient MR images were performed on a 1.5T clinical MR scanner (Signa Artist, GE Healthcare, Wauwatosa, WI, US). We created two simulated injected points based on different MR image slices. Then, we simulated hydrogel injection at these two simulated injected points, named P1 and P2, and generate simulated post-MR images (S-MRI). As **Figure 5** A2 shows, the yellow and blue points are two simulated injected points in different axial slices. P1_1 and P1_2, P2_1 and P2_2 are the extra two nearby points around simulated injected points, respectively. All the simulated injected points were selected based on axial CT scan which duodenum and HOP

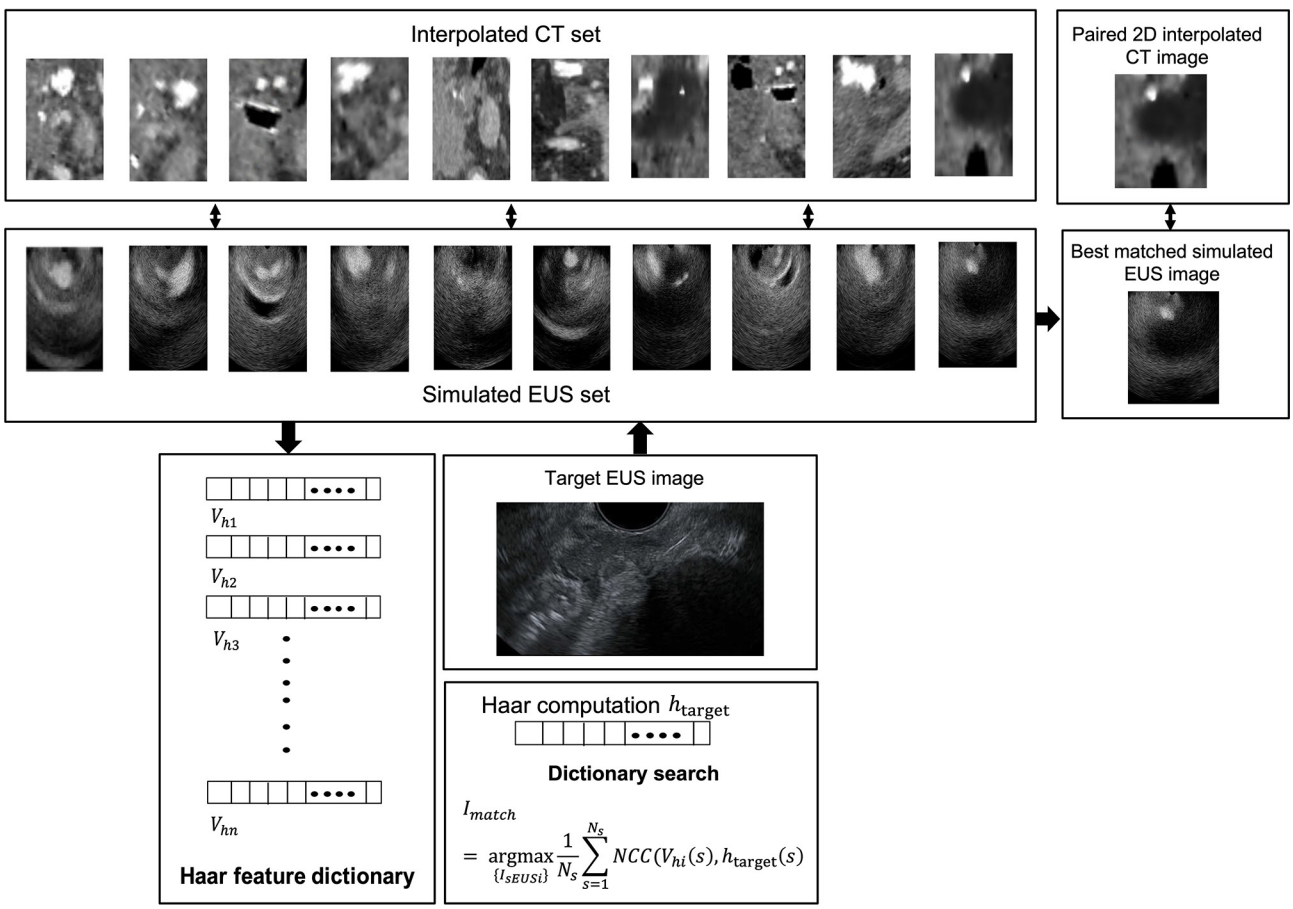

FIGURE 4 | The workflow of patient's CT experiment.

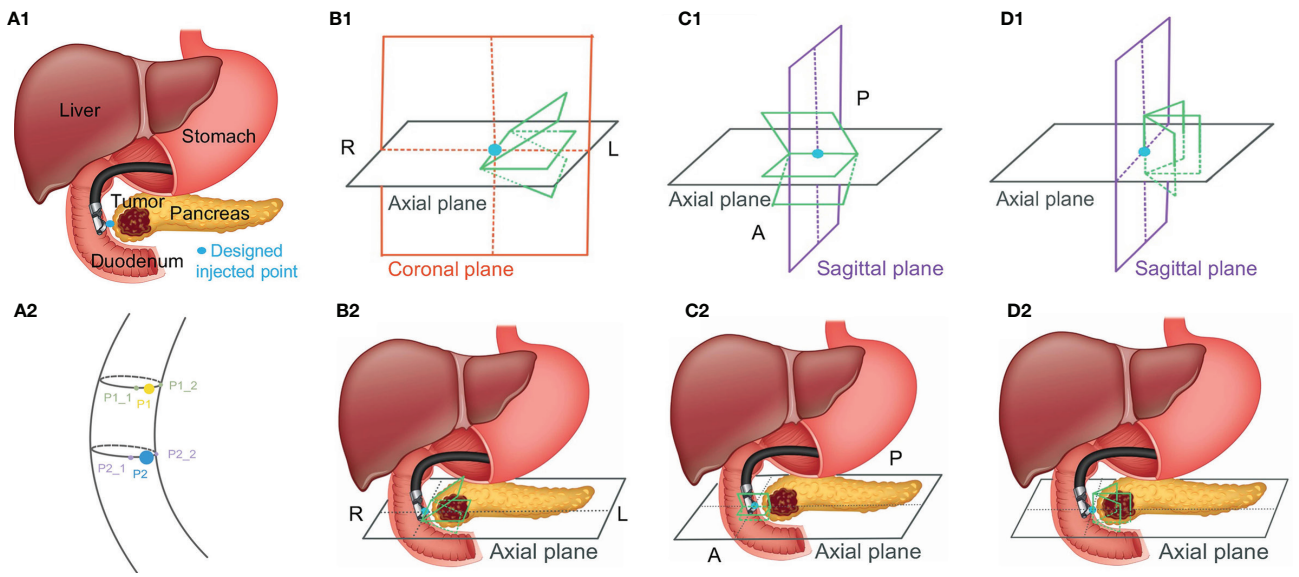

FIGURE 5 | The simulated injected point and interpolation of MRI image. R, L, P, and A represent right, left, posterior, and anterior, respectively.

were adjacent to each other. The detail of this simulation of injection was published in the previous paper from our lab (41). We generated 7 interpolated MRI slices on every simulated injected point. As **Figure 5**, B1 and C1 show, for each simulated injected point, we interpolated four MR image slices by rotating image planes ±15° around the axial plane in the patient right-to-left direction (**Figure 5**, B1, R to L) and the posterior-to-anterior (**Figure 5**, C1, P to A) direction, respectively. These simulated EUS images were aimed to mimic the EUS images obtained like radial EUS scanning. Additionally, as **Figure 5**, D1 shows, the other three interpolated MRI slices were perpendicular to the axial plane. The middle-interpolated slice was defined as a simulated injected image plane from point to the HOP and the rest of the two interpolated slices were generated by shifting ±15° around it. These simulated EUS images were used to mimic the EUS images collected as in linear EUS scanning. Therefore, two interpolated MRI sets were created based on OP-MRI and SP-MRI data sets and each of them included 42 interpolated MR images. As **Figure 6** shows, the corresponding simulated EUS data sets were generated by simulating EUS images based on interpolated O-MRI and S-MRI data sets. The simulation process was the same as patient CT experiments, including probe definition and generation of scattering phantom.

We did two validation experiments. In the first experiment, we picked one simulated EUS image (from P2 simulated injected point with **Figure 5**, B1 −15° interpolated angle) from O-MRI simulated EUS image set as the target EUS image. We assume this target EUS image is obtained before the injection process and try to track the probe location of this target EUS image. So, we searched the best matched simulated EUS image of this target EUS image from the O-MRI simulated EUS image set. In the second experiment, we picked one simulated EUS image at the same simulated injected position in the previous target EUS image (from P2 simulated injected point with **Figure 5**, B1 −15° interpolated angle) from S-MRI simulated EUS data set as the target EUS image. In this case, our scenario is to simulate this target EUS image obtained during the injection process and try to track the probe location in real-time for the guidance injection process. Thus, we searched the best matched simulated EUS image of this target EUS image from O-MRI simulated EUS image data sets.

RESULTS

In the 121 simulated EUS images with 18,801,134 scatters, the best matched simulated EUS image is the 19th in the $I_{0°}^{SUS}$. The results are shown in **Figure 7**. **Figures 7A–C** show the target EUS image, the corresponding best matched simulated EUS image, and one simulated EUS image with a different target nearby the best matched one. Four marker points are measured in the best simulated EUS image and the target EUS image. The green circles and red crosses represent the markers of best matched simulated US image and target EUS image, respectively. The locations of four marker points on the target are obtained. Because we did not have the ground truth location of the target EUS image, the distance errors between these four marker points are used to assess the process for searching best-matched result. In the x-axis, the errors of these four markers between the target EUS image and the best matched EUS simulated image are -0.36 mm, -0.71 mm, -0.71 mm, and 0.07 mm, respectively. In the y-axis, the errors of these four markers between the target EUS image and the best matched US simulated image are 0.468 mm, 0.80 mm, 0.91 mm, and 0.91 mm, respectively. **Figures 7D–F** show the Haar feature vector (1*14027) of the target EUS image,

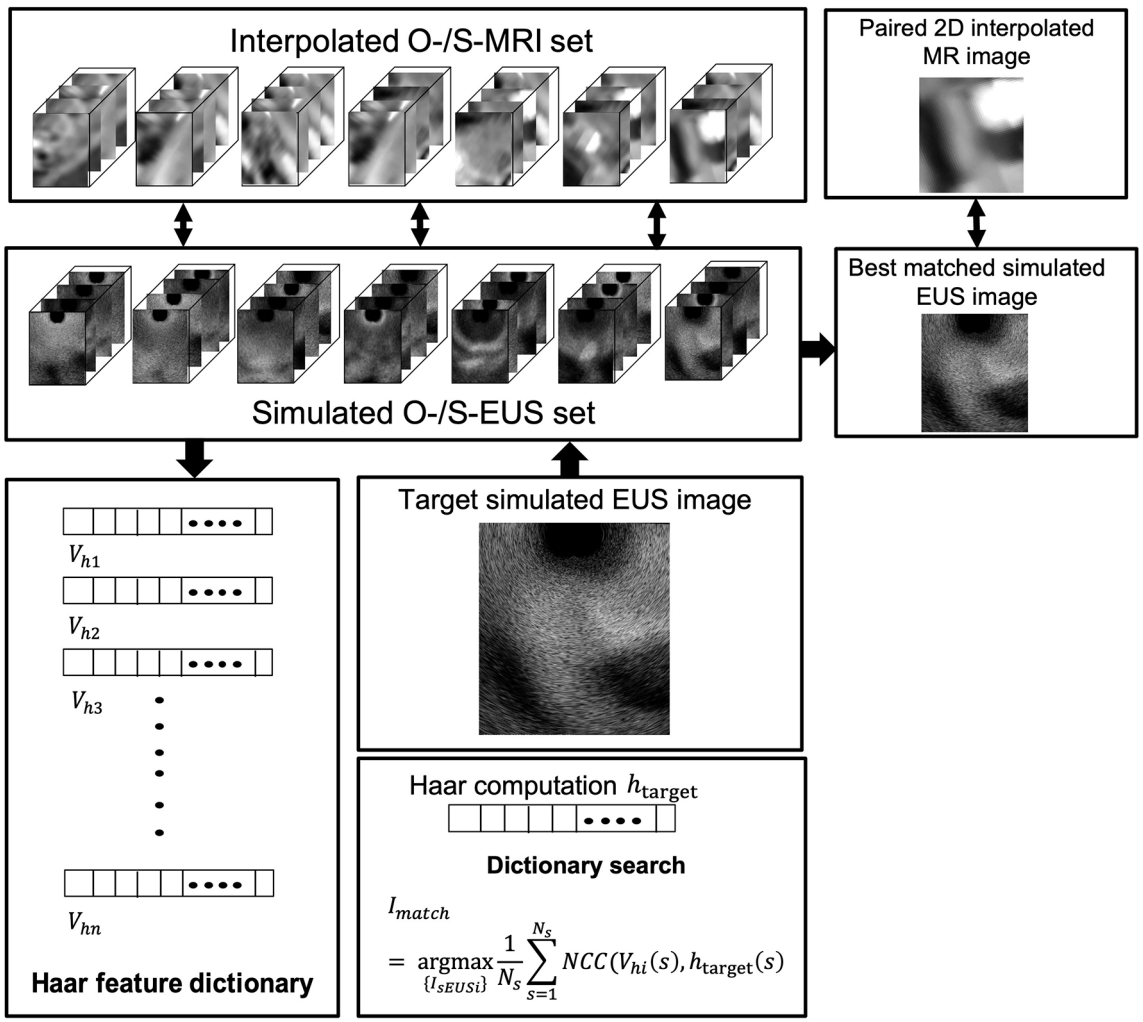

FIGURE 6 | The workflow of patient's MRI experiment.

best matched simulated EUS image, and nearby simulated EUS image, respectively.

Figure 7G plots the results of matching accuracy with different scales value and a fixed number of basis functions. N is the number of basis Haar feature functions. MC is a combination of multiple scales values. **Figure 7H** plots the results of matching accuracy with a variable number of basis functions and fixed scales. S is the scale value of the basis Haar feature function. MC is a combination of multiple scales. The locations of four marker points on the sphere target are obtained. The error was measured as the four marker points' distance errors of each target between the target EUS image and the corresponding best matched EUS image. As **Figures 7G, H** show, with a fixed basic Haar feature function, the matching accuracy will be improved by increasing scales. That is because the lower image quality of simulated EUS images did not have smooth circle edges. It is better to use large scales of basis function to detect the large gray level variation. According to **Figure 7H**, there is no significant relationship between matching error with the different number of basic Haar feature functions (fixed scales).

Figure 8 shows one example of ICT and corresponding pre-processing ICT. In the ICT, the tumor, as red contour showed, has a similar grey level with around tissue (**Figure 8A**). **Figure 8B** shows the result of the tumor region after pre-processing which was converted as a "hypoechoic" organ (red contour). A white dot (green contour) in the **Figures 8A** and 8B within the tumor is a marker for eliminating position error during radiotherapy. There are three hydrogel clusters in the ICT and PCT with yellow contours (**Figures 8A, B**). The corresponding simulation phantoms are created for EUS simulation based on these pre-processing ICT slices. **Figure 8C** shows one frame of real EUS image selected by a clinician as target EUS images to test our method. A tumor (red contour), one hydrogel cluster (yellow contour), and injected needle (blue contour) can be seen in this target EUS image. The tumor is

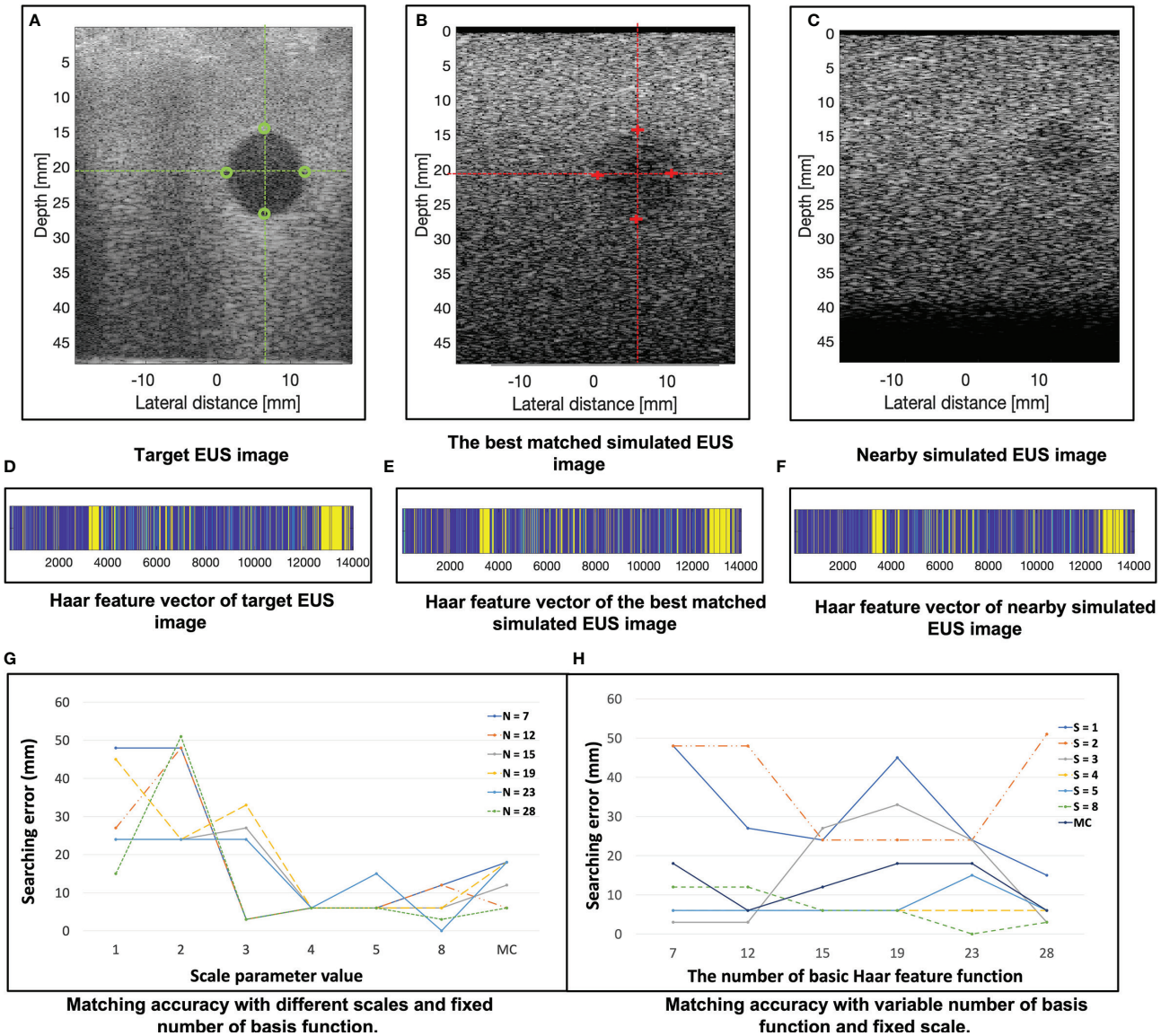

FIGURE 7 | **(A–C)** show the target EUS image, the corresponding best matched simulated EUS image, and one simulated EUS image with a different target nearby the best matched one. Four marker points are measured in the target EUS image and the best simulated US image. The green circles and red crosses represent the marker of the target EUS image and best matched simulated EUS image, respectively. **(D–F)** show the Haar feature vector of target EUS image, best matched simulated EUS image, and nearby simulated EUS image, respectively. **(G)** plots the results of matching accuracy with different scales and fixed number of basis functions. N is the number of basis functions. MC is a combination of multiple scales. **(H)** plots the results of matching accuracy with a variable number of basis functions and fixed scales. S is the scale of the basis function. MC is a combination of multiple scales. The error is calculated as the distance error of the four marker points of each target between the target EUS image and the corresponding best matched EUS image.

presented as a hypoechoic region at the bottom right of the image. By applying our proposed method, the best matched simulated EUS image is found according to the maximum NCC value. **Figure 8D** shows the corresponding best matched simulated EUS image in our simulation datasets. The tumor and hydrogel clusters are contoured in red and yellow, respectively. **Figure 8E** shows the Haar feature vectors (1*14027) of the target EUS image and all 10 simulated EUS images. Different colors represented different values. The x-axis represented the feature number. The Haar feature vectors of the real EUS image and the corresponding best-matched image were shown in the red frame (**Figure 8E**).

The results of the MRI patient experiment are shown in **Figure 9**. **Figure 9A** shows the target simulated EUS image which is chosen from O-MRI simulated EUS image set at the P2 simulated injected point with **Figure 5**, B1 -15° interpolated direction. **Figure 9D** shows the target simulated EUS image from S-MRI at the same position. **Figures 9B, E** show the

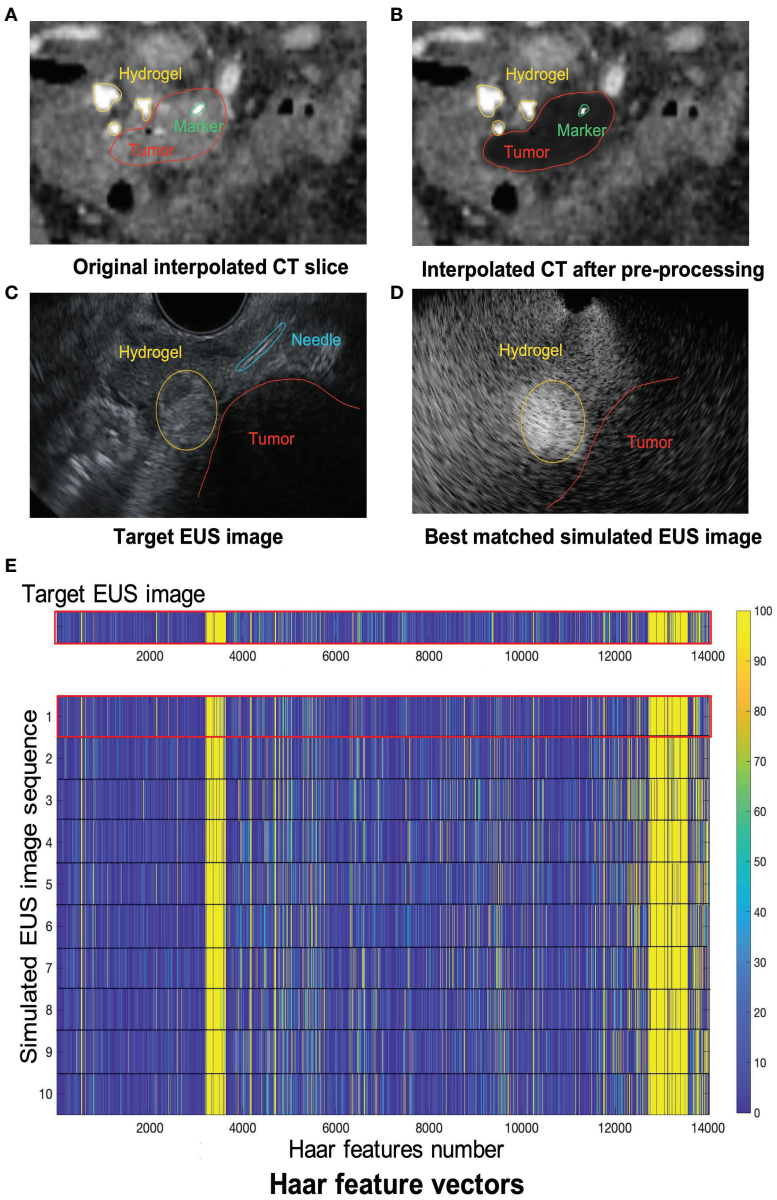

FIGURE 8 | **(A, B)** show one example of ICT and pre-processing ICT, respectively. Red, yellow and green contours represented tumor, hydrogel, and tumor marker, respectively. The target EUS image and the best matched simulated EUS image are shown in **(C, D)**, respectively. Red, yellow, and blue contours represented tumor, hydrogel, and injected needle, respectively. **(E)** shows the Haar feature vector comparison between the target EUS image and all 10 simulated EUS images. The Haar feature vector in the red frame is calculated based on the best matched simulated EUS image.

corresponding best matched simulated EUS images found in the O-MRI simulated EUS image set. Our method is capable to find the best matched simulated EUS image both before injection and during the injection process, thereby confirming the probe location. But if the target EUS image is chosen as the simulated EUS images in the same simulated injected point with different interpolated directions, the best matched simulated EUS images were found with error interpolated direction.

Figures 9C, F show the Haar feature vectors comparison between target EUS images and simulated EUS images from the same potential injected points. The target EUS image shows in **Figure 9C** is chosen from O-MRI simulated EUS image set at the P2 simulated injected point with **Figure 5**, B1 -15° interpolated direction. The Haar feature vectors of simulated EUS images are based on O-MRI from the same simulated injected point. The target EUS image shows in **Figure 9F** is chosen from S-MRI simulated EUS image set at the P2 simulated injected point with **Figure 5**, B1 -15° interpolated direction. The Haar feature vectors of simulated EUS images are based on S-MRI from the same simulated injected point. The Haar feature vectors of best

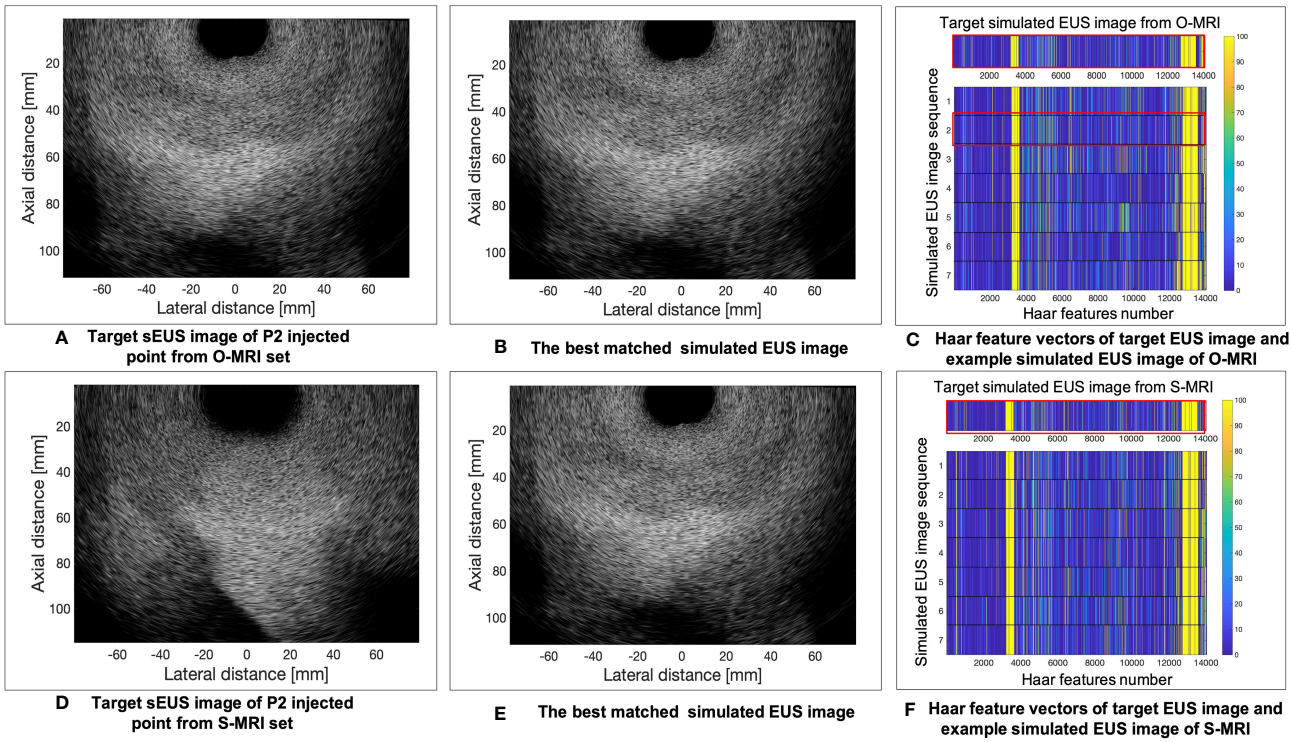

FIGURE 9 | The example results of the MRI patient experiment. **(A)** shows the target simulated EUS image which was chosen from O-MRI simulated EUS image set at the P2 simulated injected point with . B1 –15° interpolated direction. **(D)** shows the target simulated US image from S-MRI at the same position. **(B, E)** show the corresponding best matched simulated EUS images found in the O-MRI simulated EUS set. **(C, F)** show the Haar feature vectors comparison between target EUS images and simulated EUS images from the same potential injected points. The Haar feature vectors of the target EUS image and corresponding best matched simulated EUS image was in the
red frame.

matched simulated EUS image is the second vector in **Figure 9C** for both these two targets simulated EUS images (red frame in **Figure 9C, F**).

DISCUSSION

We proposed a Haar feature-based method for tracking probe position on diagnostic CT/MRI scans in the hydrogel injection process between the HOP and duodenum. We tested our method on a phantom study and two patients' experiments. Such a method can potentially increase the efficiency of hydrogel placement in common practice and obviate the need for external hardware for tracking EUS probe positions. The significance of our method is building a connection between 2D real-time EUS images and 3D pre-diagnosed CT/MRI images.

In previous research, we considered two possible risks of hydrogel injection (16). The first potential risk is about the side effects of muscularis propria after injection. Due to the unique anatomy between the HOP and duodenum, the hydrogel spacer injection process caused the injection within the muscularis propria of the duodenum in our cadaveric specimens. The second possible risk is disrupting and disseminating microscopic disease between the HOP and duodenum. Thus, we planned to evaluate and test whether the hydrogel injection causes the microscopic disease extent based on the histopathologic analysis of the resected interface between the HOP and duodenum. In this case, for better understanding the possible side effects of injection before expanding spacer application to clinical trials, it's important to control hydrogel injected in a specific location, mark and record this specific location in three-dimensional image data, and then investigate and identify whether this location is safe to place spacer with low risks. This is another potential application of our proposed method.

Besides these risks, there are two main uncertainties during hydrogel injection. First, although there is a wide application of similar hydrogel spacer placement reported for esophagus, bladder, prostate, and cervix (42–44), we have limited experience in placing this hydrogel in unique C-loop anatomy at the interface between pancreas and duodenum. It's hard for physicians to find an optimal injected point to place spacer only rely on 2D EUS images which might limit the benefit of hydrogel application. Second, the three-dimensional geometric relationship between the HOP and the duodenum can potentially change and deform since the beginning of the injection process. Similarly, 2D EUS images are not capable to

represent all these deformations and changes in three-dimensional view for guiding the injection process. Our lab's previous research (41) proposed a FEMOSSA simulation model to predict and simulate the realistic prostate-rectum spacer placement procedure. This method made it possible to design a pre-treatment injected plan based on CT scans for increasing the robustness and success rate of hydrogel placement, thereby potentially improving the clinical outcome of prostate cancer radiation therapy. Therefore, by combining the proposed method in this study with FEMOSSA, one can guide the EUS probe placing in the designed injected location and execute a pre-treatment injected plan.

The reason why the dictionary-based method of tracking probe position could be feasible and translated to our EUS guidance hydrogel injection is that probe motion pattern exists when the hydrogel is placed from the perspective of the duodenal lumen into the peripancreatic region. This kind of probe motion pattern also exists in clinical US image-guided procedures of prostate biopsy, cervical brachytherapy, and liver focal ablation (31). Plus, researchers demonstrated that Haar wavelet coefficients are sufficient and efficient to represent image features in 2D image slices to 3D volume image registration. In this case, abundant predicted EUS probe position of injection procedure is critical to generate efficient simulated EUS images and a large corresponding Haar features dictionary.

The results of the phantom and patient's experiment show the feasibility of our method and the accuracy of finding the best matched simulated EUS image. Previous research (45, 46) showed that registration error within 3 mm is comparable with electromagnetic and vision-based tracking systems for spine needle injections in the lumbar region. However, our phantom results demonstrated that the error between the best matched simulated EUS image and target EUS image is within 1 mm. Additionally, the results demonstrated that Haar features are sensitive to detect targets even with a noisy background. By incorporating the integral image method, the computation procedure is not time-consuming. Our Haar feature method makes it possible to implement the proposed ideal injection workflow for reducing the risks caused by uncertainties in the injection process.

Our method does have a good performance for searching best matched simulated EUS images within the simulated EUS image set in the phantom experiment: every 2D simulated EUS image set includes 121 simulated images (rotation range: 30 degrees in 15 intervals, image plane interval: 5 mm). This is because the EUS training phantom only includes the simplest sphere targets. But we cannot find other EUS training phantom with more various targets to mimic the endoscopic injected process. In the patient MRI experiment, a searching error with our method occurred. This is probably because of the lower resolution of the simulated EUS image dictionary. Thus, if we aim to apply this method to EUS images of the human anatomy, it is better to refine the simulated EUS images in both fine rotated intervals and image plane intervals and improve EUS image quality. However, in this way, the simulation process will require more time.

There are several limitations of our study. The first limitation involves the fact that only one real-time EUS image is available to use as a target image for evaluating our results in the phantom experiment. Therefore, we do not have enough points to quantify the registration error. In more future work, some simulated EUS images could be viewed as target images to test our method. In addition, we could use them with different resolutions or in different directions to mimic the various circumstances in the actual clinical injection process. The advantage of the second solution is that we know the ground truth of the probe/image locations. Furthermore, we could collect various real EUS images with high resolution and image quality, extracting the Haar features, which are sensitive to edge detection, to train an auto-segmentation model, like face detection. Alternatively, we could use the results of an auto-segmentation of the pancreas, the pancreas duct, and vessels as targets to register CT scans with a real-EUS image.

Secondly, in phantom experiments, we only consider the endoscopic probe direction aligned with the scan channel. The endoscopic probe has broad flexibility in terms of rotation when injecting hydrogel within the duodenum. In that our sphere target has the same 2D projection in a different direction, the only difference is in its radius. However, if we implement this method in actual patient's CT scans and EUS images, we have to consider more variations in probe direction. One previous paper (27) developed an imaging process method to generate potential/optimized planes for registration between CT and US images, which is a potential method we could combine with ours. In our patient experiment with CT scans, there is a large variation of interpolated CT slices with slightly "rotating" the probe. Thus, only 10 potential injection points are not sufficient to generate a simulated EUS dictionary. A similar limitation occurred in the patient's MRI experiment. Plus, generating a large, simulated EUS dictionary including sufficient predicted probe position is owing to the EUS image simulation on Field II which is a very time-consuming process.

At last, our EUS training phantom CT has a low contrast resolution, and we do not have ground truth with our probe position. In future work, we could attach an infrared marker to the probe to track its location with an infrared camera. In this case, we could use this location data as ground truth to evaluate our results. There is a similar limitation to a patient experiment. Plus, the breathing motion effect was not considered when we did the simulation process based on patients' CT and MRI. Since the EUS images were acquired in real time during clinical procedure, the motion breathing will probably cause no matched simulated EUS image in the dictionary even though the probe may be placed in the same position. In addition, many factors can impact the image quality and simulation process. For example, the grey level of region of interest in CT scan and EUS image are not uniform, such as stent, veins, and arteries. Some organs, like the layer of the mesentery, cannot be observed in CT scans, whereas these organs can be easily distinguished in the EUS images. Therefore, for generating a more accurate simulated EUS dictionary, additional image pre-processing steps that incorporate known anatomy are required.

CONCLUSION

This study demonstrated the feasibility of our method for tracking endoscopic probe location without external tracking hardware, thereby guiding the hydrogel injection between HOP and duodenum. Ongoing studies aim to accelerate the simulation process of generating dictionaries. Furthermore, more variable potential injection points and EUS direction must be considered and included in the simulation process.

DATA AVAILABILITY STATEMENT

The raw data supporting the conclusions of this article will be made available by the authors, without undue reservation.

ETHICS STATEMENT

The studies involving human participants were reviewed and approved by Johns Hopkins Medicine Institutional Review Boards (JHM IRBs). The patients/participants provided their written informed consent to participate in this study.

AUTHOR CONTRIBUTIONS

The study was designed by ZF, HH, and KD. All authors participated in collecting data. ZF and KD prepared the manuscript and contributed to data analysis and interpretation. All authors contributed to the article and approved the submitted version.

FUNDING

Research reported in this publication was supported by the National Institutes of Health (award numbers R37CA229417).

ACKNOWLEDGMENTS

The authors would like to thank the staff of the Carnegie Center for Surgical Innovation at Johns Hopkins University for their valuable assistance, Denise Link-Farajali (Center for Leadership education at Johns Hopkins University) for the English language consultation, and Xinyue Huang for productive advice, and the anonymous reviewers for their helpful comments.

REFERENCES

1. Siegel RL, Miller KD, Jemal A. Cancer Statistics, 2020. *CA Cancer J Clin* (2020) 70(1):7–30. doi: 10.3322/caac.21590
2. Ben-Josef E, Shields AF, Vaishampayan U, Vaitkevicius V, El-Rayes BF, McDermott P, et al. Intensity-Modulated Radiotherapy (IMRT) and Concurrent Capecitabine for Pancreatic Cancer. *Int J Radiat Oncol Biol Phys* (2004) 59(2):454–9. doi: 10.1016/j.ijrobp.2003.11.019
3. Loehrer PJ C. S.R., Feng Y, Cardenes H, Wagner L, Brell JM, Cella D, et al. Gemcitabine Alone Versus Gemcitabine Plus Radiotherapy in Patients With Locally Advanced Pancreatic Cancer: An Eastern Cooperative Oncology Group Trial. *J Clin Oncol* (2011) 29(31):4105–12. doi: 10.1200/JCO.2011.34.8904
4. Iacobuzio-Donahue CA, Fu B, Yachida S, Luo M, Abe H, Henderson CM, et al. DPC4 Gene Status of the Primary Carcinoma Correlates With Patterns of Failure in Patients With Pancreatic Cancer. *J Clin Oncol* (2009) 27 (11):1806–13. doi: 10.1200/JCO.2008.17.7188
5. Koay EJ, Hanania AN, Hall WA, Taniguchi CM, Rebueno N, Myrehaug S, et al. Dose-Escalated Radiation Therapy for Pancreatic Cancer: A Simultaneous Integrated Boost Approach. *Pract Radiat Oncol* (2020) 10(6): e495–507. doi: 10.1016/j.prro.2020.01.012
6. Krishnan S, Chadha AS, Suh Y, Chen HC, Rao A, Das P, et al. Focal Radiation Therapy Dose Escalation Improves Overall Survival in Locally Advanced Pancreatic Cancer Patients Receiving Induction Chemotherapy and Consolidative Chemoradiation. *Int J Radiat Oncol Biol Phys* (2016) 94 (4):755–65. doi: 10.1016/j.ijrobp.2015.12.003
7. Han D, Hooshangnejad H, Chen C-C, Ding K. A Beam-Specific Optimization Target Volume for Stereotactic Proton Pencil Beam Scanning Therapy for Locally Advanced Pancreatic Cancer. *Adv Radiat Oncol* (2021) 6(6):100757. doi: 10.1016/j.adro.2021.100757
8. Han-Oh S, Hill C, Kang-Hsin Wang K, Ding K, Wright JL, Alcorn S, et al. Geometric Reproducibility of Fiducial Markers and Efficacy of a Patient-Specific Margin Design Using Deep Inspiration Breath Hold for Stereotactic Body Radiation Therapy for Pancreatic Cancer. *Adv Radiat Oncol* (2021) 6 (2):100655. doi: 10.1016/j.adro.2021.100655
9. Su L, Iordachita I, Zhang Y, Lee J, Ng SK, Jackson J, et al. Feasibility Study of Ultrasound Imaging for Stereotactic Body Radiation Therapy With Active Breathing Coordinator in Pancreatic Cancer. *J Appl Clin Med Phys* (2017) 18 (4):84–96. doi: 10.1002/acm2.12100
10. Hamstra DA, Mariados N, Sylvester J, Shah D, Karsh L, Hudes R, et al. Continued Benefit to Rectal Separation for Prostate Radiation Therapy: Final Results of a Phase III Trial. *Int J Radiat Oncol Biol Phys* (2017) 97(5):976–85. doi: 10.1016/j.ijrobp.2016.12.024
11. Pinkawa M, Piroth MD, Holy R, Escobar-Corral N, Caffaro M, Djukic V, et al. Spacer Stability and Prostate Position Variability During Radiotherapy for Prostate Cancer Applying a Hydrogel to Protect the Rectal Wall. *Radiother Oncol* (2013) 106(2):220–4. doi: 10.1016/j.radonc.2012.11.010
12. Pinkawa M, Berneking V, Konig L, Frank D, Bretgeld M, Eble MJ. Hydrogel Injection Reduces Rectal Toxicity After Radiotherapy for Localized Prostate Cancer. *Strahlenther Onkol* (2017) 193(1):22–8. doi: 10.1007/s00066-016-1040-6
13. Viswanathan AN, Damato AL, Nguyen PL. Novel Use of a Hydrogel Spacer Permits Reirradiation in Otherwise Incurable Recurrent Gynecologic Cancers. *J Clin Oncol* (2013) 31(34):e446–7. doi: 10.1200/jco.2012.47.9931
14. Rao AD, Coquia S, De Jong R, Gourin C, Page B, Latronico D, et al. Effects of Biodegradable Hydrogel Spacer Injection on Contralateral Submandibular Gland Sparing in Radiotherapy for Head and Neck Cancers. *Radiother Oncol* (2018) 126(1):96–9. doi: 10.1016/j.radonc.2017.09.017
15. Rao AD, Shin EJ, Meyer J, Thompson EL, Fu W, Hu C, et al. Evaluation of a Novel Absorbable Radiopaque Hydrogel in Patients Undergoing Image Guided Radiation Therapy for Borderline Resectable and Locally Advanced Pancreatic Adenocarcinoma. *Pract Radiat Oncol* (2020) 10(6):e508–13. doi: 10.1016/j.prro.2020.01.013
16. Rao AD, Feng Z, Shin EJ, He J, Waters KM, Coquia S, et al. A Novel Absorbable Radiopaque Hydrogel Spacer to Separate the Head of the Pancreas and Duodenum in Radiation Therapy for Pancreatic Cancer. *Int J Radiat Oncol Biol Phys* (2017) 99(5):1111–20. doi: 10.1016/j.ijrobp.2017.08.006
17. Kerdsirichairat T, Narang AK, Thompson E, Kim S-H, Rao A, Ding K, et al. Feasibility of Using Hydrogel Spacers for Borderline-Resectable and Locally Advanced Pancreatic Tumors. *Gastroenterology* (2019) 157(4):933–5. doi: 10.1053/j.gastro.2019.07.012
18. Han D, Hooshangnejad H, Chen CC, Ding K. A Novel Use of Hydrogel as a Dual-Buffer in Stereotactic Body Proton Therapy for Locally Advanced Pancreatic Cancer. *Int J Radiat OncologyBiologyPhysics* (2020) 108(3, Supplement):e326–e7. doi: 10.1016/j.ijrobp.2020.07.779

19. Kim S-H, Ding K, Rao A, He J, Bhutani MS, Herman JM, et al. EUS-Guided Hydrogel Microparticle Injection in a Cadaveric Model. *J Appl Clin Med Phys* (2021) 22(6):83–91. doi: 10.1002/acm2.13266
20. Feng Z, Rao AD, Cheng Z, Shin EJ, Moore J, Su L, et al. Dose Prediction Model for Duodenum Sparing With a Biodegradable Hydrogel Spacer for Pancreatic Cancer Radiation Therapy. *Int J Radiat Oncol Biol Phys* (2018) 102(3):651–9. doi: 10.1016/j.ijrobp.2018.07.184
21. Stolka PJ, Foroughi P, Rendina M, Weiss CR, Hager GD, Boctor EM. Needle Guidance Using Handheld Stereo Vision and Projection for Ultrasound-Based Interventions. In: *Medical Image Computing and Computer-Assisted Intervention – MICCAI 2014*. Cham: Springer International Publishing (2014).
22. Khallaghi S, Sánchez CA, Nouranian S, Sojoudi S, Chang S, Abdi H, et al. *A 2D-3D Registration Framework for Freehand TRUS-Guided Prostate Biopsy* Cham: Springer International Publishing (2015).
23. Fenster A, Bax J, Neshat H, Cool D, Kakani N, Romagnoli C. 3D Ultrasound Imaging in Image-Guided Intervention. *Annu Int Conf IEEE Eng Med Biol Soc* (2014) 2014:6151–4. doi: 10.1109/embc.2014.6945033
24. Hummel J, Figl M, Bax M, Bergmann H, Birkfellner W. 2D/3D Registration of Endoscopic Ultrasound to CT Volume Data. *Phys Med Biol* (2008) 53 (16):4303–16. doi: 10.1088/0031-9155/53/16/006
25. Han-Oh S, Ding K, Song D, Narang A, Wong J, Rong Y, et al. Feasibility Study of Fiducial Marker Localization Using Microwave Radar. *Med Phys* (2021). doi: 10.1002/mp.15197
26. Hu Y, Ahmed HU, Taylor Z, Allen C, Emberton M, Hawkes D, et al. MR to Ultrasound Registration for Image-Guided Prostate Interventions. *Med Image Anal* (2012) 16(3):687–703. doi: 10.1016/j.media.2010.11.003
27. Bonmati E, Hu Y, Gibson E, Uribarri L, Keane G, Gurusami K, et al. Determination of Optimal Ultrasound Planes for the Initialisation of Image Registration During Endoscopic Ultrasound-Guided Procedures. *Int J Comput Assist Radiol Surg* (2018) 13(6):875–83. doi: 10.1007/s11548-018-1762-2
28. Shi RB, Mirza S, Martinez D, Douglas C, Cho J, Irish JC, et al. Cost-Function Testing Methodology for Image-Based Registration of Endoscopy to CT Images in the Head and Neck. *Phys Med Biol* (2020) 65(20):205011. doi: 10.1088/1361-6560/aba8b3
29. Viola P, Jones M. Rapid Object Detection Using a Boosted Cascade of Simple Features. In: *2001 IEEE Computer Society Conference on Computer Vision and Pattern Recognition, Vol 1, Proceedings*. Kauai, HI, USA: IEEE (2001). p. 511–8. doi: 10.1109/cvpr.2001.990517
30. Heinrich MP, Jenkinson M, Bhushan M, Matin T, Gleeson FV, Brady SM, et al. MIND: Modality Independent Neighbourhood Descriptor for Multi-Modal Deformable Registration. *Med Image Anal* (2012) 16(7):1423–35. doi: 10.1016/j.media.2012.05.008
31. De Silva T, Uneri A, Zhang X, Ketcha M, Han R, Sheth N, et al. Real-Time, Image-Based Slice-to-Volume Registration for Ultrasound-Guided Spinal Intervention. *Phys Med Biol* (2018) 63(21):215016. doi: 10.1088/1361-6560/aae761
32. De Silva T, Fenster A, Cool DW, Gardi L, Romagnoli C, Samarabandu J, et al. 2D-3D Rigid Registration to Compensate for Prostate Motion During 3D TRUS-Guided Biopsy. *Med Phys* (2013) 40(2):022904. doi: 10.1118/1.4773873
33. Montoya Zegarra JA, Leite NJ, da Silva Torres R. Wavelet-Based Fingerprint Image Retrieval. *J Comput Appl Math* (2009) 227(2):294–307. doi: 10.1016/j.cam.2008.03.017
34. Powell MJD. A Method for Minimizing a Sum of Squares of Non-Linear Functions Without Calculating Derivatives. *Comput J* (1965) 7(4):303–7. doi: 10.1093/comjnl/7.4.303
35. Tupholme GE. Generation of Acoustic Pulses by Baffled Plane Pistons. *Mathematika* (1969) 16(2):209–24. doi: 10.1112/S0025579300008184
36. Stepanishen PR. The Time-Dependent Force and Radiation Impedance on a Piston in a Rigid Infinite Planar Baffle. *J Acoustical Soc America* (1971) 49 (3B):841–9. doi: 10.1121/1.1912424
37. Stepanishen PR. Transient Radiation From Pistons in an Infinite Planar Baffle. *J Acoustical Soc America* (1971) 49(5B):1629–38. doi: 10.1121/1.1912541
38. Stepanishen PR. Pulsed Transmit/Receive Response of Ultrasonic Piezoelectric Transducers. *J Acoustical Soc Am* (1981) 69(6):1815–27. doi: 10.1121/1.385919
39. Jensen JA. A Model for the Propagation and Scattering of Ultrasound in Tissue. *J Acoust Soc Am* (1991) 89(1):182–90. doi: 10.1121/1.400497
40. Jensen JA, Svendsen NB. Calculation of Pressure Fields From Arbitrarily Shaped, Apodized, and Excited Ultrasound Transducers. *IEEE Trans Ultrason Ferroelectr Freq Control* (1992) 39(2):262–7. doi: 10.1109/58.139123
41. Hooshangnejad H, Youssefian S, Guest JK, Ding K. FEMOSSA: Patient-Specific Finite Element Simulation of the Prostate-Rectum Spacer Placement, a Predictive Model for Prostate Cancer Radiotherapy. *Med Phys* (2021) 48 (7):3438–52. doi: 10.1002/mp.14990
42. Jin P, Hulshof MC, de Jong R, van Hooft JE, Bel A, Alderliesten T. Quantification of Respiration-Induced Esophageal Tumor Motion Using Fiducial Markers and Four-Dimensional Computed Tomography. *Radiother Oncol* (2016) 118(3):492–7. doi: 10.1016/j.radonc.2016.01.005
43. Chao M, Ho H, Joon DL, Chan Y, Spencer S, Ng M, et al. The Use of Tissue Fiducial Markers in Improving the Accuracy of Post-Prostatectomy Radiotherapy. *Radiat Oncol J* (2019) 37(1):43–50. doi: 10.3857/roj.2018.00556
44. Bair RJ, Bair E, Viswanathan AN. A Radiopaque Polymer Hydrogel Used as a Fiducial Marker in Gynecologic-Cancer Patients Receiving Brachytherapy. *Brachytherapy* (2015) 14(6):876–80. doi: 10.1016/j.brachy.2015.08.008
45. Stolka PJ, Foroughi P, Rendina M, Weiss CR, Hager GD, Boctor EM. Needle Guidance Using Handheld Stereo Vision and Projection for Ultrasound-Based Interventions. *Med Image Comput Comput Assist Interv* (2014) 17(Pt 2):684–91. doi: 10.1007/978-3-319-10470-6_85
46. Straus BN. Chronic Pain of Spinal Origin: The Costs of Intervention. *Spine* (2002) 27(22):2614–9. doi: 10.1097/00007632-200211150-00041

Author Disclaimer: The content is solely the responsibility of the authors and does not necessarily represent the official views of the National Institutes of Health.

Conflict of Interest: The authors declare that the research was conducted in the absence of any commercial or financial relationships that could be construed as a potential conflict of interest.

Publisher's Note: All claims expressed in this article are solely those of the authors and do not necessarily represent those of their affiliated organizations, or those of the publisher, the editors and the reviewers. Any product that may be evaluated in this article, or claim that may be made by its manufacturer, is not guaranteed or endorsed by the publisher.

frontiers in Oncology

ORIGINAL RESEARCH
published: 02 December 2021
doi: 10.3389/fonc.2021.767832

Study on Motion Management of Pancreatic Cancer Treated by CyberKnife

Shenghua Jing, Changchen Jiang, Xiaoqin Ji, Xiangnan Qiu, Jing Li, Xiangdong Sun and Xixu Zhu**

Department of Radiation Oncology, East Region Military Command General Hospital, Nanjing, China

Purpose: We investigated the movement characteristics of pancreas and the clinical accuracy of tracking pancreas with the Synchrony Respiratory Tracking System (SRTS) during the CyberKnife treatment. These data provide a clinical data basis for the expansion margins of pancreatic tumor target.

Methods and Materials: Forty-two patients with pancreatic cancer treated by CyberKnife were retrospectively studied. The pancreatic displacement calculated from the x-ray images collected during the time interval between two consecutive movements constituted a data set.

Results: The total mean motion amplitudes and standard deviations of pancreatic tumors in SI, LR, AP, and radial directions were 3.66 ± 1.71 mm, 0.97 ± 0.62 mm, 1.52 ± 1.02 mm, and 1.36 ± 0.49 mm, respectively. The overall mean correlation errors and standard deviations were 0.82 ± 0.46 mm, 0.47 ± 0.33 mm, 0.41 ± 0.24 mm, and 0.98 ± 0.37 mm, respectively. The overall mean prediction errors and standard deviations were 0.57 ± 0.14 mm, 0.62 ± 0.28 mm, 0.39 ± 0.17 mm, and 1.58 ± 0.36 mm, respectively. The correlation errors and prediction errors of pancreatic tumors at different anatomical positions in SI, LR, and AP directions were statistically significant ($p < 0.05$).

Conclusions: The tumor motion amplitude, the tumor location, and the treatment time are the main factors affecting the tracking accuracy. The pancreatic tumors at different anatomical locations should be treated differently to ensure sufficient dose coverage of the pancreatic target area.

Keywords: CyberKnife, expansion margin, pancreatic cancer, SRTS, tumor motion management

OPEN ACCESS

Edited by:
Rosario Mazzola, Sacro Cuore Don Calabria Hospital, Italy

Reviewed by:
Antonio Pontoriero, University of Messina, Italy
Raphael Pfeffer, Assuta Medical Center, Israel

****Correspondence:***
Shenghua Jing
jingsh99@139.com
Xixu Zhu
zhuxixu2005@163.com

Specialty section:
This article was submitted to Radiation Oncology, a section of the journal Frontiers in Oncology

Received: *01 September 2021*
Accepted: *08 November 2021*
Published: *02 December 2021*

Citation:
Jing S, Jiang C, Ji X, Qiu X, Li J, Sun X and Zhu X (2021) Study on Motion Management of Pancreatic Cancer Treated by CyberKnife. Front. Oncol. 11:767832. doi: 10.3389/fonc.2021.767832

INTRODUCTION

Pancreatic cancer is one of the most aggressive tumors, and there is almost no effective treatment method at present. Even in resected patients, the prognosis is still very poor, and the incidence of local recurrence (1) is between 20% and 60%. Stereotactic radiosurgery for pancreatic cancer has shown promising early results (2). SBRT can maximize the protection of surrounding normal tissue

by forming a significant dose gradient around the prescription dose (3). Current evidence suggests that increasing the dose of SBRT may further improve patient outcomes (4). However, the increase of dose is limited by toxicity of surrounding normal organs. During SBRT treatment of pancreas, the surrounding normal organs, stomach, and duodenum (5) are highly sensitive to radiation and adjacent to the pancreas. Due to breathing, digestion, and heartbeat, the boundary between the tumor and nearby organs is blurred. This internal target movement may lead to insufficient local dose of tumor and excessive dose of normal organs at risk (OARs) (6).

In order to reduce the adverse effects of internal organ movement in the treatment, and compensate for the unquantified geometric uncertainty in target tumor location, scholars usually apply general margins to clinical target volume (CTV) to the planning target volume (PTV) margins. This margin estimation may not include the "current" range of motion presented by the pancreas (7, 8). At present, different methods have been proposed to deal with respiratory movement (9), such as the abdominal compression technique (10), respiratory gating technique (11), breath holding technique (12), internal-target-volume (ITV) (13), and simultaneous dynamic tumor tracking (DTT) technique.

Tumor tracking is an advanced method to manage respiratory movement. This method reduces the size of PTV. This can improve targeting and achieve better tumor control, and minimize radiation to normal tissues (14). However, there is little clinical guidance on the management of pancreatic cancer patients.

In this paper, we analyzed 219 data sets recorded by 42 patients with pancreatic cancer. By tracking external markers and implanted fiducials through the stereo x-ray imaging, we monitored the movement data of pancreas during the treatment to quantify the movement of pancreas, and deeply studied the characteristics of fractional internal movement of pancreas. This study aims to answer three key clinical questions: (1) motion characteristics of pancreatic tumors under free breathing; (2) the accuracy and related factors of tracking pancreas by the CyberKnife SRT system; and (3) the expansion margin of the pancreatic target is guided by the movement characteristics of pancreas and the tracking accuracy of the SRT system.

METHODS AND MATERIALS

Data Source

From January 2017 to December 2020, 42 patients with locally advanced pancreatic cancer received CyberKnife radiotherapy using SRTS in the radiotherapy department. The treatment characteristics of patients are listed in **Supplementary Table 1**. Previous research on the number of implanted fiducials showed that less than three fiducials can only calculate the three-dimensional translation deviation, but not the rotation angle deviation. The correlation models established with three or more fiducials are more stable compared with those less than three fiducials. In this study, the pancreas was divided into pancreatic head, neck, body, and tail to analyze the motion management of pancreatic cancer. It was necessary to ensure that the fiducials were in their respective anatomical positions to avoid overlapping and affecting the results. Finally, before treatment, two to five fiducials were implanted into or around the tumor under the guidance of CT or ultrasonic endoscopy. The patient was fixed with a vacuum pad, and his/her arm was placed above the head. Half an hour before CT positioning, the oral contrast agent was taken. During CT positioning, the contrast agent was injected intravenously to obtain the CT sectional image at the end of inspiration, with a layer thickness of 1 mm. The patient breathed freely throughout the treatment. There was no respiratory training for the patient before CT positioning and CyberKnife treatment. The design of the treatment plan was based on end-inspiratory CT image, and PTV was based on the expansion of GTV by 4 mm in all directions. The dose of PTV was defined as an isodose line of 65% to 76%, where 100% was normalized to the maximum dose.

The CyberKnife synchrony tracking system will continuously synchronize the beam transmission and breathing, thereby tracking the tumor targets without interrupting the treatment or moving the patient. After each treatment, the CyberKnife system will save a log file containing the centroid displacement of fiducials in the superior–inferior (SI), left–right (LR), and anterior–posterior (AP) directions. This can be used to analyze the organ movement during the beam transmission. The pancreatic movement is defined as the centroid displacement of fiducials relative to the planned position. Some fiducials migrate or rotate during treatment. If the fiducials exceeded the respective anatomical range, the data sets of the subsequent treatment were discarded. The respiratory motion data, pancreatic motion data, correlation error data and prediction error data were extracted from the treatment log files.

Respiratory Movement Data

Three optical markers were used to record external respiratory signals in real time. These markers were optical fiber terminals for transmitting LED signals (15, 16). Before treatment, three infrared markers were pasted on the patient's chest or abdomen. In this study, the patients were treated with two or three external optical markers. The 3D position of external markers was continuously measured by the stereo camera system at a frequency of about 30 Hz. The distance of each marker along the main axis of movement was recorded for the correlation model.

Baseline Drift

It is reported that the external substitution movement is closely related to the internal tissue movement (17). However, this correlation may change due to a baseline drift of the patient's breathing and gradual relaxation of muscles. Baseline drift was defined as the slow changes of the respiratory baseline in one direction overtime (18). Baseline drift was calculated by subtracting the absolute value of the lowest point from the highest point of the baseline, and then dividing by time. Malinowski (19) investigated patients with lung and pancreatic

tumors, and the relationship between substitutes and tumor location changed in 63% of cases.

Correlation Model

A pair of orthogonal x-ray tubes was used to take many x-ray images of patients. At different stages of the respiratory cycle, the position and direction of several fiducials implanted in or near the tumor were monitored until the SRT system showed that the respiratory cycle was 100% covered. The position of fiducials was automatically extracted from x-ray images, and its three-dimensional coordinates were reconstructed in the patient coordinate system through back projection. Finally, the marker configuration was registered to the marker configuration in the planned CT scanning images to determine the location of the tumor.

Therefore, the average errors of two or three independent models coupled with the external marker were used for each component of the movement. We chose to use the average value, because the output of the correlation model transmitted to the robot controller was the average value of all the external markers.

Prediction Model

Another component of the SRT system is the prediction model. The tumor location information was obtained 115 ms in advance in the SRT system through the prediction model. The tumor identification and beam adjustment were completed within 115 ms through the SRT system (20).

The prediction error was calculated by comparing the predicted location with the actual location after 115 ms. The overall mean errors and the standard deviations of each fraction were calculated for each patient in the SI, LR, and AP directions. The Modeler.log, the Predictor.log, the ModelPoints.log, the Markers.log, and the ERsiData.log were in the log files (21).

Data Analysis for Correlation and Prediction Errors

Treatment may be interrupted by excessive coughing, deep breathing, and slight displacement. In these cases, all existing data points were deleted by resetting the model, and a new correlation model was constructed. The output of the correlation model was used to calculate the amplitude of tumor movement. The amplitude was calculated by using a movement range of 5% to 95%. Only data matched with the dose delivery of the treatment in time were used for analysis.

The predictor provided an estimate of the future target position using the past movement pattern. The output of the correlation model for each direction component was predicted separately. The prediction error was calculated by comparing the predicted location with the actual location after 115 ms. Similarly, only data that matched with the dose delivery of the treatment in time was used for analysis. The maximum prediction error, mean prediction error, and standard deviations of each treatment were calculated. The overall mean errors and the standard deviations of each fraction were calculated for each patient in the SI, LR, and AP directions. The radial error was calculated by summing the square roots in each direction.

Statistical Analysis

Data of each patient were calculated and expressed as overall mean ± standard deviation. The Pearson correlation coefficient r was evaluated with an uncorrelated test. Comparisons were performed using t-test, and the differences were considered significant when p-value was less than 0.05. The statistical analyses are based on SPSS statistics of IBM.

The factors for the tracking accuracy were estimated through the multivariate regression analysis. Correlation errors, prediction errors, and radial errors were specified as dependent variables. Seven parameters, namely, baseline drift, respiratory amplitude, respiratory cycle, treatment time, tumor volume, tumor motion amplitude and tumor anatomical location, were extracted as independent variables.

RESULTS

Tumor Movement Characteristics

The average duration of each data set was 45.9 min, and the average volume of tracking tumor was 11.7 ± 15.3 cm^3. In **Supplementary Table 2**, the overall mean and standard deviation of tumor motion amplitude in SI, LR, AP, and radial directions were 3.65 ± 1.71 mm, 0.97 ± 0.62 mm, 1.52 ± 1.02 mm, and 1.36 ± 0.49 mm, respectively. The overall mean and standard deviation of respiratory amplitude were 21.49 ± 17.05 mm, 5.01 ± 4.99 mm, 6.18 ± 9.57 mm, and 7.62 ± 2.43 mm, respectively. The respiratory amplitude and tumor motion amplitude in SI direction were significantly greater than that in the LR and AP directions ($p = 0.000$).

Tumor Movement Characteristics at Different Anatomical Positions

The centroid movement of fiducials was used as an alternative to pancreatic movement. The value was continuously recorded over time, and 219 data sets were analyzed. The overall mean and standard deviations of tumor motion amplitude in SI, LR, AP, and radial directions are as follows (**Table 1**): (1) pancreatic head: 3.16 ± 1.38 mm, 1.14 ± 0.59 mm, 1.66 ± 0.74 mm, and 1.24 ± 0.29 mm; (2) pancreatic neck: 3.72 ± 0.81 mm, 0.88 ± 0.59 mm, 1.02 ± 0.31 mm, and 1.13 ± 0.20 mm; (3) pancreatic body: 3.85 ± 1.80 mm, 0.92 ± 0.70 mm, 1.42 ± 1.18 mm, and 1.41 ± 0.60 mm; and (4) pancreatic tail: 3.74 ± 2.10 mm, 0.78 ± 0.43 mm, 1.70 ± 1.04 mm, and 1.45 ± 0.42 mm.

Correlation and Prediction Errors

In order to evaluate the correlation and prediction errors in clinical log files, 219 data sets of 42 patients were analyzed. The histograms of correlation and prediction errors in all directions are shown in **Figures 1**, **2**, respectively. The overall mean correlation and prediction errors at different anatomical locations are summarized in **Table 2**. The average correlation and prediction errors in SI, LR, and AP directions were very small, and the average correlation error in the radial direction was less than 1 mm. The correlation errors of tumors located in pancreatic neck in SI, LR, and AP directions were significantly greater than that in other parts (SI direction: 1.02 ± 0.52 mm vs.

TABLE 1 | Overview of pancreatic tumor motion at different anatomical locations.

Locations and directions	Mean (mm)	SD (mm)	Range (mm)
Pancreatic head (*N* = 44)			
SI	3.16	1.38	1.25–5.79
LR	1.14	0.59	0.45–2.54
AP	1.66	0.74	0.59–3.14
Radial	1.24	0.29	0.79–1.84
Pancreatic neck (*N* = 40)			
SI	3.72	0.81	1.29–4.20
LR	0.88	0.59	0.26–1.84
AP	1.02	0.31	0.54–1.64
Radial	1.13	0.20	0.83–1.34
Pancreatic body (*N* = 62)			
SI	3.85	1.80	1.43–11.39
LR	0.92	0.70	0.17–3.08
AP	1.42	1.18	0.22–5.48
Radial	1.41	0.60	0.64–4.18
Pancreatic tail (*N* = 73)			
SI	3.74	2.10	1.99–9.76
LR	0.78	0.43	0.25–1.62
AP	1.70	1.04	0.58–4.57
Radial	1.45	0.42	0.85–2.18

0.84 ± 0.31 mm, 0.83 ± 0.34 mm, and 0.59 ± 0.26 mm; LR direction: 0.57 ± 0.36 mm vs. 0.56 ± 0.20 mm, 0.45 ± 0.25 mm, and 0.23 ± 0.13 mm; AP direction: 0.62 ± 0.27 mm vs. 0.48 ± 0.21 mm, 0.38 ± 0.15 mm, and 0.32 ± 0.17 mm, $p < 0.05$). The prediction errors in SI and AP directions were gradually increased from pancreatic head to pancreatic tail (SI direction: 0.49 ± 0.11 mm vs. 0.54 ± 0.13 mm, 0.58 ± 0.14 mm, and 0.62 ± 0.17 mm; AP direction: 0.35 ± 0.08 mm vs. 0.39 ± 0.11 mm, 0.42 ± 0.14 mm, and 0.43 ± 0.15 mm, $p < 0.05$).

For the anatomical location of pancreatic tumors, the correlation errors and prediction errors of different anatomical locations in SI, LR, and AP directions were statistically significant (correlation errors: $p = 0.006$, 0.00, and 0.038, respectively; prediction errors: $p = 0.011$, 0.048, and 0.031, respectively). However, the correlation errors and prediction errors of pancreatic tumors in radial direction at different anatomical locations were not statistically significant ($p = 0.401$ and 0.196).

Correlations of Tracking Parameters

The correlations of tracking parameters were counted to determine their influence on the correlation errors and

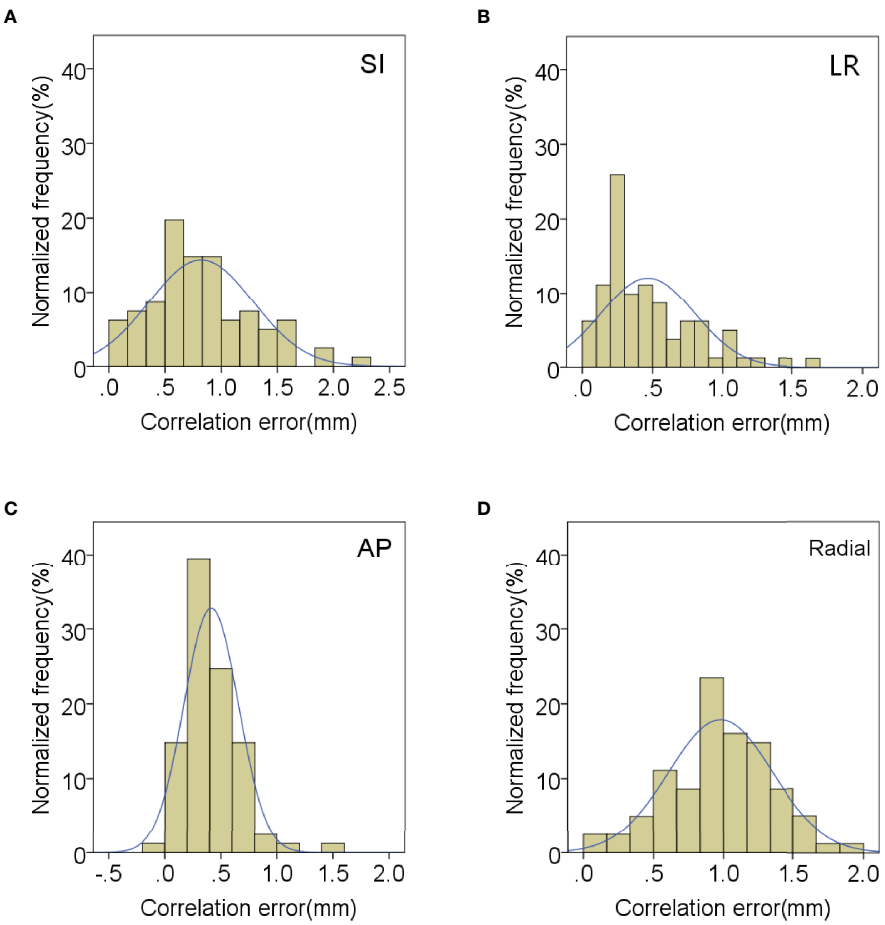

FIGURE 1 | Distribution of mean correlation errors in **(A)** SI, **(B)** LR, **(C)** AP and **(D)** radial directions.

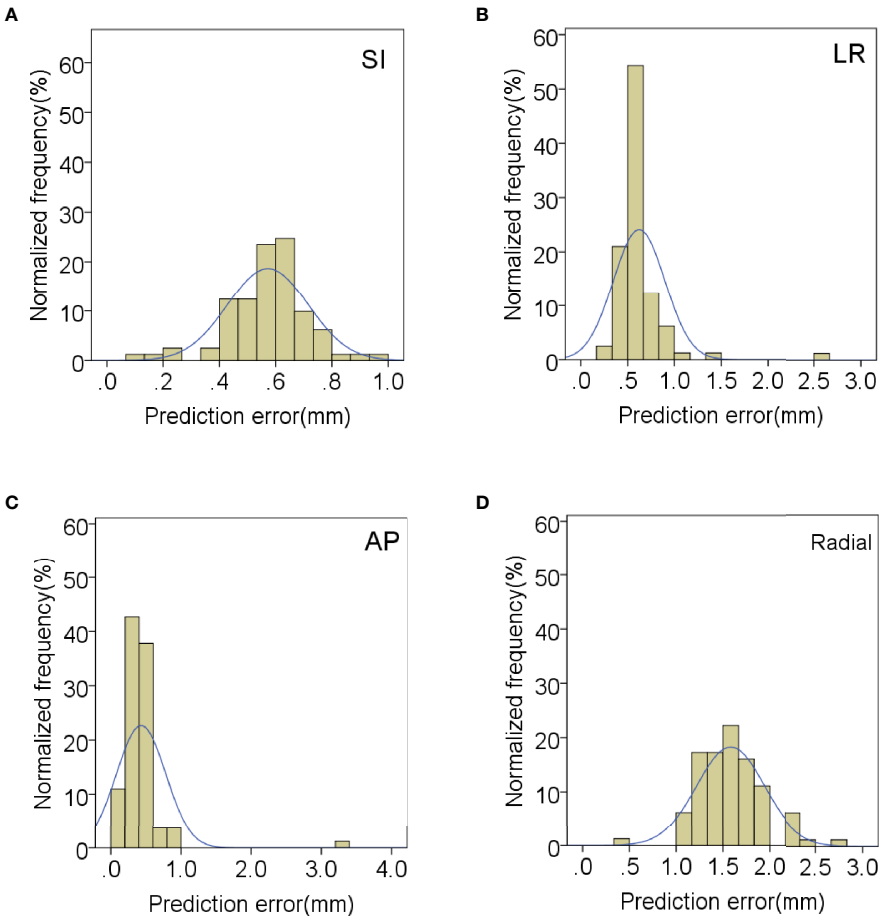

FIGURE 2 | Distribution of mean prediction errors in **(A)** SI, **(B)** LR, **(C)** AP and **(D)** radial directions.

TABLE 2 | Summary of the correlation and prediction errors in 219 fractions.

Locations and directions (Data sets)		Mean (mm)		SD (mm)		Range (mm)	
		Correlation error	Prediction error	Correlation error	Prediction error	Correlation error	Prediction error
Pancreatic head (*N* = 44)	SI	0.84	0.49	0.31	0.11	0.25–4.01	0.11–3.03
	LR	0.56	0.51	0.20	0.10	0.13–2.26	0.28–4.08
	AP	0.48	0.35	0.21	0.08	0.20–2.02	0.1–3.99
	Radial	1.01	1.55	0.36	0.20	0.04–3.39	1.08–7.49
Pancreatic neck (*N* = 40)	SI	1.02	0.54	0.52	0.13	0.17–4.58	0.21–4.51
	LR	0.57	0.61	0.36	0.09	0.08–3.23	0.44–3.91
	AP	0.62	0.39	0.27	0.11	0.12–2.43	0.06–1.38
	Radial	0.95	1.27	0.35	0.13	0.08–3.61	0.34–9.32
Pancreatic body (*N* = 62)	SI	0.83	0.58	0.34	0.14	0.06–3.98	0.26–3.10
	LR	0.45	0.66	0.25	0.19	0.02–2.15	0.36–3.21
	AP	0.38	0.42	0.15	0.14	0.08–1.82	0.13–2.05
	Radial	0.96	1.62	0.41	0.39	0.15–3.26	0.35–7.94
Pancreatic tail (*N* = 73)	SI	0.59	0.62	0.26	0.17	0.15–2.60	0.40–3.41
	LR	0.23	0.71	0.13	0.54	0.06–1.27	0.45–3.39
	AP	0.32	0.43	0.17	0.15	0.11–1.88	0.27–2.59
	Radial	0.89	1.64	0.27	0.48	0.45–2.92	1.14–7.95
Total (*N* = 219)	SI	0.82	0.57	0.46	0.14	0.06–4.58	0.11–4.51
	LR	0.47	0.62	0.33	0.28	0.02–3.23	0.28–4.08
	AP	0.41	0.39	0.24	0.17	0.08–2.43	0.06–3.99
	Radial	0.98	1.58	0.37	0.36	0.04–3.61	0.35–9.51

prediction errors. The influencing factors include individual patient differences (respiratory cycle and respiratory amplitude), tumor anatomical location, tumor movement amplitude, baseline drift, tumor volume, and treatment time. The Pearson correlation was used to analyze the correlation between seven factors and errors. The results of correlation analysis were summarized in **Supplementary Table 3**. The correlation errors and prediction errors in all directions were significantly less correlated with tumor motion amplitude ($r > 0.3$, $p < 0.01$). The correlation errors in the LR direction and the prediction errors in the AP and radial directions were correlated with tumor motion amplitude ($r > 0.5$, $p < 0.01$). The correlation errors in all directions were significantly less correlated with treatment time ($r > 0.3$, $p < 0.01$). The correlation errors in SI, LR, and AP directions were significantly less correlated with tumor anatomical location ($r > 0.3$, $p < 0.01$). The correlation error in the LR direction was correlated with tumor anatomical location ($r > 0.5$, $p < 0.01$). The correlation error in the SI direction was significantly less correlated with baseline drift ($r = -0.3$, $p = 0.006$). The correlation error in the AP direction was significantly less correlated with tumor volume ($r = 0.332$, $p = 0.002$).

The prediction error in the AP direction was significantly less correlated with respiratory amplitude and tumor volume ($r = 0.418$ and 0.385, $p < 0.01$). The prediction error in radial direction was significantly less correlated with tumor volume and respiratory cycle ($r = 0.438$ and -0.317, $p < 0.01$). The prediction error in the LR direction was significantly less correlated with baseline drift and respiratory rate ($r = 0.336$ and -0.446, respectively, $p < 0.01$). The variation of correlation error and prediction error with tumor motion amplitude in all directions is shown in **Figures 3**, **4**, respectively. Other parameters had no significant correlation with correlation or prediction error.

Tumor Expansion Margins

There are three factors for the boundary expansion during the treatment with the CyberKnife SRT system: (I) the aiming accuracy of CyberKnife; (II) correlation error; and (III) prediction error. Previous studies have found that the mechanical error was 0.1 mm and the maximum position uncertainty was 0.3 mm. In the monthly quality assurance program of CyberKnife in Indianapolis (22), the aiming error is 0.5 mm.

In this paper, the correlation errors and prediction errors were correlated with the tumor motion amplitude. In our analysis, the correlation errors were extracted from the model points log file. The mean, minimum, maximum, and standard

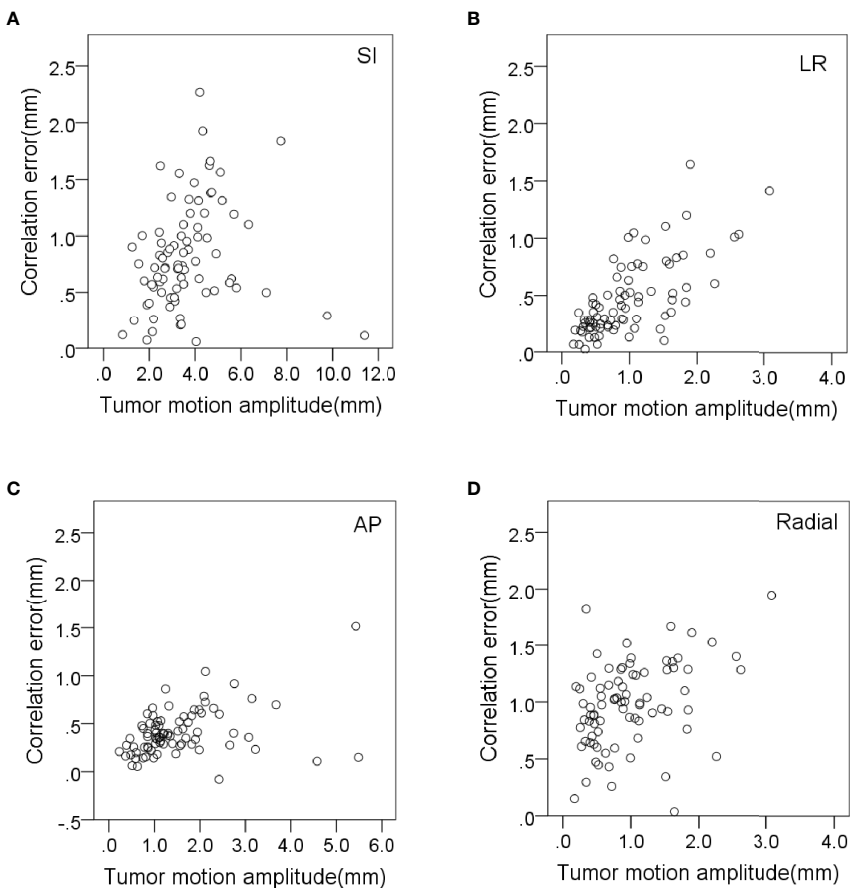

FIGURE 3 | Variation of correlation errors with tumor motion amplitude in **(A)** SI, **(B)** LR, **(C)** AP and **(D)** radial directions.

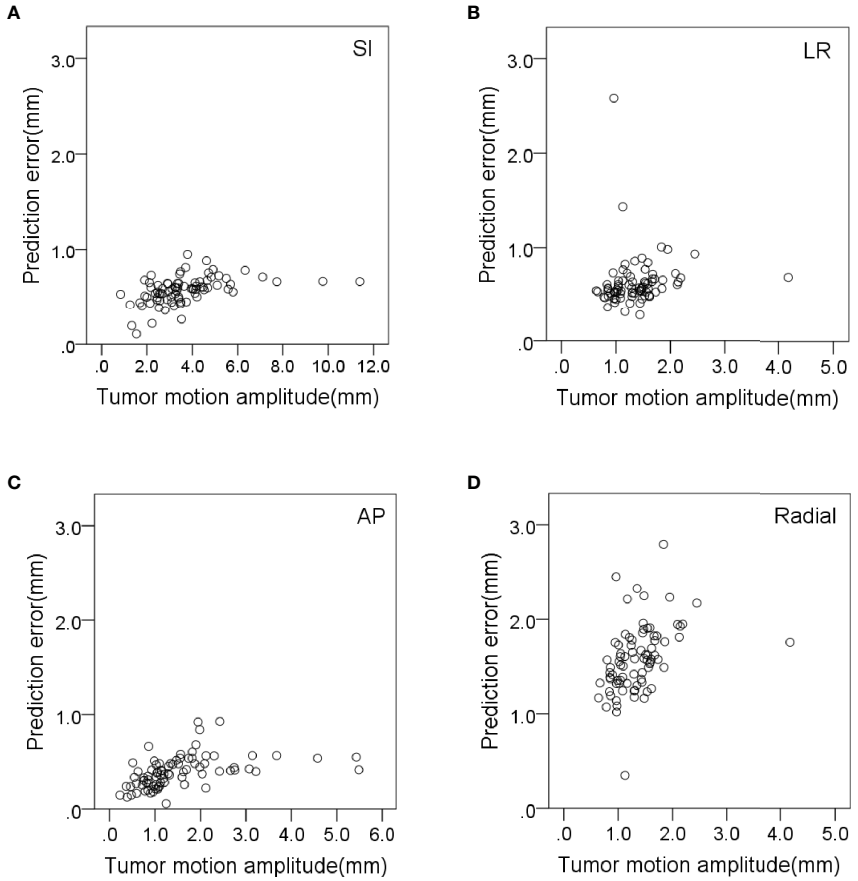

FIGURE 4 | Variation of prediction errors with tumor motion amplitude in **(A)** SI, **(B)** LR, **(C)** AP and **(D)** radial directions.

deviations of the correlation errors and prediction errors of each course were measured. Two standard deviations from the mean value of each anatomical direction were used to ensure 95% coverage of modeling points. Similarly, three standard deviations from the mean value of each anatomical direction were used to ensure 99% coverage of modeling points. However, if the minimum or maximum deviation was less than two standard deviations, they were replaced. The prediction errors in SI, LR, and AP directions did not contain direction information, so the prediction error in radial direction will be greater than the actual value. Therefore, the correlation and prediction errors in the radial direction are not shown in **Table 3**.

DISCUSSION

The results of a study on 4DCT of pancreatic tumors by Sarkar et al. showed the daily breathing inconsistency in the pancreas SBRT (23). This further indicated that the isotropic ITV edge expansion may not be appropriate because it cannot be fully considered the movement of inter- and intra-fractions. This paper analyzed the movement characteristics of pancreatic tumors at different anatomical positions through clinical log files and successfully described the correlation errors, prediction errors, and overall error of the synchronous tumor tracking system. This paper provides appropriate information for the expansion of clinical target GTV.

Tumor motion amplitude was significantly correlated with correlation errors and prediction errors (**Figures 3**, **4**). This indicates that tumors with greater movement amplitude may produce greater tracking errors. Winter et al. studied the relationship between the tracking errors and tumor motion amplitude in patients with liver cancer. They showed that there was a strong correlation between prediction error and target amplitude (24). They also reported that the correlation error was related to the target tumor volume. Our data showed that the correlation error and prediction error in AP direction were less correlated with target tumor volume (r = −0.332 and 0.385, $p < 0.01$).

It is reported that the large respiratory motion amplitude of tumors is related to the baseline drift. This will affect the reproducibility of the position between tumors (25). This correlation will have a significant impact on the calculation of ITV and PTV margins. However, this is inconsistent with our

TABLE 3 | Statistics of correlation, prediction, and total errors of pancreatic tumors at different anatomical locations.

Locations and directions		Correlation error (mm)		Prediction error (mm)		Aiming accuracy (mm)	Total error (mm)	
		95% CI	99% CI	95% CI	99% CI		95% CI	99% CI
Pancreatic head	SI	1.46	1.77	0.83	1	0.5	2.79	3.27
	LR	0.97	1.17	0.71	0.81	0.5	2.18	2.48
	AP	0.9	1.11	0.51	0.59	0.5	1.91	2.2
Pancreatic neck	SI	2.49	3.03	0.62	0.66	0.5	3.61	4.19
	LR	1.59	1.95	0.63	0.68	0.5	2.72	3.13
	AP	1.16	1.43	0.61	0.72	0.5	2.27	2.65
Pancreatic body	SI	1.87	2.39	0.82	0.94	0.5	3.19	3.83
	LR	0.95	1.2	1.04	1.23	0.5	2.49	2.93
	AP	0.68	0.83	0.7	0.84	0.5	1.88	2.17
Pancreatic tail	SI	1.11	1.37	0.9	1.04	0.5	2.51	2.91
	LR	0.49	0.62	1.79	2.33	0.5	2.78	3.45
	AP	0.66	0.83	0.73	0.88	0.5	1.89	2.21

findings. Our results showed that the tumor motion amplitude was not correlated with baseline drift in all directions (**Supplementary Figure 1**).

There are some limitations in this paper. First, tumor motion amplitude was from the movement data of fiducials. Although the use of implanted fiducials in abdominal tumor treatment has increased significantly, some potential problems related to their use need to be further studied. For example, the distance and spatial relationship between multiple implant fiducials and tumors may change because of the treatment and/or disease-related organ swelling or contraction. In addition, due to the differential movement caused by organ deformation, the distance between fiducials and the tumor may change during the respiratory cycle (26).

Second, the relationship among errors and prediction models and motion is based on external LED markers. The correlation and prediction models were constructed based on external LED signals through the SRT system. Therefore, the location of LED may affect the model errors. However, it is difficult to extract specific parameters from each patient's LED marker data, because CyberKnife treatment lasted longer than IMRT. In addition, each patient in this study can breathe freely during CyberKnife treatment. Although these abnormal data have been excluded from statistics, there were some irregular breathing patterns in the respiratory data.

Previous studies on lung patients treated with CyberKnife synchronous tracking system showed that correlation errors were not correlated with the amplitude and variability of LED markers. This indicated that the respiratory model was not the main factor for the tracking accuracy. Our study on pancreatic patients treated with CyberKnife synchronous tracking system shows that correlation errors were not correlated with the amplitude and variability of LED markers in all directions. However, only the prediction errors in AP direction were correlated with the amplitude and variability of LED markers. Our results show that the motion amplitude and location of pancreatic tumors are the main factors for the tracking accuracy. The tumor movement is mainly caused by the patient's breathing. Therefore, it is urgent to determine the effects of breathing mode on the tracking accuracy of different tumors in future clinical studies.

CONCLUSIONS

The inter-fraction movement of pancreas has been considered as one of the main limiting factors for the increase of pancreatic dose during the pancreatic cancer radiotherapy for a long time (27). A detailed understanding of pancreatic movement helps to understand the nature and extent of the adverse effects of uncertainty. In this study, we studied the internal motions and the tracking accuracies of 42 patients with pancreatic cancer treated with CyberKnife and analyzed the tracking accuracies of different anatomical locations. The results show that the tumor motion amplitude, the anatomical location of tumor, and the treatment time were the main factors for the tracking accuracy. The results emphasize the importance of the anatomical location of pancreatic tumors to the expansion margins. The pancreatic tumors at different anatomical locations should be treated differently in the calculation of the expansion margins, because of the amplitude and randomness of pancreatic movement. This is important in future pancreatic radiotherapy to ensure adequate dose coverage of pancreatic targets.

It should be noted that the CT scan images of the treatment plan in this study is based on the end of inspiration rather than the end of expiration. There are many studies on the difference between the end exhale and the end inhale position, and it is true that the end exhale position has many advantages. The end exhale position was the most stable position in the breathing cycle and tumors spent more time closer to the end exhale position than to the end inhale position. We found more overlapping volume of duodenum and stomach at the end inhale position compared to that at the end exhale position in pancreatic cancer with 4DCT scanning. Therefore, a dose to the duodenum was higher when treating during the inspiratory phase than during the expiratory phase. In order to understand the results of this study, we need to distinguish the differences between these two methods.

DATA AVAILABILITY STATEMENT

The original contributions presented in the study are included in the article/**Supplementary Material**. Further inquiries can be directed to the corresponding authors.

AUTHOR CONTRIBUTIONS

SJ and XJ designed the study and wrote the manuscript. SJ, XJ, and JL specially collected clinical data. CJ and XQ used statistics to analyze and integrate research data. Thanks to XS for supervising the manuscript research. Thanks to XZ for the feasibility analysis of the research conclusions and other data. All authors contributed to the article and approved the submitted version.

SUPPLEMENTARY MATERIAL

The Supplementary Material for this article can be found online at: https://www.frontiersin.org/articles/10.3389/fonc.2021.767832/full#supplementary-material

REFERENCES

1. Dagoglu N, Callery M, Moser J, Tseng J, Kent T, Bullock A, et al. Stereotactic Body Radiotherapy (SBRT) Reirradiation for Recurrent Pancreas Cancer. *J Cancer* (2016) 7(3):283–8. doi: 10.7150/jca.13295
2. Chuong MD, Springett GM, Freilich JM, Park CK, Weber JM, Mellon EA, et al. Stereotactic Body Radiation Therapy for Locally Advanced and Borderline Resectable Pancreatic Cancer Is Effective and Well Tolerated. *Int J Radiat Oncol Biol Phys* (2013) 86:516–22. doi: 10.1016/j.ijrobp.2013.02.022
3. Ding Y, Campbell WG, Miften M, Vinogradskiy Y, Jones BL, et al. Quantifying Allowable Motion to Achieve Safe Dose Escalation in Pancreatic SBRT. *Pract Radiat Oncol* (2019) 9(4):432–442. doi: 10.1016/j.prro.2019.03.006
4. Golden EB, Chhabra A, Chachoua A, Adams S, Donach M, Fenton-Kerimian M, et al. Local Radiotherapy and Granulocyte-Macrophage Colony-Stimulating Factor to Generate Abscopal Responses in Patients With Metastatic Solid Tumours: A Proof-of-Principle Trial. *Lancet Oncol* (2015) 16:795–803. doi: 10.1016/S1470-2045(15)00054-6
5. Yang W, Fraass BA, Reznik R, Nissen L, Lo S, Jamil LH, et al. Adequacy of Inhale/Exhale Breathhold CT Based ITV Margins and Image-Guided Registration for Free-Breathing Pancreas and Liver SBRT. *Radiat Oncol (London England)* (2014) 9:11. doi: 10.1186/1748-717X-9-11
6. Ding Y, Barrett HH, Kupinski MA, Vinogradskiy Y, Miften M, Jones BL, et al. Objective Assessment of the Effects of Tumor Motion in Radiation Therapy. *Med Phys* (2019) 46(7):3311–23. doi: 10.1002/mp.13601
7. Cao Y, Zhu X, Ju X, Liu Y, Yu C, Sun Y, et al. Optimization of Dose Distributions of Target Volumes and Organs at Risk During Stereotactic Body Radiation Therapy for Pancreatic Cancer With Dose-Limiting Auto-Shells. *Radiat Oncol* (2018) 13(1):1–6. doi: 10.1186/s13014-018-0956-7
8. Karava K, Ehrbar S, Riesterer O, Roesch J, Glatz S, Klöck S, et al. Potential Dosimetric Benefits of Adaptive Tumor Tracking Over the Internal Target Volume Concept for Stereotactic Body Radiation Therapy of Pancreatic Cancer. *Radiat Oncol* (2017) 12(1):175. doi: 10.1186/s13014-017-0906-9
9. Wilke , Lotte , Andratschke , Nicolaus , Blanck , Oliver , et al. ICRU Report 91 on Prescribing, Recording, and Reporting of Stereotactic Treatments with Small Photon Beams : Statement from the DEGRO/DGMP Working Group Stereotactic Radiotherapy and Radiosurgery. *Strahlenther Onkol* (2019) 195 (3):193–8. doi: 10.1007/s00066-018-1416-x
10. Murray B, Forster K, Timmerman R. Frame-Based Immobilization and Targeting for Stereotactic Body Radiation Therapy. *Med Dosim* (2007) 32:86–91.13. doi: 10.1016/j.meddos.2007.01.005
11. Taniguchi CM, Murphy JD, Eclov N, Atwood TF, Kielar KN, Christman-Skieller C, et al. Dosimetric Analysis of Organs at Risk During Expiratory Gating in Stereotactic Body Radiation Therapy for Pancreatic Cancer. *Int J Radiat Oncol Biol Phys* (2013) 85:1090–5. doi: 10.1016/j.ijrobp.2012.07.2366
12. Dawson LA, Brock KK, Kazanjian S, Fitch D, McGinn CJ, Lawrence TS, et al. The Reproducibility of Organ Position Using Active Breathing Control (ABC) During Liver Radiotherapy. *Int J Radiat Oncol Biol Phys* (2001) 51:1410–21. doi: 10.1016/S0360-3016(01)02653-0
13. Ehrbar S, Jöhl A, Tartas A, Stark LS, Riesterer O, Klöck S, et al. Itv, Midventilation, Gating or Couch Tracking - A Comparison of Respiratory Motion-Management Techniques Based on 4D Dose Calculations. *Radiother Oncol* (2017) 124:80–8. doi: 10.1016/j.radonc.2017.05.016
14. Papalazarou C, Klop GJ, Milder MTW, Marijnissen JPA, Gupta V, Heijmen BJM, et al. CyberKnife With Integrated CT-On-Rails: System Description and First Clinical Application for Pancreas SBRT. *Med Phys* (2017) 44:4816–27. doi: 10.1002/mp.12432
15. Inoue M, Okawa K, Taguchi J, Hirota Y, Ohta S. Factors Affecting the Accuracy of Respiratory Tracking of the Image-Guided Robotic Radiosurgery System. *Japanese J Radiol* (2019) 37(10):727–34. doi: 10.1007/s11604-019-00859-7
16. Ferris WS, Kissick MW, Bayouth JE, Culberson WS, Smilowitz JB. Evaluation of Radixact Motion Synchrony for 3D Respiratory Motion: Modeling Accuracy and Dosimetric Fidelity. *J Appl Clin Med Phys* (2020) 21(9):96–106. doi: 10.1002/acm2.12978
17. Zhang H, Zhao G, David D, Yaoqin X. Determination of Acquisition Frequency for Intrafractional Motion of Pancreas in CyberKnife Radiotherapy. *Sci World J* (2014) 2014:408019. (2014-5-13). doi: 10.1155/2014/408019
18. Akino Y, Shiomi H, Sumida I, Isohashi F, Seo Y, Suzuki O, et al. Impacts of Respiratory Phase Shifts on Motion Tracking Accuracy of the CyberKnife Synchrony Respiratory Tracking System. *Med Phys* (2019) 46(9):3757–66. doi: 10.1002/mp.13523
19. Malinowski K, McAvoy TJ, George R, Dietrich S, D'Souza WD. Incidence of Changes in Respiration-Induced Tumor Motion and Its Relationship With Respiratory Surrogates During Individual Treatment Fractions. *Int J Radiat Oncol Biol Phys* (2012) 82:1665–73. doi: 10.1016/j.ijrobp.2011.02.048
20. Subedi G, Karasick T, Grimm J, Jain S, Xue J, Xu Q, et al. Factors That May Determine the Targeting Accuracy of Image-Guided Radiosurgery. *Med Phys* (2015) 42(10):6004–10. doi: 10.1118/1.4930961
21. Hoogeman M, Prévost J-B, Nuyttens J, P?Ll J, Levendag P, Heijmen B, et al. Clinical Accuracy of the Respiratory Tumor Tracking System of the CyberKnife: Assessment by Analysis of Log Files. *Int J Radiat Oncol Biol Phys* (2009) 74(1):297–303. doi: 10.1016/j.ijrobp.2008.12.041
22. Pepin EW, Wu H, Zhang Y, Lord B. Correlation and Prediction Uncertainties in the CyberKnife Synchrony Respiratory Tracking System. *Med Phys* (2011) 38(7):4036–44. doi: 10.1118/1.3596527
23. Sarkar V, Lloyd S, Paxton A, Huang L, Su FC, Tao R, et al. Daily Breathing Inconsistency in Pancreas SBRT: A 4DCT Study. *J Gastrointestinal Oncol* (2018) 9(6):989–95. doi: 10.21037/jgo.2018.09.08
24. Winter JD, Wong R, Swaminath A, Chow T. Accuracy of Robotic radiosurgical Liver Treatment Throughout the Respiratory Cycle. *Int JRadiat Oncol Biol Phys* (2015) 93:916–24. doi: 10.1016/j.ijrobp.2015.08.031
25. Chan MK, Kwong DL, Tam E, Tong A, Ng SCY. Quantifying Variability of Intrafractional Target Motion in Stereotactic Body Radiotherapy for Lung Cancers. *J Appl Clin Med Phys* (2013) 14(5):140–52. doi: 10.1120/jacmp.v14i5.4319
26. Pettersson N, Oderinde OM, Murphy J, Simpson D, Cervio LI. Intrafractional Relationship Changes Between an External Breathing Signal and Fiducial Marker Positions in Pancreatic Cancer Patients. *J Appl Clin Med Phys* (2020) 21:153–61. doi: 10.1002/acm2.12841
27. Casamassima F, Cavedon C, Francescon P, Stancanello J, Avanzo M, Cora S, et al. Use of Motion Tracking in Stereotactic Body Radiotherapy: Evaluation of

Uncertainty in Off-Target Dose Distribution and Optimization Strategies. *Acta Oncol* (2016) 45(7):943–7. doi: 10.1080/02841860600908962

Conflict of Interest: The authors declare that the research was conducted in the absence of any commercial or financial relationships that could be construed as a potential conflict of interest.

Publisher's Note: All claims expressed in this article are solely those of the authors and do not necessarily represent those of their affiliated organizations, or those of the publisher, the editors and the reviewers. Any product that may be evaluated in this article, or claim that may be made by its manufacturer, is not guaranteed or endorsed by the publisher.

frontiers in Oncology

ORIGINAL RESEARCH
published: 06 January 2022
doi: 10.3389/fonc.2021.730646

Competing Risk Analysis of Outcomes of Unresectable Pancreatic Cancer Patients Undergoing Definitive Radiotherapy

*Yi-Lun Chen[1], Chiao-Ling Tsai[1,2], Jason Chia-Hsien Cheng[1,3,4], Chun-Wei Wang[1,2,5,6], Shih-Hung Yang[2,7], Yu-Wen Tien[8] and Sung-Hsin Kuo[1,2,3,6]**

[1] Division of Radiation Oncology, Department of Oncology, National Taiwan University Hospital, Taipei, Taiwan, [2] Cancer Research Center, College of Medicine, National Taiwan University, Taipei, Taiwan, [3] Graduate Institute of Oncology, College of Medicine, National Taiwan University, Taipei, Taiwan, [4] Graduate Institute of Clinical Medicine, College of Medicine, National Taiwan University, Taipei, Taiwan, [5] Department of Radiology, National Taiwan University Hospital, College of Medicine, National Taiwan University, Taipei, Taiwan, [6] Department of Radiation Oncology, National Taiwan University Cancer Center, College of Medicine, National Taiwan University, Taipei, Taiwan, [7] Division of Medical Oncology, Department of Oncology, National Taiwan University Hospital, Taipei, Taiwan, [8] Department of Surgery, National Taiwan University Hospital, Taipei, Taiwan

OPEN ACCESS

Edited by:
James Chow,
University of Toronto, Canada

Reviewed by:
Jian-Guo Zhou,
Zunyi Medical University, China
Carla Hajj,
Memorial Sloan Kettering Cancer Center, United States

***Correspondence:**
Sung-Hsin Kuo
shkuo101@ntu.edu.tw

Specialty section:
This article was submitted to Radiation Oncology, a section of the journal Frontiers in Oncology

Received: *25 June 2021*
Accepted: *08 December 2021*
Published: *06 January 2022*

Citation:
Chen Y-L, Tsai C-L, Cheng JC-H, Wang C-W, Yang S-H, Tien Y-W and Kuo S-H (2022) Competing Risk Analysis of Outcomes of Unresectable Pancreatic Cancer Patients Undergoing Definitive Radiotherapy. Front. Oncol. 11:730646. doi: 10.3389/fonc.2021.730646

Purpose: We investigated potential factors, including clinicopathological features, treatment modalities, neutrophil-to-lymphocyte ratio (NLR), carbohydrate antigen (CA) 19-9 level, tumor responses correlating with overall survival (OS), local progression (LP), and distant metastases (DMs), in patients with locally advanced pancreatic cancer (LAPC) who received definitive radiotherapy (RT).

Methods: We retrospectively analyzed demographic characteristics; biologically effective doses (BED_{10}, calculated with an α/β of 10) of RT; and clinical outcomes of 57 unresectable LAPC (all pancreatic adenocarcinoma) patients receiving definitive RT using modern techniques with and without systemic therapy between January 2009 and March 2019 at our institution. We used Response Evaluation Criteria in Solid Tumors (RECIST) version 1.1 to evaluate the radiographic tumor response after RT. The association between prognostic factors and OS was assessed using the Kaplan–Meier analysis and a Cox regression model, whereas baseline characteristics and treatment details were collected for competing-risk regression of the association with LP and DM using the Fine–Gray model.

Results: A median BED_{10} of 67.1 Gy resulted in a disease control rate of 87.7%, and the median OS was 11.8 months after a median follow-up of 32.1 months. The 1-year OS rate, cumulative incidences of LP, and DM were 49.2%, 38.5%, and 62.9%, respectively. Multivariate analyses showed that pre-RT NLR ≥3.5 (adjusted hazard ratio [HR] = 8.245, $p < 0.001$), CA19-9 reduction rate ≥50% (adjusted HR = 0.261, $p = 0.005$), RT without concurrent chemoradiotherapy (adjusted HR = 5.903, $p = 0.004$), and administration of chemotherapy after RT (adjusted HR = 0.207, $p = 0.03$) were independent prognostic factors for OS. Positive lymph nodal metastases (adjusted subdistribution HR [sHR] = 3.712, $p = 0.003$) and higher tumor reduction after RT (adjusted sHR = 0.922, $p < 0.001$)

were significant prognostic factors for LP, whereas $BED_{10} \geq 67.1$ Gy (adjusted sHR = 0.297, $p = 0.002$), CA19-9 reduction rate ≥50% (adjusted sHR = 0.334, $p = 0.023$), and RT alone (adjusted sHR = 2.633, $p = 0.047$) were significant prognostic factors for DM.

Conclusion: Our results indicate that pre-RT NLR and post-RT monitoring of CA19-9 and tumor size reduction can help identify whether patients belong to the good or poor prognostic group of LAPC. The incorporation of new systemic treatments during and after a higher BED_{10} RT dose for LAPC patients is warranted.

Keywords: pancreatic cancer, radiotherapy, competing risk, survival, risk factors

INTRODUCTION

Pancreatic cancer is one of the most devastating gastrointestinal malignancies in Taiwan and is the seventh leading cause of cancer-related deaths in both men and women (1). Despite the advances in chemotherapy, molecular target agents, immunotherapy, and radiotherapy (RT) techniques, the 5-year overall survival (OS) rate in patients with pancreatic cancer remains unsatisfactory, with a 91% mortality rate in 2018 (2). Furthermore, owing to limited screening methodologies, pancreatic cancer patients are often diagnosed with the late-stage disease at initial presentation; only 50% of these patients were free from distant metastases (DMs), of which 60% were considered to have unresectable or locally advanced disease (3). Regardless of the efforts made to achieve a better outcome, the improved median OS rate to 24 months among patients with locally advanced pancreatic cancer (LAPC) was rather disappointing (4, 5).

Conflicting results have illustrated the intriguing role of RT in the treatment of LAPC. For example, the Eastern Cooperative Oncology Group (ECOG) 4201 trial revealed that LAPC patients receiving concurrent RT with single-agent chemotherapy (gemcitabine) had a better OS than those receiving gemcitabine alone (11.1 vs. 9.2 months, $p = 0.017$) (6). In contrast, the LAP07 trial disclosed a lack of OS benefit with the addition of 54 Gy RT to capecitabine (concurrent chemoradiotherapy [CCRT]) for patients with LAPC after 4 months of gemcitabine with and without erlotinib (from first randomization, chemotherapy versus CCRT; 16.5 versus 15.2 months, $p = 0.83$) (7). However, from the data of the first randomization, patients who received CCRT had a significantly decreased local progression (LP) rate (32% versus 64%, $p = 0.03$) and the trend of prolonged progression-free survival (PFS) (9.9 versus 8.4 months, $p = 0.06$) than patients who received chemotherapy alone (7). According to historical autopsy studies, approximately 8%–15% of patients with pancreatic cancer die from calamitous local disease without DMs, implying the importance of local control for preventing LP-associated morbidities and mortalities in LAPC patients (8–10). Indeed, the National Comprehensive Cancer Network has recorded CCRT as one of the standard clinical practices for caring for LAPC patients with good performance status (11).

Previous retrospective studies have identified several prognostic factors for OS, LP, and DM (12–14). However, the aforementioned prognostic factors may be underestimated or unevaluated using standard statistical analyses because of the high mortality rate of LAPC patients. To overcome competing risks that appear to preclude the occurrence of the primary events of interest, recent studies have advocated the use of competing-risk regression analyses and the Fine–Gray model, both of which can serve as a better parameter and offer robust results for cancer patients in the presence of competing risks (15–17).

In the current study, we retrospectively analyzed the clinicopathological features, treatment modalities, and clinical outcomes (including OS, LP, and DM) of unresectable LAPC patients who received definitive RT using modern techniques with and without systemic treatment at our institute over the past years. Additionally, we assessed potential prognostic factors, including pre-RT carbohydrate antigen (CA) 19-9, reduction percentage of CA19-9, tumor size, pre-RT neutrophil-to-lymphocyte ratio (NLR), pre-RT platelet-to-lymphocyte ratio (PLR), and pre-RT neutrophil-to-monocyte ratio (NMR), the use of concurrent systemic therapy (chemotherapy or molecular target agents), whether or not post-RT chemotherapy was administered, biologically effective doses (BED_{10}, calculated with an α/β of 10) of RT, and the planning target volume (PTV) delineation that were associated with OS, LP, and DM in our patients. Considering that pancreatic cancer itself is a disease with a high mortality rate, and patients may not experience LP or DM before death, we adapted the Fine–Gray model in the competing-risk analyses of LP or DM in our patients to avoid erroneous statistics.

Abbreviations: RT, radiotherapy; OS, overall survival; DMs, distant metastases; LAPC, locally advanced pancreas cancer; ECOG, Eastern Cooperative Oncology Group; CCRT, concurrent chemoradiotherapy; LP, local progression; PFS, progression-free survival; CA19-9, carbohydrate antigen 19-9; NLR, neutrophil-to-lymphocyte ratio; PLR, platelet-to-lymphocyte ratio; NMR, neutrophil-to-monocyte ratio; BED, biologically effective doses; PTV, planning target volume; IMRT, intensity-modulated radiation therapy; VMAT, volumetric modulated arc therapy; KPS, Karnofsky Performance Status; GTV, gross target volume; CTV, clinical target volume; 5-FU, fluorouracil; RECIST, Response Evaluation Criteria in Solid Tumors; CR, complete remission; PR, partial remission; HR, hazard ratio; sHR, subdistribution hazard ratio; SBRT, stereotactic body radiation therapy; SD, stable disease; DCR, disease control rate; RTOG, Radiation Therapy Oncology Group; WBCs, white blood cells.

MATERIALS AND METHODS

Population of Patients With Locally Advanced Pancreatic Cancer

This retrospective cohort study included consecutive patients with histology-proven inoperable pancreatic adenocarcinoma

who underwent intensity-modulated radiation therapy (IMRT), volumetric modulated arc therapy (VMAT), or tomotherapy with and without CCRT or molecular target agents between January 2009 and March 2019. Patients who did not complete the full course of RT were excluded. Baseline characteristics and treatment details, including sex, age, Karnofsky Performance Status (KPS), radiation dose and fractions, biologically effective dose for pancreatic tumor (BED_{10}, calculated with an α/β of 10), tumor location, regional nodal metastases status, pre-RT CA19-9, chemotherapy regimens, and molecular target agents, were comprehensively reviewed and documented. Post-RT CA19-9 was also recorded. The reduction percentage of CA19-9 was defined as the difference between pre- and nadir of post-RT CA19-9 and then divided by pre-RT CA19-9. We checked the blood cell count data, including neutrophils, lymphocytes, monocytes, and platelets at baseline pre-RT for all patients. We further assessed whether NLR, PLR, and NMR at pre-RT baselines are associated with clinical outcomes, including OS, LP, and DM, in our patients with LAPC who received definitive RT with and without systemic therapy (chemotherapy or molecular target agents). The cutoff values of PLR or NMR were determined using the receiver operating characteristic curve. This retrospective study was approved by the Research Ethical Committee of National Taiwan University Hospital.

Radiotherapy Technique and Chemotherapy Regimens During Radiotherapy

The patient was immobilized in the supine position with the arms up. An abdominal CT was performed for treatment planning with a slice thickness ≤5 mm. Additionally, either a respiratory control device or a four-dimensional CT was required for simulation. The gross target volume (GTV) was defined as the primary tumor with involved lymph nodes. GTV plus 0.5–1.0 cm and elective nodal irradiation were delineated in the clinical target volume (CTV). An expansion of 0.5–1.0 cm from the CTV formed the PTV. Constraints for normal tissue in pancreatic cancer patients who received RT at our institution were routinely implemented using the following criteria: <30 Gy for mean liver dose (those patients who met the criteria of at least 700 ml of normal liver received less than 15 Gy); <50 Gy for maximal spinal cord dose; <60 Gy for the maximal stomach, duodenum, and bowel doses; and not more than 30% of the total kidney volume received ≥18 Gy.

In addition to the classic CCRT regimens using fluorouracil (5-FU), capecitabine, gemcitabine, cisplatin, or oxaliplatin in LAPC patients, current combination treatments are being used with S-1, an oral form of tegafur, gimeracil, and oteracil, and RT in patients with LAPC or metastatic pancreatic cancer (18–20). In this retrospective study, we assessed the different chemotherapy regimens, including oral 5-FU, capecitabine, S-1, and intravenous cisplatin, gemcitabine, or oxaliplatin.

Radiographic Assessment

The largest tumor diameter was measured prior to RT as baseline and assessed at the time of the best radiographic response. The percentage reduction in tumor size was defined as the difference between pre-RT tumor diameter and post-RT tumor diameter and then divided by the pre-RT tumor diameter. In the current study, we utilized the revised Response Evaluation Criteria in Solid Tumors (RECIST) version 1.1 to assess the best radiographic response after completing RT (21). Complete remission (CR) was defined as the disappearance of a visible tumor, and partial remission (PR) was defined as at least a 30% decrease in diameter; LP was defined as an increase in size of at least 20%.

Statistical Analysis

OS was calculated from the date of starting RT until death, loss of follow-up, or July 2020. The cumulative incidence of LP and DMs was evaluated from the start of RT until the event date, and adjusted death was considered a competing risk. Univariate analysis was performed, and variables with p-values <0.1 were included in the multivariate analysis. Cox's proportional hazard model (22) was used to identify prognostic factors for OS, and the results were presented as hazard ratio (HR) with 95% CI. Risk factors for LP and DM were assessed using the Fine–Gray model, a more sophisticated statistical approach (16); death was considered a competing risk and presented as a subdistribution HR (sHR) with 95% CI. In the current study, the interaction terms were included in the Fine–Gray model if they were significant. All statistical analyses were performed using either the SAS 9.4 software (SAS Institute Inc., Cary, NC) or the statistical software system R version 3.6.2, packages "survival", "cmprsk", "prodlim", and "survminer". Statistical significance was set at p-values <0.05.

RESULTS

Patient Characteristics

A total of 57 patients were included in our cohort, among whom one patient was inoperable owing to underlying medical conditions and 56 patients had unresectable LAPC. All patients received either conventional or hypofractionated RT using IMRT, VMAT, or tomotherapy techniques, except for one patient who underwent stereotactic body radiation therapy (SBRT). The majority of patients (53%) were administered RT using 55 Gy in 25 fractions, and 39% of the cohort were administered 50–50.4 Gy in 25–28 fractions. The median BED_{10} for the total cohort was 67.1 (range 49–74) Gy. CCRT was administered to 82% of patients, among whom 18 (32%) received 5-FU- or capecitabine-based chemotherapy, 13 received gemcitabine (23%), and 10 received oral S-1 (18%). The demographic baseline characteristics, doses, and fractions of the RT and RT techniques are listed in **Table 1**.

Best Radiographic Response

Overall, a decrease in tumor size was observed in 31 patients (54.4%). One patient achieved CR, and this patient was still alive 8 years after starting RT, whereas four patients achieved PR, with an overall response rate of 8.8%. Forty-five patients (78.9%) had stable disease (SD). However, seven patients (12.3%) had local progressive disease. An example of a patient who achieved PR after RT is shown in **Figures 1A–D**. The overall disease control rate (DCR), consisting of CR, PR, and SD, was 87.7%. A waterfall plot of the change in tumor diameter after completion of RT in each patient is shown in **Figure 1E**.

TABLE 1 | Clinical characteristics of patients and pancreatic tumor.

Characteristics	*N* = 57 n (%)
Median age, years (range)	63 (41–85)
Gender	
Male	35 (61)
Female	22 (39)
Tumor location	
Head region	39 (68)
Non-head region	18 (32)
Positive regional nodal metastases	34 (60)
Median KPS (range)	80 (70–100)
Median pre-RT CA19-9, U/ml (range)	342 (<1–14,958)
Median post-RT CA19-9 nadir, U/ml (range)	158 (<1–24,000)
Median pre-RT neutrophil-to-lymphocyte ratio (range)	2.41 (0.78–48)
Median pre-RT platelet-to-lymphocyte ratio (range)	49.62 (8.74–395)
Median pre-RT neutrophil-to-monocyte ratio (range)	9.73 (2.68–600)
Received induction chemotherapy	36 (63)
Concurrent chemoradiotherapy regimen	
Gemcitabine-based	13 (23)
Fluorouracil/capecitabine-based	18 (32)
Cisplatin/oxaliplatin-based	4 (7)
S-1-based	10 (18)
Other	2 (4)
No concurrent chemoradiotherapy	10 (18)
Received post-RT chemotherapy	50 (88)
Median RT dose, Gy (range)	55 (30–60)
Median RT fraction (range)	25 (3–28)
Median BED_{10}, Gy_{10} (range)	67.1 (49–74)
Median largest tumor diameter, cm (range)	4.2 (0.5–13)
Median planning target volume, cm^3 (range)	355 (32–948)

KPS, Karnofsky performance status; RT, radiotherapy; CA19-9, carbohydrate antigen 19-9; BED, biological equivalent dose.

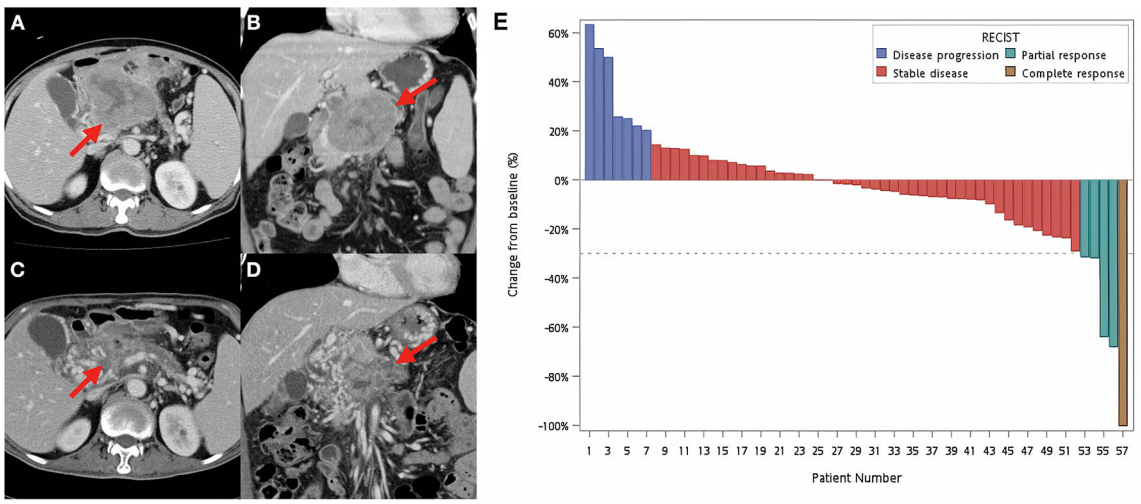

FIGURE 1 | Example of a responsive tumor and waterfall plot for all patients. Contrast-enhanced CT images before **(A, B)** and after **(C, D)** definitive concurrent chemoradiotherapy. **(A, B)** A huge necrotic pancreatic tumor around 10 cm was found (red arrows). The patient was treated by concurrent fluorouracil, erlotinib with 55 Gy in 25 fractions to the pancreatic tumor, and 45 Gy in 25 fractions to the adjacent lymphatics. **(C, D)** Follow-up CT images were obtained 1 month after the completion of definitive chemoradiotherapy. The red arrows identified the radiotherapy-treated tumor with significant volume reduction. **(E)** Waterfall plot of each patient at the best radiographic response according to Response Evaluation Criteria in Solid Tumors (RECIST) guidelines (version 1.1).

Local Progression, Distant Metastases, and Overall Survival

After a median follow-up of 32.1 months (range 3.5–97.6 months), the 1-, 2-, and 3-year OS rates were 49.2% (95% CI = 37.1%–65.3%), 15.4% (95% CI = 7.5%–31.4%), and 4.1% (95% CI = 0.7%–25%), respectively, with a median OS of 11.8 months (range 1.8–97.6 months) (**Figure 2A**). The cumulative incidence of LP at 6 months, 1 year, and 2 years was 19.6% (95% CI = 10.4%–30.9%), 38.5% (95%

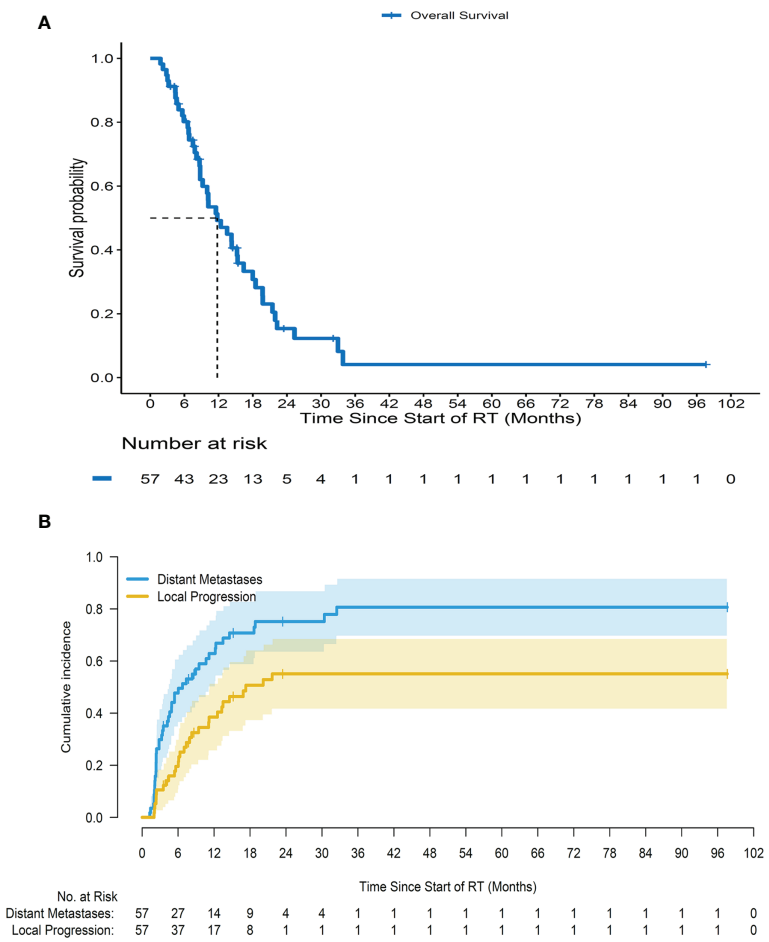

FIGURE 2 | Survival curves for all patients. **(A)** Overall survival for all patients since starting radiotherapy. **(B)** Cumulative incidence of local progression and distant metastases for a cohort of patients since starting radiotherapy after adjusting death as a competing risk.

CI = 25.5%–51.3%), and 55.1% (95% CI = 40%–67.8%), respectively; and that of DM after adjusting for death as a competing risk was 47.7% (95% CI = 34.1%–60.1%), 62.9% (95% CI = 48.4%–74.4%), and 75.2% (95% CI = 60.5%–85.1%), respectively (**Figure 2B**). The common locations of the first DM were the liver (58%) and peritoneum (40%) in all metastatic cases.

Prognostic Factors for Patients With Locally Advanced Pancreatic Cancer Who Received Curative Radiotherapy

In the univariate analysis, the nadir of post-RT CA19-9 of less than 90 U/ml, lower pre-RT NLR (NLR < 3.5), greater CA19-9 reduction percentage (≥50%), higher tumor size reduction percentage at the best radiographic response, larger PTV, the administration of systemic therapy during RT, and administration of post-RT chemotherapy were significantly associated with better OS; and positive nodal status was related to better OS (**Table 2**). However, pre-RT PLR (≥95) and pre-RT NMR (≥15) were not significantly associated with OS (**Table 2**).

After multivariate analysis, pre-RT NLR ≥3.5 (adjusted HR = 8.2451; 95% CI = 2.685–25.32, $p < 0.001$) and the lack of administration of concurrent systemic therapy (most chemotherapy) (adjusted HR = 5.903; 95% CI = 1.757–19.83, $p = 0.004$) were independent poor prognostic factors for worse OS, whereas CA19-9 reduction ≥50% (adjusted HR = 0.261; 95% CI = 0.101–0.672, $p = 0.005$) and post-RT chemotherapy (adjusted HR = 0.207; 95% CI = 0.05–0.857, $p = 0.03$) were factors significantly associated with a better OS in these patients (**Table 2**).

For the risk factors of LP (**Table 3**), two factors, including positive nodal status (adjusted sHR = 3.712; 95% CI = 1.563–8.817, $p = 0.003$) and tumor size reduction percentage at the best radiographic response (adjusted sHR = 0.922 per percent increase in tumor size reduction; 95% CI = 0.898–0.947, $p < 0.001$), remained significant in the multivariate regression analyses. Different CCRT regimens are not listed in **Table 3** because of the lack of primary events per chemotherapy regimen in our cohort, which led to inaccurate statistics results (23).

In the prediction of DM after completion of RT (**Table 4**), multivariate analysis showed three significant predictive factors for

TABLE 2 | Univariate and multivariate analyses of factors associated with overall survival in inoperable pancreatic adenocarcinoma (Cox regression).

Variables	Univariate analysis		Multivariate analysis[a]	
	HR (95% CI)	*p*-Value	HR (95% CI)	*p*-Value
Sex (male)	1.026 (0.553–1.902)	0.935		
Advanced age (years)	0.992 (0.964–1.021)	0.592		
Tumor location				
Head	Reference			
Non-head	0.719 (0.38–1.363)	0.313		
Larger tumor	1.041 (0.867–1.251)	0.664		
Positive nodal metastases	0.569 (0.31–1.044)	**0.069**	0.962 (0.357–2.592)	0.939
$BED_{10} \geq 67.1\ Gy_{10}$	0.852 (0.459–1.581)	0.611		
Pre-RT CA19-9 > 90 U/ml	1.776 (0.885–3.563)	0.106		
Post-RT CA19-9 nadir > 90 U/ml	2.773 (1.327–5.798)	**0.007**	1.813 (0.703–4.675)	0.218
Pre-RT NLR ≥ 3.5	2.349 (1.167–4.728)	**0.017**	8.245 (2.685–25.32)	**<0.001**
Pre-RT PLR ≥ 95	0.718 (0.311–1.655)	0.437		
Pre-RT NMR ≥ 15	1.461 (0.715–2.983)	0.299		
CA19-9 reduction ≥ 50%	0.237 (0.11–0.508)	**<0.001**	0.261 (0.101–0.672)	**0.005**
Higher tumor size reduction %	0.17 (0.036–0.802)	**0.025**	0.983 (0.958–1.008)	0.177
Bigger PTV (cm^3)	0.997 (0.995–0.999)	**0.011**	1 (0.998–1.003)	0.869
Received induction chemotherapy	0.65 (0.346–1.224)	0.182		
Received post-RT chemotherapy	0.318 (0.127–0.798)	**0.015**	0.207 (0.05–0.857)	**0.03**
Concurrent chemoradiotherapy regimen				
Gemcitabine-based	Reference		Reference	
Fluorouracil/capecitabine-based	0.8 (0.355–1.804)	0.591	1.514 (0.486–4.72)	0.475
Cisplatin/oxaliplatin-based	2.077 (0.568–7.599)	0.269	2.196 (0.203–23.8)	0.518
S-1-based	0.922 (0.334–2.541)	0.875	0.374 (0.089–1.563)	0.178
Others	1.046 (0.132–8.312)	0.966	10.6 (0.83–135.4)	0.069
None	2.772 (1.099–6.992)	**0.031**	5.903 (1.757–19.83)	**0.004**

HR, hazard ratio; BED_{10}, biologically effective dose; RT, radiotherapy; CA19-9, carbohydrate antigen 19-9; NLR, neutrophil-to-lymphocyte ratio; PLR, platelet-to-lymphocyte ratio; NMR, neutrophil-to-monocyte ratio; PTV, planning target volume.

[a]All factors with p < 0.1 in univariate analysis were entered in a multivariate Cox regression model.

In the univariate analysis, the bold values represented those with p value < 0.1; whereas in the multivariate analysis, it represented those with p value < 0.05.

TABLE 3 | Univariate and multivariate analyses of factors associated with local progression in inoperable pancreatic adenocarcinoma (Fine–Gray model).

Variables	Univariate analysis		Multivariate analysis[a]	
	sHR (95% CI)	*p*-Value	sHR (95% CI)	*p*-Value
Sex (male)	1.22 (0.598–2.49)	0.59		
Advanced age (years)	0.968 (0.928–1.01)	0.12		
Tumor location				
Head	Reference			
Non-head	1.75 (0.879–3.48)	0.11		
Larger tumor	1.05 (0.86–1.27)	0.65		
Positive nodal metastases	1.92 (0.893–4.12)	**0.095**	3.712 (1.563–8.817)	**0.003**
$BED_{10} \geq 67.1\ Gy_{10}$	1.07 (0.522–2.19)	0.86		
Pre-RT CA19-9 > 90 U/ml	0.951 (0.444–2.04)	0.9		
Post-RT CA19-9 nadir > 90 U/ml	0.91 (0.433–1.91)	0.8		
Pre-RT NLR ≥ 3.5	1.05 (0.47–2.37)	0.9		
Pre-RT PLR ≥ 95	0.879 (0.354–2.18)	0.78		
Pre-RT NMR ≥ 15	0.789 (0.297–2.09)	0.63		
CA19-9 reduction ≥ 50%	0.957 (0.445–2.06)	0.91		
Higher tumor size reduction %	0.935 (0.916–0.955)	**<0.001**	0.922 (0.898–0.947)	**<0.001**
Bigger PTV (cm^3)	1 (0.998–1)	0.64		
Received induction chemotherapy	1.66 (0.724–3.82)	0.23		
Received post-RT chemotherapy	2.37 (0.549–10.2)	0.25		

sHR, subdistribution hazard ratio; BED_{10}, biologically effective dose; RT, radiotherapy; CA19-9, carbohydrate antigen 19-9; NLR, neutrophil-to-lymphocyte ratio; PLR, platelet-to-lymphocyte ratio; NMR, neutrophil-to-monocyte ratio; PTV, planning target volume.

[a]All factors with p < 0.1 in univariate analysis were entered in a multivariate Fine–Gray model.

In the univariate analysis, the bold values represented those with p value < 0.1; whereas in the multivariate analysis, it represented those with p value < 0.05.

TABLE 4 | Univariate and multivariate analyses of factors associated with distant metastases in inoperable pancreatic adenocarcinoma (Fine–Gray model).

Variables	Univariate analysis		Multivariate analysis[a]	
	sHR (95% CI)	*p*-Value	sHR (95% CI)	*p*-Value
Sex (male)	1.16 (0.665–2.02)	0.6		
Advanced age (years)	0.983 (0.956–1.01)	0.25		
Tumor location				
Head	Reference			
Non-head	1.18 (0.666–2.08)	0.57		
Larger tumor	0.988 (0.837–1.17)	0.89		
Positive nodal metastases	0.716 (0.38–1.35)	0.3		
$BED_{10} \geq 67.1\ Gy_{10}$	0.539 (0.302–0.962)	**0.037**	0.297 (0.137–0.645)	**0.002**
Pre-RT CA19-9 > 90 U/ml	1.56 (0.791–3.1)	0.2		
Post-RT CA19-9 nadir > 90 U/ml	2.17 (1.13–4.14)	**0.019**	1.345 (0.634–2.856)	0.44
Pre-RT NLR ≥ 3.5	1.46 (0.686–3.09)	0.33		
Pre-RT PLR ≥ 95	0.602 (0.26–1.39)	0.24		
Pre-RT NMR ≥ 15	1.85 (0.835–4.09)	0.13		
CA19-9 reduction ≥ 50%	0.327 (0.168–0.635)	**<0.001**	0.334 (0.165–0.676)	**0.023**
Higher tumor size reduction %	0.98 (0.966–0.995)	**0.008**	0.991 (0.971–1.011)	0.36
Bigger PTV (cm^3)	1 (0.998–1)	0.95		
Received induction chemotherapy	0.633 (0.335–1.2)	0.16		
Received post-RT chemotherapy	1.56 (0.483–0.5.05)	0.46		
Concurrent chemoradiotherapy regimen				
Gemcitabine-based	Reference		Reference	
Fluorouracil/capecitabine-based	1.08 (0.493–2.36)	0.85	1.775 (0.696–4.528)	0.23
Cisplatin/oxaliplatin-based	0.617 (0.106–3.59)	0.59	1.908 (0.332–10.96)	0.47
S-1-based	0.942 (0.33–2.69)	0.91	0.786 (0.262–2.362)	0.67
Others	0.674 (0.162–2.81)	0.59	1.817 (0.247–13.37)	0.56
None	2.466 (1.106–5.5)	**0.027**	2.633 (1.011–6.86)	**0.047**

sHR, subdistribution hazard ratio; BED_{10}, biologically effective dose; RT, radiotherapy; CA19-9, carbohydrate antigen 19-9; NLR, neutrophil-to-lymphocyte ratio; PLR, platelet-to-lymphocyte ratio; NMR, neutrophil-to-monocyte ratio; PTV, planning target volume.

[a]*All factors with p < 0.1 in univariate analysis were entered in a multivariate Fine–Gray model.*

In the univariate analysis, the bold values represented those with p value < 0.1; whereas in the multivariate analysis, it represented those with p value < 0.05.

DM, including $BED_{10} \geq 67.1$ Gy (adjusted sHR = 0.297; 95% CI = 0.137–0.645, $p = 0.002$), CA19-9 reduction ≥50% (adjusted sHR = 0.334; 95% CI = 0.165–0.676, $p = 0.023$), and lack of administration of concurrent systemic therapy (most chemotherapy) (adjusted sHR = 2.633; 95% CI = 1.011–6.96, $p = 0.047$).

In addition, we analyzed and checked the interactions with all variables that were associated with LP and DM, and we found none of them to be significant. Regarding LP, there was no significant association between negative node metastases and a greater reduction in tumor size (**Supplementary Table S1**). There was no significant interaction between multivariate analyses of DM-related factors, such as $BED_{10} \geq 67.1$ Gy, post-RT CA19-9 nadir reduction >90 U/ml, CA19-9 reduction ≥50%, and higher tumor size reduction (**Supplementary Table S2**).

DISCUSSION

Several studies have investigated the appropriate regimens for treating patients with LAPC and showed that the incorporation of RT may provide survival benefits for these patients. However, the role of RT in treating LAPC patients remains elusive; for example, a phase III randomized 2000-01 FFCD/SFRO study revealed that additional RT only causes excessive side effects but with few advantages (24). In this study, we demonstrated that RT with concurrent systemic therapy (most chemotherapy) provided the optimal median OS of 14.0 months, which is in accordance with the median OS ranging from 8 to 16 months obtained from the CCRT arm of randomized phase III trials for LAPC patients (6, 7, 24). In our study, among 57 patients, 36 received induction chemotherapy followed by RT with or without concurrent systemic therapy. Of these 36 patients, the median times to progression and OS after starting chemotherapy were 12.1 and 18.7 months, respectively. The 1- and 2-year OS rates for these patients (n = 36) were 88.1% and 36.9%, respectively. Our results further support the results from the Taiwan Cooperative Oncology Group phase II study of 30 patients with LAPC who received induction chemotherapy with 6 courses of gemcitabine, oxaliplatin, and high-dose 5-FU and leucovorin followed by RT with 50.4 Gy at 28 fractions concurrent with weekly low-dose gemcitabine, in which the median times to progression and OS for these patients were 14.7 and 18.3 months; the 1- and 2-year OS rates were 86.7% and 27.4%, respectively (25).

In addition, our study is the first to use the multivariate Fine–Gray model and sHR (15, 17) to evaluate the risk factors for LP and DM in patients with unresectable pancreatic cancer who underwent RT with the goal of offering a better clinical prediction model. We demonstrated that positive regional lymph node metastases and reduced tumor size reduction are two factors that significantly correlate with LP, and $BED_{10} < 67.1$ Gy, reduction of CA19-9 <50%, and no administration of concurrent systemic therapy are important factors significantly associated with DM. Furthermore, pre-RT NLR ≥3.5, reduction of CA19-9 <50%, and no administration of chemotherapy during RT and post-RT are important prognostic factors for poor OS.

Affirmed by the Radiation Therapy Oncology Group (RTOG) 9704 study, a randomized phase III trial, postoperative CA19-9 ≥90 before adjuvant CCRT was associated with increased locoregional recurrence and distant failure, and poor OS (26, 27). Likewise, pre-RT CA19-9 levels, post-RT CA19-9 nadir status, and the magnitude of CA19-9 reduction have been reported as important factors that are associated with DM and OS in patients with LAPC (28–32). For example, Yang et al. showed that LAPC patients with a decreased reduction of CA19-9 >90% compared with baseline CA19-9 level after receiving CCRT experienced a significantly better median OS than those without a decreased reduction of CA19-9 >90% (16.2 vs. 7.5%, $p = 0.01$) (29). Vainshtein et al. showed that among LAPC patients treated with IMRT concurrent with gemcitabine, CA19-9 >90 U/ml at baseline or during CCRT was significantly associated with poor OS and PFS (30). In another retrospective analysis of 28 patients with unresectable LAPC receiving CCRT, Zschaeck et al. revealed that the reduction in CA19-9 levels during and after CCRT was significantly associated with OS ($p = 0.049$) and LP ($p = 0.029$) (32). These results are further supported by our current findings showing that the greater reduction (≥ 50%) of CA19-9 after RT significantly correlated with better OS and less DM.

In addition to the prognostic significance of CA19-9, NLR also proved its value in predicting OS and tumor metastases in patients with LAPC. Previous studies have demonstrated that neutrophils, the most important part of white blood cells (WBCs), participate in the process of metastasis in a variety of cancers, including pancreatic cancer (33, 34). Tao et al. revealed a strong interaction between circulating tumor cells and WBCs obtained from tumor-adjacent vessels of operable pancreatic cancer patients and reported that NLR ≥ 2.5 was significantly associated with a higher incidence of DM in these patients (35). In a meta-analysis of data from 1,804 patients with pancreatic cancer, Yang et al. revealed that a higher NLR was significantly associated with poor OS in these patients, irrespective of surgery or chemotherapy, or a combination of both treatments (36). Furthermore, Yang et al. showed a significant relationship between higher NLR and aggressive behaviors and rapid DM in these patients (36).

For unresectable LAPC and metastatic pancreatic cancer patients who received systemic chemotherapy, a higher NLR was also significantly associated with poor OS (37, 38). In two studies of prognostic factors in borderline operable pancreatic ductal adenocarcinoma patients who underwent surgery following neoadjuvant CCRT, Kubo et al. showed that after neoadjuvant CCRT, the NLR was ≥3, and Kawai et al. reported that post-neoadjuvant CCRT lymphocyte-to-monocyte ratio <3.0, which was significantly associated with poor OS (39, 40). In addition, Lee et al. showed that NLR ≥ 1.89 significantly correlated with poor OS and PFS in LAPC patients receiving neoadjuvant or definitive CCRT (41). However, the use of NLR cutoff values in the aforementioned results is not consistent (ranging from 1.89 to 5). In the current study, we demonstrated that pre-RT NLR ≥ 3.5, a crucially independent poor prognostic factor for OS in LAPC patients receiving definitive RT, indicating that higher neutrophils may promote proliferation, anti-apoptosis, and angiogenesis and lower lymphocytes may hamper anti-tumor response and immune response and thus cause progression of pancreatic cancer cells.

However, in *post-hoc* analyses of patients with advanced non-small cell lung cancer from four international multicenter trials (OAK, BIRCH, POPLAR, and FIR trials), Zhou et al. showed that baseline NLR was not significantly associated with OS (42). These patients received either a single agent of atezolizumab, a blockade of PD-L1, or a single chemotherapy agent (docetaxel) (42). In their analyses, the NLR and PLR on the first day of treatment cycle 5 and NMR on the first day of treatment cycle 3 were significant prognostic biomarkers for OS in patients who were treated with atezolizumab when compared with those receiving docetaxel (42). In the current study, we found that pre-RT PLR and NMR were not associated with LP, DM, and OS in patients with LAPC who received RT with or without systemic therapy (most chemotherapy). Further investigation of PLR and NMR at baseline before RT in a large cohort of LAPC patients receiving RT is warranted.

Our current results further reinforced the importance of tumor size reduction after completing RT with a median dose of 55 Gy as a protective factor for LP and DM in patients with LAPC and thus contributed to the improved OS of these patients. These findings indicate that greater responses of pancreatic cancer cells to the optimal RT dose in LAPC patients are warranted. In the current study, we also found that patients receiving CCRT had a better OS and less DM than those receiving RT alone. Our results are in line with those of previous reports showing that CCRT provided superior outcomes with respect to OS or distant control than RT alone (5, 6, 43). In two prospective phase II studies, RT combined with oral S-1 resulted in a 27% to 41% overall response rate with few grade 3 toxicities in patients with LAPC (18, 44). Moreover, the non-inferiority phase III trial showed that monotherapy with S-1 is not inferior to monotherapy with gemcitabine and combined S-1 with gemcitabine in patients with LAPC and metastatic pancreatic cancer (45). Although there are no randomized trials to evaluate the superiority of either gemcitabine or S-1 based CCRT in patients with LAPC, our current study revealed that the administration of oral S-1 is not inferior to gemcitabine in combination with RT for LAPC patients in terms of OS and DM.

Previous studies revealed that the prescription of higher radiation dose (photon therapy, BED_{10} > 70 Gy; proton therapy, 54.0–67.5 Gy in 25–33 fractions) significantly correlated with improved OS in patients with LAPC (44–46). In accordance with a previous study (46–48), our findings revealed that patients receiving a higher RT dose (BED_{10} ≥ 67.1 Gy) were less likely to develop DM, although there was no association between higher RT dose and OS. As for the positive nodal status being identified as a risk factor for LP in our study, this finding supported the fact that the presence of nodal metastases significantly correlated with the shorter 1-year freedom from LP in LAPC patients who received SBRT and chemotherapy (most gemcitabine) (49). It was noted that the administration of chemotherapy following RT significantly correlated with better OS in our patients, suggesting that the addition of maintenance treatment after CCRT for LAPC patients is warranted.

Although this study analyzed a few LAPC patients who received definitive RT with and without systemic treatment, the dose, the treated field, and the technique of RT in the current study reflect real-world clinical practice for treating unresectable LAPC patients.

In addition to potential weaknesses, including retrospective analyses and confounding factors (such as comorbidity and selection bias), the key strength that highlighted our work is the use of the Fine–Gray model to eliminate bias introduced by the competing risk in predicting LP and DM.

CONCLUSION

In summary, our results indicate that nodal negative LAPC patients with lower pre-RT NLR (<3.5) receiving higher RT dose (BED_{10} ≥ 67.1 Gy) concurrent with chemotherapy and post-RT chemotherapy and having CA19-9 reduction ≥50% and higher tumor size reduction after RT are expected to have a better OS. Investigations of novel treatments, including the incorporation of new chemotherapy, molecular target agents, or immune therapy, during and after RT for LAPC patients with higher pre-RT NLR (≥3.5) or positive regional lymph nodes are warranted. Future prospective studies should be designed according to the aforementioned risk stratifications, including pre-RT NLR, post-RT CA19-9, and tumor reductions to offer individualized clinical management for patients with LAPC.

DATA AVAILABILITY STATEMENT

The original contributions presented in the study are included in the article/**Supplementary Material**. Further inquiries can be directed to the corresponding author.

ETHICS STATEMENT

The studies involving human participants were reviewed and approved by the Research Ethical Committee of National Taiwan University Hospital, and written informed consent was obtained from the individual(s) for the publication of any potentially identifiable images or data included in this manuscript. The ethics committee waived the requirement of written informed consent for participation.

AUTHOR CONTRIBUTIONS

S-HK designed the study. Y-LC, C-LT, JC, C-WW, S-HY, Y-WT, and S-HK recruited the patients and acquired the data. Y-LC and S-HK interpreted the radiographic images. Y-LC and S-HK analyzed and interpreted the data. Y-LC conducted the statistical analysis. Y-LC, C-LT, and S-HK prepared the manuscript. Y-LC and S-HK edited the manuscript and reviewed the manuscript. All authors contributed to the article and approved the submitted version.

FUNDING

This research was funded by the Ministry of Science and Technology, Taiwan, No. MOST 110-2314-B-002-219-MY3, No. MOST 110-2811-B-002-576-MY3, No. MOST 109-2314-B-002-200-MY3, and No. MOST 110-2314-B-002-278-MY3; and the National Taiwan University Hospital, Taiwan, No. NTUH 110-S4965.

SUPPLEMENTARY MATERIAL

The Supplementary Material for this article can be found online at: https://www.frontiersin.org/articles/10.3389/fonc.2021.730646/full#supplementary-material

REFERENCES

1. *Cancer Registry Annual Report 2018*. Taiwan. Available at: https://www.hpa.gov.tw/Pages/Detail.aspx?nodeid=269&pid=13498 (Accessed March 10, 2021).
2. Rawla P, Sunkara T, Gaduputi V. Epidemiology of Pancreatic Cancer: Global Trends, Etiology and Risk Factors. *World J Oncol* (2019) 10(1):10–27. doi: 10.14740/wjon1166
3. Lau SC, Cheung WY. Evolving Treatment Landscape for Early and Advanced Pancreatic Cancer. *World J Gastrointest Oncol* (2017) 9(7):281–92. doi: 10.4251/wjgo.v9.i7.281
4. Suker M, Beumer BR, Sadot E, Marthey L, Faris JE, Mellon EA, et al. FOLFIRINOX for Locally Advanced Pancreatic Cancer: A Systematic Review and Patient-Level Meta-Analysis. *Lancet Oncol* (2016) 17(6):801–10. doi: 10.1016/s1470-2045(16)00172-8
5. Yang SH, Kuo YH, Tien YW, Hsu C, Hsu CH, Kuo SH, et al. Inferior Survival of Advanced Pancreatic Cancer Patients Who Received Gemcitabine-Based Chemotherapy But did Not Participate in Clinical Trials. *Oncology* (2011) 81 (3-4):143–50. doi: 10.1159/000330817
6. Loehrer PJSr, Feng Y, Cardenes H, Wagner L, Brell JM, Cella D, et al. Gemcitabine Alone Versus Gemcitabine Plus Radiotherapy in Patients With Locally Advanced Pancreatic Cancer: An Eastern Cooperative Oncology Group Trial. *J Clin Oncol* (2011) 29(31):4105–12. doi: 10.1200/JCO.2011.34.8904
7. Hammel P, Huguet F, van Laethem JL, Goldstein D, Glimelius B, Artru P, et al. Effect of Chemoradiotherapy vs Chemotherapy on Survival in Patients With Locally Advanced Pancreatic Cancer Controlled After 4 Months of Gemcitabine With or Without Erlotinib: The LAP07 Randomized Clinical Trial. *JAMA* (2016) 315(17):1844–53. doi: 10.1001/jama.2016.4324
8. Iacobuzio-Donahue CA, Fu B, Yachida S, Luo M, Abe H, Henderson CM, et al. DPC4 Gene Status of the Primary Carcinoma Correlates With Patterns of Failure in Patients With Pancreatic Cancer. *J Clin Oncol* (2009) 27 (11):1806–13. doi: 10.1200/JCO.2008.17.7188
9. Mao C, Domenico DR, Kim K, Hanson DJ, Howard JM. Observations on the Developmental Patterns and the Consequences of Pancreatic Exocrine Adenocarcinoma. Findings 154 autopsies. *Arch Surg* (1995) 130(2):125–34. doi: 10.1001/archsurg.1995.01430020015001
10. Kamisawa T, Isawa T, Koike M, Tsuruta K, Okamoto A. Hematogenous Metastases of Pancreatic Ductal Carcinoma. *Pancreas* (1995) 11(4):345–9. doi: 10.1097/00006676-199511000-00005
11. National Comprehensive Cancer Network. *Pancreatic Adenocarcinoma (Version 2.2021)*. Available at: https://www.nccn.org/professionals/physician_gls/pdf/pancreatic.pdf (Accessed March, 10, 2021).
12. Kishi T, Nakamura A, Itasaka S, Shibuya K, Matsumoto S, Kanai M, et al. Pretreatment C-Reactive Protein Level Predicts Outcome and Patterns of Failure After Chemoradiotherapy for Locally Advanced Pancreatic Cancer. *Pancreatology* (2015) 15(6):694–700. doi: 10.1016/j.pan.2015.09.016

13. Arcelli A, Guido A, Buwenge M, Simoni N, Mazzarotto R, Macchia G, et al. Higher Biologically Effective Dose Predicts Survival in SBRT of Pancreatic Cancer: A Multicentric Analysis (PAULA-1). *Anticancer Res* (2020) 40 (1):465–72. doi: 10.21873/anticanres.13975
14. Goto Y, Nakamura A, Ashida R, Sakanaka K, Itasaka S, Shibuya K, et al. Clinical Evaluation of Intensity-Modulated Radiotherapy for Locally Advanced Pancreatic Cancer. *Radiat Oncol* (2018) 13(1):118. doi: 10.1186/s13014-018-1063-5
15. Dutz A, Lock S. Competing Risks in Survival Data Analysis. *Radiother Oncol* (2019) 130:185–9. doi: 10.1016/j.radonc.2018.09.007
16. Fine JP, Gray RJ. A Proportional Hazards Model for the Subdistribution of a Competing Risk. *J Am Stat Assoc* (1999) 94(446):496–509. doi: 10.1080/01621459.1999.10474144
17. Dignam JJ, Zhang Q, Kocherginsky M. The Use and Interpretation of Competing Risks Regression Models. *Clin Cancer Res* (2012) 18(8):2301–8. doi: 10.1158/1078-0432.CCR-11-2097
18. Ikeda M, Ioka T, Ito Y, Yonemoto N, Nagase M, Yamao K, et al. A Multicenter Phase II Trial of S-1 With Concurrent Radiation Therapy for Locally Advanced Pancreatic Cancer. *Int J Radiat Oncol Biol Phys* (2013) 85 (1):163–9. doi: 10.1016/j.ijrobp.2012.03.059
19. Yang SH, Shao YY, Lin CC, Kuo SH, Cheng AL, Yeh KH. A Phase I Study of S-1-Based Concurrent Chemoradiotherapy Followed by Gemcitabine and S-1 in Metastatic Pancreatic Adenocarcinoma. *Anticancer Res* (2018) 38(8):4805–12. doi: 10.21873/anticanres.12790
20. Wu L, Zhou Y, Fan Y, Rao S, Ji Y, Sun J, et al. Consolidative Chemoradiotherapy After Induced Chemotherapy Is an Optimal Regimen for Locally Advanced Pancreatic Cancer. *Front Oncol* (2019) 9:1543. doi: 10.3389/fonc.2019.01543
21. Eisenhauer EA, Therasse P, Bogaerts J, Schwartz LH, Sargent D, Ford R, et al. New Response Evaluation Criteria in Solid Tumours: Revised RECIST Guideline (Version 1.1). *Eur J Cancer* (2009) 45(2):228–47. doi: 10.1016/j.ejca.2008.10.026
22. Cox DR. Regression Models and Life-Tables. *J R Stat Soc: Ser B (Methodological)* (1972) 34(2):187–202. doi: 10.1111/j.2517-6161.1972.tb00899.x
23. Austin PC, Allignol A, Fine JP. The Number of Primary Events Per Variable Affects Estimation of the Subdistribution Hazard Competing Risks Model. *J Clin Epidemiol* (2017) 83:75–84. doi: 10.1016/j.jclinepi.2016.11.017
24. Chauffert B, Mornex F, Bonnetain F, Rougier P, Mariette C, Bouche O, et al. Phase III Trial Comparing Intensive Induction Chemoradiotherapy (60 Gy, Infusional 5-FU and Intermittent Cisplatin) Followed by Maintenance Gemcitabine With Gemcitabine Alone for Locally Advanced Unresectable Pancreatic Cancer. Definitive Results of the 2000-01 FFCD/SFRO Study. *Ann Oncol* (2008) 19(9):1592–9. doi: 10.1093/annonc/mdn281
25. Ch'ang HJ, Lin YL, Wang HP, Chiu YF, Chang MC, Hsu CH, et al. Induction Chemotherapy With Gemcitabine, Oxaliplatin, and 5-Fluorouracil/Leucovorin Followed by Concomitant Chemoradiotherapy in Patients With Locally Advanced Pancreatic Cancer: A Taiwan Cooperative Oncology Group Phase II Study. *Int J Radiat Oncol Biol Phys* (2011) 81(5):e749–57. doi: 10.1016/j.ijrobp.2010.10.034
26. Berger AC, Garcia MJr., Hoffman JP, Regine WF, Abrams RA, Safran H, et al. Postresection CA 19-9 Predicts Overall Survival in Patients With Pancreatic Cancer Treated With Adjuvant Chemoradiation: A Prospective Validation by RTOG 9704. *J Clin Oncol* (2008) 26(36):5918–22. doi: 10.1200/JCO.2008.18.6288
27. Regine WF, Winter K, Abrams RA, Safran H, Kessel IL, Chen Y, et al. Postresection CA19-9 and Margin Status as Predictors of Recurrence After Adjuvant Treatment for Pancreatic Carcinoma: Analysis of NRG Oncology RTOG Trial 9704. *Adv Radiat Oncol* (2018) 3(2):154–62. doi: 10.1016/j.adro.2018.01.003
28. Golden DW, Novak CJ, Minsky BD, Liauw SL. Radiation Dose >/=54 Gy and CA 19-9 Response are Associated With Improved Survival for Unresectable, non-Metastatic Pancreatic Cancer Treated With Chemoradiation. *Radiat Oncol* (2012) 7:156. doi: 10.1186/1748-717X-7-156
29. Yang GY, Malik NK, Chandrasekhar R, Ma WW, Flaherty L, Iyer R, et al. Change in CA 19-9 Levels After Chemoradiotherapy Predicts Survival in Patients With Locally Advanced Unresectable Pancreatic Cancer. *J Gastrointest Oncol* (2013) 4(4):361–9. doi: 10.3978/j.issn.2078-6891.2013.045
30. Vainshtein JM, Schipper M, Zalupski MM, Lawrence TS, Abrams R, Francis IR, et al. Prognostic Significance of Carbohydrate Antigen 19-9 in Unresectable Locally Advanced Pancreatic Cancer Treated With Dose-Escalated Intensity Modulated Radiation Therapy and Concurrent Full-Dose Gemcitabine: Analysis of a Prospective Phase 1/2 Dose Escalation Study. *Int J Radiat Oncol Biol Phys* (2013) 86(1):96–101. doi: 10.1016/j.ijrobp.2012.11.020
31. Sutera PA, Bernard ME, Gill BS, Harper KK, Quan K, Bahary N, et al. One- vs. Three-Fraction Pancreatic Stereotactic Body Radiation Therapy for Pancreatic Carcinoma: Single Institution Retrospective Review. *Front Oncol* (2017) 7:272. doi: 10.3389/fonc.2017.00272
32. Zschaeck S, Blumke B, Wust P, Kaul D, Bahra M, Riess H, et al. Dose-Escalated Radiotherapy for Unresectable or Locally Recurrent Pancreatic Cancer: Dose Volume Analysis, Toxicity and Outcome of 28 Consecutive Patients. *PloS One* (2017) 12(10):e0186341. doi: 10.1371/journal.pone.0186341
33. Di Carlo E, Forni G, Musiani P. Neutrophils in the Antitumoral Immune Response. *Chem Immunol Allergy* (2003) 83:182–203. doi: 10.1159/000071561
34. Templeton AJ, McNamara MG, Seruga B, Vera-Badillo FE, Aneja P, Ocana A, et al. Prognostic Role of Neutrophil-to-Lymphocyte Ratio in Solid Tumors: A Systematic Review and Meta-Analysis. *J Natl Cancer Inst* (2014) 106(6): dju124. doi: 10.1093/jnci/dju124
35. Tao L, Zhang L, Peng Y, Tao M, Li L, Xiu D, et al. Neutrophils Assist the Metastasis of Circulating Tumor Cells in Pancreatic Ductal Adenocarcinoma: A New Hypothesis and a New Predictor for Distant Metastasis. *Medicine* (2016) 95(39):e4932. doi: 10.1097/MD.0000000000004932
36. Yang JJ, Hu ZG, Shi WX, Deng T, He SQ, Yuan SG. Prognostic Significance of Neutrophil to Lymphocyte Ratio in Pancreatic Cancer: A Meta-Analysis. *World J Gastroenterol* (2015) 21(9):2807–15. doi: 10.3748/wjg.v21.i9.2807
37. Piciucchi M, Stigliano S, Archibugi L, Zerboni G, Signoretti M, Barucca V, et al. The Neutrophil/Lymphocyte Ratio at Diagnosis Is Significantly Associated With Survival in Metastatic Pancreatic Cancer Patients. *Int J Mol Sci* (2017) 18(4):730. doi: 10.3390/ijms18040730
38. Iwai N, Okuda T, Sakagami J, Harada T, Ohara T, Taniguchi M, et al. Neutrophil to Lymphocyte Ratio Predicts Prognosis in Unresectable Pancreatic Cancer. *Sci Rep* (2020) 10(1):18758. doi: 10.1038/s41598-020-75745-8
39. Kubo H, Murakami T, Matsuyama R, Yabushita Y, Tsuchiya N, Sawada Y, et al. Prognostic Impact of the Neutrophil-To-Lymphocyte Ratio in Borderline Resectable Pancreatic Ductal Adenocarcinoma Treated With Neoadjuvant Chemoradiotherapy Followed by Surgical Resection. *World J Surg* (2019) 43(12):3153–60. doi: 10.1007/s00268-019-05159-9
40. Kawai M, Hirono S, Okada KI, Miyazawa M, Shimizu A, Kitahata Y, et al. Low Lymphocyte Monocyte Ratio After Neoadjuvant Therapy Predicts Poor Survival After Pancreatectomy in Patients With Borderline Resectable Pancreatic Cancer. *Surgery* (2019) 165(6):1151–60. doi: 10.1016/j.surg.2018.12.015
41. Lee BM, Chung SY, Chang JS, Lee KJ, Seong J. The Neutrophil-Lymphocyte Ratio and Platelet-Lymphocyte Ratio Are Prognostic Factors in Patients With Locally Advanced Pancreatic Cancer Treated With Chemoradiotherapy. *Gut Liver* (2018) 12(3):342–52. doi: 10.5009/gnl17216
42. Zhou JG, Wong AHH, Wang H, Jin SH, Tan F, Chen YZ, et al. *Definition of a New Blood Cell Count (BCT) Score for Early Survival Prediction for non-Small Cell Lung Cancer Patients Treated With Atezolizumab: Integrated Analysis of 4 Multicenter Clinical Trials* (2021). Available at: https://www.medrxiv.org/content/10.1101/2021.08.28.21262770v1 (Accessed November 4, 2021).
43. Moertel CG, Frytak S, Hahn RG, O'Connell MJ, Reitemeier RJ, Rubin J, et al. Therapy of Locally Unresectable Pancreatic Carcinoma: A Randomized Comparison of High Dose (6000 Rads) Radiation Alone, Moderate Dose Radiation (4000 Rads + 5-Fluorouracil), and High Dose Radiation + 5-Fluorouracil. The Gastrointestinal Tumor Study Group. *Cancer* (1981) 48 (8):1705–10. doi: 10.1002/1097-0142(19811015)48:8<1705::Aid-cncr2820480803>3.0.Co;2-4
44. Sudo K, Yamaguchi T, Ishihara T, Nakamura K, Hara T, Denda T, et al. Phase II Study of Oral S-1 and Concurrent Radiotherapy in Patients With Unresectable Locally Advanced Pancreatic Cancer. *Int J Radiat Oncol Biol Phys* (2011) 80(1):119–25. doi: 10.1016/j.ijrobp.2010.01.027
45. Ueno H, Ioka T, Ikeda M, Ohkawa S, Yanagimoto H, Boku N, et al. Randomized Phase III Study of Gemcitabine Plus S-1, S-1 Alone, or Gemcitabine Alone in Patients With Locally Advanced and Metastatic

Pancreatic Cancer in Japan and Taiwan: GEST Study. *J Clin Oncol* (2013) 31 (13):1640–8. doi: 10.1200/JCO.2012.43.3680
46. Krishnan S, Chadha AS, Suh Y, Chen HC, Rao A, Das P, et al. Focal Radiation Therapy Dose Escalation Improves Overall Survival in Locally Advanced Pancreatic Cancer Patients Receiving Induction Chemotherapy and Consolidative Chemoradiation. *Int J Radiat Oncol Biol Phys* (2016) 94 (4):755–65. doi: 10.1016/j.ijrobp.2015.12.003
47. Rudra S, Jiang N, Rosenberg SA, Olsen JR, Roach MC, Wan L, et al. Using Adaptive Magnetic Resonance Image-Guided Radiation Therapy for Treatment of Inoperable Pancreatic Cancer. *Cancer Med* (2019) 8(5):2123–32. doi: 10.1002/cam4.2100
48. Hiroshima Y, Fukumitsu N, Saito T, Numajiri H, Murofushi KN, Ohnishi K, et al. Concurrent Chemoradiotherapy Using Proton Beams for Unresectable Locally Advanced Pancreatic Cancer. *Radiother Oncol* (2019) 136:37–43. doi: 10.1016/j.radonc.2019.03.012
49. Jung J, Yoon SM, Park JH, Seo DW, Lee SS, Kim MH, et al. Stereotactic Body Radiation Therapy for Locally Advanced Pancreatic Cancer. *PLoS One* (2019) 14(4):e0214970. doi: 10.1371/journal.pone.0214970

Conflict of Interest: The authors declare that the research was conducted in the absence of any commercial or financial relationships that could be construed as a potential conflict of interest.

frontiers | Frontiers in Oncology

TYPE Original Research
PUBLISHED 29 August 2022
DOI 10.3389/fonc.2022.974728

OPEN ACCESS

EDITED BY
James Chow,
University of Toronto, Canada

REVIEWED BY
Hikaru Souda,
Yamagata University, Japan
Michael Seimetz,
Polytechnic University of Valencia, Spain

*CORRESPONDENCE
Yohsuke Kusano
y.kusano@kcch.jp

SPECIALTY SECTION
This article was submitted to Radiation Oncology, a section of the journal Frontiers in Oncology

RECEIVED 21 June 2022
ACCEPTED 03 August 2022
PUBLISHED 29 August 2022

CITATION
Kusano Y, Katoh H, Minohara S, Fujii H, Miyasaka Y, Takayama Y, Imura K, Kusunoki T, Miyakawa S, Kamada T, Serizawa I, Takakusagi Y, Mizoguchi N, Tsuchida K and Yoshida D (2022) Robust treatment planning in scanned carbon-ion radiotherapy for pancreatic cancer: Clinical verification using in-room computed tomography images. *Front. Oncol.* 12:974728. doi: 10.3389/fonc.2022.974728

Robust treatment planning in scanned carbon-ion radiotherapy for pancreatic cancer: Clinical verification using in-room computed tomography images

Yohsuke Kusano[1]*, Hiroyuki Katoh[2], Shinichi Minohara[1], Hajime Fujii[3], Yuya Miyasaka[4], Yoshiki Takayama[1], Koh Imura[1], Terufumi Kusunoki[1], Shin Miyakawa[1], Tadashi Kamada[2], Itsuko Serizawa[2], Yosuke Takakusagi[2], Nobutaka Mizoguchi[2], Keisuke Tsuchida[2] and Daisaku Yoshida[2]

[1]Section of Medical Physics and Engineering, Kanagawa Cancer Center, Yokohama, Japan, [2]Department of Radiation Oncology, Kanagawa Cancer Center, Yokohama, Japan, [3]Accelerator Engineering Corporation, Kanagawa Office, Chiba, Japan, [4]Department of Heavy Particle Medical Science, Yamagata University Graduate School of Medical Science, Yamagata, Japan

Purpose: Carbon-ion beam (C-beam) has a sharp dose distribution called the Bragg peak. Carbon-ion radiation therapy, such as stereotactic body radiotherapy in photon radiotherapy, can be completed in a short period by concentrating the radiation dose on the tumor while minimizing the dose to organs at-risk. However, the stopping position of C-beam is sensitive to density variations along the beam path and such variations can lower the tumor dose as well as cause the delivery of an unexpectedly high dose to the organs at risk. We evaluated the clinical efficacy of a robust planning technique considering gastrointestinal gas (G-gas) to deliver accurate radiation doses in carbon-ion radiotherapy for pancreatic cancer.

Materials and methods: We focused on the computed tomography (CT) value replacement method. Replacement signifies the overwriting of CT values in the CT images. The most effective replacement method for robust treatment planning was determined by verifying the effects of the three replacement patterns. We selected 10 consecutive patients. Pattern 1 replaces the CT value of the G-gas contours with the value of the region without G-gas (P1). This condition indicates a no-gas state. Pattern 2 replaces each gastrointestinal contour using the mean CT value of each contour (P2). The effect of G-gas was included in the replacement value. Pattern 3 indicates no replacement (P3). We analyzed variations in the target coverage (TC) and homogeneity index (HI) from the initial plan using in-room CT images. We then performed correlation analysis on the variations in G-gas, TC, and HI to evaluate the robustness against G-gas.

Results: Analysis of variations in TC and HI revealed a significant difference between P1 and P3 and between P2 and P3. Although no statistically significant difference was observed between P1 and P2, variations, including the median, tended to be fewer in P2. The correlation analyses for G-gas, TC, and HI showed that P2 was less likely to be affected by G-gas.

Conclusion: For a treatment plan that is robust to G-gas, P2 mean replacement method should be used. This method does not necessitate any particular software or equipment, and is convenient to implement in clinical practice.

KEYWORDS

carbon-ion radiotherapy, gastrointestinal gas, scanning beam, pancreatic cancer, robust treatment plan, in-room CT, replacement

Introduction

The mortality rate remains high for pancreatic cancer. The standard treatment for unresectable locally advanced pancreatic cancer includes chemotherapy and chemoradiotherapy (1). Good outcomes with carbon-ion radiotherapy combined with gemcitabine (GEM), in particular, have been reported. Despite this, the overall survival rate is only a median of 21.5 months, and additional improvements in treatment outcomes are desired (2–5). In this context, Kawashiro et al. (3) reported that distant metastasis can be reduced by increasing the radiation dose, and studies on increasing the radiation dose have already been conducted (6). However, the effectiveness of such radiation dose increase will be lost unless the radiation dose is precisely delivered to the tumor.

A carbon-ion particle beam has a physical characteristic called the Bragg peak, which enables the delivery of a highly concentrated radiation dose to the tumor while reducing the radiation dose to adjacent organs (7, 8). In the treatment, the depth of water where the carbon-ion particles are stopped is determined in detail; moreover, an aggregate of Bragg peaks (spread-out Bragg peaks, SOBP) is formed and irradiated to the tumor (Figure 1A). During treatment planning, the water equivalent pass length to the stopping positions of carbon particles is calculated considering the presence of gastrointestinal gas (G-gas); moreover, the beam energy of carbon particles corresponding to the stopping positions and the number of particles corresponding to the doses are determined (positions 1 and 2 are shown in Figure 1B). The stopping position of carbon-ion particles is sensitive to G-gas variations along the beam path, and such variations can lower the tumor dose as well as cause the delivery of an unexpectedly high dose to the organs at risk (OAR). For example, when the beam path condition changes from no gas to gas, the carbon-ion particle stops at a deeper position than expected because of the shallower depth of the water than the planned stopping position. This decreases the tumor doses, thereby increasing the dose to OAR (Figures 1B-D). In a sample case of the first irradiation (Figure 1C), there was no G-gas in Position 1 and a significant increase in the amount of G-gas in Position 2. The impact of the computed tomography (CT) value change in Position 2 was significant, with CT values changing from −10 to −405 Hounsfield Unit (HU), thereby approaching the CT value of air. The density reduced, energy loss decreased, and carbon particles stopped at a deeper position than that during the treatment plan. Hence, the dose distribution of the proximal side was broken (Figure 1C-a), doses of gross tumor volume (GTV) and clinical target volume (CTV) were decreased, and dose to the distal side of the gastrointestinal tract was increased (Figure 1C-b). During the ninth irradiation (Figure 1D), the G-gas at Positions 1 and 2 was cleared. CT values changed from −415 HU to 38 HU in Position 1 and from −10 HU to 64 HU at Position 2. The density increased, energy loss increased, and carbon particles stopped at a position shallower than that during the treatment plan. Moreover, the doses to the duodenum increased (Figure 1D-c), and the dose of CTV decreased (Figure 1D-d). Hence, for minimizing the radiation dose to OARs and ensuring the adequate tumor dose, it is essential to prepare a treatment plan that is highly robust to the variations caused by G-gas in each radiation fraction.

G-gas, changes in the patient's physique, and patient set-up error are some factors that can affect the tumor and OAR doses during treatment (9–16). Especially in pancreatic cancer, the target is surrounded by the gastrointestinal tract. Therefore, the dose distribution is more likely to be affected by the presence or absence of G-gas than when these organs are not involved. Kumagai et al. (10) evaluated the target coverage (TC) in carbon-ion radiotherapy of pancreatic cancer in relation to the positional changes of G-gas during irradiation using contrast-enhanced CT images and reported a reduction in TC. The ratio

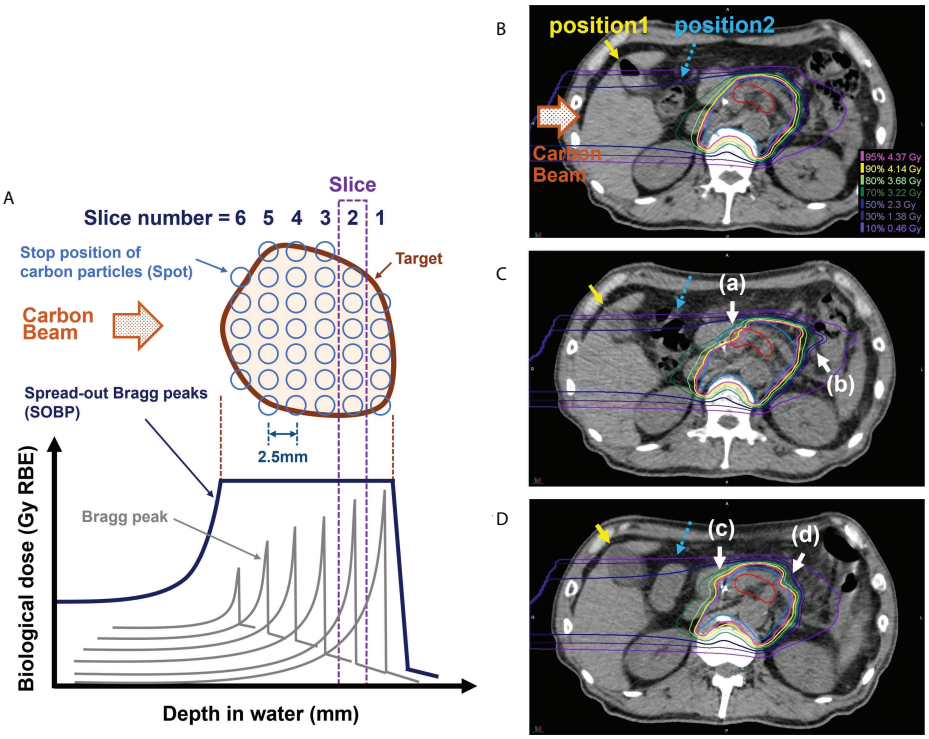

FIGURE 1
Effect of gastrointestinal gas (G-gas) on dose distribution in scanning carbon-ion radiotherapy for pancreatic cancer. **(A)** An illustration of the formation of the spread-out Bragg peaks (SOBP). **(B)** The dose distribution in the treatment planning computed tomography (CT) image in a sample case. **(C)** The dose distributions in the in-room CT images taken during the first irradiation. **(D)** The dose distributions in the in-room CT images taken during the ninth irradiation. The treatment of pancreatic cancer is conducted by performing irradiation in 12 fractions. During pancreatic cancer treatment, the stops of the carbon particles are determined at 2.5 mm water depth intervals. The red and blue contours indicate the gross tumor volume (GTV) and clinical target volume (CTV), respectively. The carbon beam direction is from the left side in each figure part.

of the target volume irradiated to the irradiated volume greater than the evaluation dose is denoted by TC. Throughout the treatment period and irradiation, the position of the G-gas regions is unstable, and it is impossible to predict the G-gas position on each treatment day. Houweling et al. (13, 14) evaluated TC during the treatment period in pancreatic cancer using cone beam CT (CBCT) and found that TC decreased by 0.5% in X-ray radiotherapy of volumetric modulated arc therapy (VMAT), 8% in proton radiotherapy, and 10% in carbon-ion radiotherapy. The beam angle selection method (10–12) is an option for minimizing the effects of G-gas; however, the effects of G-gas cannot be avoided entirely. Additionally, in some cases, the beam angle affected by G-gas must be selected, such as in patients with kidney function impairment. Although the concept of online adaptive radiotherapy has been developed, several problems remain, such as excessive time consumption (17). Online adaptive radiotherapy is a technique in which the irradiation plan is modified according to the patient's condition during each treatment procedure. In addition to the throughput, technical difficulties, such as the space allocation and magnetic field effects on equipment and beams and the implementation of in-room CT (irCT)-, CBCT-, or magnetic resonance imaging-based adaptive therapy for carbon-ion radiotherapy, will be major issues. In consideration of the hypoxic condition of the tumor, some studies have been conducted to reduce recurrence by controlling LET distribution in the tumor (18–21). In this case, as a nonuniform irradiation field was used for the treatment, high reproducibility of dose distribution during each treatment was required. Therefore, preparing a robust treatment plan that accounts for G-gas is critical.

We performed a preliminary analysis of the factors affecting the tumor dose during the treatment period in ten patients with pancreatic cancer; G-gas was one of the main factors (Supplementary Figure 1). If a robust treatment plan for G-gas can be prepared, tumor dose during the treatment period can be further improved. A robust planning method for G-gas has not been established in particle therapy. In this study, we focused on the effect of G-gas on dose distribution to help improve treatment outcomes in pancreatic cancer. Three G-gas

replacement patterns were established and their effects were examined using irCT images taken during treatment. The most robust replacement method for G-gas was determined.

Materials and methods

Patient selection

We selected ten consecutive patients who received carbon-ion radiotherapy for pancreatic cancer at our hospital from January 2019 to April 2020 (Table 1). This single-center study was conducted according to the guidelines of the Declaration of Helsinki, and approved by the Institutional Review Board of the Kanagawa Cancer Center (2019eki-106, August 30, 2021). Informed consent was obtained from all subjects, and their data were anonymized. Four-dimensional CT (4D-CT) images were obtained in the supine and prone positions for treatment planning because irradiation is performed using two fixed gantry ports from the horizontal and vertical directions (22). The irradiation angle (Figure 2A) was determined by combining the patient's supine and prone positions as well as the treatment table's rolling angle. The irCT images were obtained at least once every week during the treatment period considering each patient's physical condition and X-ray exposure.

Contouring of target and risk organs

The patients fasted at least 5 hours before the treatment planning CT (pCT) scan or treatment. An enema was performed if the patient had not defecated within the previous 24 hours. Patients were immobilized on the treatment table using patient immobilization devices (underneath: Blue BAG BodyFix, Elekta AB, Stockholm, Sweden, and upper surface: Shellfitter, Kuraray Co., Ltd., Tokyo, Japan). For all patients, 4D-CT scans were performed using a pCT scanner (Aquilion LB, Canon Medical Systems Corporation, Tochigi, Japan) under normal breathing. The raw data from 4D-CT scans are acquired at all respiratory timings based on the patient's respiratory waveform. The CT images at ten respiratory timings (10% step) were created using 4D-CT raw data, with one respiratory cycle comprising 100% (0% and 100% were the maximum inhalation phase; 50% was the maximum exhalation phase), and those CT images are referred to as 4D-CT images. In this study, the CT images of the maximum exhalation phase were selected from the CT images of the ten phases and used for calculating the dose distributions and analyses. The CT images of the maximum exhalation phase in the pCT images are described as $pCT_{50\%}$ images.

GTV was delineated on the CT images at ten respiratory time points. The distance to GTV center of gravity was calculated at each respiratory time based on the maximum

TABLE 1 Patient characteristics.

Patient	Age	Sex	Loc.	irCT scan times	Patient positioning	Volume (cm^3)	
						GTV	CTV
1	60	M	H	6	SP	11.3	219.6
					PR	11.5	189.1
2	79	M	H	7	SP	10.7	238.8
					PR	11.1	231.4
3	54	F	H	6	SP	21.7	142.1
					PR	21.5	140.7
4	64	M	HB	5	SP	39.0	370.8
					PR	39.9	391.0
5	86	F	H	4	SP	10.7	112.7
					PR	11.1	102.0
6	78	F	H	4	SP	7.8	226.7
					PR	7.8	214.7
7	75	M	H	6	SP	26.3	184.1
					PR	26.2	213.3
8	65	F	HB	4	SP	10.9	288.4
					PR	11.3	279.1
9	72	M	H	7	SP	5.9	69.2
					PR	6.1	78.2
10	61	M	H	4	SP	25.0	274.0
					PR	28.8	291.8

Loc., location of tumor; irCT, in-room CT; GTV, gross tumor volume; CTV, clinical target volume; M, male; F, female; H, pancreatic head; HB, pancreatic head and body; SP, supine position; PR, prone position.

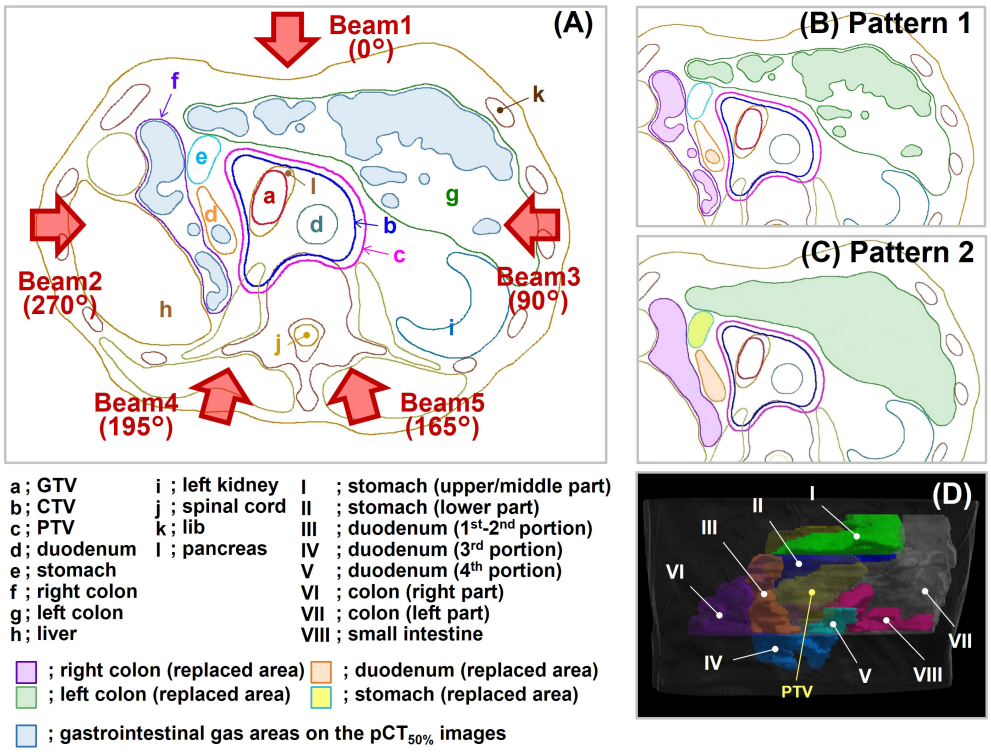

FIGURE 2
Replacement patterns and beam direction. **(A)** The supine position without replacement. This condition corresponds to Pattern 3. The blue-filled areas in the illustration represent gastrointestinal gas (G-gas). The gantry angle is indicated by a brown arrow. **(B)** The replacement condition in Pattern 1. **(C)** The replacement condition in Pattern 2. **(D)** Eight replacement regions in Pattern 2. GTV, gross tumor volume; CTV, clinical target volume; PTV, planning target volume; $pCT_{50\%}$ images, planning CT images of the maximum exhalation phase.

exhalation phase. Subsequently, the phase range in which the movement of GTV was within 5 mm was established. To create a uniform irradiation field, movement with respiratory gating "on" needs to be kept to within 5 mm (23). Due to inter-individual differences in maximum GTV and OAR movements, 4D-CT images are used to check each patient's maximum GTV and OAR movements; subsequently, the phase range is determined. In our facility, the phase range is generally 30%–60%. Respiration speed is not constant between exhalation and inhalation; typically, the latter is faster than the former. Therefore, as tumor movement corresponds to respiratory movements, it is asymmetric in exhalation and inhalation. GTV movement can be controlled to within 3 mm in this situation.

CTV was defined as the GTV including a 5 mm margin and the locoregional elective nodal and neuro-plexus region (2, 3); the entire pancreas was included in the CTV as a preventive region regardless of the tumor site. The internal CTV (ICTV) was obtained by the summation of CTV within that phase range. The OARs (stomach, duodenum, colon, and small intestine) were delineated on the CT images in that phase range, and the summed OARs were defined as the planning organ-at-risk volume (PRV). Then, the planning target volume (PTV) was prepared by adding a margin of 3 mm to the ICTV, which was reduced when PTV was close to or overlapped the PRV.

Replacement patterns of the gastrointestinal gas region

We focused on the CT value replacement method. The most effective replacement method was determined by verifying the effects of the three replacement patterns (Figure 2) using clinical data. Replacement implies that contours are drawn at the target locations of CT images and any CT values are assigned to each contour. This operation, which can be performed by the treatment planning system, can rewrite the CT values of the CT images. The carbon-ion scanning treatment planning system (Monaco for Carbon, Ver. 5.20, Elekta AB, Stockholm, Sweden) used in this study can achieve this same operation by replacing the value of the relative stopping power ratio (rSPR). The rSPR is calculated using the CT value and is equal to the CT value's replacement (24–29). The rSPR of water and air are about 1.0 and 0.0, respectively. The rSPR corresponds to the relative

electron density of photon radiotherapy. The following is a description of each pattern.

Pattern 1 (no-gas replacement condition)

In Pattern 1 (Figure 2B), the region of interest was set at a site without gas in each gastrointestinal tract, and the value of the rSPR was obtained on Monaco and used as the replacement value. The replacement region was defined by the gas contour ($Gas_{pCT50\%}$) delineated on the $pCT_{50\%}$ images. $Gas_{pCT50\%}$ was semiautomatically delineated using the threshold function of contouring software (MIM Maestro ver. 6.9.6, MIM Software Inc. Cleveland, OH, USA) with soft tissue conditions (window level = 40 HU, window width = 400 HU). The replacement values of Pattern 1 are shown in Table 2.

Pattern 2 (averaged-gas replacement condition)

In Pattern 2 (Figure 2C), the replacement regions were defined by gastrointestinal contours delineated on $pCT_{50\%}$ images. The stomach was divided into two regions comprising the upper/middle (Figure 2D-I) and lower parts (Figure 2D-II); the duodenum was divided into three regions comprising the 1^{st}–2^{nd} (Figure 2D-III), 3^{rd} (Figure 2D-IV), and 4^{th} portions (Figure 2D-V); and the colon was divided into two regions comprising the right (Figure 2D-VI) and left parts (Figure 2D-VII). In addition to the small intestine (Figure 2D-VIII), eight replacement regions were set. Because G-gas accumulation in each organ is considered different for each patient and the degree of G-gas accumulation is considered to be different for each organ section, the replacement area was divided accordingly. The replacement value was defined as the mean rSPR of each replacement range. The regions were divided manually. The replacement values of Pattern 2 are shown in Table 2.

Pattern 3 (without replacement condition)

For Pattern 3 (Figure 2A), the optimization of dose distribution was performed without replacement.

Initial plan

The replacement processing was performed using the abovementioned three patterns. With the gantry angle set to five directions as shown in Figure 2A (Gantry Angle: Beam 1 = 0°, Beam 2 = 270°, Beam 3 = 90°, Beam 4 = 195°, and Beam 5 = 165°), optimization of the initial dose distributions was

TABLE 2 Replacement values in the initial planning.

Patient	Patient positioning	Replacement value of rSPR in $pCT_{50\%}$ images, Pattern 1/Pattern 2			
		Small intestine All/All	Stomach All/[U-M, L]	Duodenum All/[1^{st}–2^{nd}, 3^{rd}, 4^{th}]	Colon All/[Rt, Lt]
1	SP	1.03/1.03	1.04/[0.86, 0.84]	1.04/[1.02, 1.03, 1.03]	1.03/[0.86, 0.90]
	PR	1.03/1.03	1.03/[0.91, 1.03]	1.05/[1.02, 1.03, 1.03]	1.03/[0.89, 0.66]
2	SP	1.02/0.95	1.04/[1.04, 1.03]	1.05/[1.01, 1.02, 0.89]	1.03/[0.80, 0.74]
	PR	1.03/1.03	1.04/[0.99, 1.03]	1.04/[1.04, 1.03, 1.03]	1.03/[0.65, 0.98]
3	SP	1.04/1.04	1.05/[0.94, 0.94]	1.03/[1.02, 1.03, 1.02]	1.03/[0.95, 0.85]
	PR	1.04/1.03	1.03/[1.03, 1.03]	1.05/[1.02, 1.02, 1.02]	1.04/[0.98, 1.00]
4	SP	1.04/0.97	1.04/[1.03, 1.03]	1.03/[1.02, 1.02, 1.02]	1.03/[0.98, 0.89]
	PR	1.04/1.04	1.03/[1.02, 1.03]	1.04/[1.02, 1.02, 1.02]	1.03/[0.80, 0.90]
5	SP	1.04/1.03	1.04/[1.03, 0.90]	1.03/[0.97, 0.81, 1.01]	1.03/[0.76, 0.85]
	PR	1.04/1.04	1.03/[0.97, 0.97]	1.04/[1.04, 1.04, 1.04]	1.03/[0.90, 0.86]
6	SP	1.03/1.01	1.02/[1.01, 0.83]	1.03/[1.03, 1.00, 0.75]	1.02/[0.94, 1.01]
	PR	1.03/1.01	1.03/[0.99, 1.02]	1.04/[0.97, 0.97, 0.75]	1.02/[0.89, 0.73]
7	SP	1.05/1.04	1.04/[0.95, 0.97]	1.04/[1.03, 1.04, 1.04]	1.03/[0.65, 0.45]
	PR	1.03/1.03	1.04/[0.97, 1.03]	1.04/[0.97, 1.04, 1.04]	1.04/[0.49, 0.47]
8	SP	1.03/0.93	1.04/[0.71, 0.80]	1.03/[1.01, 1.03, 1.03]	1.02/[0.85, 0.96]
	PR	1.04/1.04	1.04/[0.73, 1.02]	1.03/[1.02, 1.02, 1.02]	1.03/[0.95, 0.78]
9	SP	1.04/1.03	1.04/[0.97, 0.99]	1.04/[1.03, 1.03, 1.04]	1.04/[0.94, 1.00]
	PR	1.03/1.03	1.03/[1.00, 1.01]	1.03/[1.00, 1.02, 1.02]	1.04/[0.93, 0.99]
10	SP	1.04/1.02	1.02/[1.02, 0.82]	1.05/[1.05, 1.05, 1.03]	1.02/[0.93, 0.91]
	PR	1.04/0.99	1.03/[1.00/1.00]	1.04/[0.96, 1.04, 1.03]	1.04/[0.92, 0.94]

rSPR, relative stopping power ratio; $pCT_{50\%}$ images, treatment planning CT images of the maximum exhalation phase; All, all regions of contour; U, gastric fundus; M, gastric body; L, pyloric zone; 1^{st}–2^{nd}, between the first and second (descending portion) portions of duodenum; 3^{rd}, third portion (horizontal portion) of duodenum; 4^{th}, fourth portion (ascending portion) of duodenum; Rt, right part; Lt, left part; SP, supine position; PR, prone position.

performed with a single beam such that 95% of the prescribed dose covered PTV using $pCT_{50\%}$ images and contours (Figure 3-a). The prescribed dose per beam was set at a 4.6 Gy relative biological effectiveness-weighted absorbed dose (RBE), which is equivalent to a fraction dose for the pancreas (3, 30). The optimization-derived irradiation conditions were stored as templates (Figure 3-b). Subsequently, the five dose distributions of Patterns 1 and 2 were recalculated under no-replacement conditions (Figure 3-c) while maintaining the irradiation conditions determined in the optimizations. These results as well as the optimization results of Pattern 3 were used as initial planning results.

Calculation of the dose distributions using fractional in-room CT images

In treatment, the patient's irradiation position was set up by 2D–3D bone matching using front- and lateral-view X-ray images (2D) and $pCT_{50\%}$ images (3D) (31). The patient irradiation position was adjusted to the initial treatment plan based on the bone structure using the 2D and 3D images. The irradiation was performed using a high-speed scanning system for carbon-ion radiotherapy (CI-1000, TOSHIBA Corporation, Tokyo, Japan) (22, 32, 33). 4D-CT images were obtained using an irCT scanner while maintaining the patient set up at treatment. The irCT scanner is the same as the pCT scanner (22, 34). In this study, GTV, CTV, OARs, and $Gas_{irCT50\%}$ were delineated on the maximum exhalation phase in irCT images ($irCT_{50\%}$ images). The isocenter position was determined based on the markers projected onto $irCT_{50\%}$ images, and the fractional dose distributions were calculated for five gantry angles while maintaining the irradiation conditions determined in the initial plan using the templates (Figure 3-d).

Correction of other effects

Changes in factors other than the effect of G-gas are included in the calculated dose distribution using $irCT_{50\%}$ images:

$$D_{ir} = D_P \times f_{\Delta Gas} \times f_{Other} \left(f_{Other} = f_{Str} \times f_{Pos} \times f_{Sur} \times \ldots\right) \quad (1),$$

where D_{ir} indicates the dose on $irCT_{50\%}$ images, and D_P indicates the dose on $pCT_{50\%}$ images, $f_{\Delta Gas}$ indicates changes in the effect of G-gas based on the initial plan; f_{Other} indicates factors other than G-gas; f_{Str} indicates the delineation error with morphological changes in the target; f_{Pos} indicates positional changes in the target; and f_{Sur} indicates the effects of changes in the patient's physique. We calculated the dose distribution with $Gas_{irCT50\%}$ replaced by values without gas obtained on the external side of the gas region in addition to the calculations on $pCT_{50\%}$ images (Pattern 1 on Figure 2B). Using those dose distributions (Figure 3-e), we then calculated the correction

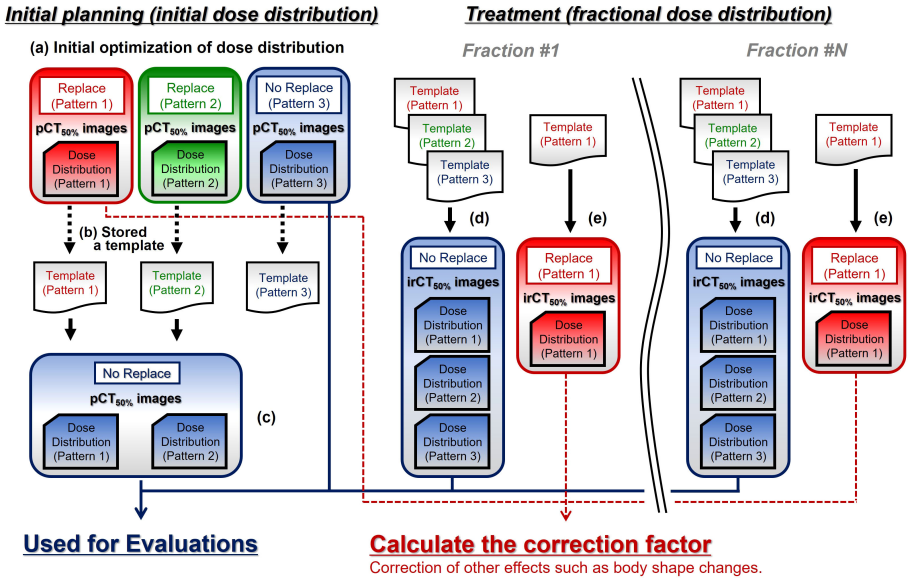

FIGURE 3
The calculation workflow of treatment planning computed tomography (CT) and fractional in-room CT (irCT) images. $pCT_{50\%}$ images, treatment planning CT images of the maximum exhalation phase; $irCT_{50\%}$ images, in-room CT images of the maximum exhalation phase; Replace, replace condition; No Replace, without replace condition; Template, irradiation conditions set (slice position, spot position in the plane of each slice position, and number of particles per spot etc.).

factor based on the dose distribution on $pCT_{50\%}$ images for change in factors other than the effect of G-gas in each dose distribution on $irCT_{50\%}$ images:

$$k = D_{ir(Rep)} / D_{P(Rep)} = (D_{P(Rep)} \times f_{Other}) / D_{P(Rep)} = f_{Other} \quad (2)$$

$$D_{ir(Cor)} = D_{ir} / k = (D_P \times f_{\Delta Gas} \times f_{Other}) / f_{Other} = D_P \times f_{\Delta Gas} \quad (3),$$

where $D_{P(Rep)}$ and $D_{ir(Rep)}$ indicate the dose at the time of G-gas replacement on the beam pathway on the $pCT_{50\%}$ and $irCT_{50\%}$ images, respectively; k indicates the correction factor that converts the change in the factor of the dose other than G-gas in the $irCT_{50\%}$ images to the factor in the $pCT_{50\%}$ images; and $D_{ir(Cor)}$ indicates the corrected dose on $irCT_{50\%}$ images. The values of k for each beam are shown in Table 3. The minimum and maximum values of k were 0.913 and 1.001 in the supine position and 0.830 and 1.010 in the prone position, respectively. The main determinant of k is believed to be changes in the tumor position (Supplementary Figure 1). These corrections enable the exclusion of changes in factors other than G-gas, thereby enabling the evaluation of the effect of G-gas alone. In this study, TC and homogeneity index (HI) were corrected by the correction factor of k.

Evaluation of CTV coverage and homogeneity variations from the initial plan

We analyzed and evaluated the variations in CTV coverage (TC_{CTV}) and HI. For TC_{CTV}, we evaluated the ratio of the volume irradiated by 95% or more of the prescribed dose ($V_{95\%}$). HI was then calculated using the following formula in accordance with ICRU83 (35):

$$HI = (D_{2\%} - D_{98\%}) / D_{50\%} \quad (4),$$

where $D_{2\%}$ indicates the maximum dose, $D_{98\%}$ indicates the minimum dose, and $D_{50\%}$ indicates the median dose. For our analyses, we used the corrected values presented in the preceding paragraph. The variations in TC_{CTV} (ΔTC_{CTV}) and HI (ΔHI) from the initial plan was defined using the following formulas:

$$\Delta TC_{CTV} = TC_{CTV(irCT50\%)} - TC_{CTV(pCT50\%)} \quad (5)$$

$$\Delta HI = HI_{irCT50\%} - HI_{pCT50\%} \quad (6),$$

where $TC_{CTV(pCT50\%)}$ and $HI_{pCT50\%}$, and $TC_{CTV(irCT50\%)}$ and $HI_{irCT50\%}$ are the values based on initial and fractional dose distributions, respectively.

TABLE 3 Changes in factors other than gastrointestinal gas (k).

Patient	Patient positioning	Value of k (min–max)				
		Beam 1 (0°)	Beam 2 (270°)	Beam 3 (90°)	Beam 4 (195°)	Beam 5 (165°)
1	SP	0.977–0.998	0.986–0.995	0.985–1.002	0.970–1.000	0.975–1.004
	PR	0.967–1.005	0.960–0.992	0.972–1.004	0.970–1.004	0.971–1.004
2	SP	0.961–0.984	0.966–1.003	0.963–1.004	0.953–1.002	0.953–1.010
	PR	0.988–1.008	0.980–0.999	0.950–0.988	0.990–1.006	0.993–1.010
3	SP	0.983–1.000	0.971–0.996	0.979–1.001	0.973–0.999	0.975–1.000
	PR	0.898–0.975	0.934–0.989	0.934–0.991	0.876–0.966	0.899–0.965
4	SP	0.978–1.011	0.965–0.985	0.975–0.991	0.987–1.002	0.995–1.002
	PR	0.980–0.991	0.958–0.992	0.965–0.989	0.960–0.963	0.984–0.993
5	SP	0.971–0.983	0.961–0.985	0.975–0.998	0.990–1.005	0.978–1.006
	PR	0.992	0.988	0.968	1.001	1.001
6	SP	0.944–0.977	0.948–0.980	0.951–0.983	0.945–0.981	0.948–0.980
	PR	0.926	0.911	0.919	0.902	0.901
7	SP	0.918–1.000	0.945–0.963	0.946–0.976	0.952–0.955	0.946–0.964
	PR	0.891–0.964	0.900–0.984	0.903–0.975	0.860–0.941	0.905–0.982
8	SP	0.992–0.999	0.991–0.996	0.985–0.994	0.959–0.997	0.953–0.993
	PR	1.008	1.007	1.007	0.994	0.993
9	SP	0.981–0.996	0.952–0.985	0.913–0.959	0.975–0.996	0.975–0.995
	PR	0.916–0.988	0.856–0.897	0.860–0.897	0.830–0.944	0.854–0.920
10	SP	0.927–0.993	0.972–1.002	0.969–1.005	0.980–1.008	0.982–1.004
	PR	0.990	0.973	0.982	0.982	0.990

min, minimum value; max, maximum value; SP, supine position; PR, prone position.

10.3389/fonc.2022.974728

Evaluation between variations in G-gas volume and variations in CTV coverage as well as the HI during the treatment period

To examine the relationship between the volume variations in G-gas (ΔG-gas) during the treatment period, we analyzed the ΔTC_{CTV} and ΔHI against ΔG-gas. Even if the volume was the same, G-gas caused variations in CT values because of differences in moisture content. Accordingly, we believe that the rSPR was calculated using the CT value, thereby resulting in different contribution levels to the beam range. Therefore, gastrointestinal gas volume (Gas_R) and ΔG-gas were defined using the formulas below, considering the effect on the beam range:

$$Gas_R = Gas_V / rSPR \quad (7)$$

$$\Delta G\text{-gas} = Gas_{R(irCT)} - Gas_{R(pCT)} \quad (8),$$

where Gas_V indicates the volume of the gas contour delineated on the CT images ($pCT_{50\%}$ images: $Gas_V = Gas_{pCT50\%}$ on the beam pathway, $irCT_{50\%}$ images: $Gas_V = Gas_{irCT50\%}$ on the beam pathway). The mean rSPR of $Gas_{pCT50\%}$ and $Gas_{irCT50\%}$ were obtained using Monaco. The Gas_R of Beams 1, 2, and 3 for each patient are shown in Table 4. The Gas_R of Beams 4 and 5 were almost nil.

Statistical analysis

The differences between the three replacement techniques were evaluated using CT images from the same patient in this study. There was no normality in each data set. The Friedman test was used because this is a three-group evaluation of quantitative data. Since the comparison of the three groups would be evaluated thrice, the obtained p values were multiplied by three using the Bonferroni method. Finally, we conducted significance tests with the p value set to <0.05. The statistical software used was SPSS (IBM SPSS Statistics, version 26.0, IBM, Inc., Armonk, NY, USA).

In the evaluation between variations in G-gas volume and ΔTC_{CTV} and ΔHI, the results were linearly fitted by the least-squares method; moreover, the correlation analysis (R^2) was performed.

In the evaluation of the positional changes of gastrointestinal gas, we used a Wilcoxon signed-rank test to evaluate two groups without normality, and then we conducted significance tests with the p value set to <0.05.

TABLE 4 Gastrointestinal gas volume considering the beam range in beam path (Gas_R).

Patient	Patient positioning	Gas_R (cm^3), $pCT_{50\%}$ images/$irCT_{50\%}$ images (min–max)		
		Beam 1 (0°)	Beam 2 (270°)	Beam 3 (90°)
1	SP	28.8/6.4–92.7	64.0/63.7–74.2	20.8/59.9–73.3
	PR	0.7/0.3–7.5	70.4/40.1–46.8	106.7/104.5–211.1
2	SP	90.0/37.6–139.1	49.1/38.2–89.3	151.6/55.7–180.9
	PR	3.3/0.0–42.2	86.8/12.5–71.1	25.5/33.8–174.9
3	SP	2.8/7.3–18.5	69.2/27.4–62.1	159.5/207.4–328.2
	PR	3.0/0.8–4.2	28.7/8.9–36.9	21.0/45.1–81.0
4	SP	3.3/14.1–49.3	1.3/22.8–42.9	23.3/16.0–75.5
	PR	0.3/0.2–0.4	4.5/1.0–6.0	30.2/32.4–71.3
5	SP	6.0/0.0–2.1	52.9/1.9–5.0	95.0/12.2–117.0
	PR	1.0/0.4	2.2/1.0	25.2/34.0
6	SP	54.9/12.4–44.6	34.9/4.7–28.0	32.0/43.8–207.4
	PR	26.2/32.0	28.8/6.6	102.5/43.3
7	SP	442.4/52.8–60.6	142.9/36.3–41.1	353.7/22.1–47.7
	PR	7.7/2.3–4.8	15.6/1.3–0.5	20.6/25.9–30.2
8	SP	21.4/10.6–400.1	65.6/32.6–46.0	69.8/42.3–50.5
	PR	0.4/0.2	25.1/20.1	195.8/11.5
9	SP	1.7/1.2–3.9	6.2/16.9–52.1	2.9/16.4–52.1
	PR	1.4/0.0–2.5	12.8/7.4–39.8	2.7/4.3–102.7
10	SP	84.0/5.9–70.3	24.4/7.8–50.4	73.0/41.6–70.5
	PR	9.7/0.0	40.9/72.1	43.3/31.1

Gas_R, gastrointestinal gas volume considering the beam range in beam path; $pCT_{50\%}$ images, treatment planning CT images of the maximum exhalation phase; $irCT_{50\%}$ images; in-room CT images of the maximum exhalation phase; min, minimum value; max, maximum value; SP, supine position; PR, prone position. The Gas_R of Beams 4 and 5 were almost nil.

Results

Evaluation of variations in CTV coverage and the HI from the initial plan

Figure 4 shows the box-and-whisker plots of ΔTC_{CTV} and ΔHI from the initial plan.

In ΔTC_{CTV} (Figure 4A), Beams 4 and 5 were almost nil because of the absence of interference from G-gas. For Beam 1, a significant difference was observed between Patterns 2 and 3. For Beam 2, variations were significantly fewer for Pattern 2 than for Patterns 1 and 3. For Beam 3, a significant difference was observed between Patterns 1 and 3 and between Patterns 2 and 3. In particular, a remarkable difference was observed for Beam 2 and 3 with which a major change was observed in the G-gas volume. These results demonstrate that the dose distribution is best optimized with G-gas replaced. Although no statistically significant difference was found between Patterns 1 and 2 except for Beam 2, ΔTC_{CTV}, including the median value, tended to be fewer with Pattern 2.

The same tendency was observed for ΔHI (Figure 4B); ΔHI with Beams 4 and 5 were almost nil. With Beams 1 to 3, variations were significantly fewer for Pattern 2 than for Patterns 1 and 3.

Evaluation of the variations in G-gas volume and the variations in CTV coverage and the HI during the treatment period

Figure 5 shows the relationship between the volume variation in G-gas (ΔG-gas) from the initial plan as well as the variation in TC_{CTV} (ΔTC_{CTV}) and HI (ΔHI) from the initial plan for each replacement pattern. Linear fitting was performed for each replacement pattern. In this figure, a steep slope indicates the large influence of G-gas. Actual dose distribution is significantly impacted by changes in G-gas, as indicated by a high R^2 correlation coefficient. For TC_{CTV}, Pattern 1 has a large absolute value of a linear fitting slope and a large R^2, indicating that it is greatly affected by G-gas, whereas Pattern 2 has a slope that is closest to zero and a very small R^2, indicating that it is less affected by G-gas (Figure 5A). For HI, the absolute value of the slope is small for all patterns; however, the value of R^2 is the smallest for Pattern 2, indicating that the effect of G-gas is also small (Figure 5B).

Discussion

In this study, we proposed a method to robustly plan for the effect of G-gas in the treatment of pancreatic cancer by carbon-ion scanning irradiation, and we evaluated the validity of the method based on clinical data. We found that the replacement area in Pattern 2 is optimal for setting the replacement region and that replacing the mean value with Pattern 2 was effective.

Using the proposed Pattern 2 mean value replacement method, the replacement value of G-gas was determined for each patient, and individual differences in the incidence of G-gas were considered. Furthermore, the replacement value was determined for each organ and section, even for the same organ, thereby considering differences in the degree of G-gas accumulation. Although the replacement regions were complicated, we were able to successfully use this method for routine treatment planning without compromising throughput. However, as shown in Figure 4, dose variations were observed in some cases even when the mean value replacement method was

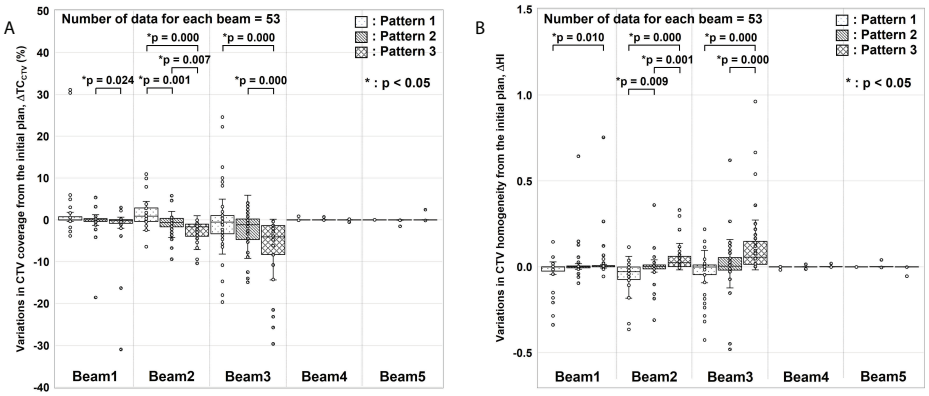

FIGURE 4
Evaluation results for variations in clinical target volume (CTV) coverage (ΔTC_{CTV}) and homogeneity index (ΔHI). **(A)** ΔTC_{CTV} and **(B)** ΔHI values from the initial plan. For each gantry angle, the median, first quartile, third quartile, maximum and minimum values, and outliers for ΔTC_{CTV} and ΔHI are presented in a box-and-whisker plot. These results were corrected for changes in factors other than gastrointestinal gas. Statistical analyses were then performed using the Friedman test. The symbol * indicate that there is a significant difference between them.

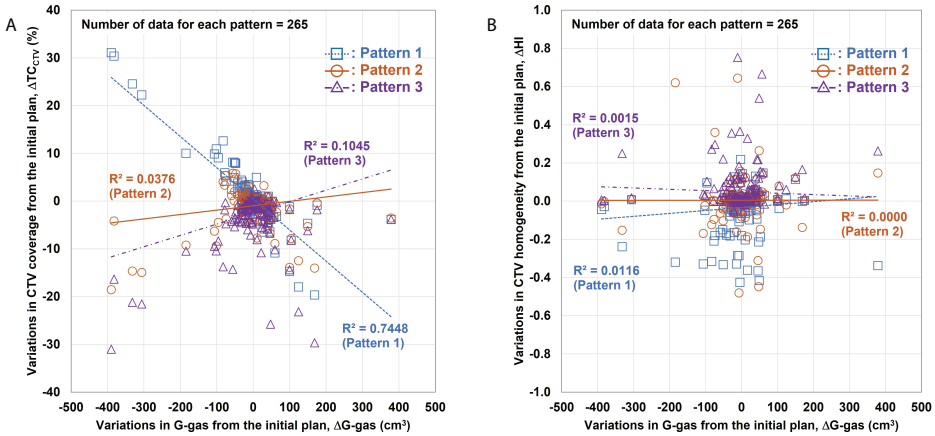

FIGURE 5
Relationship between variations in the gastrointestinal gas (ΔG-gas) volume and the variations in the clinical target volume (CTV) coverage (ΔTC_{CTV}) and homogeneity index (ΔHI). **(A)** Relationship between ΔG-gas and ΔTC_{CTV} (V95%); **(B)** ΔHI. The horizontal axis shows the volume variation in G-gas from the initial plan. The effect of the beam range is considered in ΔG-gas. The vertical axes in **(A)** and **(B)** show the variations in TC_{CTV} and HI from the initial plan, respectively. The smaller the gradient, the smaller the effect of G-gas.

used. This may be because the location or amount of G-gas varied significantly from the treatment plan. Therefore, when implementing this method in clinical practice, it is necessary to carefully observe the location and amount of G-gas in the X-ray images obtained for 2D–3D bone matching at the time of each treatment before irradiation. If the variations in the location or proportion of G-gas are significant, the precautionary measures, such as routine verification of dose distributions using irCT images, seem to be necessary. Moreover, there is a need for an institutional protocol for the dividing method of the small intestine to minimize individual differences.

We analyzed the positional changes of G-gas and the validity of the replacement regions that correspond to those set with Pattern 2 (Figure 2C). On the premise that actual treatment will be performed using 2D–3D bone matching, pCT and irCT images were fused by bone matching using the MIM software, and we evaluated the concordance rate between the gas contour ($Gas_{pCT50\%}$) delineated on the $pCT_{50\%}$ images along the beam path and the gas contour ($Gas_{irCT50\%}$) delineated on the $irCT_{50\%}$ images as per volume. Furthermore, we evaluated the concordance rate between the replacement regions in Pattern 2 and $Gas_{irCT50\%}$. Figure 6 shows the resultant concordance rate. First, the median concordance rate between gas contouring along the path of each beam on $Gas_{pCT50\%}$ and $Gas_{irCT50\%}$ was 18.6%, 28.6%, and 27.6% in Beam 1, 2, and 3, respectively. Next, the median concordance rate between the replacement region of Pattern 2 and $Gas_{irCT50\%}$ was 65.7%, 72.9%, and 81.9% in Beam 1, 2, and 3, respectively. In the radiotherapy of the abdominal region, the position of G-gas was rarely consistent; however, the majority of gas remains mobile within the region that is considered as the gastrointestinal tract. The area replacement method of Pattern 2 is expected to minimize the effects of positional changes in G-gas throughout the treatment period and during irradiation (10).

The evaluation of variations between G-gas volume and ΔTC_{CTV} and ΔHI (Figure 5), showed that Pattern 2 was the least affected but Pattern 1 was the most affected by G-gas. In the initial treatment planning of Pattern 1, the beam stop positions were determined under the no-gas state. The effect of G-gas was considered the most significant due to the large rSPR value difference between treatment planning and each treatment. As shown in Figure 6, the concordance rate of G-gas position was lower in Pattern 3 than Pattern 2. However, Pattern 3 was able to consider the effect of G-gas more than Pattern 1, and the effect of G-gas was considered to be reduced compared with that in Pattern 1. Pattern 2 was able to consider variations in the location of G-gas more than Pattern 3 due to area replacement, and robustly responded to variations in the amount of G-gas due to mean value replacement.

Finally, we calculated a dose distribution of 55.2 Gy RBE/12 fractions (3, 30), which was adjusted for the effects of G-gas (Figure 7). Based on the results of this study, we propose that a treatment plan for robustness against G-gas can be prepared in which the fractions of Beams 1, 2, and 5 in the total dose are four, two, and six. The gantry angle and ratio of the irradiation dose were decided based on the effects of G-gas, uncertainty of the RBE model, and uncertainty of beam range calculation. Concerning Pattern 2, the variation was clearly significantly low for both ΔTC_{CTV} and ΔHI; compared with the other methods, the Pattern 2 mean value replacement method is feasible for robust treatment planning. The maximum dose, which covered 2 cm^3 (D_{2cm3}) of the gastrointestinal tract was 1.3–45.8 Gy RBE/12 fractions, and the dose constraints specified

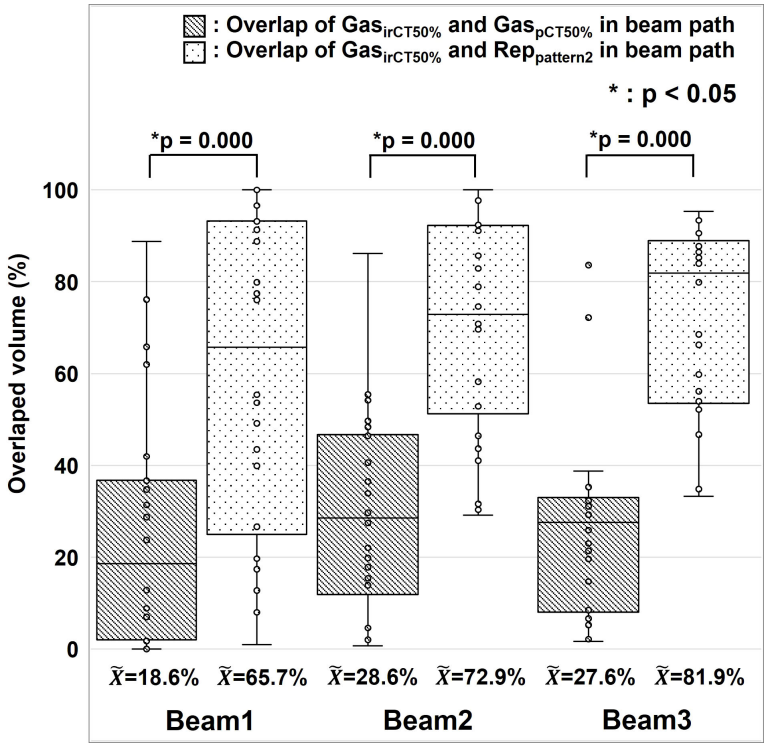

FIGURE 6
Positional changes of gastrointestinal gas. The median, first and third quartile, maximum and minimum values, and outliers for the concordance of gas contouring is presented in a box-and-whisker plot per each beam. The gas contour of the treatment planning CT images is presented as $Gas_{pCT50\%}$, the gas contour in the in-room CT images is presented as $Gas_{irCT50\%}$, and the replacement region set using Pattern 2 during treatment planning is presented as $Rep_{pattern2}$. We used the Wilcoxon signed rank test for the statistical analysis. The symbol * indicate that there is a significant difference between them.

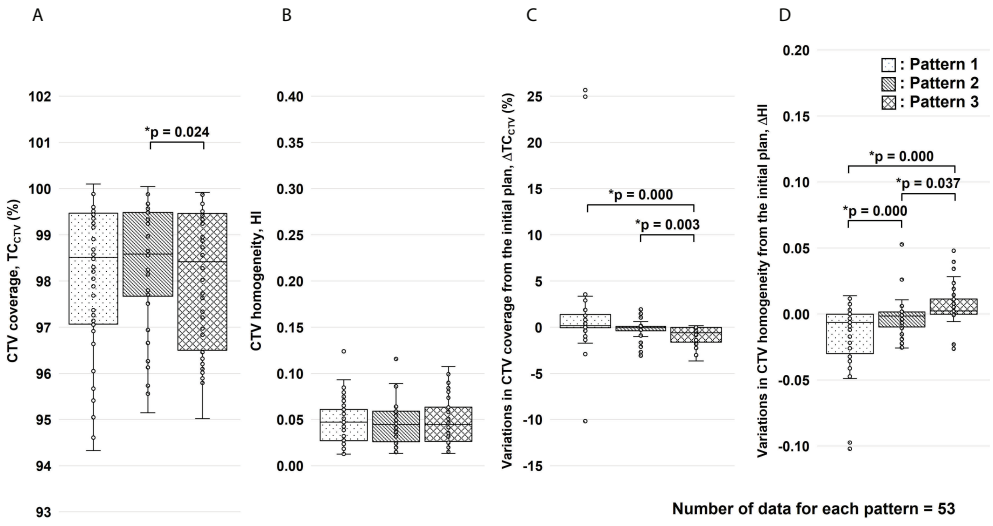

FIGURE 7
Results of the clinical target volume (CTV) coverage (TC_{CTV}) and homogeneity index (HI) evaluation for the total dose. Figure panels **(A, B)** show the results of TC_{CTV} and HI, respectively. Figure panels **(C, D)** show the results of variations in TC_{CTV} (ΔTC_{CTV}) and HI (ΔHI) from the initial plan, respectively. These results were corrected for changes in factors other than gastrointestinal gas. For each replacement pattern, the median, first and third quartiles, maximum and minimum values, and outliers for **(A)** TC_{CTV}, **(B)** HI, **(C)** ΔTC_{CTV}, and **(D)** ΔHI are presented in a box-and-whisker plot. Statistical analyses were performed using the Friedman test. The symbol * indicate that there is a significant difference between them.

by the Japan Carbon-ion Radiation Oncology Study Group (3, 30) were satisfied. This study had some limitations. First, the number of patients evaluated was 10, and the number of irCT scans was 4–7 per patient during the treatment. Although irCT scans were not performed at every treatment, the total number of beams used for evaluation in this study was considered sufficient. However, the accuracy of the analysis may be improved by increasing the number of beams. Second, individual differences in G-gas volume may have occurred due to dietary restrictions, drinking water restrictions, and medications. Reducing the effects of G-gas may be possible by taking appropriate measures for each patient, but G-gas cannot be completely removed.

Conclusions

This study demonstrated that treatment plans that were robust to changes in G-gas could be prepared by setting the replacement range as the region based on gastrointestinal contours delineated on pCT images and then replacing the range with the mean rSPR value obtained for each region. Our method improved dose delivery to the tumor. We are currently formulating treatment plans at our hospital based on this method. Despite the need for clinical follow-up, we believe that this method may help improve clinical outcomes. Furthermore, although this study focused on pancreatic cancer, this method might be used for particle beam scanning radiation for cancers that are affected by G-gas, such as cancers of the liver and abdominal cartilage, as well as gynecologic cancers. This method does not require any particular software or equipment, and it is simple to implement in clinical practice.

Data availability statement

The original contributions presented in the study are included in the article/Supplementary Material. Further inquiries can be directed to the corresponding author.

Ethics statement

The studies involving human participants were reviewed and approved by Institutional Review Board of Kanagawa Cancer Center (2019eki-106, August 30, 2021). The patients/participants provided their written informed consent to participate in this study.

Author contributions

Conceptualization, YK and HK; Methodology, YK; Validation, YK, YM, YTakay, KI, TKu, and SMiy; Formal analysis, YK; Investigation, YK and HF; Resources, YK; Data curation, YK and HF; Writing–original draft preparation, YK; Writing–review & editing, HK, SMin, YM, YTakay, KI, TKu, SMiy, TKam, IS, YTakak, NM, KT, and DY; Visualization, YK; Supervision, YK and HK; Project administration, YK, HK, SMin, and DY; Funding acquisition, HK, SMin, and DY. All authors contributed to the article and approved the submitted version.

Funding

This research was funded by Toshiba Energy Systems and Solutions Corporation (2019-Epi-102, 20 November 2019) and Japan Society for the Promotion of Science (JP20K08151).

Acknowledgments

This work was supported by JSPS KAKENHI Grant Number JP20K08151. The authors would like to thank Anna D, Ph.D., from Enago (www.enago.jp) for the English language review.

Conflict of interest

HF is employed by Accelerator Engineering Corporation. HK, SMin, and DY received research funding from Toshiba Energy Systems and Solutions Corporation.

The remaining authors declare that the research was conducted in the absence of any commercial or financial relationships that could be construed as a potential conflict of interest.

Publisher's note

Supplementary material

The Supplementary Material for this article can be found online at: https://www.frontiersin.org/articles/10.3389/fonc.2022.974728/full#supplementary-material

References

1. Balaban EP, Mangu PB, Khorana AA, Shah MA, Mukherjee S, Crane CH, et al. Locally advanced, unresectable pancreatic cancer: American society of clinical oncology clinical practice guideline. *J Clin Oncol* (2016) 34:2654–68. doi: 10.1200/JCO.2016.67.5561

2. Shinoto M, Yamada S, Terashima K, Yasuda S, Shioyama Y, Honda H, et al. Carbon ion radiation therapy with concurrent gemcitabine for patients with locally advanced pancreatic cancer. *Int J Radiat Oncol Biol Phys* (2016) 95:498–504. doi: 10.1016/j.ijrobp.2015.12.362

3. Kawashiro S, Yamada S, Okamoto M, Ohno T, Nakano T, Shinoto M, et al. Multi-institutional study of carbon-ion radiotherapy for locally advanced pancreatic cancer: Japan carbon-ion radiation oncology study group (J-CROS) study 1403 pancreas. *Int J Radiat Oncol Biol Phys* (2018) 101:1212–21. doi: 10.1016/j.ijrobp.2018.04.057

4. Shinoto M, Terashima K, Suefuji H, Matsunobu A, Toyama S, Fukunishi K, et al. A single institutional experience of combined carbon-ion radiotherapy and chemotherapy for unresectable locally advanced pancreatic cancer. *Radiother Oncol* (2018) 129:333–9. doi: 10.1016/j.radonc.2018.08.026

5. Liermann J, Shinoto M, Syed M, Debus J, Herfarth K, Naumann P. Carbon ion radiotherapy in pancreatic cancer: A review of clinical data. *Radiother Oncol* (2020) 147:145–50. doi: 10.1016/j.radonc.2020.05.012

6. Kawashiro S, Mori S, Yamada S, Miki K, Nemoto K, Tsuji H, et al. Dose escalation study with respiratory-gated carbon-ion scanning radiotherapy using a simultaneous integrated boost for pancreatic cancer: simulation with four-dimensional computed tomography. *Br J Radiol* (2017) 90:20160790. doi: 10.1259/bjr.20160790

7. Kanai T, Endo M, Minohara S, Miyahara N, Koyama-ito H, Tomura H, et al. Biophysical characteristics of HIMAC clinical irradiation system for heavy-ion radiation therapy. *Int J Radiat Oncol Biol Phys* (1999) 44:201–10. doi: 10.1016/s0360-3016(98)00544-6

8. Jäkel O, Deluca P. ICRU report 93: Prescribing, recording, and reporting light ion beam therapy. *J ICRU* (2016) 16. doi: 10.1093/jicru/ndy023

9. Dische S, Zanelli JD. Bowel gas–a cause of elevated dose in radiotherapy. *Br J Radiol* (1976) 49:148–50. doi: 10.1259/0007-1285-49-578-148

10. Kumagai M, Hara R, Mori S, Yanagi T, Asakura H, Kishimoto R, et al. Impact of intrafractional bowel gas movement on carbon ion beam dose distribution in pancreatic radiotherapy. *Int J Radiat Oncol Biol Phys* (2009) 73:1276–81. doi: 10.1016/j.ijrobp.2008.10.055

11. Batista V, Richter D, Combs SE, Jäkel O. Planning strategies for inter-fractional robustness in pancreatic patients treated with scanned carbon therapy. *Radiat Oncol* (2017) 12:94. doi: 10.1186/s13014-017-0832-x

12. Kubota Y, Okamoto M, Shiba S, Okazaki S, Ma–tsui T, Li Y, et al. Robustness of daily dose for each beam angle and accumulated dose for inter-fractional anatomical changes in passive carbon-ion radiotherapy for pancreatic cancer: Bone matching versus tumor matching. *Radiother Oncol* (2021) 157:85–92. doi: 10.1016/j.radonc.2021.01.011

13. Houweling AC, Fukata K, Kubota Y, Shimada H, Rasch CR, Ohno T, et al. The impact of interfractional anatomical changes on the accumulated dose in carbon ion therapy of pancreatic cancer patients. *Radiother Oncol* (2016) 119:319–25. doi: 10.1016/j.radonc.2016.03.004

14. Houweling AC, Crama K, Visser J, Fukata K, Rasch CR, Ohno T, et al. Comparing the dosimetric impact of interfractional anatomical changes in photon, proton and carbon ion radiotherapy for pancreatic cancer patients. *Phys Med Biol* (2017) 62:3051–64. doi: 10.1088/1361-6560/aa6419

15. Berger T, Petersen JBB, Lindegaard JC, Fokdal LU, Tanderup K. Impact of bowel gas and body outline variations on total accumulated dose with intensity-modulated proton therapy in locally advanced cervical cancer patients. *Acta Oncol* (2017) 56:1472–8. doi: 10.1080/0284186X.2017.1376753

16. Jin P, Crama KF, Visser J, van Wieringen N, Bel A, Hulshof M, et al. Density override in treatment planning to mitigate the dosimetric effect induced by gastrointestinal gas in esophageal cancer radiation therapy. *Acta Oncol* (2018) 57:1646–54. doi: 10.1080/0284186X.2018.1518590

17. Albertini F, Matter M, Nenoff L, Zhang Y, Lomax A. Online daily adaptive proton therapy. *Br J Radiol* (2020) 93:20190594. doi: 10.1259/bjr.20190594

18. Bassler N, Jäkel O, Søndergaard CS, Petersen JB. Dose- and LET-painting with particle therapy. *Acta Oncol* (2010) 49:1170–6. doi: 10.3109/0284186X.2010.510640

19. Bassler N, Toftegaard J, Lühr A, Sørensen BS, Scifoni E, Krämer M, et al. LET-painting increases tumour control probability in hypoxic tumours. *Acta Oncol* (2014) 53:25–32. doi: 10.3109/0284186X.2013.832835

20. Inaniwa T, Kanematsu N, Noda K, Kamada T. Treatment planning of intensity modulated composite particle therapy with dose and linear energy transfer optimization. *Phys Med Biol* (2017) 62:5180–97. doi: 10.1088/1361-6560/aa68d7

21. Hagiwara Y, Bhattacharyya T, Matsufuji N, Isozaki Y, Takiyama H, Nemoto K, et al. Influence of dose-averaged linear energy transfer on tumour control after carbon-ion radiation therapy for pancreatic cancer. *Clin Transl Radiat Oncol* (2020) 21:19–24. doi: 10.1016/j.ctro.2019.11.002

22. Nakayama Y, Minohara S, Nonaka T, Nomiya T, Kusano Y, Takeshita E, et al. The ion-beam radiation oncology center in kanagawa (i-ROCK) carbon ion facility at the kanagawa cancer center. *Int J Part Ther* (2016) 2:478–80. doi: 10.14338/IJPT-15-00024.1

23. Furukawa T, Inaniwa T, Sato S, Shirai T, Mori S, Takeshita E, et al. Moving target irradiation with fast rescanning and gating in particle therapy. *Med Phys* (2010) 37:4874–9. doi: 10.1118/1.3481512

24. Chen GT, Singh RP, Castro JR, Lyman JT, Quivey JM. Treatment planning for heavy ion radiotherapy. *Int J Radiat Oncol Biol Phys* (1979) 5:1809–19. doi: 10.1016/0360-3016(79)90564-9

25. Matsufuji N, Tomura H, Futami Y, Yamashita H, Higashi A, Minohara S, et al. Relationship between CT number and electron density, scatter angle and nuclear reaction for hadron-therapy treatment planning. *Phys Med Biol* (1998) 43:3261–75. doi: 10.1088/0031-9155/43/11/007

26. Jäkel O, Jacob C, Schardt D, Karger CP, Hartmann GH. Relation between carbon ion ranges and x-ray CT numbers. *Med Phys* (2001) 28:701–3. doi: 10.1118/1.1357455

27. Kanematsu N, Matsufuji N, Kohno R, Minohara S, Kanai T. A CT calibration method based on the polybinary tissue model for radiotherapy treatment planning. *Phys Med Biol* (2003) 48:1053–64. doi: 10.1088/0031-9155/48/8/307

28. Kanematsu N, Inaniwa T, Koba Y. Relationship between electron density and effective densities of body tissues for stopping, scattering, and nuclear interactions of proton and ion beams. *Med Phys* (2012) 39:1016–20. doi: 10.1118/1.3679339

29. Kanematsu N, Inaniwa T, Nakao M. Modeling of body tissues for Monte Carlo simulation of radiotherapy treatments planned with conventional x-ray CT systems. *Phys Med Biol* (2016) 61:5037–50. doi: 10.1088/0031-9155/61/13/5037

30. Shinoto M, Shioyama Y, Matsunobu A, Okamoto K, Suefuji H, Toyama S, et al. Dosimetric analysis of upper gastrointestinal ulcer after carbon-ion radiotherapy for pancreatic cancer. *Radiother Oncol* (2016) 120:140–4. doi: 10.1016/j.radonc.2016.04.040

31. Mori S, Kumagai M, Miki K, Fukuhara R, Haneishi H. Development of fast patient position verification software using 2D-3D image registration and its clinical experience. *J Radiat Res* (2015) 56:818–29. doi: 10.1093/jrr/rrv032

32. Furukawa T, Inaniwa T, Sato S, Shirai T, Takei Y, Takeshita E, et al. Performance of the NIRS fast scanning system for heavy-ion radiotherapy. *Med Phys* (2010) 37:5672–82. doi: 10.1118/1.3501313

33. Inaniwa T, Furukawa T, Kanematsu N, Mori S, Mizushima K, Sato S, et al. Evaluation of hybrid depth scanning for carbon-ion radiotherapy. *Med Phys* (2012) 39:2820–5. doi: 10.1118/1.4705357

34. Landry G, Hua CH. Current state and future applications of radiological image guidance for particle therapy. *Med Phys* (2018) 45:e1086–e95. doi: 10.1002/mp.12744

35. Deluca P, Shinoto M, Jones D, Gahbauer R, Whitmore G, Wambersie A. ICRU report 83: Prescribing, recording and reporting photon-beam intensity-modulated radiation therapy (IMRT). *J ICRU* (2010) 10:1–92. doi: 10.1093/jicru_ndq002

frontiers | Frontiers in Oncology

TYPE Original Research
PUBLISHED 18 November 2022
DOI 10.3389/fonc.2022.974454

OPEN ACCESS

EDITED BY
Timothy James Kinsella,
Brown University, United States

REVIEWED BY
Stanley Liauw,
The University of Chicago, United States
Marsha Reyngold,
Memorial Sloan Kettering Cancer Center, United States

*CORRESPONDENCE
Eui Kyu Chie
ekchie93@snu.ac.kr

SPECIALTY SECTION
This article was submitted to Radiation Oncology, a section of the journal Frontiers in Oncology

RECEIVED 21 June 2022
ACCEPTED 26 October 2022
PUBLISHED 18 November 2022

CITATION
Lee HI, Kang H-C and Chie EK (2022) Consolidatory ablative stereotactic body radiation therapy after induction chemotherapy for unresectable pancreatic cancer: A single center experience.
Front. Oncol. 12:974454.
doi: 10.3389/fonc.2022.974454

Consolidatory ablative stereotactic body radiation therapy after induction chemotherapy for unresectable pancreatic cancer: A single center experience

Hye In Lee[1,2], Hyun-Cheol Kang[1,2] and Eui Kyu Chie[1,2,3]*

[1]Department of Radiation Oncology, Seoul National University College of Medicine, Seoul, South Korea, [2]Department of Radiation Oncology, Seoul National University Hospital, Seoul, South Korea, [3]Institute of Radiation Medicine, Medical Research Center, Seoul National University, Seoul, South Korea

Background and purpose: Consolidatory radiotherapy in form of stereotactic body radiation therapy (SBRT) with an ablative dose following induction chemotherapy is emerging as a promising treatment scheme for unresectable pancreatic cancer. Outcomes of given treatment at a single center for contiguous patients with unresectable pancreatic cancer were evaluated to build the optimal treatment strategy.

Materials and methods: In this retrospective study, a total of 50 patients with unresectable pancreatic cancer who underwent induction chemotherapy and ablative dose SBRT were included. SBRT dose was 40–50 Gy in five fractions. Two strategies were adopted to adhere to the organs at risk (OAR) dose constraints: simultaneous integrated protection (SIP) technique and magnetic resonance (MR)-guided adaptive technique. Overall survival (OS) and local progression-free survival (LPFS) were calculated from the start date of SBRT.

Results: The median follow-up period for survivors was 21.1 months (range, 6.2–61.0 months). Eleven (22.0%) patients underwent resection after SBRT, which were all R0 resection. In patients with non-metastatic disease, the median OS was 26.5 months (range, 4.1–61.0 months), and the 1- and 3-year LPFS were 90.0% (95% confidence interval [CI], 72.0–96.7%) and 57.4% (95% CI, 31.7–76.4%), respectively. Patients with oligometastatic disease had inferior survival outcomes, but there was no survival difference among responders to induction chemotherapy. In the multivariable analysis, tumor size ≤4 cm, non-metastatic status, and good response to induction chemotherapy were associated with improved LPFS. In dosimetric analysis, GTV Dmin ≥50.5 Gy was the strongest prognosticator against local progression. Grade ≥3 adverse events occurred in two (4.0%) patients with non-adaptive RT, but none in patients with MR-guided adaptive RT.

Conclusion: Ablative dose SBRT following induction chemotherapy is an effective strategy for selected patients with unresectable pancreatic cancer. The SIP technique and MR-guided adaptive RT were attributed to minimizing the risk of adverse events. Further studies are needed to identify the best candidates for consolidatory SBRT in unresectable pancreatic cancer.

KEYWORDS

pancreatic cancer, stereotactic body radiotherapy, ablative dose, MR-guided adaptive radiotherapy, simultaneous integrated protection, oligometastatic disease

Introduction

Pancreatic cancer is one of the leading causes of cancer-related mortality worldwide. Most patients with pancreatic cancer present with locally advanced or metastatic disease and are not amenable to curative surgery (1). Chemotherapy is considered the standard of care for these patients, but the prognosis remains dismal, with a 5-year life expectancy of less than 10% (2). Recently, new multi-agent chemotherapy regimens have changed this paradigm (3–5). The combination regimen of 5-fluorouracil, leucovorin, irinotecan, and oxaliplatin (FOLFIRINOX) and gemcitabine with nanoparticle albumin-bound-paclitaxel (Gem/nab-paclitaxel) have become the first-line treatment options for unresectable pancreatic cancer. These regimens have been demonstrated to almost double the survival of unresectable pancreatic cancer compared with the previous monochemotherapy regimens. However, the limited gain in terms of local control may possibly expand the role of RT for local control.

Stereotactic body radiation therapy (SBRT) has emerged as an attractive approach in multimodality treatment for pancreatic cancer (6–8). SBRT offers the ability to deliver a large biologically effective dose (BED) in a highly conformal manner. Furthermore, SBRT interferes less with systemic therapy as it requires only 1–2 weeks for delivery. The optimal SBRT scheme has yet to be determined, but the administration of a higher BED is essential to achieve durable tumor control and has a significant impact on survival (9). However, SBRT for pancreatic cancer is challenging due to the proximity of radiosensitive organs-at-risk (OAR), such as the duodenum, stomach, and bowel. Although prospective data regarding pancreatic SBRT is accumulating, the optimal treatment strategy remains controversial (10).

In this study, simultaneous integrated protection (SIP) technique and magnetic resonance (MR)-guided adaptive technique are implemented as components of SBRT to deliver ablative dose SBRT while minimizing the treatment-related adverse event risk. The resultant efficacy and safety of the applied treatment is evaluated. In addition, we investigated optimal SBRT strategies, including patient selection and dosimetric parameters.

Materials and methods

Study cohort

We retrospectively identified patients with locally advanced pancreatic adenocarcinoma, including oligometastatic disease, who received induction chemotherapy followed by ablative dose SBRT between January 2017 and September 2021. Locally advanced stage was defined as a tumor with greater than 180-degree involvement of the superior mesenteric artery or celiac axis or unreconstructable involvement of the superior mesenteric vein or portal vein. Oligometastatic disease was defined as less than four metastases to a single organ. Patients were excluded if they had a prior definitive treatment history, pancreatic tumor histology other than adenocarcinoma, or double-primary malignancies. A total of 50 patients with unresectable pancreatic cancer constituted the analyzed cohort (Figure 1). This study was approved by the Institutional Review Board (IRB no. H-2105-070-1218).

Treatment

All patients received four or more cycles of induction chemotherapy before SBRT. Induction chemotherapy consisted of FOLFIRINOX (92.0%) and Gem/nab-paclitaxel (8.0%) regimens. A 3–4 week break from induction chemotherapy was required before SBRT delivery.

SBRT was performed in two ways; MR-guided adaptive SBRT was delivered using the MRIdian (ViewRay Inc.,

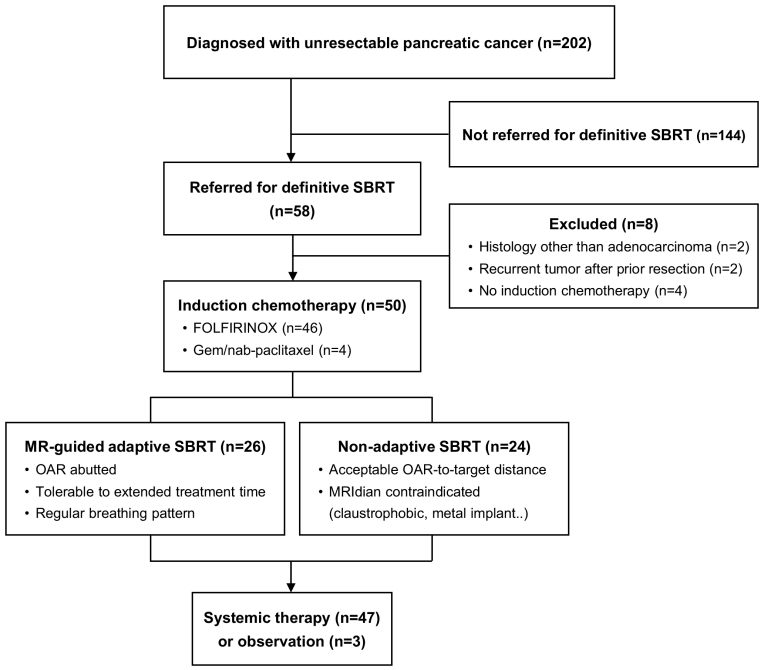

FIGURE 1
Consort diagram. MR, magnetic resonance; SBRT, stereotactic body radiotherapy; OAR, organs at risk.

Oakwood Village, OH) and non-adaptive linear accelerator (linac)-based SBRT was delivered using the TrueBeam-STX (Varian Medical Systems, Palo Alto, CA). Patients underwent both MR and computed tomography (CT) simulations on the same day. Patients were immobilized in the supine position with arms over head. A pneumatic abdominal compressor was used to reduce breathing-induced internal tumor movement. Patients who were unable to breathe regularly, could not tolerate extended treatment times, or had any contraindications to MR (e.g., claustrophobic, metal implant) were assigned to non-adaptive SBRT. Otherwise, both adaptive and non-adaptive SBRT plans were constructed, and the best plan for an individual patient was chosen based on both OAR dose and target coverage.

The principle of tumor delineation was same for both set-up (Figure 2). Gross tumor volume (GTV) was defined as pancreatic tumor based on 4-dimensional–CT and MR images. Clinical target volume (CTV) encompassed the GTV and vascular involvement, including the entire tumor-vessel interface. Planning target volume (PTV) included the CTV

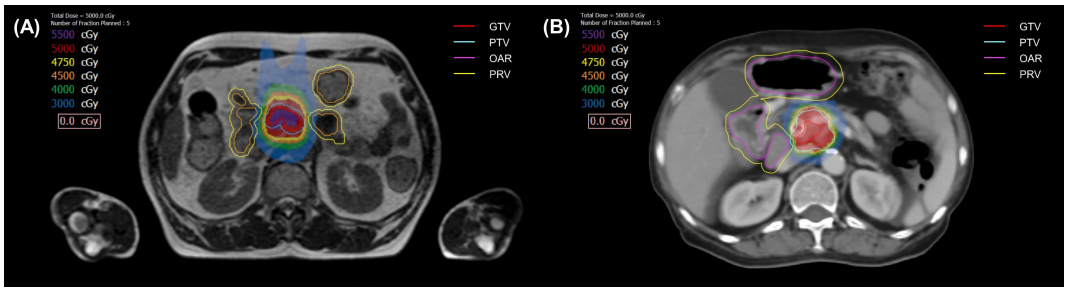

FIGURE 2
The target volumes and isodose lines for patients prescribed 50 Gy in 5 fractions with magnetic resonance-guided adaptive radiotherapy **(A)**, and linac-based nonadaptive radiotherapy **(B)**. GTV, gross tumor volume; PTV, planning target volume; OAR, organ at risk; PRV, planning OAR volume.

plus a 6 mm margin. Planning OAR volume (PRV) was defined as OAR plus a 4 mm margin. If the patient had an overlapping area between PTV and PRV, PTV was divided into two; PTV_{sip} was the overlap area between PTV and PRV, and PTV_{tumor} was the remaining, non-overlapping PTV area with PRV. Using the SIP technique, we prescribed 33 Gy to the PTV_{sip}, while simultaneously delivering a 50 Gy to the PTV_{tumor}. Exceptionally, GTV was prescribed to 50 Gy even if there was an overlapping area with PRV as long as OAR constraints, which was <33 Gy to 1cc, were met. Prescribed doses were lowered down to 40 Gy depending on the situation, including target/organ movement and target to organ distance of the individual patient. SBRT was delivered in five fractions with the goal of 95% PTV coverage with 100% of the prescription dose, prioritizing hard OAR constraints. OAR dose constraints were as follows: for the duodenum, bowel, and stomach, Dmax <35 Gy and D1cc <33 Gy; for the spinal cord, Dmax <22 Gy; for kidneys, Dmean <10 Gy; and for the liver, 700 cm3 <21 Gy. If the OAR-to-target distance was sufficient and the PTV coverage and OAR constraints were simultaneously met, the patient was often assigned to non-adaptive linac-based SBRT, due to the convenience of a shorter treatment delivery time. In contrast, if PTV coverage could not be met due to a violation of OAR constraints, the patient was usually assigned to MR-guided adaptive SBRT.

For adaptive SBRT delivery, MR imaging was performed before each fraction, and new OARs were re-contoured, reflecting inter-fractional changes. Then, the new re-optimized plan was generated. If the new plan violated OAR constraints, plan normalization was altered till OAR constraints were fulfilled. After the daily adaptive plan was determined, each fraction was delivered under MR-guided real-time gating. In non-adaptive SBRT, image-guided RT using cone beam CT was performed for all fractions. To reduce inter- and intra-fractional variability, a 6-hour fasting period before simulation and each fraction was mandated.

Follow-up

After completing SBRT, physical examination, laboratory tests, and imaging were performed every 2–6 months or when clinically indicated. Most patients continued to receive additional systemic therapy. The multidisciplinary tumor board determined resectability after reviewing the imaging and performance status. Adverse events were graded using the Common Terminology Criteria for Adverse Events (version 5.0). Acute adverse events were defined as those occurring within three months after SBRT, whereas late adverse events were defined as those occurring beyond three months after SBRT.

Statistical analysis

Response evaluation was performed using response evaluation criteria in solid tumors (RECIST). The response to induction chemotherapy was evaluated in two ways. The overall response was measured by comparing the disease status between the time of initial diagnosis and the time of SBRT. Whereas, the response at SBRT referral compared disease status between three months before SBRT and at the time of SBRT. For dosimetric analysis, all parameters were depicted from the cumulative daily delivered re-optimized plans for the adaptive treatments, whereas the original treatment plan was used for the non-adaptive treatments. GTV Dmean was defined as the mean dose absorbed by the GTV. GTV Dmin and GTV Dmax were defined as the minimum and maximum dose absorbed by 1 cc of GTV, respectively.

Local progression was defined as a 20% or more increase in tumor size on the CT scan compared to previous imaging following the RECIST criteria. Local progression-free survival (LPFS) was calculated from the start date of SBRT to the date of local progression or death. Overall survival (OS) was calculated from the start date of SBRT to the date of death. Surviving patients were censored at the date of the last follow-up. Survival outcomes were estimated using the Kaplan–Meier method. Cox proportional hazards modeling assessed whether survival outcomes varied according to risk factors. Continuous variables, including dose parameters, were divided into two subgroups at cutoff values identified by receiver operating characteristic (ROC) curves and then analyzed. All statistical tests were performed using STATA (version 15.1; StataCorp LP, College Station, TX, USA).

Results

Patient and treatment characteristics

Patients and treatment characteristics are summarized in Table 1. The median age was 62 years (range, 39–78 years), and the median tumor size was 3.0 cm (range, 1.6–5.5 cm). A total of 16 (32.0%) patients had nodal involvement and 17 (34.0%) patients had oligometastatic lesion. After induction chemotherapy for a median of 13 cycles (range, 4–29 cycles), the overall response was a partial response (PR) in 28 (56.0%), stable disease (SD) in 18 (36.0%), and progressive disease (PD) in 4 (8.0%) patients. The response at SBRT referral included fewer PR's and more SD's and PD's (PR: 44.0%, SD: 42.0%, and PD: 14.0%, respectively). The median prescribed dose was 50.0 Gy (range, 40–50 Gy), and the SIP protocol was applied in

TABLE 1 Patients and treatment characteristics (N=50).

Variable	No. (%)	
Age at diagnosis (years), median	62	(39–78)
Gender		
Male	22	(44.0%)
Female	28	(56.0%)
ECOG performance status		
ECOG 0-1	32	(64.0%)
ECOG 2-3	18	(36.0%)
Location of tumor		
Head	21	(42.0%)
Body/tail	29	(58.0%)
Tumor size at diagnosis (cm), median	3.0	(1.6–5.5)
Tumor size at SBRT (cm), median	2.4	(1.0–4.5)
Clinical T-stage		
T2	6	(12.0%)
T3	2	(4.0%)
T4	42	(84.0%)
Clinical N-stage		
N0	34	(68.0%)
N1	16	(32.0%)
Clinical M-stage		
M0	33	(66.0%)
M1	17	(34.0%)
Induction CRx regimen		
FOLFIRINOX	46	(92.0%)
Gemcitabine and nab-paclitaxel	4	(8.0%)
Induction CRx duration (mo), median	7.2	(1.5–21.9)
No. of induction CRx cycles, median	13	(4–29)
CA 19-9, baseline (U/mL), median	370	(2 to >12000)
CA 19-9, post-induction CRx/pre-SBRT (U/mL), median	36	(1 to >12000)
CA 19-9 post-SBRT (U/mL), median	19	(1 to >12000)
SBRT technique		
MR-guided adaptive SBRT	26	(52.0%)
Linac based non-adaptive SBRT	24	(48.0%)
Prescribed dose (Gy), median	50.0	(40–50)
GTV Dmin (Gy)[1], median	50.3	(40.8–58.3)
GTV Dmax (Gy)[2], median	51.8	(43.8–68.4)
GTV Dmean (Gy)[3], median	51.0	(42.4–62.1)
GTV volume (cm^3), median	13.6	(2.8–54.8)
PTV volume (cm^3), median	33.6	(9.0–107.0)
PTV_{sip} volume (cm^3), median	1.2	(0–6.4)

No, patients' number; SBRT, stereotactic body radiotherapy; ECOG, Eastern Cooperative Oncology Group; CRx, chemotherapy; mo, months; MR, magnetic resonance; Linac, linear accelerator; GTV, gross tumor volume; PTV, planning target volume; SIP, simultaneous integrated protection.
[1]GTV Dmin, the minimum dose absorbed by 1cc of the GTV.
[2]GTV Dmax, the maximum dose absorbed by 1cc of the GTV.
[3]GTV Dmean, mean dose absorbed by the GTV.

29 (58%) patients. Of the 26 patients (52.0%) who received MR-guided adaptive SBRT, the delivered dose was reduced in 16 patients (32.0%) to abide by the OAR constraint. A total of 47 (94.0%) patients received post-SBRT chemotherapy for a median number of 8 cycles (range, 1–41 cycles).

A dramatic decline in carbohydrate antigen (CA) 19-9 was observed after induction chemotherapy and SBRT. The median % change of CA 19-9 was -82.7% from baseline to post-induction chemotherapy/pre-SBRT and -38.8% from post-induction chemotherapy/pre-SBRT to post-SBRT.

Treatment outcomes

The median follow-up period was 18.8 months (range, 4.1–61.0 months) for all patients and 21.1 months (range, 6.2–61.0 months) for survivors from the start date of SBRT. In patients with non-metastatic disease, the median OS was 26.5 months (range, 4.1–61.0 months), and the 1- and 3-year OS rates were 87.3% (95% confidence interval [CI], 69.6–95.1%) and 37.0% (95% CI, 17.4–56.8%), respectively. Patients with oligometastatic disease had inferior survival outcomes with a median OS of 12.5 months (range, 6.2–40.7 months), and the 1- and 3-year OS rates of 61.6% (95% CI, 33.5–80.7%) and 16.0% (95% CI, 2.7–39.5%), respectively (Figure 3). However, this difference diminished in patients responding to induction chemotherapy (oligometastatic/PR: 1-year OS 85.7% [95% CI, 33.4–97.9%] and 3-year OS 35.7% [95% CI, 5.2–69.9%]; oligometastatic/SD-PD: 1-year OS 40.5% [95% CI, 10.0–70.1%] and 3-year OS 0%). The 1- and 3-year LPFS rates of the non-metastatic group were 90.0% (95% CI, 72.0–96.7%) and 57.4% (95% CI, 31.7–76.4%), respectively. In oligometastatic/PR group, the 1- and 3-year LPFS were 100.0% and 44.4% (95% CI, 6.6–78.5%), respectively. Meanwhile, the corresponding rates of oligometastatic/SD-PD group were 45.7% (95% CI, 8.2–78.3%) and 0%, respectively.

After SBRT, eleven (22.0%) patients underwent resection, and all had R0 resection, with three (6.0%) achieving a pathologic complete response (pCR). There were no grade ≥3 postoperative adverse events. Patients with resected tumors showed significantly improved survival outcomes compared with patients without resection (1-year OS: 90.9% [95% CI, 50.8–98.7%] vs. 75.1% [95% CI, 57.5–86.2%]; 3-year OS: 64.9% [95% CI, 24.9–87.4%] vs. 19.0% [95% CI, 6.7–36.0%]; p=0.014). At the last follow-up, 16 (32.0%) patients were in a progression-free state with normalized CA 19-9 and without imaging evidence of progression.

Prognostic factors

The univariate and multivariate Cox proportional hazards models for OS and LPFS are presented in Table 2. In the multivariate analysis, M-stage was a strong prognostic factor for both OS and LPFS (Hazard ratio [HR] 2.74, p=0.018 in OS; HR 5.32, p=0.003 in LPFS). A large initial tumor size (≥4 cm) was associated with inferior LPFS (HR 4.26, p=0.003). Response to the induction chemotherapy in overall (HR 3.79, p=0.044) and at SBRT referral (HR 4.27, p=0.001) were both significantly related to OS, but only response at SBRT referral was a significant factor for LPFS (HR 3.72, p=0.022). Among dose parameters, higher GTV Dmin (≥50.5 Gy) was significantly associated with improved LPFS (HR 3.06, p=0.045) and OS (HR 2.58, p=0.031). However, the prescribed dose (≥50 Gy), GTV Dmax (≥52 Gy), and GTV Dmean (≥51 Gy) failed to demonstrate statistical significance. Greater CA 19-9 decline after SBRT (≥50%) had a strong relationship with improved LPFS (HR 3.85, p=0.015). On the other hand, the volume of PTV and PTV_{sip} did not affect survival outcomes. SBRT technique (adaptive vs. non-adaptive) also had no significant association with both OS and LPFS.

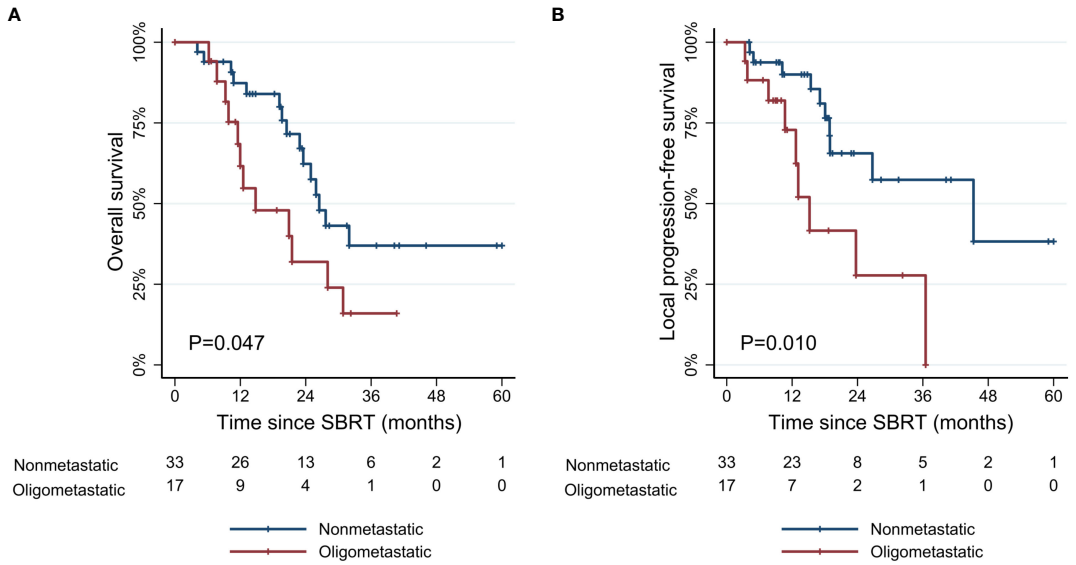

FIGURE 3
Kaplan-Meier curves of **(A)** overall survival, and **(B)** local progression-free survival according to metastatic status. SBRT, stereotactic body radiotherapy.

TABLE 2 Univariate and multivariate analysis affecting overall survival and local progression-free survival.

Variables	Overall survival						Local progression-free survival					
	Univariate			Multivariate			Univariate			Multivariate		
	HR	95% CI	p-value	HR	95% CI	p-value	HR	95% CI	p-value	HR	95% CI	p-value
Baseline characteristic												
Age at diagnosis (>60 vs. ≤60)	1.47	0.68-3.16	0.324				0.93	0.39-2.37	0.925			
Sex (male vs. female)	0.78	0.36-1.68	0.525				0.46	0.17-1.22	0.119			
Performance status (ECOG 2/3 vs. ECOG 0/1)	1.40	0.65-2.99	0.390				1.00	0.39-2.55	0.996			
Tumor location (head vs. body/tail)	1.46	0.67-3.17	0.340				1.03	0.40-2.62	0.956			
Tumor size (>4 cm vs. ≤4 cm)	1.29	0.60-2.79	0.518				3.20	1.28-7.98	**0.013**	4.26	1.61-11.24	**0.003**
T-stage (T4 vs. T1-T3)	1.12	0.39-3.25	0.833				5.59	0.71-44.2	0.103			
N-stage (N1 vs. N0)	1.05	0.47-2.33	0.914				0.84	0.32-2.23	0.735			
M-stage (M1 vs. M0)	2.13	0.99-4.57	**0.052**	2.74	1.19-6.29	**0.018**	3.23	1.27-8.25	**0.014**	5.32	1.76-16.08	**0.003**
CA 19-9 (>37.0 vs. ≤37 U/mL)	0.58	0.22-1.54	0.274				3.61	0.48-27.20	0.214			
Induction CRx												
Induction CRx regimen (FOLFIRINOX vs. Gem/nab-paclitaxel)	0.99	0.23-4.18	0.985				1.18	0.36-3.87	0.788			
Induction CRx duration (≥3 months vs. <3 months)	4.36	1.22-15.57	**0.023**	3.79	1.03-13.93	**0.044**	2.12	0.64-7.03	0.220			
Response to induction CRx, overall (SD/PD vs. PR)	3.41	1.55-7.50	**0.002**	4.27	1.82-10.02	**0.001**	1.50	0.57-3.94	0.415			
Response to induction CRx at SBRT referral (SD/PD vs. PR)	2.62	1.16-5.88	**0.020**	3.22	1.33-7.79	**0.010**	2.27	0.86-6.01	**0.093**	3.72	1.21-11.43	**0.022**
CA19-9% change after induction CRx (<50% vs. ≥50%)	1.48	0.62-3.54	0.378				1.45	0.68-3.10	0.331			
SBRT												
SBRT technique (adaptive vs. non-adaptive)	1.20	0.54-2.67	0.659				1.87	0.73-4.78	0.190			
Prescribed dose (<50 Gy vs. ≥50 Gy)	2.65	1.21-5.83	**0.015**	2.17	0.97-4.84	0.060	2.44	0.95-6.27	**0.065**	1.96	0.75-5.10	0.169
GTV Dmin[1] (<50.5 Gy vs. ≥50.5 Gy)	2.30	1.01-5.25	**0.049**	2.58	1.09-6.09	**0.031**	4.18	1.48-11.82	**0.007**	3.06	1.03-9.14	**0.045**
GTV Dmax[2] (<52 Gy vs. ≥52 Gy)	1.47	0.67-3.23	0.335				2.03	0.76-5.46	0.158			
GTV Dmean[3] (<51 Gy vs. ≥51 Gy)	1.22	0.57-2.65	0.608				1.92	0.75-4.93	0.173			
PTV volume (<23 cm^3 vs. ≥23 cm^3)	0.72	0.27-1.92	0.516				0.47	0.14-1.62	0.262			
PTV_{sip} volume (<1.6 cm^3 vs. ≥1.6 cm^3)	0.81	0.30-2.13	0.659				0.43	0.10-1.85	0.256			
CA19-9% change after SBRT (<50% vs. ≥50%)	2.90	1.25-6.71	**0.013**	2.25	0.80-6.34	0.123	3.86	1.32-11.27	**0.014**	3.85	1.31-11.35	**0.015**
Post-SBRT CRx												
Post-SBRT CRx regimen (FOLFIRINOX vs. others)	0.55	0.23-1.33	0.182				1.34	0.44-4.05	0.610			

ECOG, Eastern Cooperative Oncology Group; CRx, chemotherapy; Gem/abraxane, gemcitabine + nab-paclitaxel; SD, stable disease; PD, progressive disease; PR, partial response; SBRT, stereotactic body radiotherapy; GTV, gross tumor volume; PTV, planning target volume; SIP, simultaneous integrated protection; HR, hazard ratio; CI, Confidence interval.
[1]GTV Dmin, the minimum dose absorbed by 1cc of the GTV.
[2]GTV Dmax, the maximum dose absorbed by 1cc of the GTV.
[3]GTV Dmean, mean dose absorbed by the GTV.
p-values below 0.05 are shown in bold.

Dosimetric analysis

The values of dosimetric parameters in patients with or without local progression within three years following SBRT are shown in Table 3. The mean values were all higher in patients without local progression compared to those with local progression. Among dosimetric parameters, the difference between the two groups was significant for the prescribed dose

TABLE 3 Comparison of dosimetric parameters between patient groups with or without local progression within 3 years following SBRT.

	No local progression (N=33)	Local progression (N=17)	P-value	AUC
Prescribed dose (Gy)	48.7 ± 2.2	46.3 ± 3.9	0.006	0.664
GTV Dmin (Gy)	51.3 ± 0.5	47.8 ± 4.2	<0.001	0.789
GTV Dmax (Gy)	55.3 ± 0.9	52.1 ± 1.5	0.063	0.717
GTV Dmean (Gy)	53.4 ± 3.7	50.0 ± 1.1	0.008	0.735

SBRT, stereotactic body radiotherapy; GTV, gross tumor volume; AUC, area under curve.
GTV Dmin, the minimum dose absorbed by 1cc of the GTV; GTV Dmax, the maximum dose absorbed by 1cc of the GTV; GTV Dmean, mean dose absorbed by the GTV.
*Data are expressed as mean ± standard deviation.

(p=0.006), GTV Dmin (p<0.001), and GTV Dmean (p=0.008). According to the ROC analysis, GTV Dmin showed the highest AUC (0.789) as a predictor of local progression (Supplementary Figure 1). Patients with GTV Dmin ≥50.5 Gy showed superior OS and LPFS compared to those with GTV Dmin < 50.5 Gy (1-year OS: 82.9% [95% CI, 60.6–93.2%] vs. 74.3% [95% CI, 51.4–87.6%], p=0.049; 1-year LPFS: 91.5% [95% CI, 70.0–97.8%] vs. 77.3% [95% CI, 53.2–54.2%], p=0.007) (Figure 4).

Adverse events

The acute and late adverse events are presented in Table 4. Acute grade 2 adverse events occurred in 23 (46.0%) patients. There were no grade 3 or higher acute adverse events. The most common acute adverse events were abdominal pain (32.0%), nausea/vomiting (28.0%), and poor oral intake (16.0%). Regarding the late adverse events, grade 2 or higher events occurred in 15 (30.0%) patients. A total of two (6.0%) patients experienced grade 3 gastro-intestinal bleeding, both requiring endoscopic intervention, but were successfully managed. There were no grade 4 or higher late adverse events. Patients treated with MR-guided adaptive SBRT showed a trend toward lower rates of late adverse events compared with those treated with non-adaptive SBRT (grade 2: 19.2% vs. 33.3%; grade 3: 0% vs. 8.3%; p=0.084).

Discussion

Pancreatic cancer is perceived as a systemic disease with the eventual emergence of widespread metastases. Despite this, up to 30% of patients with pancreatic cancer are reported to be without metastatic disease at the time of death (11). This percentage is likely to further increase as systemic therapy is continuously advancing in both multiagent cytotoxic approaches and combined precision medicine-based strategies (4, 12). In an era of more effective systemic therapy, maximizing local treatment has become more important, which may eventually lead to improved treatment outcomes. However, the use of conventionally fractionated RT failed to convey survival benefits in addition to the standard of care chemotherapy in a prospective trial, despite improvement in local control (13).

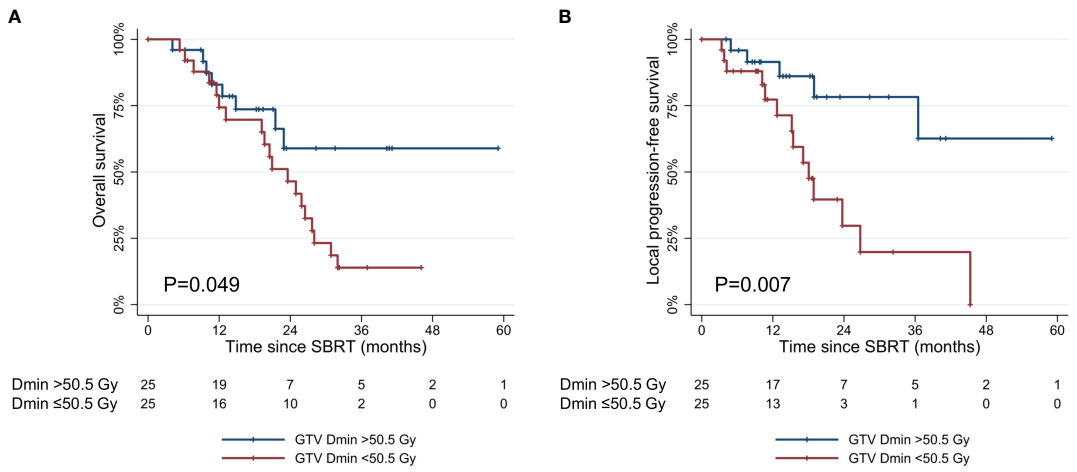

FIGURE 4
Kaplan-Meier curves of **(A)** overall survival, and **(B)** local progression-free survival according to GTV Dmin (≥50.5 Gy vs. <50.5 Gy). SBRT, stereotactic body radiotherapy; GTV, gross tumor volume. GTV Dmin = the minimum dose absorbed by 1cc of the GTV.

TABLE 4 Acute and late adverse events after SBRT.

	Grade 2		Grade 3	
Acute				
Abdominal pain	16	(32.0%)	0	(0.0%)
Nausea/Vomiting	14	(28.0%)	0	(0.0%)
Poor oral intake	8	(16.0%)	0	(0.0%)
Diarrhea	3	(6.0%)	0	(0.0%)
Total	23	(46.0%)	0	(0.0%)
Chronic				
Abdominal pain	6	(12.0%)	1	(2.0%)
Bleeding	6	(12.0%)	2	(4.0%)
Ulcer	4	(8.0%)	2	(4.0%)
Gastritis	3	(6.0%)	0	(0.0%)
Fistula	1	(2.0%)	0	(0.0%)
Total	13	(26.0%)	2	(4.0%)

*No grade 4 or 5 adverse events.

In this context, SBRT has emerged as an attractive alternative showing the potential to improve local control, with an ability to deliver a higher dose in a conformal manner and requiring shorter overall treatment time, simultaneously. A recent meta-analysis reported that SBRT significantly improved 2-year OS compared to conventionally fractionated RT (26.9% vs. 13.7%, p = 0.004) (6). Petrelli et al. performed a systemic review of 19 trials of SBRT and reported the pooled 1-year OS rate of 51.6% (95% CI 41.4-61.7%) and 1-year local control rate of 72.3% (95% CI 58.5-79%) (14). Many of these data suggest that a higher dose is needed to achieve adequate tumor control (15, 16). Toesca et al. reviewed the treatment outcomes of 149 patients who received multi-fraction SBRT for unresectable pancreatic cancer (15). They reported that patients treated with SBRT dose ≥40 Gy had superior OS and PFS compared to those who received SBRT dose <40 Gy (median OS: 23 vs. 14 months, p=0.0007; median PFS: 13 vs. 10 months, p = 0.007). In this study, we reported the 1-year OS and LPFS rates of 87.3% and 90.0%, respectively, which is in line with SBRT series with an ablative-dose (BED_{10} ≥100 Gy). However, SBRT delivering an ablative dose is still limited due to the proximity of critical neighboring radiosensitive OARs. Furthermore, the tumor and surrounding structures are highly mobile and sometimes difficult to identify using cone beam CT-based imaging. Thus, in this study, we adopted two approaches to safely deliver ablative doses.

The SIP technique allows the simultaneous delivery of ablative doses to the tumor volume, whereas the overlapping volume with critical OARs is covered by a lowered, safer dose (17). Several studies have reported the results of SIP protocol in different RT schemes (18–20). Simoni et al. performed SBRT using the SIP technique by administering 50 Gy to the tumor-vessel interface (TVI), 30 Gy to the pancreatic tumor, and 25 Gy to the SIP volume (18). They found no acute or late grade ≥3 adverse events, but a predominant incidence of in-field failures occurred. After that, the authors investigated dose escalation protocols up to 60, 40, and 33 Gy to TVI, pancreatic tumor, and SIP volume, respectively, and demonstrated the feasibility with adequate PTV coverage and acceptable OAR exposure (21). In this cohort, we prescribed 50 Gy to the TVI and tumor and 33 Gy to the SIP volume. We found favorable toxicity profiles without compromising survival outcomes. The volume of PTV and PTV_{sip} did not affect survival outcomes in multivariable analysis, although the small cohort size may have obscured the impact.

On the other hand, MR-guided adaptive RT is another powerful tool ensuring accurate treatment delivery with several advantages (22). First, MR guidance offers improved soft tissue contrast, resulting in the ability to distinguish the boundaries of pancreatic tumors. Second, a new re-optimized plan can be generated and optimized per fraction, reflecting daily anatomical changes. Hassanzadeh et al. found that duodenal dose constraints would have been violated in 67.7% of fractions for pancreatic cancer patients without per fraction optimization (23). Third, a real-time gating system enables intra-treatment monitoring of OARs. Several retrospective studies of MR-guided adaptive RT have reported promising outcomes while minimizing toxicities (24, 25). In the current study, grade ≥ 3 adverse events occurred in two (4.0%) patients with non-adaptive RT, and none in patients with MR-guided adaptive RT. It is notable that patients with close OAR-to-target distance were mostly assigned to MR-guided adaptive SBRT (Figure 1). Therefore, MR-guided adaptive RT may be more suitable for patients with a high risk of adverse events. Given the low conversion rate to surgery, safety concerns should be a top priority for SBRT treatment. The adoption of SIP technique and MR-guided adaptive RT can contribute to minimizing the risk of adverse events while delivering ablative doses to the tumor.

Currently, the optimal SBRT strategies have yet to be determined for pancreatic cancer. Published studies have used various combinations of dose and fraction schemes. Nonetheless, in order to perform SBRT effectively, particularly in daily adaptive SBRT, it is essential to identify significant dose parameters. Current dosimetric analysis nominated GTV Dmin as the most relevant parameter against local progression, with the cutoff value of 50.5 Gy, as determined by ROC analysis. Thus, patients with smaller PTV and PTV_{sip} volumes may be better candidates for SBRT that meet the dosimetric requirements and minimize adverse events. In addition, our results found that patients who had a tumor size ≤4 cm, non-metastatic status, and good response to induction chemotherapy showed a better prognosis after SBRT. Response to induction chemotherapy at three months prior to SBRT was more predictive of treatment outcomes compared to at the time of diagnosis. This may reflect that prompt delivery of consolidatory treatment would be a more effective strategy for patients with an initial response to induction chemotherapy but a stationary response afterward, compared with continued chemotherapy till progression.

Furthermore, it is notable that patients who had oligometastatic disease but achieved response to induction chemotherapy showed similar survival rates compared to non-metastatic patients in this study. Only few studies have examined the role of SBRT in metastatic pancreatic cancer. Lischalk et al. evaluated 20 patients with metastatic pancreatic cancer who received chemotherapy and SBRT (26). They reported 1-year OS and local control rates of 43% and 53%, respectively, without grade ≥3 toxicities. They also found that smaller PTV was associated with improved OS (p=0.001) and local control rates (p=0.02). Rosati et al. recommended a minimum of 6 months of chemotherapy and an observation period (4–8 weeks) before SBRT to better understand the natural history of disease (27). In this study, we found that a longer duration of induction chemotherapy (≥3 months) and good response to chemotherapy were associated with improved survival outcomes. Although based on the observation from very selected small population, SBRT to the primary site may have a role for oligometastatic patients who underwent chemotherapy over a period of time and achieve a durable response to induction chemotherapy. On the contrary, we do not advocate SBRT for patients with oligometastatic disease who did not respond to induction chemotherapy, as patients with these unfavorable factors eventually experienced disease progression within six months from SBRT. This principle is in line with selectively offering ablative local treatment in oligo-persistent disease.

There are several limitations to this study. First, the number of patients is far insufficient to draw concrete conclusion, especially in the oligometastatic disease subgroup. Additionally, as this was a retrospective study, the events could have been underestimated due to incomplete medical records. Second, the dosimetric analysis might be biased because lower doses were prescribed in patients with poor performance status. Finally, MR-guided adaptive SBRT was performed using the Cobalt-60 system in this study. Better OAR sparing may be achieved with MR-linac system with a steeper dose gradient. Nonetheless, the entire cohort was treated with the uniform treatment protocol, including dose prescription, target delineation, and decision policy for radiotherapy technique. Furthermore, they all received FOLFIRINOX or Gem/nab-paclitaxel, which are currently considered the standard of care as the first-line treatments. Thus, our findings may have better applicability and generalizability to current clinical practice.

In conclusion, consolidatory ablative dose SBRT following induction chemotherapy could be a viable treatment option for selected patients with unresectable pancreatic cancer. Patients with a tumor size ≤4 cm and achieved a durable response to induction chemotherapy may be good candidates for SBRT treatment as consolidatory measure. Prompt ablative consolidatory treatment delivery may be more appropriate approach compared to sustained chemotherapy beyond initial response. For SBRT planning, GTV Dmin (≥50.5 Gy) was identified as the most relevant parameter against local progression. The SIP technique and MR-guided adaptive RT strategies enabled the delivery of an ablative dose to the tumor while minimizing toxicity of surrounding OARs. Further studies with larger cohort sizes, better yet prospective design would help to further validate the role of the optimal SBRT strategies in pancreatic cancer.

Data availability statement

The raw data supporting the conclusions of this article will be made available by the authors, without undue reservation.

Ethics statement

The studies involving human participants were reviewed and approved by The Institutional Review Board of Seoul National University Hospital (IRB no. H-2105-070-1218). Written informed consent for participation was not required for this study in accordance with the national legislation and the institutional requirements.

Author contributions

EC contributed conception and design of the study. HL contributed to data collection, statistical analysis and wrote the first draft of the manuscript. EC and H-CK revised the manuscript. All authors contributed to the article and approved the submitted version.

Conflict of interest

The authors declare that the research was conducted in the absence of any commercial or financial relationships that could be construed as a potential conflict of interest.

Publisher's note

Supplementary material

The Supplementary Material for this article can be found online at: https://www.frontiersin.org/articles/10.3389/fonc.2022.974454/full#supplementary-material

SUPPLEMENTARY FIGURE 1
Kaplan-Meier curves of **(A)** overall survival, and **(B)** local progression-free survival according to metastatic status and overall response to the induction chemotherapy. SBRT, stereotactic body radiotherapy.

SUPPLEMENTARY FIGURE 2
Comparison of receiver operating characteristic (ROC) curves of dosimetric parameters for predicting the 3-year incidence of local progression. GTV, gross tumor volume; AUC, area under curve.GTV Dmin, the minimum dose absorbed by 1cc of the GTV; GTV Dmax, the maximum dose absorbed by 1cc of the GTV; GTV Dmean, mean dose absorbed by the GTV.

References

1. McGuigan A, Kelly P, Turkington RC, Jones C, Coleman HG, McCain RS. Pancreatic cancer: A review of clinical diagnosis, epidemiology, treatment and outcomes. *World J Gastroenterol* (2018) 24:4846–61. doi: 10.3748/wjg.v24.i43.4846

2. Siegel RL, Miller KD, Fuchs HE, Jemal A. Cancer statistics, 2021. *CA Cancer J Clin* (2021) 71:7–33. doi: 10.3322/caac.21654

3. Conroy T, Desseigne F, Ychou M, Bouché O, Guimbaud R, Bécouarn Y, et al. FOLFIRINOX versus gemcitabine for metastatic pancreatic cancer. *N Engl J Med* (2011) 364:1817–25. doi: 10.1056/nejmoa1011923

4. Suker M, Beumer BR, Sadot E, Marthey L, Faris JE, Mellon EA, et al. FOLFIRINOX for locally advanced pancreatic cancer: a systematic review and patient-level meta-analysis. *Lancet Oncol* (2016) 17:801–10. doi: 10.1016/S1470-2045(16)00172-8

5. Von Hoff DD, Ervin T, Arena FP, Chiorean EG, Infante J, Moore M, et al. Increased survival in pancreatic cancer with nab-paclitaxel plus gemcitabine. *N Engl J Med* (2013) 369:1691–703. doi: 10.1056/nejmoa1304369

6. Tchelebi LT, Lehrer EJ, Trifiletti DM, Sharma NK, Gusani NJ, Crane CH, et al. Conventionally fractionated radiation therapy versus stereotactic body radiation therapy for locally advanced pancreatic cancer (CRiSP): An international systematic review and meta-analysis. *Cancer* (2020) 126:2120–31. doi: 10.1002/cncr.32756

7. Herman JM, Chang DT, Goodman KA, Dholakia AS, Raman SP, Hacker-Prietz A, et al. Phase 2 multi-institutional trial evaluating gemcitabine and stereotactic body radiotherapy for patients with locally advanced unresectable pancreatic adenocarcinoma. *Cancer* (2015) 121:1128–37. doi: 10.1002/cncr.29161

8. Mahadevan A, Miksad R, Goldstein M, Sullivan R, Bullock A, Buchbinder E, et al. Induction gemcitabine and stereotactic body radiotherapy for locally advanced nonmetastatic pancreas cancer. *Int J Radiat Oncol Biol Phys* (2011) 81:615–22. doi: 10.1016/j.ijrobp.2011.04.045

9. Mahadevan A, Moningi S, Grimm J, Li XA, Forster KM, Palta M, et al. Maximizing tumor control and limiting complications with stereotactic body radiation therapy for pancreatic cancer. *Int J Radiat Oncol Biol Phys* (2021) 110:206–16. doi: 10.1016/j.ijrobp.2020.11.017

10. Oar A, Lee M, Le H, Hruby G, Dalfsen R, Pryor D, et al. Australasian Gastrointestinal trials group (AGITG) and trans-Tasman radiation oncology group (TROG) guidelines for pancreatic stereotactic body radiation therapy (SBRT). *Pract Radiat Oncol* (2020) 10:e136–46. doi: 10.1016/j.prro.2019.07.018

11. Lacobuzio-Donahue CA, Fu B, Yachida S, Luo M, Abe H, Henderson CM, et al. DPC4 gene status of the primary carcinoma correlates with patterns of failure in patients with pancreatic cancer. *J Clin Oncol* (2009) 27:1806–13. doi: 10.1200/JCO.2008.17.7188

12. Pishvaian MJ, Blais EM, Brody JR, Lyons E, DeArbeloa P, Hendifar A, et al. Overall survival in patients with pancreatic cancer receiving matched therapies following molecular profiling: a retrospective analysis of the know your tumor registry trial. *Lancet Oncol* (2020) 21:508–18. doi: 10.1016/S1470-2045(20)30074-7

13. Hammel P, Huguet F, Van Laethem JL, Goldstein D, Glimelius B, Artru P, et al. Effect of chemoradiotherapy vs chemotherapy on survival in patients with locally advanced pancreatic cancer controlled after 4 months of gemcitabine with or without erlotinib the LAP07 randomized clinical trial. *JAMA - J Am Med Assoc* (2016) 315:1844–53. doi: 10.1001/jama.2016.4324

14. Petrelli F, Comito T, Ghidini A, Torri V, Scorsetti M, Barni S. Stereotactic body radiation therapy for locally advanced pancreatic cancer: A systematic review and pooled analysis of 19 trials. *Int J Radiat Oncol Biol Phys* (2017) 97:313–22. doi: 10.1016/j.ijrobp.2016.10.030

15. Toesca DAS, Ahmed F, Kashyap M, Baclay JRM, von Eyben R, Pollom EL, et al. Intensified systemic therapy and stereotactic ablative radiotherapy dose for patients with unresectable pancreatic adenocarcinoma. *Radiother Oncol* (2020) 152:63–9. doi: 10.1016/j.radonc.2020.07.053

16. Arcelli A, Guido A, Buwenge M, Simoni N, Mazzarotto R, Macchia G, et al. Higher biologically effective dose predicts survival in SBRT of pancreatic cancer: A multicentric analysis (PAULA-1). *Anticancer Res* (2020) 40:465–72. doi: 10.21873/anticanres.13975

17. Brunner TB, Nestle U, Adebahr S, Gkika E, Wiehle R, Baltas D, et al. Simultan integrierte protektion: Ein neues konzept für die hochpräzisionsbestrahlung. *Strahlentherapie und Onkol* (2016) 192:886–94. doi: 10.1007/s00066-016-1057-x

18. Rossi G, Simoni N, Paiella S, Rossi R, Venezia M, Micera R, et al. Risk adapted ablative radiotherapy after intensive chemotherapy for locally advanced pancreatic cancer. *Front Oncol* (2021) 11:662205. doi: 10.3389/fonc.2021.662205

19. Mellon EA, Hoffe SE, Springett GM, Frakes JM, Strom TJ, Hodul PJ, et al. Long-term outcomes of induction chemotherapy and neoadjuvant stereotactic body radiotherapy for borderline resectable and locally advanced pancreatic adenocarcinoma. *Acta Oncol (Madr)* (2015) 54:979–85. doi: 10.3109/0284186X.2015.1004367

20. Simoni N, Micera R, Paiella S, Guariglia S, Zivelonghi E, Malleo G, et al. Hypofractionated stereotactic body radiation therapy with simultaneous integrated boost and simultaneous integrated protection in pancreatic ductal adenocarcinoma. *Clin Oncol* (2021) 33:e31–8. doi: 10.1016/j.clon.2020.06.019

21. Mazzarotto R, Simoni N, Guariglia S, Rossi G, Micera R, De Robertis R, et al. Dosimetric feasibility study of dose escalated stereotactic body radiation therapy (SBRT) in locally advanced pancreatic cancer (LAPC) patients: It is time to raise the bar. *Front Oncol* (2020) 10:600940. doi: 10.3389/fonc.2020.600940

22. Hall WA, Small C, Paulson E, Koay EJ, Crane C, Intven M, et al. Magnetic resonance guided radiation therapy for pancreatic adenocarcinoma, advantages, challenges, current approaches, and future directions. *Front Oncol* (2021) 11:628155. doi: 10.3389/fonc.2021.628155

23. Hassanzadeh C, Rudra S, Bommireddy A, Hawkins WG, Wang-Gillam A, Fields RC, et al. Ablative five-fraction stereotactic body radiation therapy for inoperable pancreatic cancer using online MR-guided adaptation. *Adv Radiat Oncol* (2021) 6:1–8. doi: 10.1016/j.adro.2020.06.010

24. Rudra S, Jiang N, Rosenberg SA, Olsen JR, Roach MC, Wan L, et al. Using adaptive magnetic resonance image-guided radiation therapy for treatment of inoperable pancreatic cancer. *Cancer Med* (2019) 8:2123–32. doi: 10.1002/cam4.2100

25. Chuong MD, Bryant J, Mittauer KE, Hall M, Kotecha R, Alvarez D, et al. Ablative 5-fraction stereotactic magnetic resonance–guided radiation therapy with on-table adaptive replanning and elective nodal irradiation for inoperable pancreas cancer. *Pract Radiat Oncol* (2021) 11:134–47. doi: 10.1016/j.prro.2020.09.005

26. Lischalk JW, Burke A, Chew J, Elledge C, Gurka M, Marshall J, et al. Five-fraction stereotactic body radiation therapy (SBRT) and chemotherapy for the local management of metastatic pancreatic cancer. *J Gastrointest Cancer* (2018) 49:116–23. doi: 10.1007/s12029-016-9909-2

27. Rosati LM, Herman JM. Role of stereotactic body radiotherapy in the treatment of elderly and poor performance status patients with pancreatic cancer. *J Oncol Pract* (2017) 13:157–66. doi: 10.1200/JOP.2016.020628

frontiers | Frontiers in Oncology

TYPE Original Research
PUBLISHED 24 November 2022
DOI 10.3389/fonc.2022.1063577

OPEN ACCESS

EDITED BY
Antonio Pontoriero,
University of Messina, Italy

REVIEWED BY
Toshiya Rachi,
National Cancer Centre (Japan), Japan
Maria F. Chan,
Memorial Sloan Kettering Cancer Center, United States

*CORRESPONDENCE
Jianrong Dai
dai_jianrong@cicams.ac.cn

SPECIALTY SECTION
This article was submitted to Radiation Oncology, a section of the journal Frontiers in Oncology

RECEIVED 07 October 2022
ACCEPTED 07 November 2022
PUBLISHED 24 November 2022

CITATION
Ma P, Tian Y, Li M, Niu C, Song Y and Dai J (2022) Delivery of intensity-modulated electron therapy by mechanical scanning: An algorithm study. *Front. Oncol.* 12:1063577. doi: 10.3389/fonc.2022.1063577

Delivery of intensity-modulated electron therapy by mechanical scanning: An algorithm study

Pan Ma, Yuan Tian, Minghui Li, Chuanmeng Niu, Yuchun Song and Jianrong Dai*

Department of Radiation Oncology, National Cancer Center/National Clinical Research Center for Cancer/Cancer Hospital, Chinese Academy of Medical Sciences and Peking Union Medical College, Beijing, China

Purpose: In principle, intensity-modulated electron therapy (IMET) can be delivered through mechanical scanning, with a robotic arm mounting a linac.

Materials and methods: Here is a scanning algorithm to identify the back-and-forth, top-to-bottom (zigzag) pattern scan sequence. The algorithm includes generating beam positions with a uniform resolution according to the applicator size; adopting discrete energies to achieve the depth of 90% dose by compositing energies; selecting energy by locating the target's distal edge; and employing the energy-by-energy scan strategy for step-and-shoot discrete scanning. After a zigzag scan sequence is obtained, the delivery order of the scan spots is optimized by fast simulated annealing (FSA) to minimize the path length. For algorithm evaluation, scan sequences were generated using the computed tomography data of 10 patients with pancreatic cancer undergoing intraoperative radiotherapy, and the results were compared between the zigzag path and an optimized path. A simple calculation of the treatment delivery time, which comprises the irradiation time, the total robotic arm moving time, the time for energy switch, and the time to stop and restart the beam, was also made.

Results: In these clinical cases, FSA optimization shortened the path lengths by 12%–43%. Assuming the prescribed dose was 15 Gy, machine dose rate was 15 Gy/s, energy switch time was 2 s, stop and restart beam time was 20 ms, and robotic arm move speed was 50 mm/s, the average delivery time was 124±38 s. The largest reduction in path length yielded an approximately 10% reduction in the delivery time, which can be further reduced by increasing the machine dose rate and the robotic arm speed, decreasing the time for energy switch, and/or developing more efficient algorithms.

Conclusion: Mechanically scanning IMET is potentially feasible and worthy of further exploration.

KEYWORDS

electron radiotherapy, scanning, optimization, energy composition, mechanical

1 Introduction

Intensity-modulated electron therapy (IMET) uses multiple electron beams, each of differing energy and intensity patterns, to deliver a dose distribution that conforms the 90% dose surface to the distal surface of the PTV (1). IMET research on fluence and energy modulation has several pioneers (2–7).

IMET was tried to be delivered using X-ray multileaf collimators (MLCs), similar to X-ray MLCs employed in delivering intensity-modulated X-ray therapy (8–11). However, the air gap of X-ray MLCs is too great; thus, adequate conformity could hardly be acquired (12). Some intensity modulation was realized with scanned electron beams (13), but it requires helium in the treatment head to reduce multiple Coulomb scattering caused by air (14). Furthermore, electron MLC (eMLC) was designed (15–20) and made available by a third party (Euromechanics, Schwarzenbruck, Germany). However, this technology has not been widely applied, possibly because of the high cost of an add-on eMLC, need for integration into commercially available treatment planning systems, and low number of patients requiring electron radiotherapy.

Intraoperative electron radiotherapy also uses a newly designed multirobotic arm apparatus, which comprises a main robotic arm mounted a linac for moving the radiation beam and two subrobotic arms for gripping the accessories. By the cooperative operation of multirobotic arms with automatic control technologies, treatment precision can be improved while greatly reducing the workload (21). This kind of apparatus, that is, the robotic linac, could be used not only for intraoperative radiotherapy (IORT) but also for external radiotherapy, such as skin cancer and keloid excision, with the following beneficial effects (1): multirobotic arms could be integrated together into a flexible on-line image-guided radiotherapy equipment (e.g., a main robotic arm mounted a linac, multiple subrobotic arms selectively mounted a ultrasound device or other imaging devices, an end-gripper for gripping treatment accessories [cone or applicator for electron therapy], and/or a beam stopper to attenuate radiation); (2) a uniform coordinate system may be established for all the robotic arms, allowing the main robotic arm to be guided in aligning the linac to the tumor target with high precision according to the images acquired by the image device; (3) the robotic arm, which has six degrees of freedom, can maneuver and point the beam almost anywhere in space; (4) treatment beams in robotic arm linac have no fixed isocenter, thereby not restricted to isocentric geometry and consequently, can be directed independently; (5) after mounting an X-band accelerator (a beam stopper on the opposite side of the source to reduce the shielding requirements for primary radiation), the linac could be lightweight and compact, thereby delicate and suitable for IORT.

In recent years, the researches on "FLASH" radiotherapy have attracted a great attention for the potential electron clinical applications due to a remarkable sparing of normal tissue. A flexible on-line image-guided radiotherapy equipment integrating multirobotic arms could deliver conformal modulated dose distributions with scanning ultra-high dose rate electron beam and substantially further enhance the therapeutic window in radiotherapy.

Currently, the most advanced proton radiotherapy technique is intensity-modulated radiotherapy, with active scanning being the most advanced mode. Considering the extremely large number of proton beams, the large number of selectable energies, and the complexity of calculations, several optimization methods have been established for active scanning paths for proton radiotherapy (22–26). The three-dimensional scanning intensity-modulated radiotherapy technique for protons can be referenced to achieve scanning intensity-modulated electron therapy (sIMET) using a robotic arm mounting a linac.

This study primarily aimed to establish the mechanical sIMET algorithm, and the following three aspects were considered: (1) determining the scan parameters and strategy, (2) optimizing the scan path, and (3) solving equations.

2 Methods

2.1 Scan parameter and strategy determination

2.1.1 Scan parameters

This study presumed that an electron accelerator with four discrete energies (E1, E2, E3, and E4) is capable of a depth of 90% dose (R_{90}) spanning 10–37 mm for a square field with a side length of 5 mm. This devise might also have dynamic, intensity-controlled discrete spot scanning capabilities with perfect positioning accuracy. The beam R_{90} could be varied in 1 mm steps by compositing two discrete energies. The ratio of the two compositing energies was determined by an exhaustive method with 0.5% accuracy, and then a table of R_{90} and energy correspondence was formed; this table was queried during optimization to identify the beam's energy.

Next, the scan spots and energies were plainly described. On the beam direction determined by the distribution of a tumor at a certain depth, the beam positions were distributed in one plane. A uniform lateral resolution of beam positions was chosen for the entire plane. After the beam positions were placed at these pixels, energy selection started by locating the target's distal edge. The appropriate energy values (R_{90}) were then matched to the distance between the distal edge and the proximal edge.

2.1.2 Scan strategy

After the scan beam size, position, energy, and dose were determined, the scan strategy was implemented, assigning the mode and sequence of scanning. For a single beam position, two energies may be needed to increase the beam R_{90} in 1 mm steps. In other words, two scan spots may be generated for one beam position. Owing to the differences in target depths, differences in

electron beam energies for adjacent beam positions also differed, leading to frequent energy switching and ultimately increasing the delivery time. Therefore, the scanning mode was "energy by energy," where all scan spots are first grouped by energy, with the same energy grouped into one group. The scanning sequence was the path where the scanning order was optimized to shorten the scanning path and delivered by step-and-shoot discrete scanning.

2.2 Scan path length minimization

2.2.1 Traveling salesman formulation

Minimizing the scan path length was a variation on the traveling salesman problem (TSP) in combinatorial optimization. In the classic TSP formulation, one has a map of N cities and must travel a round-trip circuit visiting each city exactly once and returning to the first city, finding the least costly route. The TSP is well researched, and numerous algorithms can be used to solve it. This algorithmic problem can now be applied to electron beam scanning sequences. It is slightly modified in this case, given that the scanner is not required to return to the first scan spot before moving to the next energy. The scan path for each is optimized independently from other energies because the time required to switch to the next beam energy (typically 1–2 s) exceeds that for the robotic arm to move to any scan spot in the next energy (21). The scanning time might have a directly proportional relationship to the path length of the scan. By following this simple model, the scan path length can be optimized, and the cost to move from one scan spot to another is then merely the Euclidean distance, which is expressed as follows:

$$f(P) = \sum_{n=1}^{N-1} \sqrt{(x_{n+1} - x_n)^2 + (y_{n+1} - y_n)^2} \tag{1}$$

where N is the number of scan spots, $(x_{n,}\, y_n)$ represents the Cartesian coordinates of the n-th scan spot in a given energy group, and P indicates the total scan path.

2.2.2 Fast simulated annealing (FSA) algorithm

The FSA was adopted to solve the modified TSP, using a modified cooling function in which the temperature decreases faster than by the logarithmic cooling schedule (27). The neighborhood of states was generated according to a Cauchy probability density distribution, which allows a more efficient search of the solution space. The temperature as a function of the iteration number k is expressed as follows:

$$T(k) = \frac{T_0}{k^{1/N}} \tag{2}$$

where T_0 is the initial temperature, and N is the number of scan spots. Typically, T_0 is set large enough to accept almost all transitions in the beginning. The Cauchy distribution that allows for occasional jumps in the solution space and faster convergence to a global minimum is defined as

$$P(x) = \frac{1}{\pi(1 + x^2)} \tag{3}$$

2.3 Clinical cases

The most important dosimetric feature of an electron beam is its limited range, which can effectively avoid irradiation of organs behind the tumor target. In addition, it is used in IORT for head and neck (28), abdominal (29, 30), breast (31, 32), and sarcoma (33) tumors.

The FSA algorithm was evaluated retrospectively using computed tomography (CT) data from 10 patients with pancreatic cancer undergoing IORT with 15 Gy prescription dose at our hospital. A flow chart of the sIMET procedure is shown in Figure 1. For IORT, form patient's setup to completion of irradiation, it will be acceptable to take no more than 20 minutes, including less than 10 minutes for acquisition of images, delineation and planning. The GTV was defined as the lesion visible on preoperative contrast-enhanced CT while the operative recording and additional diagnostic imaging (MR/PET) were considered. PTV resulted from a 5 mm expansion of GTV, with the expansion restricted at anatomical boundaries such as the duodenum, intestine, and colon, around which a 5 mm margin was added. The scan beam size, position, energy, and dose were determined from the PTV and the prescription. Subsequently, the back-and-forth, top-to-bottom (zigzag) pattern scan sequence were identified.

2.4 Estimating treatment delivery time

A simple calculation was made on the sIMET for each plan to estimate the treatment delivery time. The delivery time ($T_{delivery}$) includes the irradiation time ($T_{irradiation}$) from the first scan spot to the last one, the total robotic arm moving time (T_{move}), the time for switching beam energy from one to the next ($T_{energyswitching}$), and the time to stop and restart the electron beam ($T_{on/off}$). The time function given by

$$T_{delivery} = T_{irradiation} + T_{move} + T_{energyswitching} + T_{on/off} \tag{4}$$

where

$$T_{irradiation} = \frac{D_P}{\dot{D}} \cdot N_B \tag{5}$$

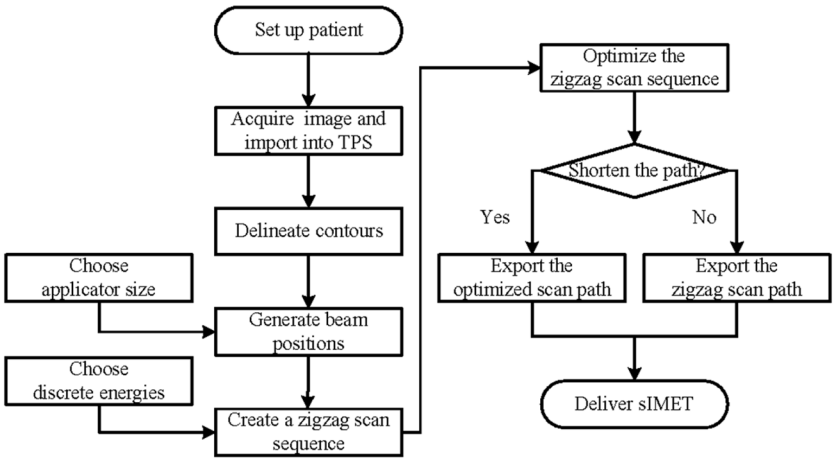

FIGURE 1
Flow chart of scanning intensity-modulated electron therapy.

$$T_{move} = \frac{L}{V_S} \tag{6}$$

$$T_{energyswitching} = T_E \cdot (N_E - 1) \tag{7}$$

$$T_{on/off} = 2T_O \cdot N_S \tag{8}$$

where D_P, $\dot{D}$, and N_B refer to the prescription dose, dose rate, and the number of beam positions, respectively; L and V_S are the path length and the robotic arm's motion speed, respectively; T_E and N_E denote the time for switching the beam energy from one to the next and the number of energies adopted, respectively; T_O and N_S are the time to stop and restart the electron beam during the discrete scanning and the number of scan spots, respectively.

Taking the initial zigzag path length as a reference, the reduction in treatment delivery time was evaluated due to path length minimization. The motion speed of a realistic robotic arm was 50 mm/s. The robotic arm was stationary at a scan spot until prescription dose delivery, which would take 1 s with a dose rate of 15 Gy/s. The time to prepare a new electron energy was 2 s. The electron beam might need 20 s to stop and restart. This approach suffices to obtain a basic impression of expected relative improvement.

3 Results

3.1 Results of discrete energy composition

Figure 2 shows the percentage depth dose for four discrete energies and three composited energies. The R_{90} values of E1, E2, E3, and E4 were 9, 19, 29, and 37 mm, respectively. E5, E6, and E7 were composited by 20.5% E1 and 79.5% E2, 27.5% E2 and 72.5% E3, and 23.5% E3 and 76.5% E4, whose R_{90} values were 14, 24, and 33 mm, respectively.

3.2 Performance of the FSA algorithm

The computation time for a TSP had become tractable for the optimization of proton therapy scan path (22). In using MATLAB (www.mathworks.com) on a computer with a 3.2 GHz processor, FSA optimization required approximately 82 s for patient 1, comprising 4 energies and 238 scan spots.

3.2.1 Results of scan path length minimization

For the 10 patients, the mean number of scan spots was 18, 39, 55, and 55 for E1, E2, E3, and E4, respectively. Each of these energy groups was optimized independently, with $1 \le N \le 200$. After FSA minimization, the change (ΔS) in the total path length (S) for every patient was reduced by 12.22%–43.07% (Table 1).

A larger N following FSA could lead to a good improvement; in fact, the largest improvement was found in patient 1 who had the largest N. Figure 3 illustrates the comparison between initial solution and FSA solution from patient 1. For E1, E2, E3, and E4, the path length was reduced by 50.79%, 62.06%, 55.79%, and 0.00%, respectively. Path length reduction was pronounced for sparsely distributed scan spots, whereas for uniform and dense scanning regions, its optimization yielded little or no benefit. Of note, owing to energy composition, one beam position could possibly have two energies; thus, the four energies had 14, 41, 65, and 118 scan spots, for a total of 238, which was more than the number of beam positions (n = 159).

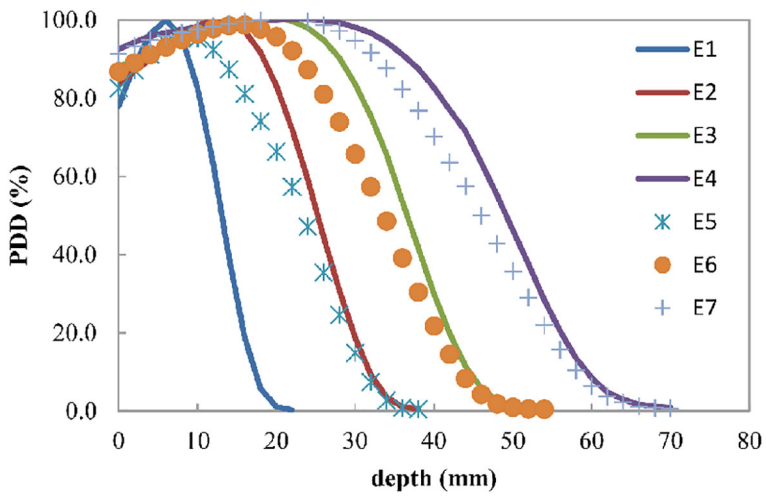

FIGURE 2
Electron beam percent depth dose curve for the four discrete energies E1, E2, E3, and E4, which can have R_{90} values of 9, 19, 29, and 37 mm, respectively. E5, E6, and E7 are the composited energies, generated by adding 20.5% E1 and 79.5% E2, 27.5% E2 and 72.5% E3, and 23.5% E3 and 76.5% E4, respectively.

3.2.2 Reduction in treatment delivery time

For the 10 patients, with the mean reduction of 5% due to scan path length optimization, the mean treatment delivery time was 124 ± 38 s, of which the irradiation accounted for 60%. For patient 1, the initial delivery time was 224 s, and the optimized delivery time was 203, of which the irradiation time was 78%.

4 Discussion

4.1 Path length reduction

In proton radiotherapy, some discontinuities in scanning maps generally result from the inhomogeneity of the patient's anatomy in the beam line before the target, the use of multiple fields, and the consideration of organs at risk by the optimization process (22). In IORT, few discontinuities could result from the following conditions: only one irradiation field is parallel to the direction of the tumor depth, the tumor is exposed, the organs are pushed away from the irradiation field, and the irradiation field is within 10 cm. The precision in selecting the beam energy, dependent on the tumor depth, determines the number of energy groups. Higher precision indicates more energy, more sparse distribution, and more path length reduction.

4.2 Treatment delivery time

Scientists are working on shortening the treatment delivery time because of its multiple benefits, including the increase in the

TABLE 1 Results of the FSA optimization of the total scan path for sIMET plans. S_i, S_f, and ΔS refer to the initial, final, and change in path length, respectively.

Patient	Tumor volume(cc)	Number of beam positions	S_i(mm)	S_f(mm)	ΔS(%)
1	141.34	159	2462.99	1402.08	-43.07
2	97.94	119	1737.54	1065.31	-38.69
3	100.84	129	1969.26	1306.14	-33.67
4	62.78	93	1344.76	910.32	-32.31
5	62.79	90	1365.73	947.37	-30.63
6	48.11	67	867.6	701.88	-19.1
7	48.13	88	1122.31	909.26	-18.98
8	20.7	42	618.76	526.89	-14.85
9	37.28	75	907.99	774.6	-14.69
10	39.25	75	963.16	845.47	-12.22

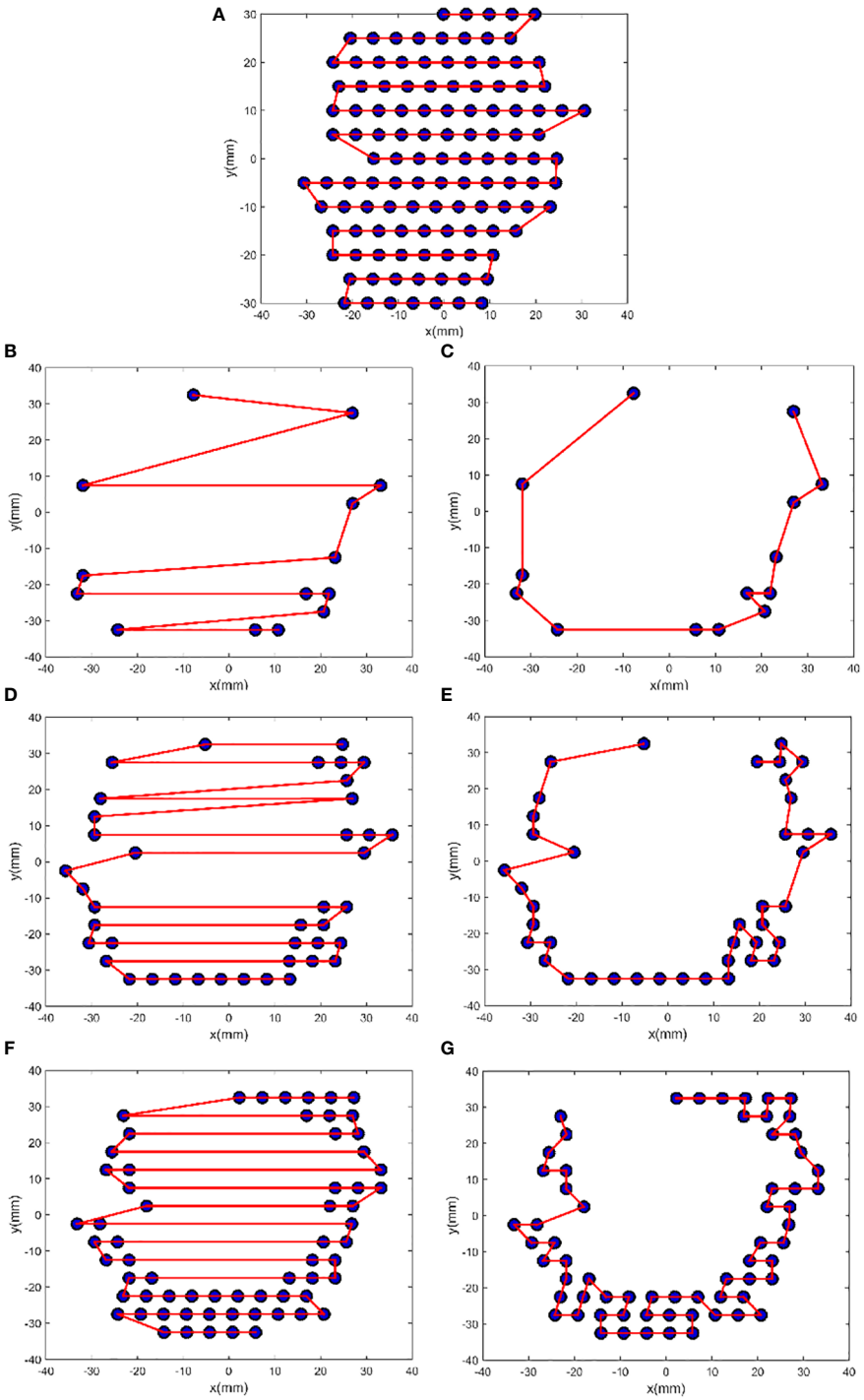

FIGURE 3
FSA optimization results from patient 1. The plots **(A)**, **(B)**, **(D)**, and **(F)** show the initial zigzag scan path for the energies E4, E1, E2, and E3, and the plots **(C)**, **(E)**, and **(G)** show the FSA solution for E1, E2, and E3, respectively. For E1, N = 14, S_i = 386.28 mm, S_f = 190.09 mm, and ΔS = −50.79%; for E2, N = 41, S_i = 703.00 mm, S_f = 266.70 mm, and ΔS = −62.06%; for E3, N = 65, S_i = 767.93 mm, S_f = 339.51 mm, and ΔS = −55.79%; and for E4, N = 118, S_i = 605.78 mm, and ΔS = 0.00%.

number of patients treated per unit of time, mitigation of patients' unbearable anxiety, and reduction of the treatment cost. The IORT has very strict total time requirements, and it should ideally be controlled to 15–20 minutes, which is a huge challenge for sIMET. In addition to the treatment delivery time evaluated in this study, extra time for equipment preparation, simulation, planning, and equipment withdrawal are needed.

Using four discrete energies to composite R_{90} with 1 mm accuracy has several advantages in terms of treatment delivery time consumption. First, during the scanning process, switching energy frequently is unnecessary. For patient 1, if the energy increased by 1 for every 1 mm increase in path length, more than 30 energies were needed. Therefore, the time spent on switching energy was more than 60 s. Second, the lower the number of energy, the shorter the path length is. Conversely, the higher the number of energy, the easier it is to form multiple discontinuous scan positions that increase the scanned path length; additionally, the delivery time will still increase even if the path could be shortened by optimization.

There is a difference between the conventionally installed energies and composited energies, and the greater the difference between discrete energies and composited energies, the greater the difference. In this study, only four energies were used for calculation, but are four actually enough? Theoretically, for different tumors, the magnitude and amount of energy used to generate the composited energies should be different, which would be preferably determined using an optimization method. Increasing the number of discrete energies allows for better conformity and more uniform dose and distribution. This approach could be considered if the energy can be switched quickly (e.g., within 50 ms). For patient 1, when the dose rate could be increased to 600 Gy/s (IntraOp Medical Corporation, Sunnyvale, USA), the time after scan path optimization was relatively reduced to 30%. With the 50 mm/s motion speed of a robotic arm, the treatment delivery time could be less than 1 minute.

4.3 Intensity modulation and scan beam size

This study revealed that by adjusting the intensity of the scan beam, IMET can be achieved with nonuniform dose distributions according to the intraoperative images such as the CT image (34) and the three-dimensional ultrasound images (35). The electron beam is collimated by the applicator, which determines the scan beam size. Theoretically, the more different the size of the applicators is, the more conformal the dose distributions are for sIMET in the direction perpendicular to the scan beam. However, replacing the applicators with those of various sizes increases the complexity of delivery and prolongs the delivery time. In practice, the selection varies from patient to patient, and a balance between dose conformity and delivery time is needed. Further research is warranted for this direction.

To explore the dose distributions of the scan beams, we have adopted the validated head of the Mobetron (36) to simulate 3D dose distributions in the homogeneous cubic phantom for a square field with a side length of 5 mm of energies 4, 6, 9 and 12 MeV, whose R_{90} were 6, 8, 10 and 12 mm, respectively. Besides, the 3D dose distributions of two fields formed by sixteen and seven these square fields have been calculated (Figure 4). The results show that using the square field can deliver irregular dose distributions, whose boundary is influenced by the side length of square fields. However, we also observed that the dose uniformity deteriorated with increasing depth, which is caused by the inherent dosimetric property of high-energy electron beams that the higher isodose levels tend to show lateral constriction. This might be improved by designing new shaped applicator and adopting repainting scanning method. It should be noted that these dose distributions were not validated due to the conditions.

For sIMET, to ensure the robustness of dose distribution, special considerations are required compared to the processes used for photon. Similar to the unique physical properties of protons, the vulnerability of electrons to uncertainties exists, especially from inter- and intra-fractional variations in anatomy. In addition to anatomy variations, other sources of uncertainty in dose delivered to the patient include the stability of the scan beam, the abutment of the adjacent scan beams. Although the promising results of this algorithm study are encouraging, sIMET may show some limitations. Compared with the conventional IORT, the total treatment deliver time is lengthened due to the addition of simulation, planning, and scan treatment. In addition, due to the scan beam motion, there are organ motion and scanning interactions that need to be considered as well as that the control system and more accurate beam delivery are needed.

These uncertainties and current technological limitations of sIMET may limit the achievement of its true potential. Further study could aim at better understanding the consequences of the various uncertainties on sIMET, reducing the uncertainties and breaking through the technological limitations by image-guidance, adaptive radiotherapy, robust optimization techniques, automatic intelligent planning, ultra-high dose rate, etc. We assert that, with such research, sIMET will be an applied radiotherapy modality in the future.

5 Conclusion

This study presents an algorithm that can identify the zigzag pattern scan sequence. The FSA technique is also introduced to optimize the scanning path for mechanical sIMET. Their efficiency has been tested using CT data from 10 patients undergoing IORT for pancreatic cancer. The average delivery time is 124 ± 38 s, which can be further reduced by increasing

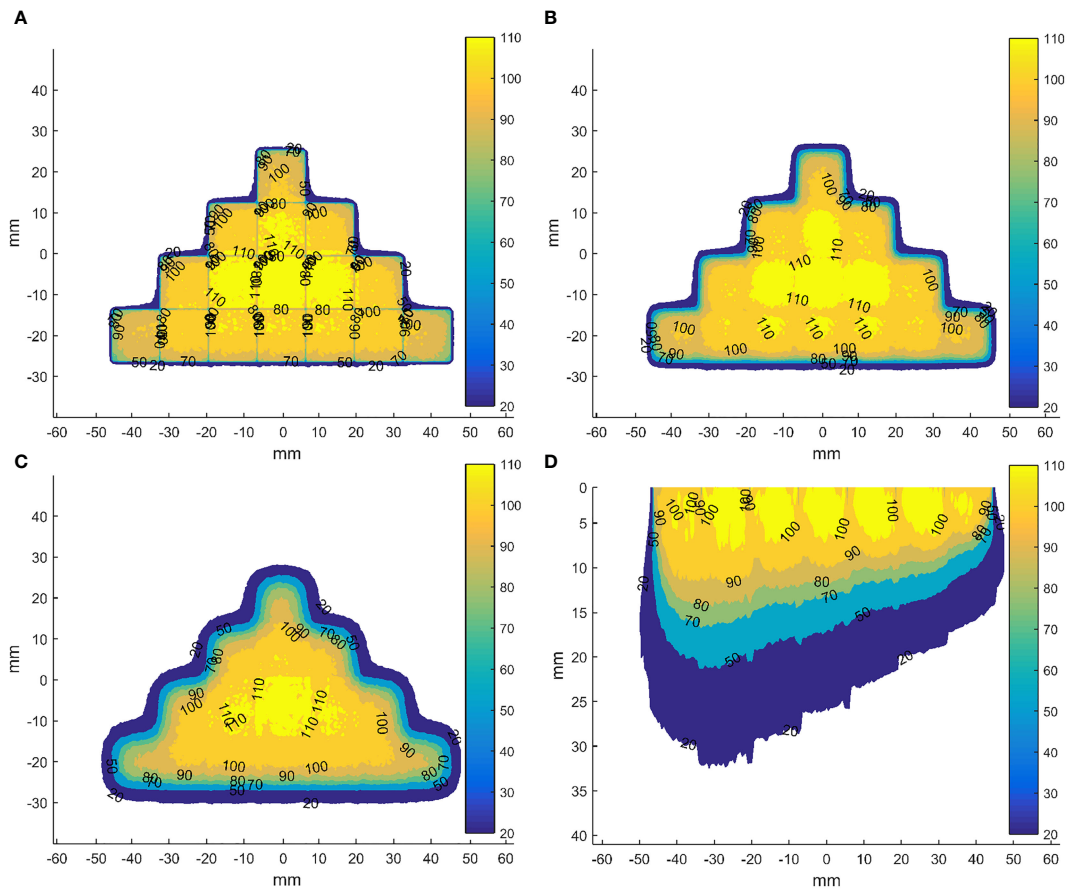

FIGURE 4
Dose distributions in the coronal planes (perpendicular to the direction of incident electron beam) for the field formed by sixteen abutted square fields of energy 12 MeV with a side length of 5 mm in four rows at depth of 0 **(A)**, 5 **(B)** and 10 mm **(C)** from the phantom surface and in axial plane (parallel to the direction of incident electron beam) through the centre of the field formed by seven abutted square fields with a side length of 5 mm along the negative direction of x-axis, whose R_{90}s range from 6 to 12 mm in step of 1 mm by energy composition **(D)**. The dose data has been normalized to the max dose in each square field before abutment.

the machine dose rate and robotic arm speed, decreasing the time for energy switch, and/or developing more efficient algorithms. Mechanically scanning IMET is potentially feasible and worth further exploration.

Data availability statement

The original contributions presented in the study are included in the article/supplementary material. Further inquiries can be directed to the corresponding author.

Ethics statement

The studies involving human participants were reviewed and approved by The Clinical Research Committee and the Ethics Committee at the Cancer Hospital, Chinese Academy of Medical Sciences (Approval No. NCC2020C-100). Written informed consent for participation was not required for this study in accordance with the national legislation and the institutional requirements.

Author contributions

PM and JD contributed to the conception and design of the study. JD provided administrative support. PM, YT, ML, CN and YS provided the materials or patients of the study. PM and JD performed the data analysis and interpretation. PM wrote the first draft of the manuscript. All authors contributed to the article and approved the submitted version.

Funding

This work was supported by the National Natural Science Foundation of China (82003244), Beijing Municipal Natural Science Foundation (7222314) and National key research and development program of China (2021YFC2400304).

Acknowledgments

A patent was granted for system and method for planning a scan path for intraoperative radiation therapy in China (patent number 2017103374912).

Conflict of interest

The authors declare that the research was conducted in the absence of any commercial or financial relationships that could be construed as a potential conflict of interest.

Publisher's note

All claims expressed in this article are solely those of the authors and do not necessarily represent those of their affiliated organizations, or those of the publisher, the editors and the reviewers. Any product that may be evaluated in this article, or claim that may be made by its manufacturer, is not guaranteed or endorsed by the publisher.

References

1. Hogstrom KR, Antolak JA, Kudchadker RJ, Ma CMC, DD L. (2003), 749–86.

2. Asell M, Hyödynmaa S, Gustafsson A, Brahme A. Optimization of 3D conformal electron beam therapy in inhomogeneous media by concomitant fluence and energy modulation. *Phys Med Biol* (1997) 11(42):2083–100. doi: 10.1088/0031-9155/42/11/006

3. Ebert MA, Hoban PW. Possibilities for tailoring dose distributions through the manipulation of electron beam characteristics. *Phys Med Biol* (1997) 11 (42):2065–81. doi: 10.1088/0031-9155/42/11/005

4. Hyödynmaa S, Gustafsson A, Brahme A. Optimization of conformal electron beam therapy using energy- and fluence-modulated beams. *Med Phys* (1996) 5 (23):659–66. doi: 10.1118/1.597710

5. Lee MC, Jiang SB, Ma CM. Monte Carlo And experimental investigations of multileaf collimated electron beams for modulated electron radiation therapy. *Med Phys* (2000) 12(27):2708–18. doi: 10.1118/1.1328082

6. Ma CM, Pawlicki T, Lee MC, Jiang SB, Li JS, Deng J, et al. Energy- and intensity-modulated electron beams for radiotherapy. *Phys Med Biol* (2000) 8 (45):2293–311. doi: 10.1088/0031-9155/45/8/316

7. Lee MC, Deng J, Li J, Jiang SB, Ma CM. Monte Carlo Based treatment planning for modulated electron beam radiation therapy. *Phys Med Biol* (2001) 8 (46):2177–99. doi: 10.1088/0031-9155/46/8/310

8. Mihaljevic J, Soukup M, Dohm O, Alber M. Monte Carlo Simulation of small electron fields collimated by the integrated photon MLC. *Phys Med Biol* (2011) 3 (56):829–43. doi: 10.1088/0031-9155/56/3/018

9. Olofsson L, Karlsson MG, Karlsson M. Effects on electron beam penumbra using the photon MLC to reduce bremsstrahlung leakage for an add-on electron MLC. *Phys Med Biol* (2005) 6(50):1191–203. doi: 10.1088/0031-9155/50/6/010

10. Plessis FD, Leal A, Stathakis S, Xiong W, Ma CM. Characterization of megavoltage electron beams delivered through a photon multi-leaf collimator (pMLC). *Phys Med Biol* (2006) 8(51):2113–29. doi: 10.1088/0031-9155/51/8/011

11. Salguero FJ, Arrans R, Palma BA, Leal A. Intensity- and energy-modulated electron radiotherapy by means of an xMLC for head and neck shallow tumors. *Phys Med Biol* (2010) 5(55):1413–27. doi: 10.1088/0031-9155/55/5/010

12. Klein EE. Modulated electron beams using multi-segmented multileaf collimation. *Radiother Oncol* (1998) 3(48):307–11. doi: 10.1016/s0167-8140(98)00050-4

13. Lief EP, Larsson A, Humm JL. Electron dose profile shaping by modulation of a scanning elementary beam. *Med Phys* (1996) 1(23):33–44. doi: 10.1118/1.597786

14. Karlsson M, Nyström H, Svensson H. Electron beam characteristics of the 50-MeV racetrack microtron. *Med Phys* (1992) 2(19):307–15. doi: 10.1118/1.596933

15. Connell T, Alexander A, Evans M, Seuntjens J. An experimental feasibility study on the use of scattering foil free beams for modulated electron radiotherapy. *Med Phys* (2012) 11(57):3259–72. doi: 10.1088/0031-9155/57/11/3259

16. Ma CM, Ding M, Li JS, Lee MC, Pawlicki T, Deng J, et al. A comparative dosimetric study on tangential photon beams, intensity-modulated radiation therapy (IMRT) and modulated electron radiotherapy (MERT) for breast cancer treatment. *Phys Med Biol* (2003) 7(48):909–24. doi: 10.1088/0031-9155/48/7/308

17. Gauer T, Albers D, Cremers F, Harmansa R, Pellegrini R, Schmidt R, et al. Design of a computer-controlled multileaf collimator for advanced electron radiotherapy. *Phys Med Biol* (2006) 23(51):5987–6003. doi: 10.1088/0031-9155/51/23/003

18. Gauer T, Sokoll J, Cremers F, Harmansa R, Luzzara M, Schmidt R, et al. Characterization of an add-on multileaf collimator for electron beam therapy. *Phys Med Biol* (2008) 4(53):1071–85. doi: 10.1088/0031-9155/53/4/017

19. Hogstrom KR, Boyd RA, Antolak JA, Svatos MM, Faddegon BA, Rosenman JG, et al. Dosimetry of a prototype retractable eMLC for fixed-beam electron therapy. *Med Phys* (2004) 3(31):443–62. doi: 10.1118/1.1644516

20. O'Shea TP, Ge Y, Foley MJ, Faddegon BA. Characterization of an extendable multi-leaf collimator for clinical electron beams. *Phys Med Biol* (2011) 23 (56):7621–38. doi: 10.1088/0031-9155/56/23/018

21. Dai J, Niu C, Ma P, Li M. *Multi-robotic arm apparatus for intraoperative radiotherapy* Vol. 13. OFFICE USPAT, editor. (United States of America: USPTO, United States Patent and Trademark Office) (2021).

22. Kang JH, Wilkens JJ, Oelfke U. Demonstration of scan path optimization in proton therapy. *Med Phys* (2007) 9(34):3457–64. doi: 10.1118/1.2760025

23. Pardo J, Donetti M, Bourhaleb F. Heuristic optimization of the scanning path of particle therapy beams. *Med Phys* (2009) 6Part1(36):2043–51. doi: 10.1118/1.3121506

24. Cao W, Lim G, Li X, Li Y, Zhang X. Incorporating deliverable monitor unit constraints into spot intensity optimization in intensity-modulated proton therapy treatment planning. *Phys Med Biol* (2013) 15(58):5113–25. doi: 10.1088/0031-9155/58/15/5113

25. Cao W, Lim G, Liao L, Li Y, Jiang S, Li X, et al. Proton energy optimization and reduction for intensity-modulated proton therapy. *Phys Med Biol* (2014) 21 (59):6341–54. doi: 10.1088/0031-9155/59/21/6341

26. Dias MF, Riboldi M, Seco J, Castelhano I, Pella A, Mirandola A, et al. Scan path optimization with/without clustering for active beam delivery in charged particle therapy. *Phys Med* (2015) 2(31):130–36. doi: 10.1016/j.ejmp.2015.01.001

27. Harold S, Ralph H. Fast simulated annealin. *Phys Lett* (1987) 3(122):157–62. doi: 10.1063/1.36250

28. Wald P, Grecula J, Walston S, Wei L, Bhatt A, Martin D, et al. Intraoperative electron beam radiotherapy for locoregionally persistent or recurrent head and neck cancer. *Head Neck* (2019) 7(41):2148–53. doi: 10.1002/hed.25673

29. Coelho TM, Fogaroli RC, Pellizzon A, Castro D, Ramos H. Intraoperative radiation therapy for the treatment of recurrent retroperitoneal and pelvic tumors: a single-institution analysis. *Radiat Oncol* (2018) 1(13):224. doi: 10.1186/s13014-018-1168-x

30. Faca B, Mk C, Jmad E, Serrano J, Poortmans P, Roeder F, et al. ESTRO IORT task Force/ACROP recommendations for intraoperative radiation therapy in

unresected pancreatic cancer. *Radiother Oncol* (2020) 148):57–64. doi: 10.1016/j.radonc.2020.03.040

31. Julia K, Roland R, Peter K, Christoph G, Fischer M. Intraoperative electron radiotherapy (IOERT) in the treatment of primary breast cancer. *Breast Care* (2018) 3(13):162–67. doi: 10.1159/000489637

32. Bhandari T, Babaran W, Forouzannia A, Williams V, Harness J, Carpenter M, et al. A prospective phase I comparison of toxicity and cosmesis outcomes of single-fraction IORT and hypofractionated radiotherapy with IORT boost in early-stage breast cancer. *Brachytherapy* (2017) 16:1232–38. doi: 10.1016/j.brachy.2017.09.002

33. Roeder F, Alldinger I, Uhl M, Saleh-Ebrahimi L, Schimmack S, Mechtersheimer G, et al. Intraoperative electron radiation therapy inRetroperitoneal sarcoma. *Int J Radiat Oncol Biol Phys* (2018) 2(100):516–27. doi: 10.1016/j.ijrobp.2017.10.034

34. García-Vázquez V, Calvo FA, Ledesma-Carbayo MJ, Sole CV, Calvo-Haro J, Desco M, et al. Intraoperative computed tomography imaging for dose calculation in intraoperative electron radiation therapy: Initial clinical observations. *PloS One* (2020) 1(15):e0227155. doi: 10.1371/journal.pone.0227155

35. Ma P, Li M, Chen X, Tian Y, Niu C, Feng Q, et al. Ultrasound-guided intraoperative electron beam radiation therapy: A phantom study. *Phys Med* (2020) 78(78):1–7. doi: 10.1016/j.ejmp.2020.06.021

36. Ma P, Li Y, Tian Y, Liu B, Zhou F, Dai J. Design of a spherical applicator for intraoperative radiotherapy with a linear accelerator-a Monte Carlo simulation. *Phys Med Biol* (2018) 64):1361–6560. doi: 10.1088/1361-6560/aaec59

frontiers | Frontiers in Oncology

TYPE Original Research
PUBLISHED 28 November 2022
DOI 10.3389/fonc.2022.1009916

OPEN ACCESS

EDITED BY
Antonio Pontoriero,
University of Messina, Italy

REVIEWED BY
Zhitao Dai,
Chinese Academy of Medical Sciences and Peking Union Medical College, China
Alex Price,
Washington University in St. Louis, United States

*CORRESPONDENCE
Sankar Arumugam
Sankar.Arumugam@health.nsw.gov.au

SPECIALTY SECTION
This article was submitted to Radiation Oncology, a section of the journal Frontiers in Oncology

RECEIVED 02 August 2022
ACCEPTED 01 November 2022
PUBLISHED 28 November 2022

CITATION
Arumugam S, Young T, Johnston M, Pavey D and Lee M (2022) The delivered dose assessment in pancreas SBRT with the target position determined using an in-house position monitoring system. *Front. Oncol.* 12:1009916. doi: 10.3389/fonc.2022.1009916

The delivered dose assessment in pancreas SBRT with the target position determined using an in-house position monitoring system

Sankar Arumugam[1,2]*, Tony Young[1,3], Meredith Johnston[4], Darren Pavey[5] and Mark Lee[4]

[1]Department of Medical Physics, Liverpool and Macarthur Cancer Therapy Centres and Ingham Institute, Sydney, NSW, Australia, [2]South Western Clinical School, University of New South Wales, Sydney, NSW, Australia, [3]Institute of Medical Physics, School of Physics, University of Sydney, Sydney, NSW, Australia, [4]Department of Radiation Oncology, Liverpool and Macarthur Cancer Therapy Centres, Sydney, NSW, Australia, [5]Department of Radiology, Liverpool and Macarthur Cancer Therapy Centres and Ingham Institute, Sydney, NSW, Australia

Purpose: This study assessed the delivered dose accuracy in pancreas SBRT by incorporating the real-time target position determined using an in-house position monitoring system.

Methods and materials: An online image-based position monitoring system, SeedTracker, was developed to monitor radiopaque marker positions using monoscopic x-ray images, available from the Elekta XVI imaging system. This system was applied to patients receiving SBRT for pancreatic cancer on the MASTERPLAN Pilot trial (ACTRN 12617001642370). All patients were implanted pre-treatment with at least three peri-tumoral radiopaque markers for target localisation. During treatment delivery, marker positions were compared to expected positions delineated from the planning CT. The position tolerance of ±3mm from the expected position of the markers was set to trigger a gating event (GE) during treatment. The dosimetric impact of position deviations and actual dose delivered with position corrections was assessed by convolving the plan control point dose matrices with temporal target positions determined during treatment.

Results: Eight patients were treated within this study. At least one GE was observed in 38% of the treatment fractions and more than one GE was observed in 10% of the fractions. The position deviations resulted in the mean(range) difference of -0.1(-1.1 - 0.4)Gy in minimum dose to tumour and 1.9(-0.1- 4.6)Gy increase to Dmax to duodenum compared to planned dose. In actual treatment delivery with the patient realignment, the mean difference of tumour min dose and duodenal Dmax was reduced to 0.1(-1.0 – 1.1)Gy and 1.1 (-0.7 - 3.3)Gy respectively compared to the planned dose.

Conclusions: The in-house real-time position monitoring system improved the treatment accuracy of pancreatic SBRT in a general-purpose linac and enabled assessment of delivered dose by incorporating the temporal target position during delivery. The intrafraction motion impacts the dose to tumour even if target position is maintained within a 3mm position tolerance.

KEYWORDS

pancreatic cancer, intrafraction motion, real-time monitoring, SBRT, delivered dose assessment

Introduction

Pancreatic cancer is the 12th most common cancer worldwide, accounting for 495 773 new cases and 466 003 deaths in 2020 (1). The management of pancreatic cancer continues to be challenging with high mortality and a poorer prognosis compared to other cancers; the 5-years overall survival is only 9% (2). The majority of pancreatic cancer patients are diagnosed at an advanced stage and 80-90% of patients have unresectable cancer at the time of diagnosis which attributes to the poor prognosis (2). Recent studies have shown improvement in survival for locally advanced and borderline resectable pancreatic cancer patients treated with neoadjuvant chemotherapy followed by Stereotactic body radiotherapy (SBRT) (3, 4). This combined treatment approach is shown to have a high success rate in downstaging locally advanced and borderline resectable pancreatic tumours to resectable disease, with a negative microscopic margin (R0) in relatively high percentage of cases (3, 4). Additional studies have been carried out to determine the role of dose escalation in SBRT for improved local control and survival benefits (5, 6).

Accurate and safe delivery of pancreatic SBRT is imperative, but challenging due to the proximity of radiosensitive gastrointestinal Organs at Risk (OARs) to the tumour. Additionally, the pancreas and abdominal organ motion due to respiration, deformation and peristalsis poses a greater challenge in the safety and accuracy of pancreatic SBRT. This necessitates the use of appropriate motion management and quantification of patient specific target motion for radiotherapy planning to mitigate the uncertainties arising from this motion. The Internal Target Volume (ITV), derived using respiratory correlated four-dimensional Computed Tomography (4D CT) image sets, are widely used to determine and encompass the position of target volume during treatment. Gated or breath-hold radiotherapy offers the best method of reducing respiratory motion, however not all patients are suitable for breath-hold or gated treatments (7, 8). Other methods used to reduce motion include abdominal compression (AC) or voluntary breath-hold.

Whilst motion management strategies ensure the target motion is accounted for based on the planning dataset, it does not ensure the accuracy of target position during treatment delivery. Studies have shown inconsistencies in the target motion range between planning and treatment fractions (9, 10). These studies also have reported the difference in the reproducibility of target position between breath-hold sessions during treatment (9, 10). The target position uncertainties due to these factors can result in suboptimal treatment delivery in pancreatic SBRT with reduced dose to the tumour and potentially very high dose to OARs.

SBRT dedicated linear accelerators (linacs) such as Cyberknife and Vero systems, have real-time target position monitoring and tracking abilities, enabling the safe delivery of pancreatic SBRT. These systems use stereoscopic images to identify the position of fiducial markers implanted in or in the vicinity of tumours to determine the target position during treatment. Recent studies have shown the successful implementation of Magnetic Resonance image guided radiotherapy delivery systems in pancreatic SBRT and its ability to safely limit the dose to OARs using online adaption and gated treatment delivery (11, 12). The demonstrated efficacy of pancreatic SBRT has enabled its widespread uptake in clinics worldwide using general-purpose C-arm linacs. Vinogradskiy et al. reported the fiducial marker-based real-time position monitoring in pancreatic SBRT using the triggered imaging option available in the Varian linac (13). Recently our group reported the first clinical implementation of real-time position monitoring in pancreatic SBRT on an Elekta linac using planar images acquired from the XVI system and an in-house developed position monitoring software (14). In this study, we investigated the accuracy of dose delivered to pancreatic SBRT patients treated within 'Mfolfirinox And STEreotactic Radiotherapy for Patients with Locally Advanced paNcreas cancer (MASTERPLAN): a feasibility study' (ACTRN 12617001642370) by incorporating the real-time position information derived using in-house developed position monitoring system, SeedTracker.

10.3389/fonc.2022.1009916

Material and methods

Patient data

Patients treated within the MASTERPLAN pilot study were considered for this study. The MASTERPLAN pilot study is a three-centre feasibility study investigating whether SBRT in addition to chemotherapy with modified FOLFIRINOX (Oxaliplatin, irinotecan, 5-fluorouracil; mFOLFIRINOX), is a feasible treatment option for patients with borderline resectable pancreatic adenocarcinoma (BRPC) or unresectable pancreatic adenocarcinoma (UPC). Eight patients were recruited for this pilot study. The characteristics and tumour staging of the patient cohort is shown in Table 1.

Radiotherapy treatment simulation

Radiotherapy commenced 2 to 4 weeks after 4 cycles of mFOLFIRINOX as per the study protocol. Prior to the radiotherapy simulation process, the patients were inserted with 4 gold fiducial markers (EchoTip Ultra Fiducial Needle, Cook Medical LLC, IN, USA) in or in the vicinity of tumour in the pancreas with endoscopic ultrasound guidance. The markers were implanted with Endoscopic Ultrasound guidance and typically inserted *via* a needle through the duodenum or stomach. The placement of 4 markers were recommended to be on the periphery but not within the tumour to reduce the risk of bleeding. One marker was recommended to be between the duodenum and right sided aspect of the tumour to allow accurate delineation of the duodenum. The other markers were to be inserted on the periphery of the tumour on each of the other planes where possible (e.g. superior, to the left of the tumour and inferior). This was not always possible due to the location of the tumour and vessels. The small needle used for insertion through the stomach or duodenum does not have significant risk for damage of the OARs and is a routine part of biopsy and diagnosis for pancreatic cancer.

Patients were assessed for an appropriate motion management strategy by the Radiation Oncologist at a minimum of 3 days post fiducial marker insertion. The choice of motion management depended upon patients' ability to tolerate and comply with a particular motion management requirement and was decided under fluoroscopic x-ray image guidance by the following hierarchical process:

1. If the patient could tolerate the Active Breathing Coordinator (ABC) device (Elekta Ltd, UK) and was able to hold their breath in an exhale state for a minimum 15 seconds(s) with the stability and reproducibility of the marker positions within 2mm, the simulation and treatment was performed using ABC assisted Exhale Breath Hold (EBH) strategy.
2. If the patient did not comply with EBH requirements, firstly the Superior-Inferior (SI) motion range of the markers in a free breathing state was determined using fluoroscopic images. Abdominal compression (AC) using Omni V SBRT position System (Bionix, USA) was performed and the markers' motion range was reassessed with the optimal abdominal compression that was comfortable to the patient. If the AC reduced the markers' motion range ≥ 5mm in comparison to free breathing, AC compression was selected as a motion management option
3. If neither the ABC device nor AC was tolerable or had <5mm difference compared to free breathing, the patient was simulated and treated using a free breathing approach.

For the patients who were eligible for the EBH motion management option, the planning CT with contrast was acquired in EBH with an ABC device. For patients who were eligible for AC and free breathing, the planning CT with contrast was acquired at comfortable voluntary EBH of the patient. Additionally, 4D CT images were acquired to generate the ITV for treatment planning.

TABLE 1 The characteristics and tumour staging of patients treated with in MASTERPLAN pilot study.

Patient No	Age (yrs)	Weight (kgs)	Sex	Stage	Tumour volume (cc)	Tumour location within Pancreas	Motion management
1	60	58.4	M	III	50.5	Head	FB
2	63	57.0	F	Ib	33.7	Body	FB
3	45	79.2	M	III	40.8	Duct	AC
4	59	91.6	M	IIb	19.0	Tail	FB
5	64	78.6	M	Ib	19.4	Head	EBH
6	73	74.4	M	Ib	28.0	Head	EBH
7	72	58.0	M	IIa	13.1	Head	AC
8	69	93.7	M	IIb	23.3	Head	AC

FB, Free Breathing; AC, Abdominal Compression; EBH, Exhale Breath Hold.

Treatment planning

The following two Planning Target Volumes (PTVs), receiving 30 Gy and 45 Gy in 5 fractions, were contoured by a radiation oncologist for treatment planning:

PTV 30Gy: ITV + 5mm safety margin

PTV 45Gy: PTV 30Gy excluding Stomach, Duodenum and Small Bowel with 5mm safety expansion

A dual arc Volumetric Modulated Arc Therapy (VMAT) plan for Elekta linac with Agility treatment head was generated using Pinnacle treatment planning system (TPS). The motion management techniques used for the patients are shown in Table 1. The PTV 45Gy was planned with an inhomogeneous dose within the volume with D1cc not exceeding 58.5 Gy (130% of 45Gy). The GI OARs doses were limited to the guideline values during the planning process (5, 15).

Treatment delivery

The treatment was delivered on an alternate treatment day schedule. The stability and reproducibility of the EBH and reproducibility of AC on each treatment day was verified using fluoroscopic x-ray images prior to the acquisition of the verification CBCT. For patients simulated with EBH, the verification CBCT was acquired during EBH, with the CBCT images registered with the reference planning CT to ensure the accurate match of fiducial positions and the internal organs that can be seen on CBCT images. For the AC and free breathing patients cohort, 4D CBCT images were acquired for position verification. The exhale phase of the 4D CBCT dataset was matched with the reference CT to quantify the position offset and table corrections. The 4D CBCT dataset was used to ensure the motion range of fiducials/target volume within the ITV determined from the planning 4D CT.

Real-time position monitoring

The positional accuracy of the target during treatment delivery was monitored using an in-house developed software system, SeedTracker. The fluoroscopic x-ray images acquired during treatment delivery using the XVI system were processed by the SeedTracker system in real-time to identify the position of the implanted markers and compared to the expected positions based on the reference planning position at each imaging angle. If the position of the markers exceeds the set tolerance value the system will alert the user to interrupt the treatment and reposition the patient. In the events where position deviations were observed, the table corrections were performed based on the 3D offsets determined by CBCT based verification. The details on the principle of operation of the SeedTracker system can be found elsewhere (14, 16, 17).

A position tolerance of ±3mm with a maximum deviation duration of 5s was set to trigger the gating event (GE) to interrupt the treatment delivery and perform the patient realignment. For the treatment with AC and free breathing techniques the position tolerance + ITV extent was used as a tolerance window, while for EBH treatment only the position tolerance was used as a tolerance window.

Delivered dose assessment

The actual dose delivered to the tumour and OARs in each treatment fraction was calculated by convolving the control point (CP) dose matrices of the treatment plan with the target positions determined during the delivery of the respective CPs. The 3D position of the target for this convolution process was determined using the real-time 2D monitoring data. In FB and AC motion management techniques the 3D position of the tumours was calculated using the following two steps:

- Firstly, the SI trajectory of each breath cycle was divided into 10 equidistant positions between maximum inhale and exhale positions. The 3D position of the target at each of these discrete position was determined using the 2D data with the angular separation of 45° using the variable angle stereoscopic method (17).
- Based on this 3D position distribution cloud, the 3D position corresponding to the 2D data of the real-time trajectory was determined using the Maximum Likelihood Estimation (MLE) method.

For the 3D position estimation in the EBH technique, firstly the 3D position of the tumour at identical SI positions was calculated based on the variable angle stereoscopic method, then the 3D position corresponding to the 2D data of the real-time trajectory was determined using MLE.

In the gating events (GE) where the treatment was interrupted and position correction was performed, the dose that would have been delivered with the position deviation was calculated by introducing the determined position deviations to the CP dose.

The difference in dose volume histogram (DVH) metrics such as D98, Dmax, minimum and mean dose to Gross Tumour Volume (GTV) and Dmax to duodenum, small bowel and stomach were compared between planned and delivered dose. The statistical difference between the DVH metrics of the dose delivered with and without position correction was performed using the Wilcoxon signed rank test.

Results

Motion management

Of the 8 patients treated within this feasibility study, EBH and AC techniques were used for 2 and 3 patients respectively. The remaining patients who could not tolerate the ABC device and had no benefit from AC were treated with a free breathing approach (Table 1).

Real-time target position

Figures 1A, B show the online trajectory of target position determined by the SeedTracker system for patients treated with free breathing and EBH motion management options during the delivery of treatment arc 1 in fraction 1. The magnitude of tumour motion, derived from the 4D CT scan, for patients treated with free breathing and abdominal compression techniques is different in both AP and LR directions. This results in varying magnitudes of position tolerance in the AP-LR direction during the VMAT arc delivery (Figure 1A). The tumour position determined during the delivery of each of the treatment fractions along with planned ITV + 3mm position tolerance is shown in Figure 2. The median position of the target in each of the treatment fractions is represented by the central mark of the box, the bottom and top edges of the box indicate the 25th and 75th percentile respectively. The outlier position of the target during each of the treatment fraction is represented by the red + markers.

Gating events

The number of GEs resulting in each of the treatment fractions is shown in Figure 3A. At least one GE occurred in 7 of the 8 patients and a total of 19 GEs occurred in 40 treatment fractions. In patient 3, GEs occurred in 4 of the 5 treatment fractions. The magnitude of 3D position correction that triggered GEs is shown in Figure 3B. Of the observed GEs 7

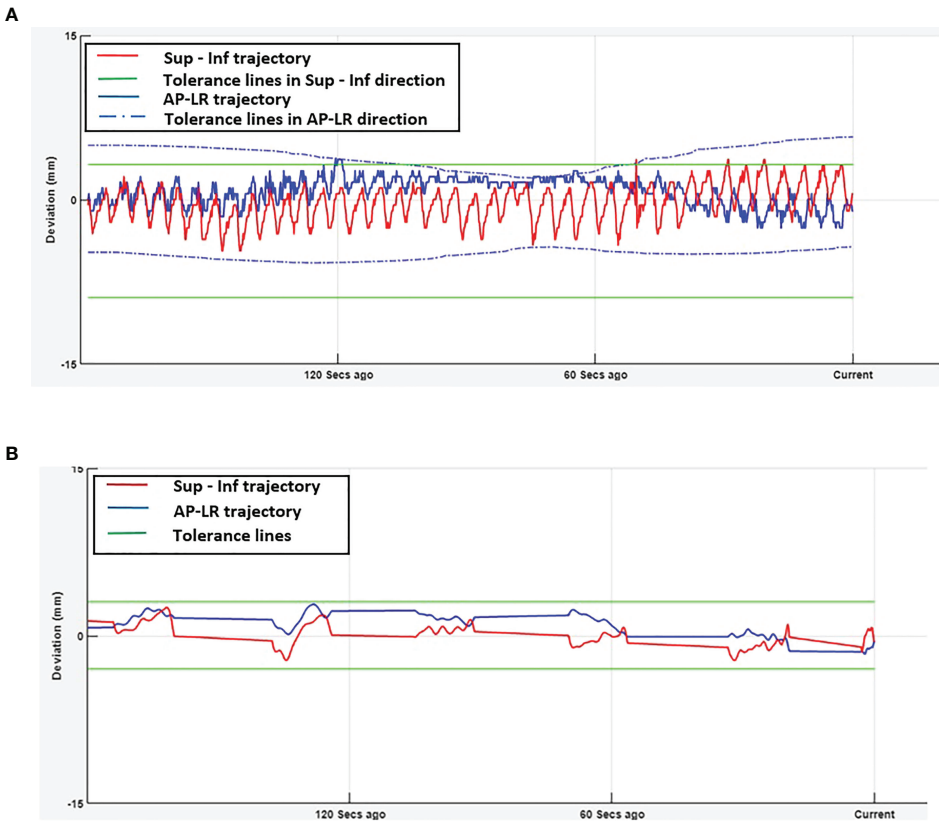

FIGURE 1
Real-time tumour trajectory determined by SeedTracker system. **(A)** Target trajectory determined during Arc-1 of a patient treated using free-breathing technique. The tolerance window consists of the ITV extent + 3mm position tolerance. The green (solid) and blue (dotted) lines represent the tolerance window in SI and AP-LR directions respectively. **(B)** Target trajectory determined during Arc-1 of a patient treated using EBH technique. The green (solid) lines represent the tolerance window in SI and AP-LR directions.

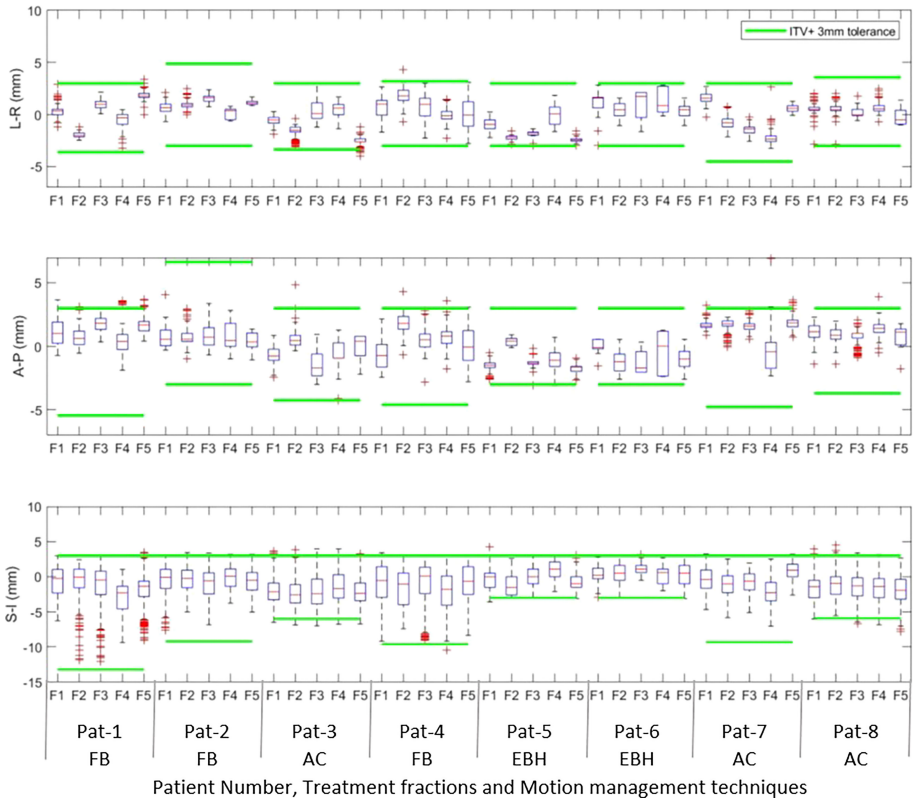

FIGURE 2
The intrafraction position of the tumour in Left –Right (LR), Anterior-Posterior(AP) and Superior-Inferior (SI) directions during treatment delivery in each of the treatment fractions. The outlier position of the target volume in each of fractions is represented by the red + markers.

occurred just before the start of treatment after initial CBCT based verification, 7 occurred just before the start of the second treatment arc and 4 occurred during the delivery of the treatment arc. A maximum position difference of 6mm, 4mm and 4mm was observed in Lat, AP and SI direction in one GE of patient 6.

Delivered dose

Figure 4 shows the original planned and delivered GTV and OARs dose as assessed by DVH metrics for each of the fractions with real-time monitoring and position corrections. The dose that would have been delivered without position corrections is also shown in the same figures. The mean (range) difference between the planned and delivered dose with and without position correction for the whole treatment is shown in Table 2. The planned Dmax to GTV and the delivered Dmax with and without position corrections is shown in Figure 5. The mean dose, minimum dose and D98 to GTV agreed with the planned dose in both corrected and not corrected treatment scenarios with the mean difference of -0.4Gy,0.1Gy and 0.2Gy respectively (Figures 4A, B and Table 2). In 7 out of 8 patients the delivered Dmax to duodenum was higher than the planned dose in each of the treatment fractions (Figure 4C). If the position correction were not performed the Dmax to duodenum would have seen a mean increase of 0.8Gy in comparison to the planned dose (Figure 4C and Table 2). In individual fractions, the Dmax to stomach and small bowel for treatment delivered without position corrections are within the range of actual treatment delivered with corrections (Figures 4D, E). The mean difference between planned and delivered Dmax to stomach was -0.5Gy and this difference would have been -0.9Gy for treatment without position corrections (Table 2). The Dmax to small bowel would have received higher than the planned dose, maximum by 1.6Gy in fraction 5 of patient 1, if position corrections were not performed (Figure 4E). The statistical significance of the dose difference between the treatment fractions delivered with and without position correction is shown in Table 2. The statistically significant differences was found in Dmax to the duodenum between treatments delivered with and without position corrections.

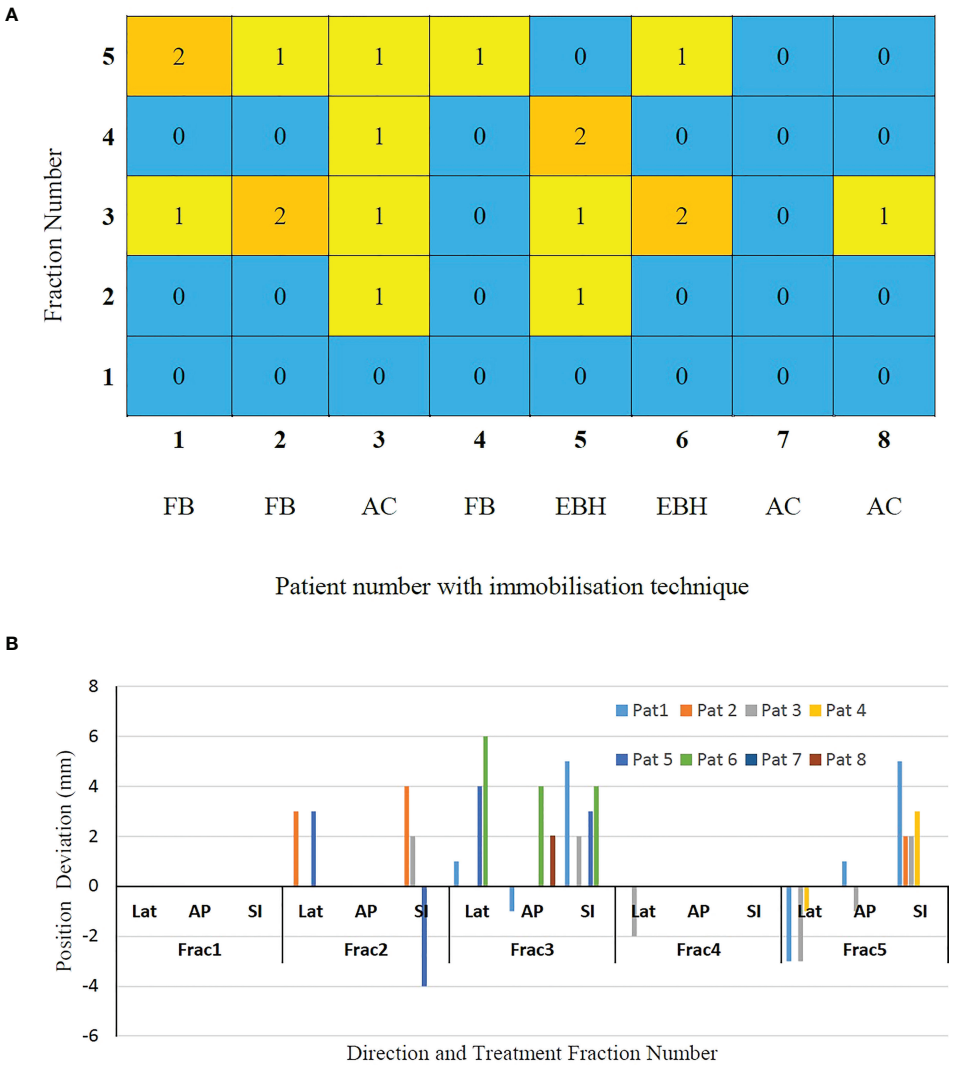

FIGURE 3
(A) The gating events (GEs) occurred in individual treatment fractions and **(B)** The magnitude of position deviations determined using CBCT based verification after GEs.

Discussion

In this work we reported the feasibility of real-time position monitoring using an in-house developed system for the safe and accurate delivery of pancreas SBRT on a general purpose linear accelerator. This is to our knowledge the first implementation for pancreas treatment on an Elekta Linear accelerator, with the patient cohort treated in this study covering both free breathing and the application of motion management techniques such as AC and EBH. A number of intrafraction position deviations during the treatment delivery were detected by the system in the studied patient cohort and position corrections were performed to improve the accuracy of treatment delivery. The delivered dose assessment, by incorporating the target position during treatment delivery, showed that the dose delivered to the duodenum and stomach would have been higher than the planned if the position deviations were not identified and corrected.

The pancreas real-time position monitoring and target tracking using implanted gold fiducials has been in practice for some time in SBRT dedicated treatment delivery systems such as Cyberknife and Vero (18–20). Zhang et al. reported various movement patterns of pancreas in 498 datasets for 29 patients' Cyberknife treatments and observed position deviations of >5mm in 50% of the datasets analysed with treatment times that exceeding > 240s (19). Recently, Vinogradskiy et al. reported the real-time pancreas position monitoring in SBRT using a Varian True beam accelerator with triggered imaging capability

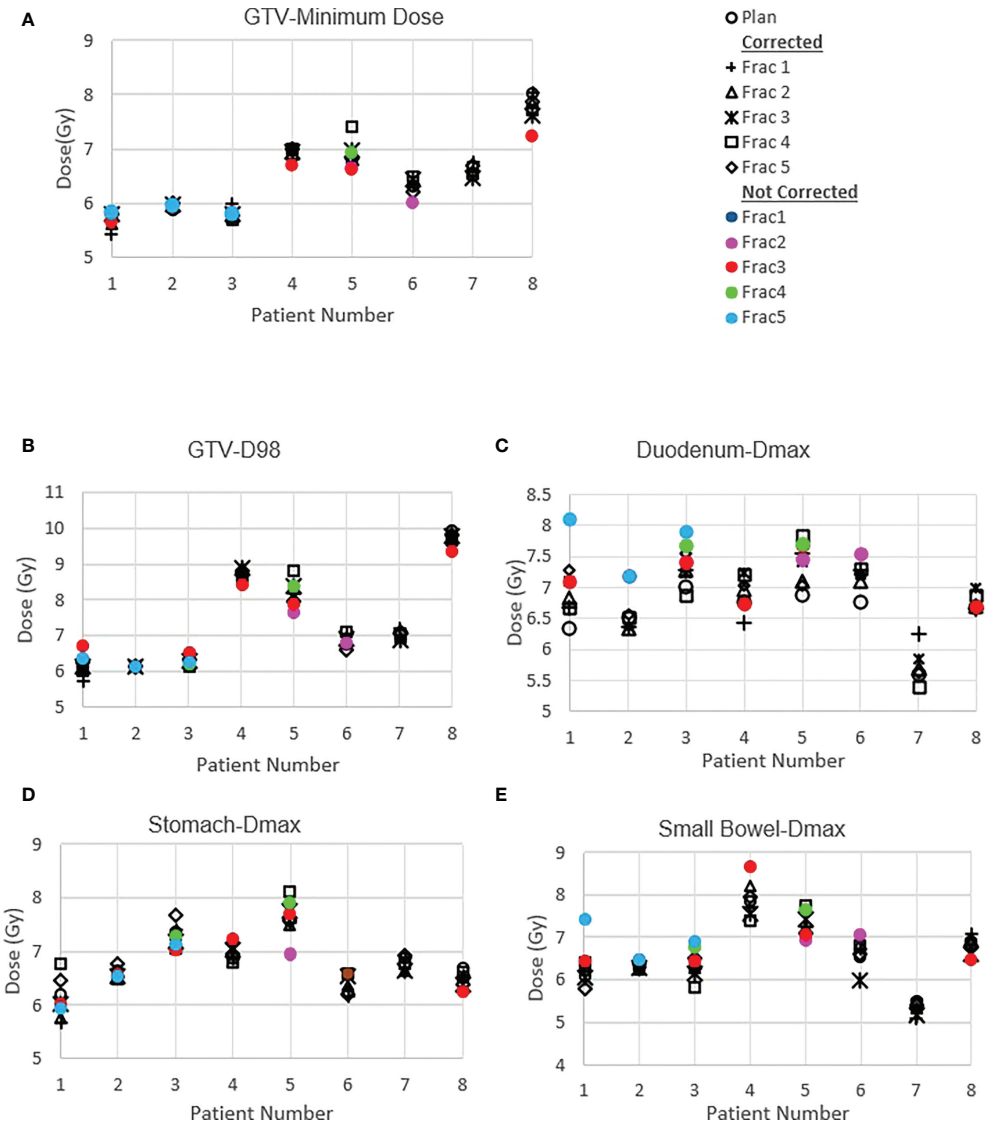

FIGURE 4
Planned and delivered DVH metrics, corrected for position deviations, of GTV **(A, B)** and gastrointestinal OARs Duodenum **(C)**, Stomach **(D)** and Small Bowel **(E)** for individual treatment fractions. The delivered DVH metrics are derived from the CP dose matrices convolved with the real-time target position determined during treatment delivery. The dose that would have been delivered with position deviations not corrected in the absence of real-time position monitoring also shown in the same figures.

(13). The tracking data from 68 patients treated with AC or respiratory gating were analysed in this study and reported that 32% of all treatment fractions required patient realignment due to position deviations. This is comparable to our study results, with GEs and patient realignment occurring in 38% of the treatment fractions. The small sample number could be the reason for the relatively higher rate of GEs observed in this study.

Akimoto et al. quantified the intrafraction pancreas tumour motion using the orthogonal kV imaging subsystem available in Vero system and reported a greater magnitude of motion in SI direction followed by AP and LR directions (20). In our study the intrafractional tumour position determined using the SeedTracker system showed similar results for patients treated with FB and AC techniques (Figure 2) and was consistent with the motion determined using the planning 4D CT dataset. The intrafraction tumour motion determined by SeedTracker showed that the tumour movement range does exceed the ITV in the majority of the fractions for patients treated with the FB and AC technique (Figure 2). In particular for two of the patients (Patients 3 and 8) treated using the AC technique, the magnitude of motion in SI direction during treatment delivery was

10.3389/fonc.2022.1009916

TABLE 2 The mean (range) difference between planned and delivered dose to GTV and gastrointestinal OARs with and without position corrections.

Structure	Difference between total plan and delivered DVH metric(Gy/cc)Mean (min-max)			Statistical difference between delivery with and without corrections where position deviations were detected
	Metric	With position correction	Without position correction	p value
GTV	Mean dose	-0.4 (-1.1 - 0.9)	-0.4 (-0.8 - -0.1)	0.66
	Min dose	0.1 (-1.0 – 1.1)	-0.1 (-1.4 – 0.5)	0.33
	D98	0.2 (-0.6 - 1.8)	0.2 (-0.8 - 1.2)	0.10
Duodenum	Dmax	1.1 (-0.7 - 3.3)	1.9 (-0.1- 4.6)	0.02
Stomach	Dmax	-0.5 (-1.6 - 1.2)	-0.9 (-1.7- 0.3)	0.12
Small bowel	Dmax	-0.3 (-1.1 - 1.4)	0.4 (-0.4 - 2.4)	0.05

consistently less than the ITV magnitude in the SI direction derived based on the planning 4D CT. Minn et al. compared the pancreatic tumour motion quantified using planning 4D CT with the intrafraction motion determined using the imaging subsystem available in Cyberknife system and found that tumour motion determined during treatment did not correlate with the motion quantified using 4D CT (9). In EBH treatment, the stability and reproducibility of tumour position varies during the treatment and results in the spread of tumour position in all three directions during dose delivery (Figure 2). Studies have reported variations in tumour position of up to 1cm during the Deep Inspiration Breath Hold treatment in Liver SBRT due to poor breath-hold reproducibility (21, 22). The position deviations detected in the patients treated with EBH technique in our study agree with previous studies (Figure 3B) (21, 22).

The accuracy of dose delivered to the target and OARs is paramount in understanding the efficacy of treatment; this is particularly important in pancreas SBRT as the evidence continuously evolves favoring the improvement in overall survival. The error in target position, interplay effects between target motion and treatment delivery parameters and inter and intrafraction internal anatomy position changes and deformation contributes to the accuracy of dose delivered to the target volume and OARs. In this study, both the dose difference that resulted from detected position deviations and the actual delivered dose with patient realignment was calculated by incorporating actual target positions determined during delivery to the 3D dose resulting from each CP of the VMAT plan generated for each of the patients. The spread in GTV dose volume metrics indicates that in actual delivery with patient realignment the min dose and D98 to GTV were reduced by 1.0Gy and 0.6Gy respectively (Table 2). This could be attributed to the residual error and relatively high sensitivity of the plan to interplay effects between the target motion and dose delivery. In four of the six patients treated with either FB or AC, the target motion during the treatment delivery and position deviations blurs the Dmax to GTV (Figure 5). In the patients treated with BH techniques the Dmax delivered to GTV was marginally high,

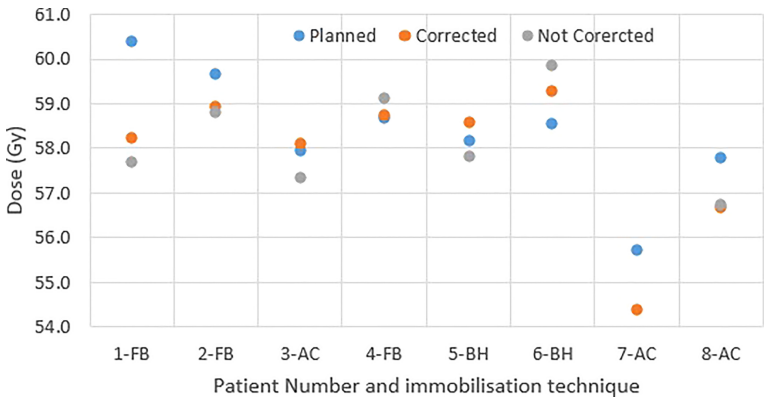

FIGURE 5
The GTV Dmax of original plan and delivery with and without position corrections.

maximum by 0.7Gy, compared to planned dose. Whilst generally the target motion and random position deviations blurs the dose, the reason for the increase in Dmax with motion and position deviation in the studied cases could be due to the position of the high fluence in the VMAT arcs and its interplay with the target motion.

Vinogradskiy et al. reported that the target shift observed in their study resulted in point dose differences averaging 23 ± 22% of the prescription dose to tumour (13). This is relatively high in comparison to the tumour dose difference observed in our study. In their study they have reported the position shift up to 10mm in SI direction with an average radial shift of 5.9mm. Moreover, in the dose estimation, it was assumed that the position deviation occurred during the entire fraction of the treatment. In our study majority of the position, shifts were ≤5mm with one exception where 6mm in SI direction was detected (Figure 3B). In this study the dosimetric impact of the position shifts was accounted for only the duration of time it was present in the treatment delivery and the dose calculation was performed using the actual plan which is more realistic than the estimation based on a dosimetric model. Potentially with improved accuracy of dose delivery, PTV margins may also be reduced safely to limit OAR dose while increasing dose delivered to the target.

The impact of motion and position deviations on the dose delivered to OARs was also evaluated in this study. Overall, the mean (range) dmax to duodenum was increased by 1.1 (-0.7 - 3.3)Gy compared to the plan delivered with position corrections (Table 2 and Figure 4C). This increase in dose could be due to the combined effect of residual position error (Figure 2), dose gradient in the target and duodenum interface and interplay effect between the motion and dose delivery. In contrast to the duodenum, the Dmax to the stomach and small bowel was reduced in comparison to the planned dose. The range of deviation of some of the metrics are larger with position correction in comparison to without position correction (Table 2). This could be due to the combined effect of interplay between the dynamic delivery, target volume and OARs motion, and the direction of position deviation during treatment. The direction of position deviation occurring during treatment may reduce the dose to one structure (e.g. target volume) and improve agreement between planned and delivered dose for other structures (e.g. OARs).

In addition to the improved treatment accuracy, the other main advantage of real-time position monitoring is that it enables calculation of delivered dose by incorporating the target position determined during treatment delivery. In our study, we found that due to residual set-up error and target motion (Figure 2) the minimum dose and D98 to GTV was reduced by up to 1Gy and duodenal Dmax was increased by up to 3.3Gy in some patients (Table 2 and Figure 4). A position tolerance limit of 3mm was applied in this study. Though reducing the magnitude of tolerance limit may reduce the dose difference arising from residual error, the influence of interplay between target motion and treatment delivery remains. Moreover, reducing the tolerance limit may increase the occurrence of treatment interruptions and increase the treatment time which is inconvenient to patients, particularly those treated with AC and EBH techniques. Robust plan optimisation methods are shown to generate an optimal treatment plan which increases the robustness of target coverage to set-up uncertainties and sparing of OARs (23, 24). Future studies are warranted to investigate the application of robust planning methods to pancreatic SBRT which could minimise the dose difference to tumour and OARs arising from setup uncertainties and target motion. It should be considered that when such robust optimisation planning methods are clinically implemented, the real- time monitoring and dose assessment process presented in this study would play a vital role in the evaluation, validation and quality assurance of the treatment delivered.

Bae et al. reported that duodenal Dmax is the best predictor of duodenal toxicity in pancreatic SBRT and Verma et al. reported that V35,V30 and V25 to duodenum correlates well with duodenal toxicity (25, 26). The dosimetric predictors reported in these studies are based on the planned dose against the histopathologic and clinician-assessed outcome measures. The dosimetric assessment performed in this study quantified the magnitude of difference in the delivered dose when treatment is performed with commonly practiced position tolerance limit in the clinics.

We acknowledge that this study has some limitations. Firstly, the patient number in this study is small being a pilot trial to assess the safety of pancreatic SBRT, which was new to Australian centres at the time, and this trial allowed successful implementation of an in-house developed real-time position monitoring system. The tools developed and the process implemented in this study could be expanded to a larger study or routine clinical practice to improve the safety and accuracy of pancreatic SBRT. Secondly, the implanted fiducial markers were used as a surrogate to determine the target position - these are subject to inaccuracies that could arise due to target deformation or marker migration. Previous studies have demonstrated the inter and intrafraction deformation of tumour border in the pancreas (27). However, using multiple markers for tracking minimises the errors arising from these sources. The intrafraction deformation of tumour borders is shown to be in the range of 1-2mm, which is smaller compared to the magnitude of uncertainties arising from breathing motion and position deviations (28). In this study, 4 markers were implanted and used for tracking in 7 out of 8 patients and in one patient 3 markers were used as the implantation of the 4^{th} marker was not clinically achievable. Further, the interfraction deformation of target and OARs are not considered in this study as the visualisation of tumour and OARs is challenging on the daily setup CBCT images and may lead to larger uncertainties. MR images acquired on MR guided RT systems enable daily plan adaption to account for target and OARs variations and are

shown to benefit the pancreatic cancer patients where the tumour to adjacent OAR distance is ≤ 3mm (29, 30). Finally, for the delivered dose assessment, the OARs motion is assumed to be the same magnitude and moves in synchronisation with the target. Whilst it is a reasonable approximation for the OARs close to the fiducials/tumour, this may have limitations in the motion quantification for distal OARs as they may exhibit varying magnitude, phase and direction of motion. However, the OARs receiving high dose is likely to be the proximal regions to the tumour volume and the delivered dose calculated in this study will be closer to the actual dose than the assumption of planned dose.

Conclusion

An in-house developed position monitoring system for multiple fiducial based target position tracking in pancreas SBRT treated with free-breathing, abdominal compression and EBH motion management techniques was successfully implemented. Position corrections were required in 38% of the treatment fractions and resulted in improved accuracy of the dose delivered to tumour and OARs. To our knowledge, this is the first study to assess and report the delivered dose that incorporates temporal target position during treatment delivery in pancreatic SBRT. The intrafraction motion impacts the dose to tumour even if the target position is maintained within a 3mm position tolerance.

Data availability statement

The original contributions presented in the study are included in the article/supplementary material. Further inquiries can be directed to the corresponding author.

Ethics statement

The studies involving human participants were reviewed and approved by Human Research and Ethics Committee, South Western Sydney Local Health District, Sydney, New South Wales, Australia. The patients/participants provided their written informed consent to participate in this study.

Author contributions

SA developed the study concept and drafted the manuscript. TY, MJ, DP and ML contributed to study administration, data analysis and manuscript revision. All authors were involved in the running of the study and the revision and approval of the final manuscript.

Conflict of interest

The authors declare that the research was conducted in the absence of any commercial or financial relationships that could be construed as a potential conflict of interest.

Publisher's note

References

1. Sung H, Ferlay J, Siegel RL, Laversanne M, Soerjomataram I, Jemal A, et al. Global cancer statistics 2020: GLOBOCAN estimates of incidence and mortality worldwide for 36 cancers in 185 countries. *CA Cancer J Clin* (2021) 71(3):209–49. doi: 10.3322/caac.21660

2. Rawla P, Sunkara T, Gaduputi V. Epidemiology of pancreatic cancer: Global trends, etiology and risk factors. *World J Oncol* (2019) 10(1):10. doi: 10.14740/wjon1166

3. Boone BA, Steve J, Krasinskas AM, Zureikat AH, Lembersky BC, Gibson MK, et al. Outcomes with FOLFIRINOX for borderline resectable and locally unresectable pancreatic cancer. *J Surg Oncol* (2013) 108(4):236–41. doi: 10.1002/jso.23392

4. Kharofa J, Kelly TR, Ritch PS, George B, Wiebe LA, Thomas JP, et al. 5-FU/leucovorin, irinotecan, oxaliplatin (FOLFIRINOX) induction followed by chemoXRT in borderline resectable pancreatic cancer. *J Clin Oncol* (2012) 30 (15_suppl). doi: 10.1200/jco.2012.30.15_suppl.e14613

5. Colbert LE, Rebueno N, Moningi S, Beddar S, Sawakuchi GO, Herman JM, et al. Dose escalation for locally advanced pancreatic cancer: How high can we go? *Adv Radiat Oncol* (2018) 3(4):693–700. doi: 10.1016/j.adro.2018.07.008

6. Zaorsky NG, Lehrer EJ, Handorf E, Meyer JE. Dose escalation in stereotactic body radiation therapy for pancreatic cancer. *Am J Clin Oncol* (2019) 42(1):46–55. doi: 10.1097/COC.0000000000000472

7. Campbell WG, Jones BL, Schefter T, Goodman KA, Miften M. An evaluation of motion mitigation techniques for pancreatic SBRT. *Radiother Oncol* (2017) 124 (1):168–73. doi: 10.1016/j.radonc.2017.05.013

8. Brandner ED, Chetty IJ, Giaddui TG, Xiao Y, Huq MS. Motion management strategies and technical issues associated with stereotactic body radiotherapy of thoracic and upper abdominal tumors: A review from NRG oncology. *Med Phys* (2017) 44(6):2595–612. doi: 10.1002/mp.12227

9. Minn AY, Schellenberg D, Maxim P, Suh Y, McKenna S, Cox B, et al. Pancreatic tumor motion on a single planning 4D-CT does not correlate with intrafraction tumor motion during treatment. *Am J Clin Oncol* (2009) 32(4):364–8. doi: 10.1097/COC.0b013e31818da9e0

10. Ge J, Santanam L, Noel C, Parikh PJ. Planning 4-dimensional computed tomography (4DCT) cannot adequately represent daily intrafractional motion of abdominal tumors. *Int J Radiat Oncol Biol Phys* (2013) 85(4):999–1005. doi: 10.1016/j.ijrobp.2012.09.014

11. Rudra S, Jiang N, Rosenberg SA, Olsen JR, Roach MC, Wan L, et al. Using adaptive magnetic resonance image-guided radiation therapy for treatment of inoperable pancreatic cancer. *Cancer Med* (2019). doi: 10.1002/cam4.2100

12. Boldrini L, Cusumano D, Cellini F, Azario L, Mattiucci GC, Valentini V. Online adaptive magnetic resonance guided radiotherapy for pancreatic cancer: State of the art, pearls and pitfalls. *Radiat Oncol* (2019) 14:71. doi: 10.1186/s13014-019-1275-3

13. Vinogradskiy Y, Goodman KA, Schefter T, Miften M, Jones BL. The clinical and dosimetric impact of real-time target tracking in pancreatic SBRT. *Int J Radiat Oncol Biol Phys* (2019) 103(1):268–75. doi: 10.1016/j.ijrobp.2018.08.021

14. Arumugam S, Pavey D, Oar A, Holloway L, Sidhom M, Lee M. The first real-time intrafraction target position monitoring in pancreas SBRT on an elekta linear accelerator. *Phys Eng Sci Med* (2021) 44:625–38. doi: 10.1007/s13246-021-01007-0

15. Petrelli F, Comito T, Ghidini A, Torri V, Scorsetti M, Barni S. Stereotactic body radiation therapy for locally advanced pancreatic cancer: A systematic review and pooled analysis of 19 trials. *Int J Radiat Oncol Biol Phys* (2017) 97(2):313–22. doi: 10.1016/j.ijrobp.2016.10.030

16. Arumugam S, Sidhom M, Xing A, Holloway L. An online x-ray based position validation system for prostate hypofractionated radiotherapy. *Med Phys* (2016) 43(2):961–74. doi: 10.1118/1.4940351

17. Arumugam S, Sidhom M, Truant D, Xing A, Udovitch M, Holloway L. Variable angle stereo imaging for rapid patient position correction in an in-house real-time position monitoring system. *Phys Med* (2017) 33:170–8. doi: 10.1016/j.ejmp.2016.12.014

18. Sothmann T, Blanck O, Poels K, Werner R, Gauer T. Real time tracking in liver SBRT: Comparison of CyberKnife and vero by planning structure-based γ-evaluation and dose-area-histograms. *Phys Med Biol* (2016) 61(4):1677. doi: 10.1088/0031-9155/61/4/1677

19. Zhang H, Zhao G, Djajaputra D, Xie Y. Determination of acquisition frequency for intrafractional motion of pancreas in CyberKnife radiotherapy. *Sci World J* (2014) 2014. doi: 10.1155/2014/408019

20. Akimoto M, Nakamura M, Nakamura A, Mukumoto N, Kishi T, Goto Y, et al. Inter-and intrafractional variation in the 3-dimensional positions of pancreatic tumors due to respiration under real-time monitoring. *Int J Radiat Oncol Biol Phys* (2017) 98(5):1204–11. doi: 10.1016/j.ijrobp.2017.03.042

21. Lu L, Ouyang Z, Lin S, Mastroianni A, Stephans KL, Xia P. Dosimetric assessment of patient-specific breath-hold reproducibility on liver motion for SBRT planning. *J Appl Clin Med Phys* (2020) 21(7):77–83. doi: 10.1002/acm2.12887

22. Stick LB, Vogelius IR, Risum S, Josipovic M. Intrafractional fiducial marker position variations in stereotactic liver radiotherapy during voluntary deep inspiration breath-hold. *Br J Radiol* (2020) 93(1116):20200859. doi: 10.1259/bjr.20200859

23. Wagenaar D, Kierkels RGJ, Free J, Langendijk JA, Both S, Korevaar EW. Composite minimax robust optimization of VMAT improves target coverage and reduces non-target dose in head and neck cancer patients. *Radiother Oncol* (2019) 136:71–7. doi: 10.1016/j.radonc.2019.03.019

24. Zhang X, Rong Y, Morrill S, Fang J, Narayanasamy G, Galhardo E, et al. Robust optimization in lung treatment plans accounting for geometric uncertainty. *J Appl Clin Med Phys* (2018) 19(3):19–26. doi: 10.1002/acm2.12291

25. Bae SH, Kim M-S, Cho CK, Kang J-K, Lee SY, Lee K-N, et al. Predictor of severe gastroduodenal toxicity after stereotactic body radiotherapy for abdominopelvic malignancies. *Int J Radiat Oncol Biol Phys* (2012) 84(4):e469–74. doi: 10.1016/j.ijrobp.2012.06.005

26. Verma V, Lazenby AJ, Zheng D, Bhirud AR, Ly QP, Are C, et al. Dosimetric parameters correlate with duodenal histopathologic damage after stereotactic body radiotherapy for pancreatic cancer: Secondary analysis of a prospective clinical trial. *Radiother Oncol* (2017) 122(3):464–9. doi: 10.1016/j.radonc.2016.12.030

27. Feng M, Balter JM, Normolle D, Adusumilli S, Cao Y, Chenevert TL, et al. Characterization of pancreatic tumor motion using cine MRI: Surrogates for tumor position should be used with caution. *Int J Radiat Oncol Biol Phys* (2009) 74 (3):884–91. doi: 10.1016/j.ijrobp.2009.02.003

28. Liu F, Erickson B, Peng C, Li XA. Characterization and management of interfractional anatomic changes for pancreatic cancer radiotherapy. *Int J Radiat Oncol Biol Phys* (2012) 83(3):e423–9. doi: 10.1016/j.ijrobp.2011.12.073

29. Tyran M, Jiang N, Cao M, Raldow A, Lamb JM, Low D, et al. Retrospective evaluation of decision-making for pancreatic stereotactic MR-guided adaptive radiotherapy. *Radiother Oncol* (2018) 129(2):319–25. doi: 10.1016/j.radonc.2018.08.009

30. Bohoudi O, Bruynzeel AME, Meijerink MR, Senan S, Slotman BJ, Palacios MA, et al. Identification of patients with locally advanced pancreatic cancer benefitting from plan adaptation in MR-guided radiation therapy. *Radiother Oncol* (2019) 132:16–22. doi: 10.1016/j.radonc.2018.11.019

frontiers | Frontiers in Oncology

TYPE Original Research
PUBLISHED 14 December 2022
DOI 10.3389/fonc.2022.1050070

OPEN ACCESS

EDITED BY
Antonio Pontoriero,
University of Messina, Italy

REVIEWED BY
Xiaofei Zhu,
Second Military Medical University, China
Zhuo Shao,
Changhai Hospital, China

*CORRESPONDENCE
Jin-Hyeok Hwang
woltoong@snu.ac.kr

SPECIALTY SECTION
This article was submitted to Radiation Oncology, a section of the journal Frontiers in Oncology

RECEIVED 21 September 2022
ACCEPTED 23 November 2022
PUBLISHED 14 December 2022

CITATION
Jung JH, Song C, Jung IH, Ahn J, Kim B, Jung K, Lee JC, Kim J and Hwang JH (2022) Induction FOLFIRINOX followed by stereotactic body radiation therapy in locally advanced pancreatic cancer. *Front. Oncol.* 12:1050070. doi: 10.3389/fonc.2022.1050070

Induction FOLFIRINOX followed by stereotactic body radiation therapy in locally advanced pancreatic cancer

Jae Hyup Jung[1], Changhoon Song[2], In Ho Jung[1], Jinwoo Ahn[1], Bomi Kim[1], Kwangrok Jung[1], Jong-Chan Lee[1], Jaihwan Kim[1] and Jin-Hyeok Hwang[1*]

[1]Division of Gastroenterology, Department of Internal Medicine, Seoul National University Bundang Hospital, Seoul National University College of Medicine, Seongnam, Republic of Korea, [2]Department of Radiation Oncology, Seoul National University Bundang Hospital, Seoul National University College of Medicine, Seongnam, Republic of Korea

Introduction: FOLFIRINOX (the combination of 5-fluorouracil, leucovorin, irinotecan, and oxaliplatin) is the preferred systemic regimen for locally advanced pancreatic cancer (LAPC). Furthermore, stereotactic body radiation therapy (SBRT) is a promising treatment option for achieving local control in these patients. However, clinical outcomes in patients with LAPC treated using FOLFIRINOX followed by SBRT have not been clarified. Therefore, we aimed to evaluate clinical outcomes of induction FOLFIRINOX treatment followed by SBRT in patients with LAPC.

Methods: To this end, we retrospectively reviewed the medical records of patients with LAPC treated with induction FOLFIRINOX followed by SBRT in a single tertiary hospital. We evaluated overall survival (OS), progression-free survival (PFS), resection rate, SBRT-related adverse events, and prognostic factors affecting survival.

Results: Fifty patients were treated with induction FOLFIRINOX for a median of 8 cycles (range: 3–28), which was followed by SBRT. The median OS and PFS were 26.4 (95% confidence interval [CI]: 22.4–30.3) and 16.7 months (95% CI: 13.0–20.3), respectively. Nine patients underwent conversion surgery (eight achieved R0) and showed better OS than those who did not (not reached vs. 24.1 months, p = 0.022). During a follow-up period of 23.6 months, three cases of grade 3 gastrointestinal bleeding at the pseudoaneurysm site were noted, which were managed successfully. Analysis of the factors affecting clinical outcomes revealed that a high radiation dose (≥ 35 Gy) resulted in a higher rate of conversion surgery (25% [8/32] vs. 5.6% [1/18], respectively) and was an independent favorable prognostic factor for OS in the adjusted analysis (hazard ratio: 2.024, 95% CI: 1.042–3.930, p = 0.037).

Conclusion: Our findings suggest that induction FOLFIRINOX followed by SBRT in patients with LAPC results in better survival with manageable toxicities. A high total SBRT dose was associated with a high rate of conversion surgery and could afford better survival.

KEYWORDS

pancreatic cancer, locally advanced pancreatic cancer, FOLFIRINOX, stereotactic body radiation therapy (SBRT), conversion surgery, prognosis

Introduction

Pancreatic cancer (PC) is the third leading cause of cancer-related deaths in the United States and it has been responsible for 49,830 deaths thus far in 2022. The death rate for PC has increased slightly since the mid-2000s (1, 2). Surgical resection is the only curative treatment for PC; however, only 10-15% of affected patients are considered suitable for surgical resection at the time of diagnosis. Approximately 30–35% of patients were diagnosed with locally advanced PC (LAPC), and the 5-year survival rate in LAPC was less than 15% (3). Conventionally, systemic chemotherapy with or without traditional fractionated external-beam radiotherapy (EBRT) was considered the standard of treatment for patients with LAPC (4–6). However, some randomized controlled trials (7, 8) investigating EBRT have reported unsatisfactory results in terms of efficacy, with considerable radiation-related adverse events (AEs). Moreover, conventional EBRT with concurrent chemotherapy may require quite a few weeks for completion (9).

Since the publication of a randomized trial by Conroy et al. in 2011 (10), the combination of folinic acid, fluorouracil, irinotecan, and oxaliplatin (FOLFIRINOX) has become the standard of care for metastatic PC (11). Several studies have demonstrated that FOLFIRINOX is also effective in LAPC; thus, FOLFIRINOX is the preferred systemic chemotherapy regimen in patients with good performance status (12, 13). Furthermore, the 2022 National Comprehensive Cancer Network guidelines recommend FOLFIRINOX as the preferred systemic treatment for patients with LAPC (14).

However, over 70% of patients with LAPC are ineligible candidates for resection even after induction chemotherapy because either their lesions are not sufficiently reduced in size to be suitable for surgery or due to locoregional progression (15–18). Therefore, local ablative therapies have been explored as new therapeutic options for patients with LAPC, which could increase locoregional disease control rates (19–21). Among them, stereotactic body radiation therapy (SBRT) is a promising treatment that can overcome radio-resistance because it allows precise delivery of high-dose radiation while reducing radiation treatment-related AEs. The latter is achieved by decreasing the radiation dose delivered to adjacent healthy tissue compared to that associated with conventional EBRT (6, 22, 23).

In 2004, Koong et al. (24) conducted a dose-escalation study using SBRT for pancreatic cancer, which showed favorable results in terms of local disease control. In several retrospective (25–29) and single-arm prospective studies (LAPC-1 trial) (30, 31), sequential treatment with induction chemotherapy (FOLFIRINOX or other regimens) followed by SBRT yielded encouraging results in terms of local control in patients with LAPC. Moreover, SBRT was associated with a favorable rate of conversion surgery among patients with LAPC, which could result in better survival (32).

The addition of SBRT is a promising treatment option for patients with LAPC; however, no consensus exists regarding the patients suitable for this treatment, when it should be administered, and the clinical factors that should be considered for better clinical outcomes (14, 33, 34). Therefore, in the present study, we aimed to evaluate clinical outcomes of induction FOLFIRINOX followed by SBRT in patients with LAPC at a single tertiary teaching hospital.

Patients and methods

Study patients

Electronic medical records of patients with LAPC who were treated between December 2015 and September 2020 at a single tertiary teaching hospital (Seoul National University Bundang Hospital, Seoungnam, South Korea) were retrospectively reviewed. The patients were treated with induction FOLFIRINOX regimen (oxaliplatin, 85 mg per m^2 of the body-surface area; irinotecan, 180 mg per m^2; leucovorin, 400 mg per m^2; and fluorouracil, 400 mg per m^2 delivered as a bolus followed by 2400 mg per square meter administered as a 46-hour continuous infusion, every 2 weeks) followed by SBRT (11). The inclusion criteria were as follows: (1) patients with LAPC diagnosed based on the results of radiological evaluations and a multidisciplinary conference, (2) patients who had received induction FOLFIRINOX (≥1 cycle) and were unsuitable candidates for

conversion surgery despite induction FOLFIRINOX based on multidisciplinary discussion, (3) patients who revealed no evidence of metastatic disease or gastric or duodenal invasion at the time of SBRT, (4) patients who had not previously received abdominal radiotherapy, and (5) patients without a history of other malignancies within 5 years.

Study design and definition of clinical outcomes

The patients' baseline characteristics were assessed at diagnosis and before SBRT. Overall survival (OS), progression-free survival (PFS), resection rate, SBRT-related AEs, and prognostic factors were assessed. Furthermore, survival, disease progression, and resection data until 31 March 2022 were evaluated. OS was defined as the time from histological diagnosis to all-cause death or the last follow-up. PFS was defined as the time from histological diagnosis to radiological progression according to the Response Evaluation Criteria in Solid Tumors criteria version 1.1, all-cause death, or last follow-up. Locoregional progression was defined as disease progression within the primary tumor or peripancreatic lymph nodes, and distant progression was defined as distant metastasis. For those who underwent conversion surgery, T and N stages were assessed using resected specimens according to the eighth edition of the American Joint Committee on Cancer Staging System. The pathological response of the tumor to previous chemotherapy or radiotherapy was assessed according to the tumor regression scoring system of the College of American Pathologists (CAP) version 4.2. SBRT-related AEs were assessed according to the National Cancer Institute Common Terminology for Adverse Events version 5.0. SBRT-related acute and late AEs were defined as AEs occurring within 90 days and after 90 days from radiation therapy, respectively.

SBRT procedure

Patients were treated with five-fraction SBRT on 5 consecutive business days by using a Varian TruBeam linear accelerator (Varian Medical Systems Inc., Palo Alto, CA, USA). SBRT was initiated within 2 weeks after the completion of chemotherapy. At the time of simulation, a four-dimensional computed tomography (CT) (Philips Brilliance Big Bore CT scanner, Philips Medical Systems, Cleveland, OH, USA) simulation was performed during free breathing to determine the position variation of the pancreas and organ at risk (OAR). The respiratory cycle was recorded using an abdominal bellows strap (Philips Healthcare, Best, Netherlands). Thin-sliced CT scans with intravenous contrast were obtained, with patients positioned supine and arms above the head in a Body Pro-Lok ONE device (CIVCO Medical Solutions, Orange City, IA, USA) for immobilization. Pre-treatment diagnostic CT or magnetic resonance imaging (MRI) scans were matched if they provided better delineation of the tumor than did simulation CT images.

The Eclipse planning system was used for target and OAR delineation and treatment planning. Gross tumor volume (GTV) included the gross tumor and adjacent vessels, such as the common hepatic artery, celiac axis, and/or superior mesenteric vessels. The internal target volume (ITV) was obtained by summing the GTVs for all respiratory phases. The planning target volume (PTV) was generated by adding a 2-mm margin circumferentially and a 4- to 6-mm margin craniocaudally to the ITV. A 3-mm margin was added to the OAR volumes to obtain the planning OAR volume (PRV). The modified PTV was obtained from the PTV by subtracting the PRV. The desired prescribed dose was 40 Gy delivered in five fractions. Ninety-five percent of the modified PTV should be covered by the prescribed dose and at least 95% of the PTV should be covered by 30 Gy. If the desired prescribed dose violated the constraints of the OARs, the prescription dose was lowered from 40 to 35, 33, or 30 Gy. The OAR constraints were as follows: stomach and duodenum: Dmax $\leq$ 32 Gy, V20 < 3 cc, and V15 < 9 cc, and other small bowel intestine: Dmax: 35 Gy and V20 < 20 cc. Cone-beam CT was performed for positional validation before the delivery of each fraction. Daily cone beam CT 3-dimensional images without fiducial were registered to planning CT images. Patients were aligned to the spine and then shifted to align to great vessels, including the aorta, celiac axis, and/or superior mesenteric artery. Although the soft tissue is rarely visible on cone beam CT, soft tissue was sometimes used in alignment when visible.

Statistical analysis

To compare the patients' baseline characteristics, chi-square or Fisher's exact test was used for categorical scales, and the t-test or Mann-Whitney U test was used for numerical scales. OS and PFS were evaluated using the Kaplan-Meier method, and differences in survival were analyzed using the log-rank test. The Cox proportional hazards model was used to analyze survival and other factors. The values of all continuous variables were dichotomized on the entire sample (< median vs. $\geq$ median) in univariate and multivariate cox proportional analyses. All tests were double-sided with a p-value of less than 0.05 being statistically significant. Multivariate analysis was performed using variables with p-values of less than 0.1 in the univariate analyses. All statistical analyses were performed using SPSS software version 25 (IBM Corporation, New York, USA) and R software version 4.2.0 (R Foundation for Statistical Computing, Vienna, Austria).

Results

Patient characteristics

Fifty patients were retrospectively evaluated, and the median follow-up period was 23.6 months. Among them, 39 (78.0%) patients died during the follow-up period and 11 (22.0%) were alive until March 31, 2022. The median age of the patients was 64.1 (range: 47.8–81.6) years. Twenty-eight (56.0%) patients were female, and 30 (60.0%) had pancreatic head or neck cancer. The median body mass index was 22.7 kg/m^2 at diagnosis and before SBRT. The median serum albumin and CA 19-9 levels changed from 4.0 to 3.9 g/dL and from 106.0 to 48.5 U/mL, respectively, after induction FOLFIRINOX. The median tumor size changed from 3.2 to 2.9 cm after induction FOLFIRINOX. The median number of cycles and duration of FOLFIRINOX treatment was 8 (range: 3–28) and 4.9 (range: 1.4–21.7) months, respectively. Thirty-nine (78.0%) patients showed stable disease as the best response during induction FOLFIRINOX, while 11 (22.0%) showed partial response. The median time to SBRT from diagnosis, the total dose of SBRT, and SBRT dose per fraction was 6.1 (range: 2.8–22.3) months, 35 (range: 30–40) Gy in five fractions, and 7 (6–8) Gy, respectively. Nine (18.0%) patients underwent conversion surgery after SBRT during the follow-up period (median: 3.5 months, range: 0.8–11.7 months) (Table 1).

Efficacy

The patients' median OS and PFS were 26.3 months (95% confidence interval [CI]: 22.4–30.3) and 16.7 months (95% CI: 13.0–20.3), respectively (Figures 1A, B). Nine patients (18%) who underwent conversion surgery showed longer OS than did those who did not (not reached vs. 24.1 months, p = 0.022). (Figure 2A) and longer median PFS (35.2 months vs. 16.0 months, p = 0.001) (Figure 2B). Among them, eight underwent margin-negative resection. The T and N stage distributions were as follows: five in T1 and four in T2 and seven in N0 and two in N1. One patient revealed a near-complete response (CAP grade 1), and eight exhibited a partial response (CAP grade 2) (Table 2). Among the 34 patients who exhibited disease progression after SBRT, 9 (26.5%) showed locoregional progression without distant metastasis (Table 3).

SBRT-related acute and late AEs

SBRT-related AEs of grade 3 or higher occurred within 1 year of SBRT in three patients who had gastrointestinal (GI) bleeding at the pseudoaneurysm site. These bleeding events were controlled by supportive management and transarterial embolization (dose ≥ 35 Gy in two patients and < 35 Gy in one). SBRT-related acute AEs of grade 2 or lower included anorexia (three patients), fatigue (three patients), nausea (three patients), vomiting (one patient), and diarrhea (five patients). SBRT-related late AEs of grade 2 or lower were gastritis (two patients), GI ulcer (four patients), and non-significant GI bleeding (one patient). These complications were well-managed conservatively, and there were no deaths due to these complications (Table 4).

Clinical factors affecting survival

The two variables (Tumor size (pre-SBRT) and Total SBRT dose) with a p-value of less than 0.1 in univariate cox analysis were used for adjusted analysis in OS and PFS. Analysis of OS by using adjusted variables showed that a high total dose of SBRT was an independent and significant favorable prognostic factor

TABLE 1 Baseline characteristics.

Characteristics	Statistical value
Age (yr), median	64.1 (47.8–81.6)
Sex	
Female	28 (56.0)
Male	22 (44.0)
Primary site	
Head or Neck	30 (40.0)
Body or Tail	20 (60.0)
At diagnosis	
BMI (kg/m^2), median	22.7 (17.5–26.1)
Serum albumin (g/dL), median	4.0 (2.7–4.8)
CA 19-9 (U/mL), median	106.0 (2–7999)
Tumor size (cm), median	3.2 (1.9–8.3)
Pre-SBRT	
BMI (kg/m^2), median	22.7 (16.5–27.6)
Serum albumin (g/dL), median	3.9 (2.5–4.7)
CA 19-9 (U/mL), median	48.5 (5–1780)
Tumor size (cm), median	2.9 (1.4–5.7)
Induction FOLFIRINOX cycles, median	8.0 (3–28)
Induction FOLFIRINOX duration (months), median	4.9 (1.4–21.7)
Best response during induction FOLFIRINOX	
SD	39 (78.0)
PR	11 (22.0)
Time to SBRT from diagnosis (months), median	6.1 (2.8–22.3)
Total SBRT dose (Gy), median	35 (30–40)
SBRT dose per fraction (Gy), median	7 (6–8)
Conversion surgery	
Yes	9 (18.0)
No	41 (82.0)
Time to conversion surgery from SBRT (months), median	3.5 (0.8–11.7)

Data are presented as median (range) or No. of patients/total no. (n%), unless otherwise stated; BMI, body mass index; CA 19-9, carbohydrate antigen 19-9; SD, stable disease; PR, partial response; SBRT, stereotatic body radiation therapy; Gy, gray.

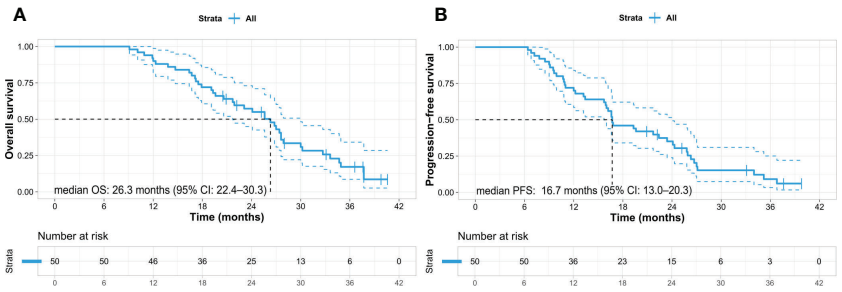

FIGURE 1
Kaplan–Meier survival curves in the entire cohort of pancreatic cancer patients. **(A)** Overall survival and **(B)** progression-free survival. OS, overall survival; PFS, progression-free survival; CI, confidence interval.

(≥ 35 vs. < 35 Gy; 27.0 vs. 24.1 months; hazard ratio [HR] 2.024; 95% CI 1.042–3.930; p = 0.037) (Table 5, Figure 3A), although there were no statistically significant differences between the high and low total SBRT dose groups in terms of baseline characteristics (Supplementary Table). Moreover, a higher total dose of SBRT resulted in a higher resection rate than did a lower total dose of SBRT (25.0% vs. 5.6%, p = 0.086). Analysis of PFS using adjusted variables showed that a high total dose of SBRT (≥ 35 vs. < 35 Gy; 19.3 vs. 13.2 months; HR 2.364; 95% CI 1.218–4.588, p = 0.011) and small tumor size (< 2.9 vs. ≥ 2.9 cm; 23.4 vs. 15.9 months; HR: 1.853; 95% CI: 1.005–3.416, p = 0.048) were independent and significant favorable prognostic factors (Table 6 and Figure 3B).

Discussion

In the present study, we investigated the feasibility of induction FOLFIRINOX followed by SBRT as a strategy for local control and increased possibility of conversion surgery in patients with LAPC. Furthermore, we explored whether this strategy improves survival. After discussing multidisciplinary approach for one patient whose disease was stable but remained unresectable after sufficient FOLFIRINOX, sequential SBRT was conducted on patients who considered it helpful. Resultantly, 18.0% of patients who were considered unsuitable candidates for surgery despite induction FOLFIRINOX could undergo conversion surgery, and most patients achieved R0 resection. Moreover, the first recurrency occurred more often at the distant site than at the locoregional site, and SBRT-related AEs were rare and manageable. Therefore, induction FOLFIRINOX followed by SBRT may be a promising treatment strategy for patients who remained unresectable despite induction FOLFIRINOX, given its considerable efficacy (conversion rate and locoregional control rate) and acceptable SBRT-related AEs.

Several recent studies have investigated the issue of induction chemotherapy followed by SBRT. Mellon EA et al. (27) studied 49 patients with LAPC who received induction chemotherapy (43% of them were treated with FOLFIRINOX) followed by SBRT (30 Gy in five fractions), and their results showed a median OS of 15 months. Moningi S et al. (28) also reported similar results in 74 patients with LAPC who received induction chemotherapy (24% of them were treated with FOLFIRINOX) followed by SBRT (25–33 Gy in five fractions),

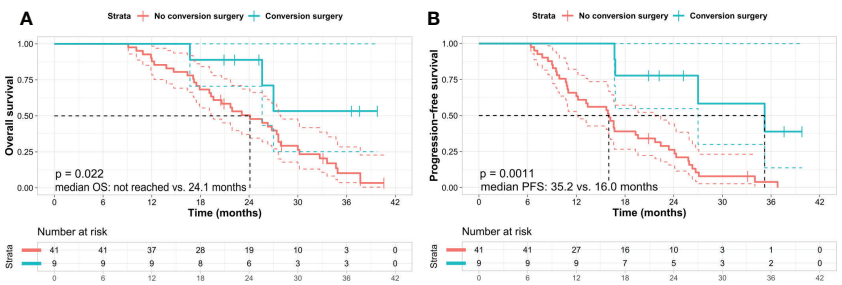

FIGURE 2
Kaplan–Meier survival curves in patients according to the conversion surgery. **(A)** Overall survival and **(B)** progression-free survival. Kaplan–Meier analysis shows that the patients who underwent conversion surgery exhibit better OS and PFS than those who did not. Log-rank test *p*-value was **(A)** 0.022 and **(B)** 0.001 between the two subgroups, respectively. OS, overall survival; PFS, progression-free survival.

TABLE 2 Pathological and clinical characteristics of patients who underwent conversion surgery.

Pathology	No. of patients
Total patients	9
Resection margin	
R0	8
R1	1
T stage	
T1	5
T2	4
N stage	
N0	7
N1	2
Response to previous treatment	
Grade 0 (complete response)	0
Grade 1 (near complete response)	1
Grade 2 (partial response)	8
Grade 3 (poor or no response)	0
Death within 6 months postoperatively[a]	1

T stage and N stage were assessed using American Joint Committee on Cancer staging system 8th; Response of tumor to previous CT or RT was assessed using tumor regression scoring system in College of American Pathologists [version 4.2]. [a]One patient died of bowel perforation, a surgical complication.

with a median OS of 18.4 months. These results were worse than our results (median OS of 26.3 months), probably due to the reduced dose of SBRT and lower potency of induction chemotherapy. This suggestion is supported by a previous study (29) in which a combination of modified FOLFIRINOX and a higher SBRT dose (≥ 40 Gy in five fractions) reported results similar to ours (median OS of 24 months). Conversely, a small prospective trial (LAPC-1 trial) (30, 31) reported an OS of 18 months in 39 patients treated with induction FOLFIRINOX followed by SBRT (40 Gy in five fractions), which was worse than the OS (26 months) we identified.

Not all patients in the present study could undergo resection despite prior induction FOLFIRINOX. However, after additional SBRT, nine patients (18%) could undergo curative resection (R0 resection in eight and N0 in seven); this finding was similar to that shown in other studies (27, 28, 30, 31). However, results of the present study cannot be explained solely based on SBRT because of selection bias due to the retrospective nature of the study. Nevertheless, considering that 18% of the patients who were unsuitable candidates for surgery after sufficient induction chemotherapy (median eight cycles of FOLFIRINOX) were able to undergo resection after continuing FOLFIRINOX with simultaneous SBRT, SBRT may arguably play a role in these patients. Recently, in a phase 2 randomized clinical trial (35), neoadjuvant FOLFIRINOX was used in patients with borderline resectable PC with or without hypofractionated radiation therapy. That trial showed that additional hypofractionated radiation therapy did not improve the 18-month OS and R0 resection rates. However, 12.5% of the patients in the study received a lower radiation dose (hypofractionated image-guided radiotherapy: 25 Gy in five fractions), which could have influenced the outcomes, since a higher radiation dose was associated with better outcomes in ours and other studies (29, 36).

TABLE 3 Pattern of disease progression.

Category	No. of patients (%)
Disease progression	34 (68)
Locoregional progression only	9
Distant progression	23
Liver	12
Peritoneal seeding	7
Lung	2
Distant lymph node	1
Multiple sites	3
No disease progression [a]	16 (32)

Data are presented as the no. of patients/total no. (n%). [a]Three patients who died without radiological evidence of disease progression due to liver abscess, gastric variceal bleeding, and bowel perforation were included.

SBRT-related AEs in the present study were well tolerated and managed, which was similar to that in previous studies (24–31). Furthermore, these AEs were less frequent than those associated with conventional EBRT (7–9). It is well known that GI bleeding is a severe late complication in patients and is more often observed in those who receive single-fraction SBRT compared with that in those who receive multi-fraction SBRT (37). In the present study, in which all patients received five fractions, three cases of grade 3 GI bleeding at the pseudoaneurysm site were noted and were well controlled by transarterial embolization, which was similar to the results of other studies (29, 30). One patient who died due to bowel perforation occurred sequentially superior mesenteric artery and superior mesenteric vein thrombosis, bowel infarction, and bowel perforation within five months after surgery. SBRT could contribute to the increased difficulty of surgery that resulted in severe surgical complications. Still, it is difficult to determine a direct causality and cannot be explained solely based on SBRT.

A higher total dose of SBRT (35 Gy) showed a trend toward better OS than did a dose of 30 Gy or less. This finding was similar to that in other studies (29, 36). Moreover, 25% (8 of 32) of the patients treated with a higher total dose of SBRT underwent surgery subsequently, compared with 5% (1 of 18) treated with a lower total dose of SBRT. However, the two groups were not significantly different in terms of radiation-related AEs. Taken together, these findings suggest that when additional SBRT is necessary and feasible for LAPC, a higher total dose of SBRT may be recommended, considering its efficacy and safety. More prospective studies are needed to determine the appropriate SBRT protocols and whether they have clinical benefits.

This study has some limitations. First, this was a retrospective study conducted in a single tertiary center, which may have resulted in selective bias. However, the enrolled

TABLE 4 Radiation treatment-related acute and late adverse events.

Category	Grade 1	Grade 2	Grade 3
Acute adverse effects			
Anorexia	2	1	0
Fatigue	2	1	0
Nausea	2	1	0
Vomiting	1	0	0
Diarrhea	1	4	0
Late adverse effects			
Gastritis	0	2	0
GI ulcer	0	4	0
GI bleeding	0	1[a]	3[b]

Adverse events are assessed using the National Cancer Institute Common Terminology for Adverse Events [version 5.0].; Acute adverse events denote adverse events within 90 days from radiation therapy; Late adverse events denote adverse events after 90 days from radiation therapy.; [a]Gastric ulcer bleeding (1 in ≥ 35 Gy), [b]Three pseudoaneurysm site bleeding (2 in ≥ 35 Gy, 1 in < 35 Gy).

patients had a uniform disease status and remained unsuitable candidates for resection after induction FOLFIRINOX and received radiation therapy using a uniform SBRT protocol, which provided informative results that were easy to apply in clinical practice. Second, we did not use fiducial marker placement to target tumors accurately during SBRT because this product was unavailable for clinical practice in Korea. However, SBRT without fiducial markers in our study was

TABLE 5 Univariate and multivariate analyses of the overall survival at diagnosis.

Variables	No. of patients	OS (median, months)	95% CI	Univariate analysis			Multivariate analysis		
				HR	95% CI	*p* value	HR	95% CI	*p* value
Total patients	50	26.4	22.4–30.3						
Age (years)									
< 65	29	26.8	17.2–36.5						
≥ 65	21	25.6	21.0–30.2	1.044	0.568–1.918	*0.891*			
Sex									
Male	22	27.4	18.9–35.9						
Female	28	25.6	22.2–29.0	1.269	0.663–2.430	*0.472*			
Primary site									
Body and Tail	20	27.6	25.6–29.6						
Head and Neck	30	23.1	15.2–31.0	1.554	0.806–2.996	*0.189*			
CA 19-9 (Pre-SBRT)									
< 48.5 U/mL	25	26.8	24.6–29.1						
≥ 48.5 U/mL	25	24.1	18.9–29.2	1.187	0.626–2.253	*0.599*			
Tumor size (cm) (Pre-SBRT)									
< 2.9	25	27.0	24.5–29.6						
≥ 2.9	25	21.7	15.1–28.2	1.722	0.914–3.244	*0.093*	1.723	0.914–3.249	*0.093*
Induction FOLFIRINOX cycles									
≥ 8	34	25.6	22.0–29.2						
< 8	16	26.8	19.6–34.1	0.950	0.485–1.859	*0.880*			
Best response									
PR	11	25.6	13.9–37.3						
SD	39	26.4	21.7–31.0	1.007	0.693–1.465	*0.969*			
Total SBRT dose									
≥ 35 Gy	32	27.0	20.7–33.4						
< 35 Gy	18	24.1	19.3–28.9	2.017	1.043–3.901	*0.037*	2.024	1.042–3.930	*0.037*

OS, overall survival; CI, coefficient index; HR, hazard ratio; SBRT, stereotactic body radiation therapy; CA 19-9, carbohydrate antigen 19-9; PR, partial response; SD, stable disease; Gy, gray.

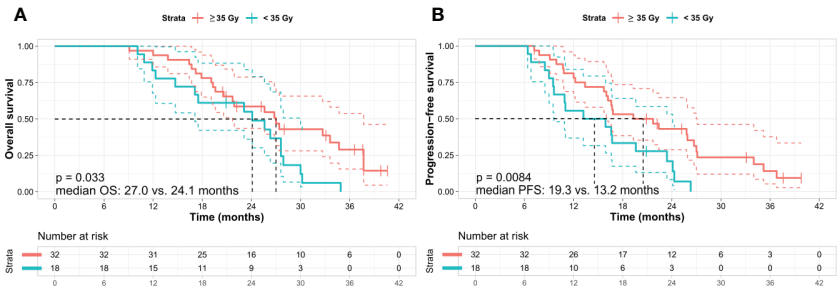

FIGURE 3
Kaplan–Meier survival curves according to the total dose of SBRT. **(A)** Overall survival and **(B)** progression-free survival. Kaplan–Meier analysis shows that the patients treated with a high total dose of SBRT (≥ 35 Gy in five fractions) exhibit better OS and PFS than those who received a low total dose of SBRT (< 35 Gy in five fractions). Log-rank test *p*-values were **(A)** 0.033 and **(B)** 0.008 between the two subgroups, respectively. OS, overall survival; PFS, progression-free survival; Gy, gray.

TABLE 6 Univariate and multivariate analyses of the progression-free survival at diagnosis.

Variables	No. of patients	PFS (median, months)	95% CI (months)	Univariate analysis			Multivariate analysis		
				HR	95% CI	*p* value	HR	95% CI	*p* value
Total patients	50	16.7	13.0–20.3						
Age (years)									
< 65	29	16.7	11.9–21.6						
≥ 65	21	16.6	15.3–18.0	1.044	0.568–1.918	*0.891*			
Sex									
Female	28	16.7	8.9–24.6						
Male	22	16.6	15.4–17.7	1.227	0.667–2.257	*0.510*			
Primary site									
Body and Tail	20	16.6	16.4–16.8						
Head and Neck	30	16.7	7.2–26.2	0.986	0.532–1.857	*0.986*			
CA 19-9 (Pre-SBRT)									
< 48.5 U/mL	25	19.3	8.2–30.4						
≥ 48.5 U/mL	25	16.6	15.4–17.7	1.330	0.724–2.442	*0.358*			
Tumor size (Pre-SBRT)									
< 2.9 cm	25	23.4	11.7–35.1						
≥ 2.9 cm	25	15.9	7.9–24.0	1.860	1.012–3.418	*0.046*	1.853	1.005–3.416	*0.048*
Induction FOLFIRINOX cycles									
≥ 8	34	16.7	12.7–20.6						
< 8	16	16.0	14.0–17.9	1.124	0.597–2.117	*0.716*			
Best response									
PR	11	16.7	13.0–20.4						
SD	39	16.7	12.4–20.9	0.936	0.647–1.354	*0.725*			
Total SBRT dose									
≥ 35 Gy	32	19.3	11.8–26.8						
< 35 Gy	18	13.2	3.0–23.4	2.369	1.226–4.580	*0.010*	2.364	1.218–4.588	*0.011*

PFS, progression free survival; CI, coefficient index; HR, hazard ratio; SBRT, stereotactic body radiation therapy; CA 19-9, carbohydrate antigen 19-9; PR, partial response; SD, stable disease; Gy, gray.

associated with manageable AEs compared with those associated with SBRT in other studies that used fiducial markers (38). Third, the interval and total cycles of FOLFIRINOX were not standardized because of this study's retrospective design. FOLFIRINOX was continued until sequential SBRT was initiated, which was decided in a multidisciplinary discussion. However, except for one extreme case (28 cycles), the FOLFIRINOX cycles for the remaining patients ranged from 3 to 16. Moreover, the median cycle of FOLFIRINOX was similar to that used in other studies (30, 31).

The strategy of adding SBRT to LAPC patients who had received FOLFIRINOX was not standardized. LAPC-1 trial (30, 31) showed the advantage of SBRT followed by induction FOLFIRINOX in improving survival in patients initially inoperable at diagnosis. A large-sample size study (Gemenetzis et al.) (32) revealed that additional SBRT would contribute to an increased resection rate in patients with LAPC suitable for surgical exploration after FOLFIRINOX. However, there has yet to be a consensus on the role of SBRT in which clinical situations SBRT may be beneficial in LAPC patients who have received induction chemotherapy. Our study enrolled patients who remained unresectable (with reduced CA 19-9 but no significant change in tumor size) despite sufficient chemotherapy. Furthermore, among nine patients who underwent resection in our study, five patients received induction FOLFRINOX for more than eight cycles (range 10-15 cycles), unlike the LAPC-1 trial (induction FOLFIRINOX up to 8 cycles). SBRT may be helpful when curative resection is not possible despite sufficient induction chemotherapy in actual clinical practice. Our results may be valuable when making a decision (adding SBRT vs. continuing FOLFIRINOX) in the patients who remained unresectable despite sufficient chemotherapy. Furthermore, our study aimed to identify clinical factors influencing a better prognosis for these strategies and revealed that a higher total dose of SBRT could result in a better resection rate and OS.

In conclusion, induction FOLFIRINOX followed by SBRT in LAPC results in favorable OS and PFS with manageable AEs related to SBRT. A high total dose of SBRT (≥ 35 Gy in five fractions) can improve survival with a higher resection rate.

Data availability statement

The raw data supporting the conclusions of this article will be made available by the authors, without undue reservation.

Ethics statement

The studies involving human participants were reviewed and approved by the institutional review board of Seoul National University Bundang Hospital. Written informed consent for participation was not required for this study in accordance with the national legislation and the institutional requirements.

Author contributions

JJ, CS, and J-HH conceived and designed research. JJ, IJ, JA, BK, and KJ collected and assembled the data. JJ and J-HH performed or supervised analyses. JJ, J-CL, JK, CS, and J-HH interpreted the results. JJ and J-HH performed statistical expertise. JJ, CS, and J-HH wrote sections of the initial draft. J-CL and JK provided substantive suggestions for revision. J-CL, JK, CS, J-HH provided the provision of study materials or patients. All authors contributed to the article and approved the submitted version.

Conflict of interest

The authors declare that the research was conducted in the absence of any commercial or financial relationships that could be construed as a potential conflict of interest.

Publisher's note

All claims expressed in this article are solely those of the authors and do not necessarily represent those of their affiliated organizations, or those of the publisher, the editors and the reviewers. Any product that may be evaluated in this article, or claim that may be made by its manufacturer, is not guaranteed or endorsed by the publisher.

Supplementary material

The Supplementary Material for this article can be found online at: https://www.frontiersin.org/articles/10.3389/fonc.2022.1050070/full#supplementary-material

References

1. Siegel RL, Miller KD, Fuchs HE, Jemal A. Cancer statistics, 2022. *CA Cancer J Clin* (2022) 72(1):7–33. doi: 10.3322/caac.21708

2. Rahib L, Wehner MR, Matrisian LM, Nead KT. Estimated projection of US cancer incidence and death to 2040. *JAMA Netw Open* (2021) 4(4):e214708. doi: 10.1001/jamanetworkopen.2021.4708

3. Park W, Chawla A, O'Reilly EM. Pancreatic cancer: A review. *JAMA* (2021) 326(9):851–62. doi: 10.1001/jama.2021.13027

4. Neoptolemos JP, Stocken DD, Friess H, Bassi C, Dunn JA, Hickey H, et al. A randomized trial of chemoradiotherapy and chemotherapy after resection of pancreatic cancer. *N Engl J Med* (2004) 350(12):1200–10. doi: 10.1056/NEJMoa032295

5. Tempero MA, Malafa MP, Behrman SW, Benson AB 3rd, Casper ES, Chiorean EG, et al. Pancreatic adenocarcinoma, version 2.2014: Featured updates to the NCCN guidelines. *J Natl Compr Canc Netw* (2014) 12(8):1083–93. doi: 10.6004/jnccn.2014.0106

6. de Geus SWL, Eskander MF, Kasumova GG, Ng SC, Kent TS, Mancias JD, et al. Stereotactic body radiotherapy for unresected pancreatic cancer: A nationwide review. *Cancer* (2017) 123(21):4158–67. doi: 10.1002/cncr.30856

7. Chauffert B, Mornex F, Bonnetain F, Rougier P, Mariette C, Bouche O, et al. Phase III trial comparing intensive induction chemoradiotherapy (60 gy, infusional 5-FU and intermittent cisplatin) followed by maintenance gemcitabine with gemcitabine alone for locally advanced unresectable pancreatic cancer. definitive results of the 2000-01 FFCD/SFRO study. *Ann Oncol* (2008) 19(9):1592–9. doi: 10.1093/annonc/mdn281

8. Hammel P, Huguet F, van Laethem J-L, Goldstein D, Glimelius B, Artru P, et al. Effect of chemoradiotherapy vs chemotherapy on survival in patients with locally advanced pancreatic cancer controlled after 4 months of gemcitabine with or without erlotinib: The LAP07 randomized clinical trial. *JAMA* (2016) 315 (17):1844–53. doi: 10.1001/jama.2016.4324

9. Sultana A, Smith CT, Cunningham D, Starling N, Tait D, Neoptolemos JP, et al. Systemic review, including meta-analyses, on the management of locally advanced pancreatic cancer using Radiation/Combined modality therapy. *Br J Cancer* (2007) 96(8):1183–90. doi: 10.1038/sj.bjc.6603719

10. Conroy T, Desseigne F, Ychou M, Bouche O, Guimbaud R, Becouarn Y, et al. FOLFIRINOX versus gemcitabine for metastatic pancreatic cancer. *N Engl J Med* (2011) 364(19):1817–25. doi: 10.1056/NEJMoa1011923

11. De Dosso S, Siebenhuner AR, Winder T, Meisel A, Fritsch R, Astaras C, et al. Treatment landscape of metastatic pancreatic cancer. *Cancer Treat Rev* (2021) 96:102180. doi: 10.1016/j.ctrv.2021.102180

12. Matsumoto I, Kamei K, Omae K, Suzuki S, Matsuoka H, Minzuno N, et al. FOLFIRINOX for locally advanced pancreatic cancer: Results and prognostic factors of subset analysis from a nation-wide multicenter observational study in Japan. *Pancreatology* (2019) 19(2):296–301. doi: 10.1016/j.pan.2019.01.001

13. Suker M, Beumer BR, Sadot E, Marthey L, Faris JE, Mellon EA, et al. FOLFIRINOX for locally advanced pancreatic cancer: a systemic review and patient-level meta-analysis. *Lancet Oncol* (2016) 17(6):801–10. doi: 10.1016/S1470-2045(16)00172-8

14. National Comprehensive Cancer Network. *Pancreatic adenocarcinoma. version 1.2022* (2022). Available at: https://www.nccn.org/professionals/physician_gls/pdf/pancreatic_blocks.pdf (Accessed 06 July 2022).

15. Ushida Y, Inoue Y, Oba A, Mie T, Ito H, Ono Y, et al. Optimizing indications for conversion surgery based on analysis of 454 consecutive Japanese cases with unresectable pancreatic cancer who received modified FOLFIRINOX or gemcitabine plus nab-paclitaxel: A single-center retrospective study. *Ann Surg Oncol* (2022) 29(8):5038–50. doi: 10.1245/s10434-022-11503-6

16. Yoo C, Hwang I, Song TJ, Lee SS, Jeong JH, Park DH, et al. FOLFIRINOX in borderline resectable and locally advanced unresectable pancreatic adenocarcinoma. *Ther Adv Med Oncol* (2020) 16(12):1758835920953294. doi: 10.1177/1758835920953294

17. Takano N, Yamada S, Sonohara F, Inokawa Y, Takami H, Hayashi M, et al. The impact of early tumor shrinkage on conversion surgery and the survival in patients with unresectable locally advanced pancreatic cancer. *Surg Today* (2021) 51(7):1099–107. doi: 10.1007/s00595-020-02220-2

18. Nitsche U, Wenzel P, Siveke JT, Braren R, Holzapfel K, Schlitter AM, et al. Resectability after first-line FOLFIRINOX in initially unresectable locally advanced pancreatic cancer: A single-center experience. *Ann Surg Oncol* (2015) 22 Suppl 3: S1212–20. doi: 10.1245/s10434-015-4851-2

19. Maxwell JE, Katz MHG. Radiotherapy for resectable and borderline resectable pancreas cancer: When and why? *J Gastrointest Surg* (2021) 25 (3):843–8. doi: 10.1007/s11605-020-04838-6

20. Hahadevan A, Jain S, Goldstein M, Miksad R, Pleskow D, Sawhney M, et al. Stereotactic body radiotherapy and gemcitabine for locally advanced pancreatic cancer. *Int J Radiat Oncol Biol Phys* (2010) 78(3):735–42. doi: 10.1016/j.ijrobp.2009.08.046

21. Sutera PA, Bernard ME, Gill BS, Harper KK, Quan K, Bahary N, et al. One- vs. three-fraction pancreatic sterotactic body radiation therapy for pancreatic carcinoma: Single institution retrospective review. *Front Oncol* (2017) 14(7):272. doi: 10.3389/fonc.2017.00272

22. Swaminath A, Chu W. Stereotactic body radiotherapy for the treatment of medically inoperable primary renal cell carcinoma: Current evidence and future directions. *Can Urol Asso J* (2015) 9(7-8):275–80. doi: 10.5489/cuaj.2900

23. Qiu B, Aili A, Xue L, Jiang P, Wang J. Advances in radiobiology of stereotactic ablative radiotherapy. *Front Oncol* (2020) 7(10):1165. doi: 10.3389/fonc.2020.01165

24. Koong AC, Le QT, Ho A, Fong B, Fisher G, Cho C, et al. Phase I study of stereotactic radiosurgery in patients with locally advanced pancreatic cancer. *Int J Radiat Oncol Biol Phys* (2004) 58(4):1017–21. doi: 10.1016/j.ijrobp.2003.11.004

25. Gurka MK, Collins SP, Slack R, Tse G, Charabaty A, Ley L, et al. Stereotactic body radiation therapy with concurrent full-dose gemcitabine for locally advanced pancreatic cancer: A pilot trial demonstrating safety. *Radiat Oncol* (2013) 1(8):44. doi: 10.1186/1748-717X-8-44

26. Jung J, Yoon SM, Park JH, Seo DW, Lee SS, Kim MH, et al. Stereotactic body radiation therapy for locally advanced pancreatic cancer. *PloS One* (2019) 14(4): e0214970. doi: 10.1371/journal.pone.0214970

27. Mellon EA, Hoffe SE, Springett GM, Frakes JM, Strom TJ, Hodul PJ, et al. Long-term outcomes of induction chemotherapy and neoadjuvant stereotatic body radiotherapy for borderline resectable and locally advanced pancreatic adenocarcinoma. *Acta Oncol* (2015) 54:979–85. doi: 10.3109/0284186X.2015.1004367

28. Moningi S, Dholakia AS, Raman SP, Blackford A, Cameron JL, Le DT, et al. The role of stereotactic body radiation therapy for pancreatic cancer: A single-institution experience. *Ann Surg Oncol* (2015) 22(7):2352–8. doi: 10.1245/s10434-014-4274-5

29. Toesca DAS, Ahmed F, Kashyap M, Baclay JRM, von Eyben R, Pollom EL, et al. Intensified systemic therapy and stereotactic ablative radiotherapy dose for patients with unresectable pancreatic adenocarcinoma. *Radiother Oncol* (2020) 152:63–9. doi: 10.1016/j.radonc.2020.07.053

30. Suker M, Nuyttens JJ, Eskens FALM, Haberkorn BCM, Coene P-PLO, van der Harst E, et al. Efficacy and feasibility of stereotactic radiotherapy after FOLFIRINOX in patients with locally advanced pancreatic cancer (LAPC-1 trial). *EClinicalMedicine* (2019) 19(17):100200. doi: 10.1016/j.eclinm.2019.10.013

31. Teriaca MA, Loi M, Suker M, Eskens FALM, van Eijck CHJ, Nuyttens JJ. A phase II study of stereotactic radiotherapy after FOLFIRINOX for locally advanced pancreatic cancer (LAPC-1 trial): Long-term outcome. *Radiother Oncol* (2021) 155:232–6. doi: 10.1016/j.radonc.2020.11.006

32. Gemenetzis G, Groot VP, Blair AB, Laheru DA, Zheng L, Narang AK, et al. Survival in locally advanced pancreatic cancer after neoadjuvant therapy and surgical resection. *Ann Surg* (2019) 270(2):340–7. doi: 10.1097/SLA.0000000000002753

33. Klaiber U, Hackert T. Conversion surgery for pancreatic cancer-the impact of neoadjuvant treatment. *Front Oncol* (2020) 14(9):1501. doi: 10.3389/fonc.2019.01501

34. Myrehaug S, Sahgal A, Russo SM, Lo SS, Rosati LM, Mayr NA, et al. Stereotactic body radiotherapy for pancreatic cancer: Recent progress and future directions. *Expert Rev Anticancer Ther* (2016) 16(5):523–30. doi: 10.1586/14737140.2016.1168698

35. Katz MHG, Shi Q, Meyers J, Herman JM, Chuong M, Wolpin BM, et al. Efficacy of preoperative mFOLFIRINOX vs mFOLFIRINOX plus hypofractionated radiotherapy for borderline resectable adenocaricnoma of the pancreas: The A021501 phase 2 randomized clinical trial. *JAMA Oncol* (2022) 8(9):1263–70. doi: 10.1001/jamaconcol.2022.2319

36. Arcelli A, Guido A, Buwenge M, Simoni N, Mazzarotto R, Macchia G, et al. Higher biologically effective dose predicts survival in SBRT of pancreatic cancer: A multicentric analysis (PAULA-1). *Anticancer Res* (2020) 40(1):465–72. doi: 10.21873/anticanres.13975

37. Simoni N, Rossi G, Cellini F, Vitolo V, Orlandi VV, Valentini V, et al. Ablative radiotherapy (ART) for locally advanced pancreatic cancer (LAPC): Toward a new paradigm? *Life (Basel)* (2022) 12(4):465. doi: 10.3390/life12040465

38. Moningi S, Jaoude JA, Kouzy R, Lin D, Nguyen ND, Garcia CJG, et al. Impact of fiducial marker placement before stereotactic body radiation therapy on clinical outcomes in patients with pancreatic cancer. *Adv Radiat Oncol* (2020) 6 (2):100621. doi: 10.1016/j.adro.2020.11.006

frontiers | Frontiers in Oncology

TYPE Original Research
PUBLISHED 24 January 2023
DOI 10.3389/fonc.2022.983984

OPEN ACCESS

EDITED BY
Antonio Pontoriero,
University of Messina, Italy

REVIEWED BY
Kengo Ito,
Tohoku Medical and Pharmaceutical University, Japan
Silvana Parisi,
Università degli Studi di Messina, Italy

*CORRESPONDENCE
Claudio Fiorino
fiorino.claudio@hsr.it

SPECIALTY SECTION
This article was submitted to Radiation Oncology, a section of the journal Frontiers in Oncology

RECEIVED 01 July 2022
ACCEPTED 19 December 2022
PUBLISHED 24 January 2023

CITATION
Broggi S, Passoni P, Tiberio P, Cicchetti A, Cattaneo GM, Longobardi B, Mori M, Reni M, Slim N, Del Vecchio A, Di Muzio NG and Fiorino C (2023) Stomach and duodenum dose–volume constraints for locally advanced pancreatic cancer patients treated in 15 fractions in combination with chemotherapy. *Front. Oncol.* 12:983984. doi: 10.3389/fonc.2022.983984

Stomach and duodenum dose–volume constraints for locally advanced pancreatic cancer patients treated in 15 fractions in combination with chemotherapy

Sara Broggi[1], Paolo Passoni[2], Paolo Tiberio[1], Alessandro Cicchetti[1,3], Giovanni Mauro Cattaneo[1], Barbara Longobardi[1], Martina Mori[1], Michele Reni[4,5], Najla Slim[2], Antonella Del Vecchio[1], Nadia G. Di Muzio[2,5] and Claudio Fiorino[1]*

[1]Medical Physics, San Raffaele Scientific Institute, Milano, Italy, [2]Radiotherapy, San Raffaele Scientific Institute, Milano, Italy, [3]Unit of Data Science, Department of Epidemiology and Data Science, Fondazione IRCCS Istituto Nazionale dei Tumori, Milan, Italy, [4]Oncology, San Raffaele Scientific Institute, Milano, Italy, [5]Vita-Salute San Raffaele University, Milano, Italy

Purpose: To assess dosimetry predictors of gastric and duodenal toxicities for locally advanced pancreatic cancer (LAPC) patients treated with chemo-radiotherapy in 15 fractions.

Methods: Data from 204 LAPC patients treated with induction+concurrent chemotherapy and radiotherapy (44.25 Gy in 15 fractions) were available. Forty-three patients received a simultaneous integrated boost of 48–58 Gy. Gastric/duodenal Common Terminology Criteria for Adverse Events v. 5 (CTCAEv5) Grade ≥2 toxicities were analyzed. Absolute/% duodenal and stomach dose–volume histograms (DVHs) of patients with/without toxicities were compared: the most predictive DVH points were identified, and their association with toxicity was tested in univariate and multivariate logistic regressions together with near-maximum dose ($D_{0.03}$) and selected clinical variables.

Results: Toxicity occurred in 18 patients: 3 duodenal (ulcer and duodenitis) and 10 gastric (ulcer and stomatitis); 5/18 experienced both. At univariate analysis, V44cc (duodenum: p = 0.02, OR = 1.07; stomach: p = 0.01, OR = 1.12) and $D_{0.03}$ (p = 0.07, OR = 1.19; p = 0.008, OR = 1.12) were found to be the most predictive parameters. Stomach/duodenum V44Gy and stomach $D_{0.03}$ were confirmed at multivariate analysis and found to be sufficiently robust at internal, bootstrap-based validation; the results regarding duodenum $D_{0.03}$ were less

robust. No clinical variables or %DVH was significantly associated with toxicity. The best duodenum cutoff values were V44Gy < 9.1 cc (and $D_{0.03}$ < 47.6 Gy); concerning the stomach, they were V44Gy < 2 cc and $D_{0.03}$ < 45 Gy. The identified predictors showed a high negative predictive value (>94%).

Conclusion: In a large cohort treated with hypofractionated radiotherapy for LAPC, the risk of duodenal/gastric toxicities was associated with duodenum/stomach DVH. Constraining duodenum V44Gy < 9.1 cc, stomach V44Gy < 2 cc, and stomach $D_{0.03}$ < 45 Gy should keep the toxicity rate at approximately or below 5%. The association with duodenum $D_{0.03}$ was not sufficiently robust due to the limited number of events, although results suggest that a limit of 45–46 Gy should be safe.

KEYWORDS

pancreatic cancer, radiotherapy, gastric toxicity, duodenum, dose-volume effects

1 Introduction

Pancreatic cancer is one of the leading causes of cancer-related death in Europe and North America (1). Most patients are still unresectable at diagnosis, with the large majority presenting at locally advanced stage or metastatic (2, 3). Despite some advancements, the prognosis of locally advanced pancreatic cancer (LAPC) remains poor, with median overall survival around approximately 12–15 months (2–7). A major cause for this unsatisfactory result lies in the prevalent metastatic progression; however, the role of improving local control through local therapy intensification has been underlined suggesting the exploration of "safe" ways to escalate the dose to the tumor (8–11). There is, in fact, some mounting evidence that a fraction not negligible of patients could benefit in terms of overall survival from improved local control, although this is not yet precisely quantified (9–14).

The technological developments in radiotherapy imaging and precision delivery (15) pushed researchers in investigating dose-escalated protocols, mostly using image-guided radiation therapy (IGRT) aiming to reduce planning target volumes (PTVs) around more precisely defined target volumes (clinical target volume (CTV) and internal target volume (ITV)). A relevant issue concerns the proximity of organs at risk (OARs), primarily the stomach and duodenum, whose sparing is crucial to avoid severe toxicities. The way these OARs are spared heavily influences the ability to deliver sufficiently high doses to the tumor. The small and uncertain benefit of stereotactic body radiotherapy (SBRT) delivered in 1–5 fractions (14, 16–21) is likely to depend on this issue, despite the use of advanced technology to reduce the impact of inter- and intra-fraction motion (15, 22–25); new developments in MRI-Linacs (23) promise to improve the picture, but the experience is still too early, and the spread of these machines is not expected to move rapidly.

In the last years, the interest toward moderate hypofractionation, also combined with concomitant dose escalation on portions of PTV (8, 9, 11, 12, 22), is increasing, suggesting that schedules with a number of fractions equal to 15 or around this value may represent an optimal window to deliver sufficiently high dose by keeping low the rate of gastric/duodenal toxicities (9, 12, 26). Moreover, the relatively large number of fractions intrinsically reduces the impact of unusual anatomy deformation in single fractions, compared to SBRT (25). However, there is still an evident lack of knowledge of dose–volume effects for these organs under these fractionations, with few published studies regarding relatively small populations (22, 26–29). This lack may reflect a limitation in exploiting the potential of dose escalation, due to a likely "over-safe" approach in sparing OARs. Our institute was among the first ones to adopt a moderate hypofractionation approach using 15 fractions since 2004, including concomitant dose escalation in sub-volumes within a Phase I trial (8).

In a pilot investigation on the first 61 patients, Cattaneo et al. (27) found a significant association between stomach/duodenum dose–volume histograms (DVHs) and gastric/duodenal toxicities.

The aim of the current study was to update the previous results on a much larger population of 204 LAPC patients treated in a quite homogeneous way, delivering 44.25 Gy in 15 fractions using helical tomotherapy (HT); based on these results, rational constraints were derived even in the light of a renewed interest toward the promising field of dose-escalated radiotherapy delivered in 15 fractions (30).

2 Materials and methods

2.1 Eligibility criteria

The current analysis refers to patients with histologically confirmed LAPC treated according to an institutional protocol (see below), from 2004 to 2019 at San Raffaele Institute in Milan. Patients excluded from surgery because judged unresectable were submitted to induction chemotherapy; schedules changed over time, consisting in most patients of four to six cycles of four-drug combinations: cisplatin, epirubicin, 5-fluorouracil or capecitabine, and gemcitabine (acronyms PEFG and PEXG). After completing induction chemotherapy, patients were restaged and discussed at multidisciplinary team meetings. Considered for radio-chemotherapy (RCT) were 1) patients in stage III still deemed not resectable due to vascular encasement, including patients with local progression after chemotherapy or with increased CA 19.9 compared to the nadir value reached during chemotherapy, and 2) patients in stage IV with complete response of metastases stable over a period of at least 4 months after the end of induction chemotherapy. Among those treated with RCT, the criteria for inclusion in the current analysis were as follows: a) histological diagnosis of pancreatic adenocarcinoma, b) radiotherapy delivered with HT, c) Karnofsky performance status scale >70, d) age > 18 years, and e) availability of complete treatment planning data. In total, the resulting cohort included 204 patients.

2.2 Treatment characteristics

RCT was generally planned 2–4 weeks after the completion of induction chemotherapy. It consisted of the delivery of 44.25 Gy in 15 fractions, concomitant to capecitabine, 1,250 mg/day weekend included, for 3 weeks. Details of radiotherapy procedures are reported elsewhere (8, 27, 31). In short, patients were immobilized and underwent simulation contrast-enhanced CT and FDG-PET/CT. Primary tumors and enlarged lymph nodes visible on the contrast-enhanced CT images or 4D-CT images were defined as gross tumor volume (GTV). When a standard CT was performed, ITV was defined as GTV with a margin of 0.5 cm in anterior–posterior and left directions, and of 1.0 cm in cranial–caudal direction. In the case of 4D-CT, GTV was contoured on at least four phases, and an ITV was obtained by the union of four GTVs. The PET-positive volume and the biological target volume (BTV), when available, were merged with ITV to create the ITV/BTV. A further margin of 0.5 cm in all directions was added to ITV/BTV to create PTV. The stomach, duodenum, liver, kidneys, and spinal cord were contoured as OARs. Constraints for the stomach were V40 < 18 cc and V30 < 23 cc; constraints for duodenum were V45 < 1 cc, V40 < 15 cc, and V30 < 35 cc. The dose prescription to the overlap between PTV and the stomach/duodenum was 44.25, 43.25, and 42.25 Gy, when the overlap volume was <14, 30, and 50 cc, respectively. In case of overlap >50 cc or dose constraints were not recognized, the dose to the whole PTV was reduced to 40 Gy. All treatment plans were generated using the HT planning system. With regard to PTVs, the goal was to deliver ≥95% of the prescribed dose to ≥95% of the volume while keeping the dose as homogenous as possible. During the optimization process, the planner had to reduce the volume of irradiated stomach+duodenum as much as possible while maintaining tumor coverage as the highest priority.

All treatment plans were generated using tomotherapy inverse planning software, using the same convolution/superposition dose calculation algorithm.

Fifteen patients received an additional boost to a sub-volume PTV2 obtained from the infiltrating vessels with doses ranging from 48 to 58 Gy. Details are described elsewhere (8). In addition, 28 patients with favorable tumor dimensions or tumor anatomic sites with respect to dose constraints received a simultaneous integrated boost of 48 Gy to BTV. Patients with simultaneous integrated boost (SIB) to infiltrating vessels were included in a Phase I trial. The protocol was approved by our Institutional Ethical Committee. Once it was confirmed that the delivery of 44.25 Gy in 15 fractions was feasible, the Phase I protocol was amended, and a subsequent observational perspective trial was approved for the remaining patients; all patients provided written informed consent. For all patients, a megavoltage CT was performed before each fraction and co-registered with the planning CT by means of automatic matching on bony anatomy, followed by manual refinement based on daily patient anatomy. The physician further checked and corrected the patient setup by means of direct visualization of other anatomical details. Of note, patients were carefully instructed to have empty stomach both at planning CT and during treatment delivery.

2.3 Toxicity scoring, end-point definition, and DVH recovery

Patients were examined once a week during treatment by radiation and medical oncologists. Adverse events were classified as acute or late toxicity when taking place during the treatment and within 3 months after RCT completion or 3 months after, respectively. Toxicity was scored by the National Cancer Institute Common Terminology Criteria for Adverse Events (CTCAE). For the current study, gastric and duodenal CTCAEv5 Grade ≥2 toxicities were considered. Due to the limited number of events, acute and late events were considered together. DVHs (absolute and %) of the stomach and duodenum as previously contoured by the treating physician were recovered. Percentage and absolute stomach

10.3389/fonc.2022.983984

and duodenum volumes receiving more than XGy, with X ranging at 1–60 Gy, were extracted with a 1-Gy step.

2.4 Quantifying the relationship between DVH and toxicity

Average absolute/% DVHs of the stomach/duodenum for patients with/without toxicity were compared through a two-sided *t*-test, according to a previously applied approach (32–34): the DVH regions corresponding to the lowest p-values were considered as candidate values to be tested in a logistic regression analysis as potential dosimetry predictors. The best cutoff values discriminating patients with/without toxicity were also assessed by receiver operating characteristic (ROC) curves, according to the DeLong method, using Youden's index (35), aiming to define optimal constraints. Univariable logistic regression (UVA) was performed to assess the correlation between the considered end-points and the selected dosimetric parameters; selected clinical variables were also tested (gender, age, stage (III *vs.* IV), drugs used as induction chemotherapy (one *vs.* multiple drugs), number of induction chemotherapy cycles (≥6 *vs.* <6), Karnofsky performance status, and patient's weight). Variables with p-value <0.1 at UVA and without cross-correlations (Pearson's or Spearman's coefficient, in the range of −0.25 to 0.25) were entered into a backward stepwise multivariable logistic regression (MVA). The goodness of fit was assessed by the Hosmer–Lemeshow test (H&L). Analyses were performed with the MedCalc software (v.19.0.4, MedCalc Software bvba, Ostend, Belgium) and the R software version 3.2.4 (©The R Foundation for Statistical Computing, Vienna, Austria). Due to the limited number of events, an internal validation procedure was performed using a dedicated script in Matlab by repeating the regression fit for the major dosimetry predictors on 500 data sets obtained by bootstrapping the original cohort. Median and inter-quartile ranges of p-values, odd ratios (ORs), and AUC values obtained by the procedure were reported and compared with the results obtained on the original cohort, as a measure of the results' robustness.

3 Results

3.1 Patient characteristics

The main characteristics of patients were summarized in Table 1: 184 patients were in stage III, and 20 were in stage IV. Most patients (n = 177) received a combination of at least two drugs as induction chemotherapy. The median number of cycles was 6 (range, 2–13), and 108 patients received ≥6 cycles. Most patients (n = 135) were treated with a dose of 44.25 Gy; 26 patients with 40 Gy and 43 patients received a SIB of up to 48–58 Gy. The median follow-up was 18 months, and the median overall survival was 19.5 months (from the start of induction chemotherapy). Eighteen patients (8.8%) had gastric and/or duodenal mucosal damage CTCAEv5 Grade ≥2 toxicities (5 acute and 13 late): 3 patients only duodenal, 10 patients only gastric, and 5 patients both duodenal and gastric damage. Of 18 patients, 10 were treated with SIB. The median time to toxicity was 5 months (range, 1–10) from the end of RCT.

TABLE 1 Main characteristics of considered patients.

All patients: 204	
Age	65 (40–86)
Gender	Male: 92 Female: 112
KPS	90 (70–100)
Stage	III: 184 IV: 20
Weight	66.5 (41–104)
Location of primary tumor	Head (+uncinato): 103 Head/isthmus: 13 Head/body: 10 Isthmus: 10 Body: 30 Body/isthmus: 16 Body/tail: 20 Tail: 2
Induction chemotherapy	One drug: 27 Multiple drugs: 177
Number of chemotherapy cycles	≥6 cycles: 108 <6 cycles: 83
Doses	40 Gy: 26 44.25 Gy: 135 48–58 Gy (infiltrating vessels):15 48–50 Gy (BTV SIB): 28

KPS, Karnofsky Performance Status; BTV, biological target volume; SIB, simultaneous integrated boost.

3.2 Assessing dosimetry predictors

In Figures 1 and 2, the average absolute/percentage DVHs for the duodenum and stomach for patients with and without toxicities were reported. In Figures S1 and S2 (Supplementary Material), the *t*-test graphs for absolute and percentage DVHs were shown. For both duodenum and stomach absolute DVHs, the absolute volumes (in cc) that receive 15 Gy (V15cc) and 44 Gy (V44cc) were selected through a two-sided *t*-test as the most promising discriminating DVH parameters. For percentage DVHs, V20 (%) and V44 (%) were found to be the most discriminating DVH parameters for duodenum; V15 (%), V20 (%), and V44 (%) were found to be the most discriminating DVH parameters for the stomach.

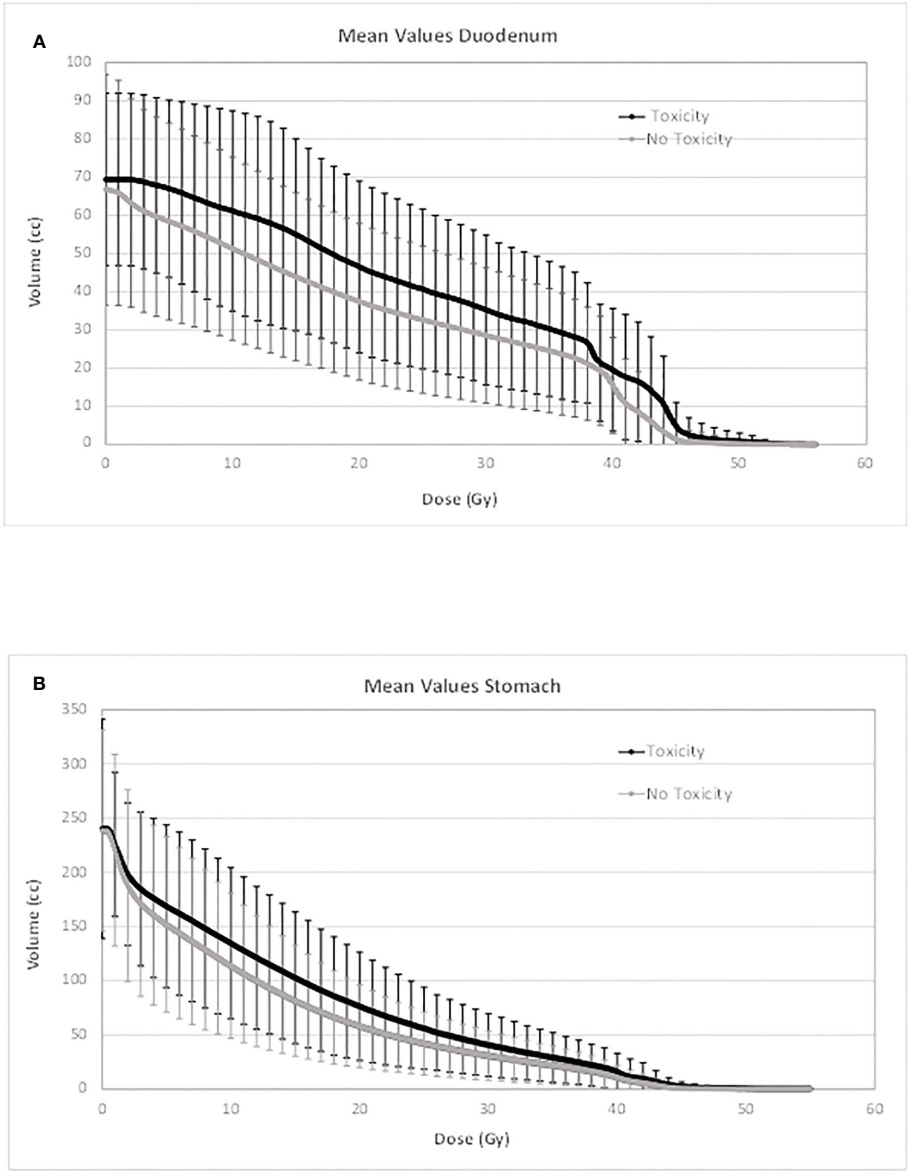

FIGURE 1
Average absolute DVH for duodenum **(A)** and stomach **(B)** for patients with and without toxicities. DVH, dose–volume histogram.

At univariate logistic regression analysis, the previously selected DVH parameters and Dmax ($D_{0.03}$) were tested as potential dosimetry predictors of gastric and duodenal toxicity. Duodenum V44Gy(cc) (p = 0.02; OR = 1.07) was found as the only significative predictive parameter for duodenal toxicity; stomach $D_{0.03}$ (p = 0.008; OR = 1.23) and V44Gy(cc) (p = 0.01; OR = 1.12) were found as the most predictive parameters for gastric toxicity. A borderline significance was found for duodenum $D_{0.03}$ (p = 0.07; OR = 1.19) for duodenal toxicity. None of the percentage dosimetric parameters selected through a two-sided *t*-test were found predictive, neither for duodenal nor gastric toxicity (Table S1, Supplementary Material). Based on a ROC analysis, duodenum V44Gy > 9.1 cc was found to be the best cutoff value for duodenal toxicity with a negative predictive value (NPV) of 97.6%; although near to the significance, $D_{0.03}$ > 47.6 Gy was found as the best cutoff value for duodenal toxicity. For the stomach, $D_{0.03}$ > 45 Gy and V44Gy > 2 cc were found as the best cutoff values for gastric toxicity, with NPVs equal to 95.8% and 95.4%, respectively (Figure S3, Supplementary Material).

The crude rate of duodenal toxicity was 4/176 (2.3%) *vs.* 4/28 (14.3%) (p = 0.012) if duodenum V44Gy <9.1 or ≥9.1 cc, respectively. The crude rate of gastric toxicity was 6/145 (4.1%) *vs.* 9/58 (15.5%) (p = 0.012) if stomach $D_{0.03}$ <45 or

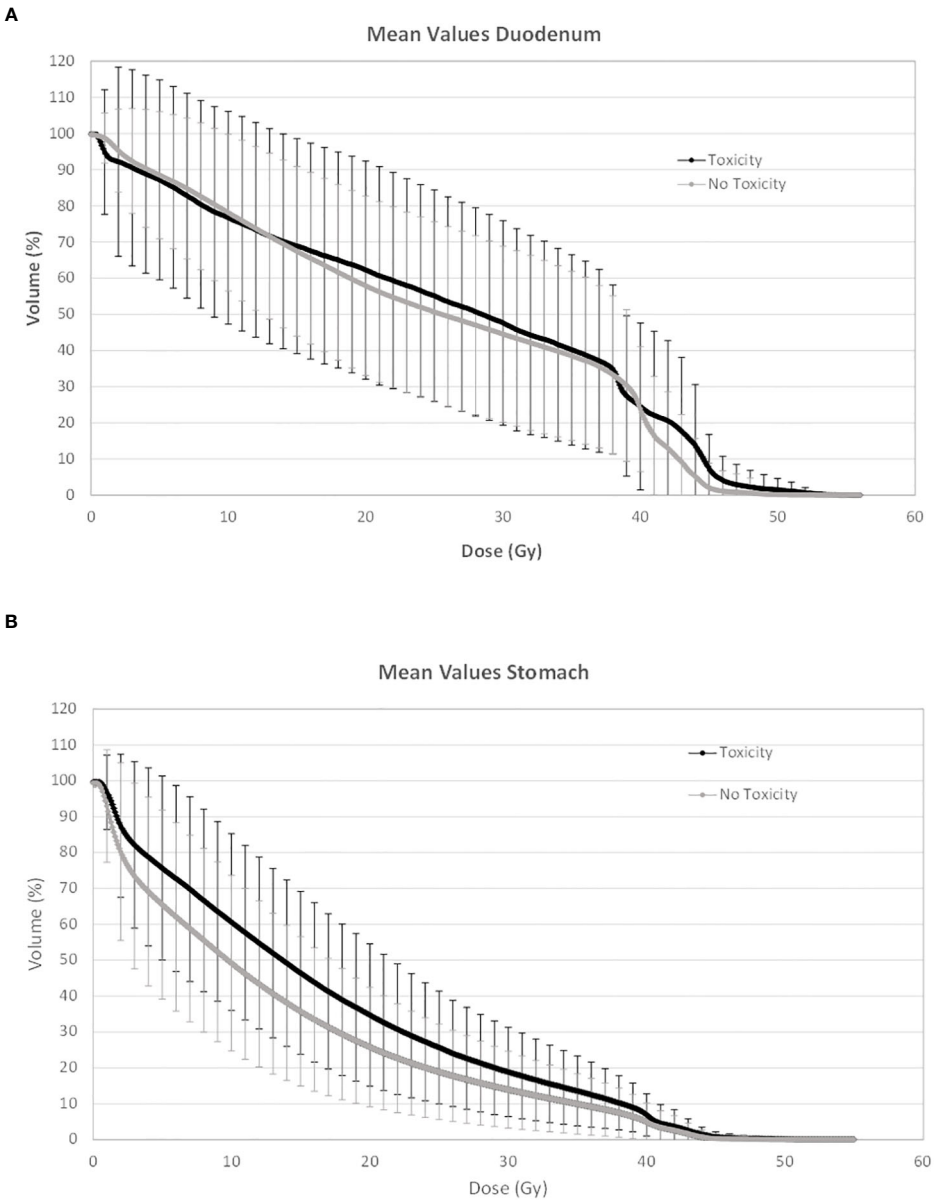

FIGURE 2
Average percentage DVH for duodenum **(A)** and stomach **(B)** for patients with and without toxicities. DVH, dose–volume histogram.

≥45 Gy, and 7/158 (4.4%) *vs.* 8/45 (17.8%) (p = 0.007) if V44Gy <2 or ≥2 cc. Of note, the incidence of Grade ≥2 mucosal damage was 10/43 (23.3%) for patients treated with doses 48–58 Gy *vs.* 8/161 (5.0%) for patients treated with 44.25 Gy or less (p = 0.0002).

The internal validation procedure was applied to V44Gy and $D_{0.03}$ of both the duodenum and stomach, respectively, for duodenal and gastric toxicity end-points. Results, reported in the Supplementary Material Results, confirmed sufficiently high robustness of the found associations, confirming duodenum V44Gy and stomach $D_{0.03}$ as the most robust predictors for duodenal and gastric toxicities, respectively.

3.3 Multivariable analysis

For both duodenal and gastric toxicities, no significant correlations were found with clinical variables at univariable analysis (Table S2, Supplementary Material). In a backward stepwise logistic multivariate analysis, considering the previously selected dosimetry predictors and the clinical variables, only stomach $D_{0.03}$ (Gy) and duodenum V44Gy were confirmed at multivariate analysis for gastric and duodenal toxicities, respectively (H&L > 0.05). In Figures 3 and 4, the risk of duodenal and gastric toxicities against

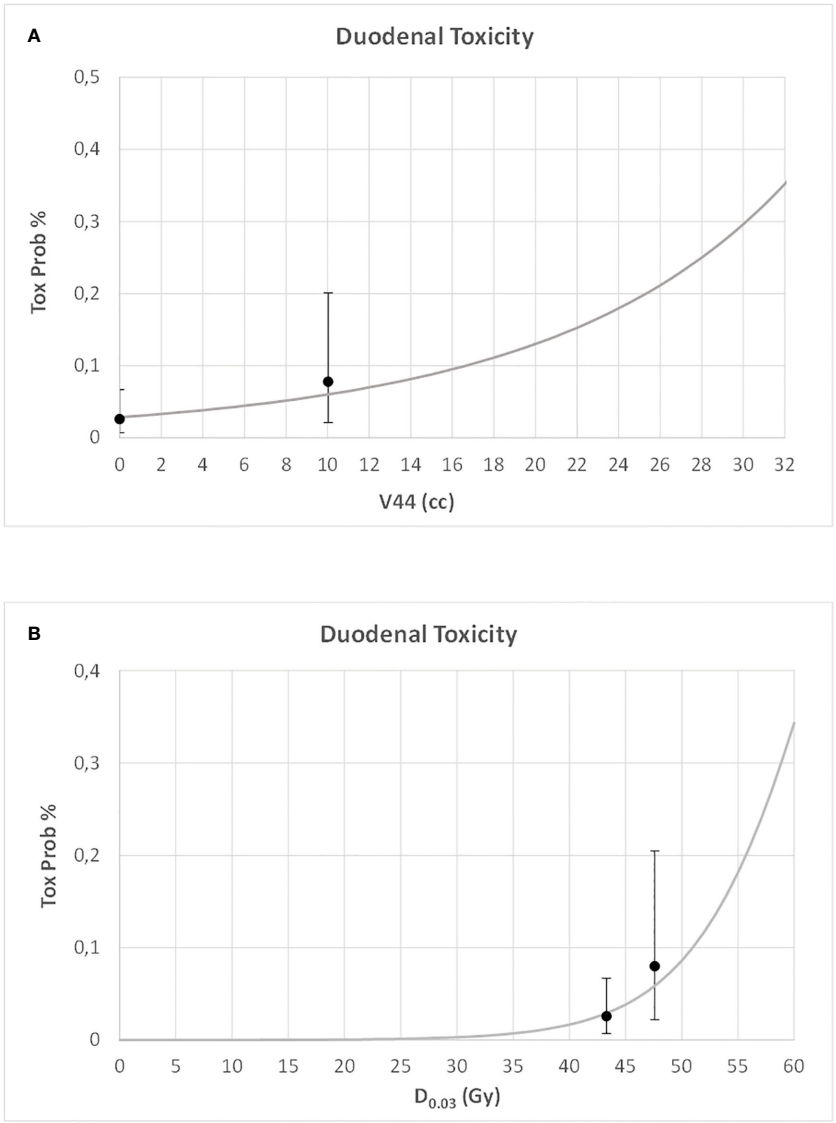

FIGURE 3
Risk of duodenal toxicity against duodenum V44 **(A)** and maximum dose **(B)** (D0.03), together with the true rates and their standard deviations.

duodenum/stomach V44Gy/$D_{0.03}$ is plotted together with the true rates.

4 Discussion

Knowledge concerning quantitative relationships between dose or dose–volume metrics and the risk of toxicity for the stomach and duodenum after radiotherapy is still lacking. However, a recently accomplished review (36) showed substantial improvement in the last few years. More quantitative information was reported in the contexts of conventionally fractionated radiotherapy (i.e., 1.8–2.0 Gy/fr) and SBRT (delivered in 1–5 fractions). Concerning conventional fractionation, most studies were consistent in suggesting a prevalent dose effect when considering moderate/severe duodenal and gastric toxicities, with the risk rapidly increasing for prescribed doses above 55–60 Gy and fractions of duodenum/stomach receiving more than 35–55 Gy above few %/few to tens of cubic centimeters (28, 36–40): similar findings were suggested for mild hypofractionation (2.15–2.25 Gy/fr) in a cohort of 105 patients treated with intensity-modulated radiotherapy (IMRT) for esophageal cancer at 60.2 Gy (29). Regarding SBRT, safe constraints for stomach and duodenum were suggested for one/three/five fractions, with quite consistent recent updates based on patient data, mostly for the duodenum with the 5-fraction scheme, as reviewed by Cattaneo and Marrazzo (36).

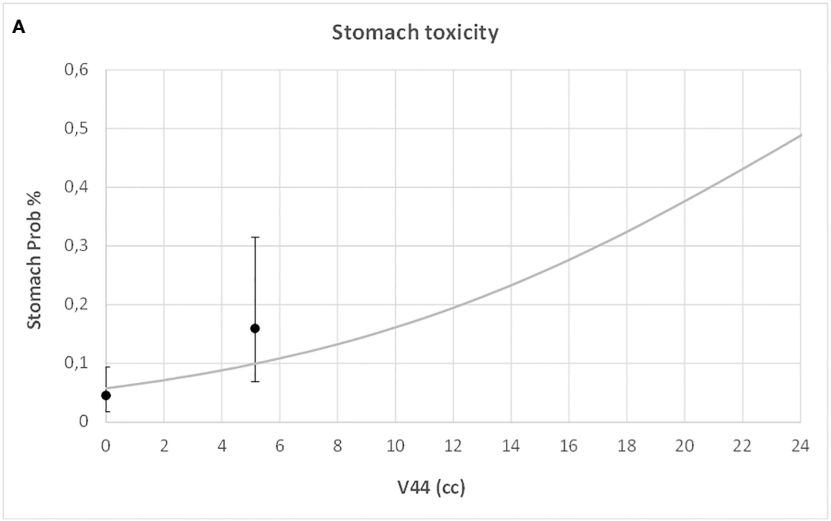

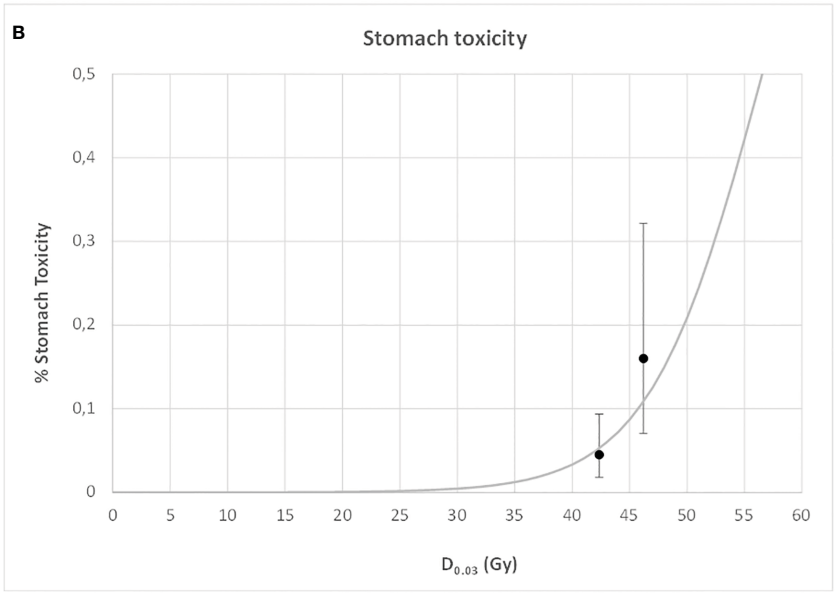

FIGURE 4
Risk of gastric toxicity against stomach V44 **(A)** and maximum dose **(B)** (D0.03), together with the true rates and their standard deviations.

It is worth mentioning that a quite large variability in terms of treated site and variable usage of chemotherapy may partly jeopardize the generalizability of the reported results.

Approaches using moderate hypofractionation have been suggested by us and other groups as a promising way to deliver higher BED to LAPC patients to reduce the risks of delivering a too-high dose to the adjacent stomach and/or duodenum. Different from SBRT, the smaller dosimetry gap between the prescribed dose and the constrained dose to these organs could limit severe underdosing to fractions of GTV in a large part of patients. The choice of a number of fractions of approximately 15 seems to be a good compromise, and several groups recently reported promising results using this fractionation scheme (8–11, 22, 30). However, the lack of knowledge concerning the dose–volume relationships, in this case, is pushing researchers to apply strict dose limits to the stomach/duodenum (11, 22), resulting in very mild toxicity profiles (10, 22, 30). This point suggests that it is likely that a larger window exists to be explored once dose and/or dose/volume limits are better assessed, with the potential to further reinforce the impact of dose escalation on local control. In this scenario, our experience with the 15-fraction scheme with limited dose escalation to sub-volumes of PTV (in a fraction of patients) may help in better assessing refined constraints. As a matter of fact, our results, representing the largest series analyzed with this aim to our knowledge, confirm that the

10.3389/fonc.2022.983984

shape of the DVH tail of the stomach and duodenum is associated with the risk of moderate/severe toxicities. Regarding the stomach, $D_{0.03}$ < 45 Gy and V44Gy < 2 cc may be suggested as sufficiently safe; however, V44Gy < 9 cc was found to be a robust constraint for duodenum, while the association with $D_{0.03}$ was found to be of borderline significance: despite that the best cutoff value suggested a threshold of 47.6 Gy, the lack of robustness seen at internal validation suggests a safer limit in the range 45–46 Gy as reasonable. These values are slightly higher than the ones applied in recent dose escalation trials for duodenum and similar for the stomach (22), suggesting a likely larger potential to be exploited by dose escalation. In Table 2 a summary of recent studies dealing with dose–volume relationships of the stomach and duodenum with moderate hypofractionation is shown. The different planning techniques, toxicity definitions, and the number of fractions make the comparison among these studies quite difficult. However, it is important to underline that the current study is the largest in terms of the number of treated patients. Compared to our previous preliminary analysis on 61 patients, only the result regarding Dmax of the duodenum was substantially confirmed, while only %DVH was analyzed in those studies. Current analysis revealed that, as expected, the absolute DVH (in cc) resulted in a better

TABLE 2 Summary of the literature for moderate hypofractionation.

Stomach								
Study	No.	End-point	No. fr	Dose Gy	Cht	Dmax Gy	DVH	Notes
Cattaneo (26)	61	≥2 CTCAE v.3	15	44.25	Ind +conc	–	V20<31%	SIB to infiltrating vessels PTV in 23/61 pts (48–55 Gy; overlap with stomach, 44.25 Gy)
Shinoto (25)	58	1 year ≥2 ulcer	12	55.2	Ind +conc	–	V10 < 102 cc V20 < 24 cc V30 < 6 cc	RBE-weighted dose (carbon ions). D2cc of GI tract constrained to 46 Gy
Liu (28)	68	≥2 CTCAE v.4	15 or 20	50/60 or 70/80	Conc 29/68	–	–	High rate of tox (late, 26%); no separation between 15 and 20 fractions in the analysis: stomach constraints: D_{max} < 60; D1 < 55; D3 < 50; D5 < 45; D10 < 40
Koay (21)	–	n.a.	15	37.5	Ind +conc	45	–	Suggested, based on experience. SIB to PTV derived from GTV and 4D CT to 67.5 Gy
Current study	204	≥2 CTCAE v.5	15	44.25	Ind +conc	45 $D_{0.03cc}$	V44 < 9.1 cc	SIB to infiltrating vessels PTV/GTV in 43/204 pts (48–58 Gy); overlap with stomach constrained to 40–44.25 Gy depending on volume
Duodenum								
Study	No.	End-point	No. fr	Dose Gy	Cht	Dmax	DVH	Notes
Cattaneo (26)	61	≥2 CTCAE v.3	15	44.25	Ind +conc	–	V40 < 16% V45 < 2.6%	SIB to infiltrating vessels PTV in 23/61 pts (48–55 Gy; overlap with stomach, 44.25 Gy)
Huang (40)	46	≥2 CTCAE v.3 ≥3 CTCAE v.3	15	36	Conc		V25 < 45% V35 < 20%	High rate (37% 1 year). 87% pts treated with 3D RCT ≥3 CTCAE v.3 analyzed only for 28 pts without erlotinib
Liu (28)	68	≥2 CTCAE v.4	15 or 20	50/60 or 70/80	Conc 29/68	–	V45 < 0.5cc	High rate of tox (late, 26%); no separation between 15 and 20 fractions in the analysis: stomach constraints: D_{max} < 55; D1 < 50; D3 < 45; D5 < 40; D10 < 35
Koay (21)	–	n.a.	15	37.5	Ind +conc	45	–	Suggested, based on experience. SIB to PTV derived from GTV and 4D CT to 67.5 Gy
Current study	204	≥2 CTCAE v.5	15	44.25	Ind +conc	*45–46** $D_{0.03cc}$	V44 < 9.1 cc	SIB to infiltrating vessels PTV/GTV in 43/204 pts (48-58 Gy); overlap with stomach constrained to 40–44.25 Gy depending on volume

CTCAE, Common Terminology Criteria for Adverse Events; SIB, simultaneous integrated boost; BTV, biological target volume; RBE, relative biological effectiveness; GI, gastrointestinal; PTV, planning target volume; GTV, gross tumor volume.
*Best cutoff value, 47.6 Gy; suggested 45–46 Gy as safer due to limited number of events.

association with toxicity compared to %DVH. Huang et al. (41) also used %DVH, finding an association for duodenal toxicity: however, their study included almost only 3D conformal radiotherapy (CRT) patients, resulting in large fractions of duodenum included in the high dose regions, which is quite far from the actually delivered dose distributions. The results reported by Liu et al. (29) regarding duodenum are quite consistent with our results despite the limited number of patients: no relationships were found for the stomach.

A major limitation of the current analysis consists in the consideration of both acute and late toxicities in a unique end-point. This was necessary in order to consider a sufficient number of events, being the late events only 11/204 (5.5%): of note, the longer time between the end of treatment and toxicity was 10 months, suggesting that the occurrence of late toxicities is in continuity with more acute events. The low number of toxicities confirmed that the irradiation to a total dose of approximately 44–45 Gy is safe, as demonstrated by the much higher rate of toxicities in the sub-groups of patients treated with SIB. However, it is important to underline that the current cohort represents the largest group analyzed with this intent and that the suggested constraints should be considered as a robust basis for future "safe" dose-escalation trials to be prospectively confirmed.

5 Conclusions

Current analysis suggests that constraining Dmax ($D_{0.03}$) and V44Gy of the stomach and duodenum within 45 and 45–46 Gy and a few cubic centimeters (2 cc for the stomach and 9 cc for the duodenum, respectively) should be effective in maintaining duodenal and gastric toxicities at approximately or below 5% when delivering radiotherapy in 15 fractions to LAPC patients, combined with chemotherapy. These values are consistent with the possibility of substantially escalating the dose to the tumor without relevant risks of toxicity in a likely large fraction of patients, corroborating the promise of significantly increasing local control without any relevant increase of toxicity in future trials.

Data availability statement

The datasets analyzed during the current study is not available due to restrictions inherent to EC approval. Requests to access the datasets should be directed to fiorino.claudio@hsr.it.

Ethics statement

The studies involving human participants were reviewed and approved by San Raffaele Hospital. The patients/participants provided their written informed consent to participate in this study.

Author contributions

CF, SB, and PP designed the study; PP, NS, and SB took care of data base building and data extraction; PT, AC, BL, and SB extracted and analyzed 3D planning data; SB, CF, and MM performed data and statistical analyses; SB, CF, and PP interpreted results; SB, CF, and PP wrote the main text; CF, MR, GC, AV, and NM supervised the discussion; All authors read and edited the text. All authors contributed to the article and approved the submitted version.

Funding

This work has been supported by Fondazione Regionale per la Ricerca Biomedica, project nr. 110-JTC PerPlanRT ERA PerMed, GA 779282.

Conflict of interest

The authors declare that the research was conducted in the absence of any commercial or financial relationships that could be construed as a potential conflict of interest.

Publisher's note

Supplementary material

The Supplementary Material for this article can be found online at: https://www.frontiersin.org/articles/10.3389/fonc.2022.983984/full#supplementary-material

References

1. *WHO report on cancer*. Geneve (2020).

2. American Cancer Society. *Cancer facts & figures 2020*. Atlanta: American Cancer Society (2020).

3. Vincent A, Herman J, Schulick R. Pancreatic cancer. *Lancet* (2011) 378:607–20. doi: 10.1016/S0140-6736(10)62307-0

4. Loehrer PJSr, Feng Y, Cardenes H, Wagner L, Brell JM, Cella D, et al. Gemcitabine alone versus gemcitabine plus radiotherapy in patients with locally advanced pancreatic cancer: an Eastern cooperative oncology group trial. *J Clin Oncol* (2011) 29:4105–12. doi: 10.1200/JCO.2011.34.8904

5. Hammel P, Huguet F, van Laethem JL, Chen HC, Rao A, Das P, et al. Effect of chemoradiotherapy vs chemotherapy on survival in patients with locally advanced pancreatic cancer controlled after 4 months of gemcitabine with or without erlotinib: The LAP07 randomized clinical trial. *JAMA* (2016) 315:1844–53. doi: 10.1001/jama.2016.4324

6. Suker M, Beumer BR, Sadot E, Marthey L, Faris JE, Mellon EA, et al. FOLFIRINOX for locally advanced pancreatic cancer: A systematic review and patient-level meta-analysis. *Lancet Oncol* (2016) 17:801–10. doi: 10.1016/S1470-2045(16)00172-8

7. Milella M, Bassi C, Boggi U, Brunetti O, Cavaliere A, Crippa S, et al. Evolving pancreatic cancer treatment: From diagnosis to healthcare management. *Crit Rev Oncol Hemat.* (2022) 169:103571. doi: 10.1016/j.critrevonc.2021.103571

8. Passoni P, Reni M, Cattaneo GM, Slim N, Cereda S, Balzano G, et al. Hypofractionated image-guided IMRT in advanced pancreatic cancer with simultaneous integrated boost to infiltrated vessels concomitant with capecitabine: A phase I study. *Int J Radiat Oncol Biol Phys* (2013) 87:1000–6. doi: 10.1016/j.ijrobp.2013.09.012

9. Krishnan S, Chadha AS, Suh Y, Chen HC, Rao A, Das P, et al. Focal radiation therapy dose escalation improves overall survival in locally advanced pancreatic cancer patients receiving induction chemotherapy and consolidative chemoradiation. *Int J Radiat Oncol Biol Phys* (2016) 94:755–65. doi: 10.1016/j.ijrobp.2015.12.003

10. Colbert LE, Moningi S, Chadha A, Amer A, Lee Y, Wolff RA, et al. Dose escalation with an IMRT technique in 15 to 28 fractions is better tolerated than standard doses of 3DCRT for LAPC. *Advanc Radiat Oncol* (2017) 2(3):403–15. doi: 10.1016/j.adro.2017.02.004

11. Reyngold M, Parikh P, Crane CH. Ablative radiation therapy for locally advanced pancreatic cancer: Techniques and results. *Radiat Oncol* (2019) 14:95. doi: 10.1186/s13014-019-1309-x

12. Reyngold M, O'Reilly EM, Varghese AM, Fiasconaro M, Zinovoy M. Romesser PB et al: Association of ablative radiation therapy with survival among patients with inoperable pancreatic cancer. *JAMA Oncol* (2021) 7:735–8. doi: 10.1001/jamaoncol.2021.0057

13. Chung SY, Chang JS, Lee BM, Kim KH, Lee KJ, Seong J. Dose escalation in locally advanced pancreatic cancer patients receiving radiochemotherapy. *Radiother Oncol* (2017) 123:438–45. doi: 10.1016/j.radonc.2017.04.010

14. Herman JM, Chang DT, Goodman KA, Dholakia AS, Raman SP, Hacker-Prietz A, et al. Phase 2 multi-institutional trial evaluating gemcitabine and stereotactic body radiotherapy for patients with locally advanced pancreatic cancer. *Int J Radiat Oncol Biol Phys* (2015) 121:1128–37. doi: 10.1002/cncr.29161

15. Fiorino C, Guckemberger M, Schwarz M, van der Heide UA, Heijmen B. Technology-driven research for radiotherapy innovation. *Mol Onc*. (2020) 14:1500–13. doi: 10.1002/1878-0261.12659

16. Tchelebi LT, Lehrer EJ, Trifiletti DM, Sharma NK, Niraj J Gusani NJ, Christopher H. Crane CH et al: Conventionally fractionated radiation therapy versus stereotactic body radiation therapy for locally advanced pancreatic cancer (CRiSP): An international systematic review and meta-analysis. *Cancer* (2020) 126:2120–31. doi: 10.1002/cncr.32756

17. Petrelli F, Comito T, Ghidini A, Torri V, Scorsetti M, Barni S. Stereotactic body radiation therapy for locally advanced pancreatic cancer: A systematic review and pooled analysis of 19 trials. *Int J Radiat Oncol Biol Phys* (2017) 97:313–22. doi: 10.1016/j.ijrobp.2016.10.030

18. Zaorsky NG, Lehrer EJ, Handorf E, Meyer JE. Dose escalation in stereotactic body radiation therapy for pancreatic cancer: A meta-analysis. *Am J Clin Oncol* (2019) 42:46–55. doi: 10.1097/COC.0000000000000472

19. Brunner TB, Nestle U, Grosu A-L, Partdridge M. SBRT in pancreatic cancer: what is the therapeutic window? *Radiother Oncol* (2015) 114:109–16. doi: 10.1016/j.radonc.2014.10.015

20. de Geus SWL, Eskander MF, Kasumova GG, Ng SC, Kent TS, Mancias JD, et al. Stereotactic body radiotherapy for unresected pancreatic cancer: A nationwide review. *Cancer* (2017) 123:4158–67. doi: 10.1002/cncr.30856

21. Parisi S, Ferini G, Cacciola A, Lillo S, Tamburella C, Santacaterina A, et al. A non-surgical COMBO-therapy approach for locally advanced unresectable pancreatic adenocarcinoma: Preliminary results of a prospective study. *La radiologia Med* (2022) 127:214–9. doi: 10.1007/s11547-021-01441-w

22. Koay EJ, Hanania AN, Hall WA, Taniguchi CM, Rebueno N, Myrehaug, et al. Dose-escalated radiation therapy for pancreatic cancer: A simultaneous integrated boost approach. *Pract Radiat Oncol* (2020) 10:e495–507. doi: 10.1016/j.prro.2020.01.012

23. Hall WA, Small C, Paulson E, Koay EJ, Crane C, Intven M, et al. Magnetic resonance guided radiation therapy for pancreatic adenocarcinoma, advantages, challenges, current approaches, and future directions. *Front Oncol* (2021) 11:628155. doi: 10.3389/fonc.2021.628155

24. Dieterich S, Green O, Booth J. SBRT targets that move with respiration. *Phys Med* (2018) 56:19–24. doi: 10.1016/j.ejmp.2018.10.021

25. Loi M, Magallon-Baro A, Suker M, van Eijck C, Sharma A, Hoogeman M, et al. Pancreatic cancer treated with SBRT: Effect of anatomical interfraction variations on dose to orgnas at risk. *Radiother Oncol* (2019) 134:67–73. doi: 10.1016/j.radonc.2019.01.020

26. Shinoto M, Shioyama Y, Matsunobu A, Okamoto K, Suefuji H, Toyama S, et al. Dosimetric analysis of upper gastrointestinal ulcer after carbon-ion radiotherapy for pancreatic cancer. *Radiother Oncol* (2016) 120:140–4. doi: 10.1016/j.radonc.2016.04.040

27. Cattaneo GM, Passoni P, Longobardi B, Slim N, Reni M, Cereda S, et al. Dosimetric and clinical predictors of toxicity following combined chemotherapy and moderately hypofractionated rotational radiotherapy of locally advanced pancreatic adenocarcinoma. *Radiother Oncol* (2013) 108:66–71. doi: 10.1016/j.radonc.2013.05.011

28. Kelly P, Das P, Pinnix CC, Beddar S, Briere T, Pham M, et al. Duodenal toxicity after fractionated chemoradiation for unresectable pancreatic cancer. *Int J Radiat Oncol Biol Phys* (2013) 85:e143–9. doi: 10.1016/j.ijrobp.2012.09.035

29. Liu X, Ren G, Li L, Xia T. Predictive dosimetric parameters for gastrointestinal toxicity with hypofractioned radiotherapy in pancreatic adenocarcinoma. *OncoTargets Ther* (2013) 9:2489–94. doi: 10.2147/OTT.S102035

30. Horowitz DP, Goodman K, Kachnic LA. Ablative radiotherapy for patients with inoperable pancreas cancer: Ready for prime time? *JAMA Oncol* (2021) 7:687–8. doi: 10.1001/jamaoncol.2021.0028

31. Mori M, Passoni P, Incerti E, Bettinardi V, Broggi S, Reni M, et al. Training and validation of a robust PET radiomic-based index to predict distant-relapse-free-survival after radio-chemotherapy for locally advanced pancreatic cancer. *Radiother Oncol* (2020) 153:258–64. doi: 10.1016/j.radonc.2020.07.003

32. Sini C, Noris Chiorda B, Gabriele P, Sanguineti G, Morlino S, Badenchini F, et al. Patient-reported intestinal toxicity from whole pelvis intensity-modulated radiotherapy: First quantification of bowel dose-volume effects. *Radiother Oncol* (2017) 124:296–301. doi: 10.1016/j.radonc.2017.07.005

33. Bresolin A, Faiella A, Garibaldi E, Munoz F, Cante D, Vavassori V, et al. Acute patient-reported intestinal toxicity in whole pelvis IMRT for prostate cancer: Bowel dose-volume effect quantification in a multicentric cohort study. *Radiother Oncol* (2021) 158:74–82. doi: 10.1016/j.radonc.2021.02.026

34. Mori M, Cattaneo GM, Dell'Oca I, Foti S, Calandrino R, Di Muzio NG, et al. Skin DVHs predict cutaneous toxicity in head and neck cancer patients treated with tomotherapy. *Phys Med* (2019) 59:133–41. doi: 10.1016/j.ejmp.2019.02.015

35. DeLong ER, DeLong DM, Clarke-Pearson DL. Comparing the areas under two or more correlated receiver operating characteristic curves: A nonparametric approach. *Biometrics* (1988) 44:837–45. doi: 10.2307/2531595

36. Cattaneo GM, Marrazzo L. Stomach, duodenum, liver and central hepatobiliary tract. In: Rancati T, Fiorino C, editors. *Modelling radiotherapy side-effect: practical applications for planning optimization*. Boca Raton, FL: CRC press, Taylor & Francis group 2019. p. 137–69.

37. Nakamura A, Shibuya K, Matsuo Y, Nakamura M, Shiinoki T, Mizowaki T, et al. Analysis of dosimetric parameters associated with acute gastrointestinal toxicity and upper gastrointestinal bleeding in locallyu advanced pancreatic cancer patients treated with gemcitabine-based concurrent chemotherapy. *Int J Radiat Oncol Biol Phys* (2012) 84:369–75. doi: 10.1016/j.ijrobp.2011.12.026

38. Holyoake DLP, Warren DR, Hurt C, Aznar M, Partridge M, Mukherjee S, et al. Stomach dose–volume predicts acute gastrointestinal toxicity in chemoradiotherapy for locally advanced pancreatic cancer. *Clin Oncol* (2018) 30:418–26. doi: 10.1016/j.clon.2018.02.067

39. Verma V, Sulman EP, Jhingran A, Tucker SL, M Rauch GM, Eifel PJ, et al. Dosimetric predictors of duodenal toxicity after intensity-modulated radiation therapy for treatment of the para-aortic nodes in gynecological cancer. *Int J Radiat Oncol Biol Phys* (2014) 88:357–62. doi: 10.1016/j.ijrobp.2013.09.053

40. George G, Lewis S, Chopra S, Phurailatpam R, Engineer. A retrospective study of the dosimetric parameters and duodenal toxicity in patients with upper gastrointestinal and gynaecological cancers treated with radiation therapy. *Clin Oncol* (2020) 32:e53–9. doi: 10.1016/j.clon.2019.08.003

41. Huang P, Robertson JM, Ye H, Margolis J, Nadeau I, Yan D, et al. Dose-volume analysis of predictors for gastrointestinal toxicity after concurrent full-dose gemcitabine and radiotherapy for locally advanced pancreatic cancer patients. *Int J Radiat Oncol Biol Phys* (2012) 83:1120–5. doi: 10.1016/j.ijrobp.2011.09.022

frontiers | Frontiers in Oncology

TYPE Original Research
PUBLISHED 30 January 2023
DOI 10.3389/fonc.2022.1021058

OPEN ACCESS

EDITED BY
Antonio Pontoriero,
University of Messina, Italy

REVIEWED BY
Carla Hajj,
Memorial Sloan Kettering Cancer Center, United States
Gianluca Ferini,
REM Radioterapia, Italy

*CORRESPONDENCE
Huojun Zhang
chyyzhj@163.com

†These authors have contributed equally to this work and share first authorship

SPECIALTY SECTION
This article was submitted to Radiation Oncology, a section of the journal Frontiers in Oncology

RECEIVED 17 August 2022
ACCEPTED 07 December 2022
PUBLISHED 30 January 2023

CITATION
Cao Y, Zhu X, Yu C, Jiang L, Sun Y, Guo X and Zhang H (2023) Dose evaluations of organs at risk and predictions of gastrointestinal toxicity after re-irradiation with stereotactic body radiation therapy for pancreatic cancer by deformable image registration.
Front. Oncol. 12:1021058.
doi: 10.3389/fonc.2022.1021058

Dose evaluations of organs at risk and predictions of gastrointestinal toxicity after re-irradiation with stereotactic body radiation therapy for pancreatic cancer by deformable image registration

Yangsen Cao†, Xiaofei Zhu†, Chunshan Yu†, Lingong Jiang, Yongjian Sun, Xueling Guo and Huojun Zhang*

Department of Radiation Oncology, Changhai Hospital Affiliated to Naval Medical University, Shanghai, China

Purpose: Re-irradiation of locally recurrent pancreatic cancer may be an optimal choice as a local ablative therapy. However, dose constraints of organs at risk (OARs) predictive of severe toxicity remain unknown. Therefore, we aim to calculate and identify accumulated dose distributions of OARs correlating with severe adverse effects and determine possible dose constraints regarding re-irradiation.

Methods: Patients receiving two courses of stereotactic body radiation therapy (SBRT) for the same irradiated regions (the primary tumors) due to local recurrence were included. All doses of the first and second plans were recalculated to an equivalent dose of 2 Gy per fraction (EQD_2). Deformable image registration with the workflow "Dose Accumulation-Deformable" of the MIM® System (version: 6.6.8) was performed for dose summations. Dose–volume parameters predictive of grade 2 or more toxicities were identified, and the receiver operating characteristic (ROC) curve was used to determine optimal thresholds of dose constraints.

Results: Forty patients were included in the analysis. Only the V_{10} of the stomach [hazard ratio (HR): 1.02 (95% CI:1.00–1.04), P = 0.035] and D_{mean} of the intestine [HR: 1.78 (95% CI: 1.00–3.18), P = 0.049] correlated with grade 2 or more gastrointestinal toxicity. Hence, the equation of probability of such toxicity was $P = \frac{1}{1+e^{-(-4.155+0.579Dmean\ of\ the\ intestine+0.021V10\ of\ the\ stomach)}}$. Additionally, the area under the ROC curve and threshold of dose constraints of V_{10} of the stomach and D_{mean} of the intestine were 0.779 and 77.575 cc, 0.769 and 4.22 Gy_3 (α/β = 3), respectively. The area under the ROC curve of the equation was 0.821.

10.3389/fonc.2022.1021058

Conclusion: The V_{10} of the stomach and D_{mean} of the intestine may be vital parameters to predict grade 2 or more gastrointestinal toxicity, of which the threshold of dose constraints may be beneficial for the practice of re-irradiation of locally relapsed pancreatic cancer.

KEYWORDS

pancreatic cancer, stereotactic body radiation therapy, dose distributions, re-irradiation, organs at risk (OARs)

Introduction

Despite the advances of modality and treatment regimens, pancreatic cancer still remains a lethal disease with a low survival rate and increasing mortality (1). Similar findings were also identified in China (2). Although surgical resection is considered as a curative option, only less than 20% of patients were candidates for up-front surgery at the initial diagnosis. Hence, chemoradiotherapy may be an alternative for most patients with advanced pancreatic cancer. However, a significant number of patients would still develop local recurrences within the primary regions after aggressive treatment. Those patients may not be amenable to surgery or second-line chemotherapy due to the high incidences of perioperative complications or chemotherapy-induced toxicities (3–5). A second radiotherapy may be employed with caution at the physician's discretion. In the case of radiotherapy technique, stereotactic body radiation therapy (SBRT) has commonly been used in locally advanced pancreatic cancer. Additionally, previous studies have clarified the feasibility of delivery of re-irradiation with SBRT for pancreatic cancer (6–10).

Regarding retreatment, it is a challenge to achieve good local control with proper radiation doses without compromise of protection of organs at risk (OARs), namely, keeping the doses under desired limits. Moreover, no standards about the dose constraints in the second radiotherapy have been proposed. Hence, in clinical practice, dose evaluations of the normal tissues might depend on dose distributions in the first treatment projecting to those in the second radiotherapy *via* image registration, which resulted in direct dosimetric comparisons of the plans other than assessment based on biological quantities. Only maximum doses to OARs may be converted into equivalent dose in 2 Gy/f and summed by the linear quadratic model (11).

Additionally, the fusion of images from the first and second radiotherapy for dose summations and evaluations was an obstacle of precise delivery, especially for SBRT. Typically, the rigid image registration (RIR) was employed for registrations of the first images with the second one, where the processed translation and rotation of the first images were compromised to be aligned with the second images. Most SBRT systems are equipped with the RIR, although the deformable image registration (DIR) has been developed. However, in the case of re-irradiation, due to gastrointestinal motility, tumor growth, or changes in the patient's weight, discrepancies between the alignment of the first and second images may contribute to the inaccurate evaluations of summed doses albeit calculated with the RIR.

In this scenario, the DIR provides both geometric and dosimetric accuracy compared to the RIR, which is pivotal to map, overlap, and integrate information from different images. As a result, quantifications of summed doses to OARs over the courses of treatment could be achieved by doses mapped back to a common reference anatomy with the DIR (12–15). Dose accumulations are calculated by warping dose grids to the reference anatomy based on the obtained deformation vector field (12–14).

Limited studies have investigated re-irradiation with SBRT for pancreatic cancer, which demonstrated high local control with a 1-year rate of 62%–81% and acceptable toxicities (6–8, 16, 17). Nonetheless, no further studies have evaluated accumulated doses to OARs and the correlation between doses and toxicities so far. Additionally, previous studies about re-irradiation all adopted conventional radiotherapy as the first treatment. Therefore, the aim of the study was to calculate accumulated dose distributions of OARs from two courses of SBRT and identify the correlations between radiation-induced toxicities with the doses to OARs, which might provide evidence for the determination of potential acceptable dose constraints for re-irradiation with SBRT.

Methods

Eligibility

From 2012 to 2017, patients with biopsy- and radiographically proven pancreatic cancer who received two courses of SBRT were screened for eligibility. Patients undergoing the second SBRT for other targets other than the

primary lesions were excluded from the study. A total of 40 patients received two courses of SBRT for the same irradiated regions (the primary tumors) due to local recurrence.

Dose constraints

The baseline dose constraints referred to TG-101 (18). The maximum dose of the OAR was calculated as 50% more than the normal constraint in the case of re-irradiation. Due to different doses to target regions and OARs and fractionation schemes, all treatment schedules were recalculated to an equivalent dose of 2 Gy per fraction (EQD_2) based on the following formula: $EQD_2 = d \star n \star \frac{d+\frac{\alpha}{\beta}}{2+\frac{\alpha}{\beta}}$An α/β value of 10 Gy ($Gy_{10}$) was employed for the tumor dose and acute effects, and the value determined as 3 Gy (Gy_3) concerns late effects. Secondly, the correlation between dose attenuation and time interval between two courses of radiotherapy was based on a previous study (120). Therefore, we allowed a dose reduction of 50% of the first radiation dose to OARs as the baseline for a re-irradiation 12 months after the last radiation. A dose reduction of 25% of the first radiation dose to OARs as the baseline was allowed for re-irradiation after 6–12 months. No dose reduction was used when re-irradiation was done within 6 months (19).

Treatment planning

The protocol of SBRT was similar to our previous studies (20–22). SBRT was delivered *via* CyberKnife® (Accuray Incorporated, Sunnyvale, CA, USA). Three to five gold fiducials within or adjacent to the pancreatic tumor were preferable. A radiographically evident gross disease was regarded as the gross tumor volume (GTV). The clinical target volume (CTV) was defined as areas of the potential subclinical disease spread. In most cases, the CTV was equal to the GTV. The planning target volume (PTV) included a 2–5-mm margin on the GTV. The dose was prescribed to the 70%–80% isodose line, covering at least 90% of the PTV. However, doses would be reduced at the physician's discretion if the tumor was located one-third or more to the duodenum or stomach circumference, or if the tumor abutted the bowel in only one area, as determined by the relationship of the tumor to the duodenum in axial, coronal, and sagittal planes in CT scans, or if the distance between the tumor and the bowel wall less than 3 mm.

Dose summation

Delineations of OARs depended on the treatment schemes. The liver, stomach, duodenum, and kidneys were contoured completely. The esophagus and bowels were contoured based on the extent of radiation fields of the two treatment plans, and the volumes should coincide. The difference of volumes of the duodenum, stomach, and bowel between the two plans should be less than 15, 30, and 80 cm^3, respectively. Hence, the OARs in the first plan were required to be the same as those in the second plan (Figure 1). Dose distributions, structures sets, and CT scans of the two treatment plans were extracted from the Multiplan® System (version: 4.0.2) and sent to the MIM® System (version: 6.6.8) for analysis. Firstly, two CT scans were aligned rigidly *via* automatic bone matches (translation and rotations). Therefore, for each plan before summation, each of the contoured OARs was registered rigidly. Subsequently, the DIR with the workflow "Dose Accumulation-Deformable" of MIM was performed for dose summations, which has been used in dose distributions of other cancers (23–25). After the DIR, the dose distributions of the first plan were projected to the second treatment with both doses converted to EQD_2, which were summed up finally (Figure 2). The modifications of image fusions with the DIR were performed by Reg Refine and Reg Reveal, the quality control modes in MIM. Afterward, the dose–volume histograms (DVHs) were derived from the summed plans of patients with two courses of SBRT by summed dose distributions. The OARs with maximum doses exceeding the redefined dose constraints were selected, and the correlations between excessive doses and toxicities were reanalyzed. The overlap target volume was defined as the volume covered by 95% isodose line of the summed dose.

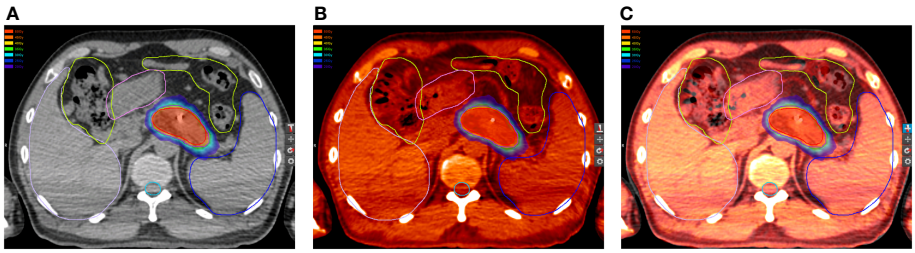

FIGURE 1
Organs at risk (OARs) in the **(A)** first and **(B)** second plan. **(C)** OARs in the first plan projected to the second plan.

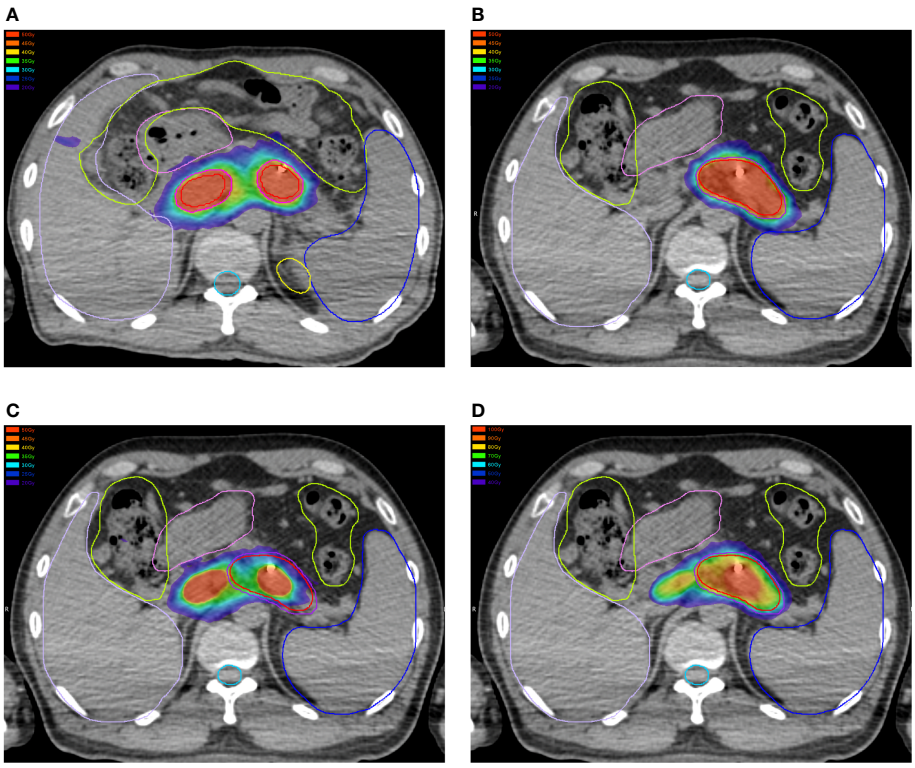

FIGURE 2
Dose distributions in the **(A)** first and **(B)** second plan. **(C)** Dose distributions in the first plan projected to the second CT scans. **(D)** Summations of dose distributions of the first and second plan by deformable image registration.

Quality assurance of the deformable image registration (DIR)

Reg Reveal and Reg Refine are the primary tools used to evaluate and adjust a deformation in order to achieve accurate results. Reg Reveal was developed for this purpose and is currently the only tool available for the specific purpose of efficient quality assurance (QA) of the DIR. Reg Reveal allows the user to interrogate the registration in specific regions of interest and draw conclusions about its accuracy. Reg Refine allows the user to influence the registration algorithm to achieve a more accurate result.

Reg Refine is an input into multiple DIR algorithms. It allows the user to define local rigid alignments to provide additional information to help guide the deformation algorithm near these areas. It can be used iteratively to execute a DIR, evaluate the local DIR accuracy, and suggest local alignments to improve the DIR result until an optimal alignment is achieved. The DIR was first evaluated with Reg Reveal to determine areas of the registration that needed improvement. Rigid registration adjustment tools were then used in areas where the naive DIR was determined to be inaccurate to allow the observer to manually adjust the local registration or to execute an automatic rigid registration within a box of interest. The observer then recorded this preferable local alignment. When re-executing the DIR, these recorded local rigid alignments were used as inputs to influence the algorithm to achieve a local DIR closer to this observer-defined result.

Toxicity and efficacy

The toxicity of treatment was evaluated in detail and scored for each patient. In addition, the efficacy of two courses of SBRT was assessed based on the tumor response, amelioration of pain, improvement of quality of life, and gain of weight during follow-up. Acute toxicities were determined using the "Acute radiation morbidity scoring criteria" from the Radiation Therapy Oncology Group, while late toxicities were evaluated using the "Late radiation morbidity scoring schema" from the Radiation Therapy Oncology Group/European Organization for Research on the Treatment of Cancer (26).

Statistical analysis

The correlation between doses and toxicities was determined by logistic regression (backward conditional), where the

potential dose–volume parameters predictive of toxicities were identified. The goodness of fit of the logistic model was analyzed using the Hosmer–Lemeshow test. The optimal risk threshold of each predictor was determined by the receiver operating characteristic (ROC) curve. Afterward, the probability of each patient developing gastrointestinal toxicity derived from predictors in the logistic regression analysis was also analyzed with the ROC curve to identify the optimal thresholds of probability. Two-sided P values<0.05 were considered statistically significant. Statistical analyses were performed using SPSS version 22.0 (IBM Corporation, Armonk, NY, USA).

Results

Dose distributions

Patients' characteristics were demonstrated in Table 1. The median time interval of the two courses of SBRT was 11.4 months (range: 3.8–29.1 months). The median prescription dose of the initial and second courses of SBRT was 35.5 Gy/5–7f and 32 Gy/5–8f, respectively. The median EQD_2 of PTV in the first and second SBRT was 49.58 Gy_{10} (range: 40 Gy_{10}–71.25 Gy_{10}) and 41.85 Gy_{10} (range: 31.25 Gy_{10}–55.73 Gy_{10}), respectively. Details were shown in Table 2. The accumulated doses of the OARs, including the stomach, duodenum, bowel, liver, spinal cord, and kidneys were demonstrated in Table 3.

Toxicity

Eighteen patients experienced grade 2 or more adverse events. Among these patients, one patient had grade 3 vomiting as an acute gastrointestinal toxicity and one patient had grade 3 gastrointestinal bleeding as a late toxicity. They all recovered after the treatment. The radiation doses to the stomach, duodenum, and bowel of these two patients were extracted and compared with the median summed does of those OARs (Table 4). As a result, most of the doses to the OARs of these two patients were higher than the median accumulated doses.

Due to low incidences of grade 3 gastrointestinal toxicity, grade 2 adverse effects were included for the identification of potential predictors. After multivariate analysis, the V_{10} of the stomach [hazard ratio (HR): 1.02 (95% CI: 1.00–1.04), P = 0.035] and D_{mean} of the intestine [HR: 1.78 (95% CI: 1.00–3.18), P = 0.049] correlated with grade 2 or more gastrointestinal toxicity (Table 5).

TABLE 1 Patient characteristics.

Characteristic	(n=40)
Age (years)	60.7 ± 10.9
Sex	
Male	28
Female	12
T category	
T1	1
T2	7
T3	8
T4	24
Pancreas location	
Head and neck	25
Body and tail	15

Prediction of grade 2 or more gastrointestinal toxicity

After multivariate analysis, the equation was as follows: P = $\frac{1}{1+e^{-(-4.155+0.579X1+0.021X2)}}$. X1 = D_{mean} of the intestine, X2 = V_{10} of the stomach. The value of the goodness of fit of the model derived from the V_{10} of the stomach and D_{mean} of the intestine was 0.514, which was better than that of the model from each one (V_{10} of the stomach: 0.376, D_{mean} of the intestine: 0.067). In addition, the threshold and area under the curve (AUC) of the V_{10} of the stomach were 77.575 cc and 0.779, while the threshold and AUC of the D_{mean} of the intestine were 4.22 Gy_3 and 0.769, respectively (Figures 3A, B). Based on the probability of toxicity of each patient from logistic analysis with the two factors, further analysis with ROC curves showed that the threshold of probability of grade 2 or more gastrointestinal toxicity if patients receive the doses above the threshold of the D_{mean} of the intestine and V_{10} of the stomach was 0.4345 and the AUC was 0.821 (Figure 3C).

Discussion

Due to the high dose per fraction of SBRT, even a small geometric inaccuracy or uncertainty after image registration could potentially reduce the therapeutic ratio and lead to radiation-induced toxicity. However, direct dose summations with the RIR may contribute to the inaccurate delivery of SBRT due to different patient postures, tumor growth, or gastrointestinal motility. The employment of the DIR technique may provide the potential to obtain more realistic plan sums. So far, it has been previously demonstrated that the DIR had been investigated in dose accumulations in head and neck tumor (27, 28), thoracic tumor (29, 30), and pelvic tumor (31–33). However, no studies have focused on dose summations of re-irradiation with SBRT in pancreatic cancer. Therefore, in

TABLE 2 Prescription doses to the PTV.

	First SBRT	Second SBRT
Prescription doses	35.5 Gy (30-46.8 Gy)	32.25 Gy (25-38 Gy)
EQD_2	49.58 Gy_{10} (40-71.25 Gy_{10})	41.85 Gy_{10} (31.25-55.73 Gy_{10})
PTV	37.75 cc (10.70-196.07 cc)	23.62 cc (8.81-278.42 cc)

EQD2, equivalent dose in 2Gy per fraction; PTV, planning target volume.

TABLE 3 Accumulated doses after the deformable image registration.

OARs	Dose	First radiation	Re-irradiation	Summed doses	Summed doses based on the correlation of dose attenuation and time
Stomach	$D_{max}(Gy_3)$	30.20 (3.18-55.27)	18.89 (3.01-44.25)	43.25 (7.56-90.47)	36.75 (5.79-76.74)
	$D_{1cc}(Gy_3)$	22.24 (2.28-34.78)	14.83 (2.57-35.18)	35.08 (4.88-76.88)	27.86 (4.30-65.69)
	$D_{10cc}(Gy_3)$	15.27 (2.10-25.11)	9.87 (1.79-1.05)	24.59 (3.49-60.72)	19.78 (2.97-50.80)
	$D_{mean}(Gy_3)$	5.02 (0.65-9.96)	3.07 (0.67-6.83)	7.97 (1.55-13.38)	6.42 (1.33-10.98)
	$V_{10}(cm^3)$	36.57 (0-154.05)	9.37 (0-71.38)	99.69 (0-337.81)	66.41 (0-202.16)
	$V_{20}(cm^3)$	2.66 (0-32.01)	0.01 (0-12.04)	22.73 (0-121.58)	7.69 (0-111.30)
	$V_{30}(cm^3)$	0.04 (0-3.39)	0 (0-2.02)	3.59 (0-43.95)	0.40 (0-46.50)
Duodenum	$D_{max}(Gy_3)$	24.43 (1.67-51.53)	15.45 (1.55-35.11)	35.61 (3.12-73.62)	30.36 (2.74-58.23)
	$D_{1cc}(Gy_3)$	18.18 (1.29-28.45)	11.00 (0.81-20.78)	26.82 (2.58-63.70)	22.13 (2.27-39.85)
	$D_{5cc}(Gy_3)$	12.44 (1.06-21.31)	7.04 (0.70-17.98)	20.77 (2.30-60.31)	15.99 (2.03-37.96)
	$D_{10cc}(Gy_3)$	9.58 (1.03-18.95)	5.34 (0.69-16.40)	16.26 (1.99-57.25)	12.82 (1.73-35.69)
	$D_{mean}(Gy_3)$	5.10 (1.02-12.58)	2.81 (0.68-9.25)	7.75 (1.93-23.75)	6.18 (1.63-19.59)
	$V_{10}(cm^3)$	9.05 (0-48.85)	1.47 (0-71.86)	23.26 (0-176.92)	18.66 (0-151.23)
	$V_{20}(cm^3)$	0.50 (0-7.52)	0 (0-1.71)	5.37 (0-112.89)	1.72 (0-56.03)
	$V_{30}(cm^3)$	0 (0-0.72)	0 (0-0.13)	0.56 (0-48.44)	0.05 (0-4.20)
Intestine	$D_{max}(Gy_3)$	30.77(17.51-43.46)	20.64(10.89-37.48)	44.07(29.70-92.47)	35.76(22.04-63.17)
	$D_{1cc}(Gy_3)$	23.95(13.50-33.21)	16.20 (8.51-29.63)	35.25(20.99-74.75)	28.06(17.28-46.80)
	$D_{5cc}(Gy_3)$	19.94(11.11-28.38)	13.41 (6.64-25.71)	28.86(16.89-43.45)	22.54(13.05-39.69)
	$D_{mean}(Gy_3)$	2.92 (0.90-8.28)	2.10 (0.97-5.63)	5.23 (2.04-14.04)	4.03 (2.15-11.64)
	$V_{20}(cm^3)$	4.93 (0-88.89)	0.07 (0-25.98)	31.91(1.42-309.13)	8.56 (0.01-109.21)
	$V_{30}(cm^3)$	0.07 (0-3.14)	0 (0-0.86)	5.02 (0-67.70)	0.30 (0-25.42)
Spinal Cord	$D_{max}(Gy_3)$	5.62 (1.43-14.54)	3.41 (1.04-16.92)	8.51 (3.61-18.88)	6.43 (3.07-17.36)
	$D_{0.35cc}(Gy_3)$	5.07 (1.38-13.34)	3.03 (0.93-13.64)	7.83 (3.47-16.25)	5.83 (2.69-14.17)
Left Kidney	$D_{mean}(Gy_3)$	3.18 (0.53-11.62)	2.16 (0.72-8.78)	5.47 (1.21-17.56)	4.62 (1.04-15.34)
	$D_{2/3}(Gy_3)$	1.94 (0.35-2.32)	1.32 (0.62-5.40)	3.55 (1.00-10.87)	3.03 (0.85-28.00)
	$V_5(cm^3)$	13.98 (0-87.7)	3.87 (0-70.76)	42.17 (0-98.94)	28.13 (0-94.16)
	$V_{10}(cm^3)$	0.76 (0-38.35)	0 (0-28.79)	9.34 (0-71.45)	5.12 (0-63.29)

(Continued)

TABLE 3 Continued

OARs	Dose	First radiation	Re-irradiation	Summed doses	Summed doses based on the correlation of dose attenuation and time
Right Kidney	$D_{mean}(Gy_3)$	1.93 (0.87-9.26)	1.37 (0.90-7.27)	3.51 (2.24-16.07)	2.68 (1.70-13.87)
	$D_{2/3}(Gy_3)$	1.40 (0.67-4.93)	1.01 (0-4.70)	2.66 (1.49-8.25)	2.11 (1.24-7.06)
	$V_5(cm^3)$	2.03 (0-65.04)	0 (0-60.87)	10.49 (0.11-87.23)	3.90 (0-79.71)
	$V_{10}(cm^3)$	0 (0-29.18)	0 (0-20.95)	0.61 (0-53.16)	0 (0-44.12)
Liver	$D_{mean}(Gy_3)$	3.22 (0.45-8.72)	1.89 (0.69-8.23)	5.35 (1.18-12.49)	4.28 (1.00-10.72)
	$D_{1/2}(Gy_3)$	2.13 (0.35-8.21)	1.25 (0.40-6.67)	3.76 (0.87-11.43)	3.03 (0.57-9.53)
	$V_{10}(cm^3)$	3.08 (0-35.31)	0.21 (0-28.1)	10.93 (0.03-55.26)	3.42 (0-47.67)
	$V_{30}(cm^3)$	0 (0-1.60)	0 (0-0.88)	0.06 (0-3.86)	0 (0-2.66)

this pilot study, the propagation of OAR contouring and transferring of dose distributions were performed for comparisons between standard dose constraints in TG-101 and accumulated doses and evaluations of correlations of radiation-induced gastrointestinal toxicities and dose distributions of OARs from the two treatment plans.

In this study, the dose–volume parameters of each OAR at the first and second SBRT were all below the corresponding standard dose constraints. However, some of the accumulated dose parameters to the stomach, duodenum, and intestine surpassed the dose constraints without consideration of heal assumption, while doses to the spinal cord, kidneys, and liver far from the target volume were all lower than the dose constraints. Even if dose downscaling due to the time interval between the two courses was taken into account, there were still some but fewer dose parameters above the dose constraints, which might be attributable to gastrointestinal toxicity. Additionally, further analyses on the dose distributions and OAR contouring regarding patients with accumulated doses above the dose constraints were performed. We found significant displacement of the stomach and duodenum in three patients at the second SBRT compared with the first one due to tumor shrinkage after the first treatment. Therefore, some of the dose distributions in the target volume at the first SBRT were projected to the OAR at the second SBRT (Figure 4), which resulted in the accumulated doses of OAR above the direct summation of the first and second doses. This error may be ascribed to the failure to compensate for the displacement of OARs due to the significant changes of the tumor volume with the DIR. This was one of the limitations of the DIR known as tissue appearance or disappearance (TAD) (29). Additionally, TAD was also common in the image registration when the second images were taken after surgery, which led to significant anatomical changes between the two images. Actually, TAD has not been taken into consideration in the deformation models of the DIR. Continuity, smoothness, or diffeomorphism may be considered during image registrations in the case of the underlying assumption used to model the deformations. However, these factors were different from TAD. The displacement field abutting to the TAD was distorted resulting in inaccurate accumulated dose distributions. Therefore, several frameworks had been proposed. Nithiananthan et al. (34) had proven that the Demons deformable registration process to include segmentation and an extra dimension in the deformation field could accommodate missing tissues between image acquisitions. Another study also provided a non-rigid registration framework for accommodation of resection and retraction (35). Nevertheless, it still remained a problem during the performance of the DIR, and adoption of dose accumulations in the case of TAD should be taken with caution.

Moreover, dose attenuations between the two courses of radiotherapy were also a challenge for dose prescriptions at re-irradiation and image registrations. The radiobiological rationale for heal assumption between different time intervals has been rarely investigated. In terms of re-irradiation, the summation of doses from different dose-fractionation schedules remained controversial, although normal tissue response might be predicted with the linear-quadratic (LQ) model (36). However, the role of the LQ model in predicting the normal tissue complication probability (NTCP) was limited because this model was derived from survival assays of cancer cell lines *in vitro*. Therefore, dose distributions of normal tissues *in vivo* could not be imitated well with the LQ model. Moreover, the optimal α/β ratio for each normal tissue was unknown. So far, only Abusaris et al. (19) reported the potential correlation between dose downscaling and time periods but without biological evidence when performing dose summation and evaluation of toxicity after re-irradiation for lung tumors. It was proposed in their study that

10.3389/fonc.2022.1021058

TABLE 4 Comparisons of doses to OARs of patients with grade 3 toxicity and median summed doses.

		Median summed dose*	Summed dose (case 1)*	Summed dose (case 2)*
Stomach	$D_{max}(Gy_3)$	36.75	33.93	43.46
	$D_{1cc}(Gy_3)$	27.86	27.86	35.07
	$D_{10cc}(Gy_3)$	19.78	21.95	27.36
	$D_{mean}(Gy_3)$	6.42	9.19	10.98
	$V_{10}(cm^3)$	66.41	157.73	160.69
	$V_{20}(cm^3)$	7.69	16.55	39.01
	$V_{30}(cm^3)$	0.40	0.33	5.35
Duodenum	$D_{max}(Gy_3)$	30.36	45	39.21
	$D_{1cc}(Gy_3)$	22.13	39.85	32.3
	$D_{5cc}(Gy_3)$	15.99	37.96	23.41
	$D_{10cc}(Gy_3)$	12.82	35.69	20.84
	$D_{mean}(Gy_3)$	6.18	15.94	9.91
	$V_{10}(cm^3)$	18.66	151.23	60.39
	$V_{20}(cm^3)$	1.72	56.03	12.33
	$V_{30}(cm^3)$	0.05	4.2	0.54
Intestine	$D_{max}(Gy_3)$	35.76	38.1	43.1
	$D_{1cc}(Gy_3)$	28.06	31.14	33.78
	$D_{5cc}(Gy_3)$	22.54	28.79	31.5
	$D_{mean}(Gy_3)$	4.03	9.92	8.92
	$V_{20}(cm^3)$	8.56	33.34	43.89
	$V_{30}(cm^3)$	0.30	0.59	3.03

*All of the summed doses were calculated based on the correlation between dose attenuation and time interval.

25% and 50% heal assumption could be estimated 6–12 months and 12 months after radiotherapy, respectively. Similarly, Meijneke et al. (37) recalculated all doses from different plans based on the EQD_2. Hence, the results in the pilot study should be extrapolated in clinical practice with great caution, which needs to be further validated. Additionally, many relevant factors, in addition to dose distributions and time intervals, should be taken into account in the case of assessment of doses to normal tissues, including the expected survival, curative or palliative intent, OARs overlap with or adjacent to target volumes, and anticipated NTCP based on detailed dosimetry from two or more schedules.

Additionally, it was elucidated in the study that the V_{10} of the stomach and D_{mean} of the intestine were predictors of grade 2 or more gastrointestinal toxicity. The derived thresholds indicated a lower risk of adverse effects with the V_{10} of the stomach below 77.575 cc and D_{mean} of the intestine below 4.22 Gy_3. Furthermore, combined with these two factors, the equation demonstrated the probability of toxicity. Also, the threshold of the probability based on the probability of each patient having toxicity from logistic analysis with the two factors implied that the risk of radiation-induced severe gastrointestinal toxicity could be increased in the event of the probability above 0.4345. So far, previous studies only focused on gastrointestinal dose tolerance at the first SBRT. However, due to the high incidence of local recurrence of pancreatic cancer, SBRT has been employed in the re-irradiation of the local progression with good local control and mild toxicity (8, 16, 17). Therefore, it was required that evaluations of dose distributions of OARs should be given the first priority at the re-irradiation, albeit no investigations had been performed. Compared with previous studies, the thresholds of the stomach and intestine dose–volume were higher. The underlying reason may be attributable to the residual doses to the OARs from the first SBRT. Combined with the two factors, the AUC was larger than that of each one alone. Therefore, the threshold of probability from two factors by logistic analysis may be more accurate in the prediction of toxicity. Great attention should be placed when the probability of severe gastrointestinal toxicity was above the threshold calculated from the equation.

10.3389/fonc.2022.1021058

TABLE 5 Factors predictive of grade 2 or more gastrointestinal toxicity.

OAR	Dose	Univariate analysis		Multivariate analysis	
		HR (95% CI)	P value	HR (95% CI)	P value
Stomach	D_{max}(Gy$_3$)	1.04 (0.99-1.09)	0.081	NA	NA
	D_{1cc}(Gy$_3$)	1.06 (0.99-1.21)	0.080	NA	NA
	D_{10cc}(Gy$_3$)	1.16 (1.03-1.31)	0.016	NA	NA
	D_{mean}(Gy$_3$)	1.66 (1.16-2.38)	0.006	NA	NA
	V_{10}(cm^3)	1.02 (1.01-1.04)	0.006	1.02 (1.00-1.04)	0.035
	V_{20}(cm^3)	1.10 (1.02-1.20)	0.018	NA	NA
	V_{30}(cm^3)	1.24 (0.87-1.76)	0.228	NA	NA
Duodenum	D_{max}(Gy$_3$)	1.01 (0.96-1.07)	0.691	NA	NA
	D_{1cc}(Gy$_3$)	1.04 (0.96-1.13)	0.311	NA	NA
	D_{5cc}(Gy$_3$)	1.08 (0.98-1.19)	0.142	NA	NA
	D_{10cc}(Gy$_3$)	1.10 (0.98-1.23)	0.114	NA	NA
	D_{mean}(Gy$_3$)	1.17 (0.96-1.43)	0.130	NA	NA
	V_{10}(cm^3)	1.04 (0.99-1.08)	0.107	NA	NA
	V_{20}(cm^3)	1.09 (0.94-1.26)	0.258	NA	NA
	V_{30}(cm^3)	1.49 (0.67-3.30)	0.324	NA	NA
Intestine	D_{max}(Gy$_3$)	0.99 (0.92-1.06)	0.676	NA	NA
	D_{1cc}(Gy$_3$)	1.04 (0.94-1.15)	0.415	NA	NA
	D_{5cc}(Gy$_3$)	1.07 (0.95-1.22)	0.263	NA	NA
	D_{mean}(Gy$_3$)	2.08 (1.18-3.67)	0.012	1.78 (1.00-3.18)	0.049
	V_{20}(cm^3)	1.06 (1.00-1.11)	0.050	NA	NA
	V_{30}(cm^3)	1.20 (0.84-1.73)	0.319	NA	NA

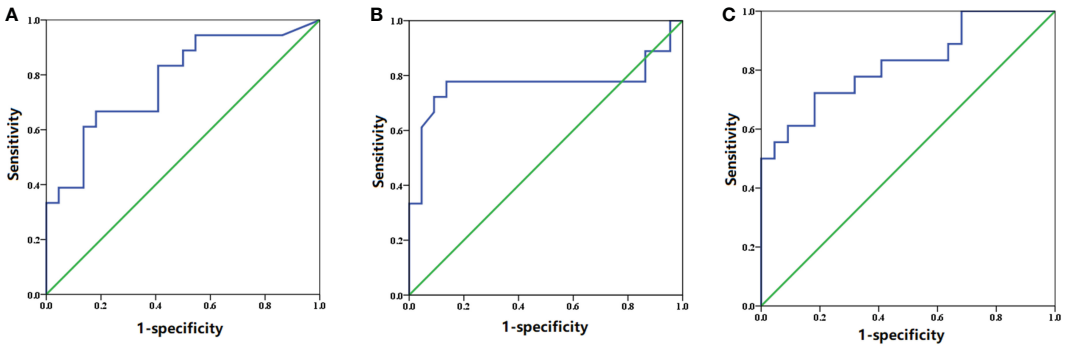

FIGURE 3
ROC curve of the **(A)** V_{10} of the stomach, **(B)** D_{mean} of the intestine, and **(C)** combination of the two factors.

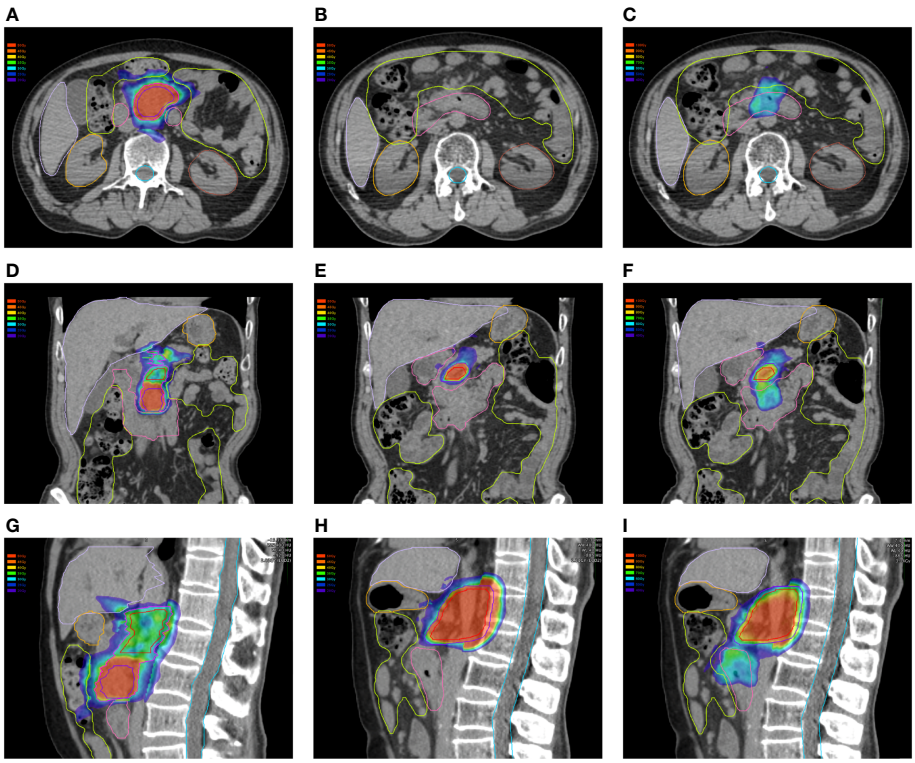

FIGURE 4
Dose distributions of the first plan in the **(A)** horizontal plane, **(D)** coronal plane, and **(G)** sagittal plane. Dose distributions of the first plan in the **(B)** horizontal plane, **(E)** coronal plane, and **(H)** sagittal plane. Dose distributions of the first plan projected to the second CT scans in the **(C)** horizontal plane, **(F)** coronal plane, and **(I)** sagittal plane.

Nevertheless, there were some limitations in the study. The first one was that no radiobiological model could precisely predict the dose downscaling after the first SBRT. Also, owing to the failure to accommodate the TAD in the DIR, the accumulated doses may not be as accurate as the actual ones. Therefore, the clinical practice of the dose thresholds of the stomach and intestine as dose constraints at the re-irradiation, the equation, and the threshold probability of the gastrointestinal toxicity should be taken with great caution. Another one was that the equation and the thresholds have not been internally and externally validated because of the limited number of patients. Additionally, due to careful evaluations of patients in re-SBRT to reduce the risk of severe adverse events, we could not deliver a high radiation dose; therefore, few grade 2 or more toxicities were observed. Third, due to interoperator variability in contouring the intestine, the D_{mean} of the intestine may vary between physicians. This might result in the overestimation or underestimation of the risk of gastrointestinal toxicity. Therefore, the interpretation of the equation should be done cautiously. However, compared with previous studies about re-irradiation with SBRT for pancreatic cancer, the number in this study was relatively large.

In conclusion, this pilot study demonstrated that the V_{10} of the stomach and D_{mean} of the intestine correlated with severe gastrointestinal toxicity after two courses of SBRT. The prediction of gastrointestinal toxicity may be more accurate with these two factors compared to each one alone. Additionally, a higher risk of toxicity may be found in patients with a V_{10} of the stomach above 77.575 cc or D_{mean} of the intestine above 4.22 Gy_3 or the probability above 0.4345. Nevertheless, these thresholds and the equation should be further validated.

Data availability statement

The raw data supporting the conclusions of this article will be made available by the authors, without undue reservation.

Ethics statement

The studies involving human participants were reviewed and approved by Changhai Hospital. The patients/participants

provided their written informed consent to participate in this study.

Author contributions

HZ was supervised the study. YC, CY and YS designed the treatment plans. XZ, LJ and XG performed patients' follow-up. XZ analyzed data. YC, XZ and CY drafted the manuscript. HZ revised the manuscript. All authors contributed to the article and approved the submitted version.

Funding

The study was funded by Shanghai Shenkang Center Innovation Research Program (SHDC2020CR3087B) and Changhai Hospital Clinical Investigation Program (2019YPT004) and the Ministry of Science and Technology of the People's Republic of China (2022YFC2503700, 2022YFC2503701).

Acknowledgments

We appreciated Dr. Jiuhong Chen for her precise comments and LinkDoc for their constructive advice in patients' follow-up.

Conflict of interest

The authors declare that the research was conducted in the absence of any commercial or financial relationships that could be construed as a potential conflict of interest.

Publisher's note

References

1. Siegel RL, Miller KD, Jemal A. Cancer statistics, 2018. *CA Cancer J Clin* (2018) 68:7–30. doi: 10.3322/caac.21442

2. Chen W, Zheng R, Baade PD, Zhang S, Zeng H, Bray F, et al. Cancer statistics in China, 2015. *CA Cancer J Clin* (2016) 66:115–32. doi: 10.3322/caac.21338

3. Conroy T, Desseigne F, Ychou M, Bouché O, Guimbaud R, Bécouarn Ye, et al. FOLFIRINOX versus gemcitabine for metastatic pancreatic cancer. *N Engl J Med* (2011) 364:1817–25. doi: 10.1056/NEJMoa1011923

4. Burris HA3rd, Moore MJ, Andersen J, Green MR, Rothenberg ML, Modiano MR, et al. Improvements in survival and clinical benefit with gemcitabine as first-line therapy for patients with advanced pancreas cancer: a randomized trial. *J Clin Oncol* (1997) 15:2403–13. doi: 10.1200/JCO.1997.15.6.2403

5. Lee MG, Lee SH, Lee SJ, Lee YS, Hwang JH, Ryu JK, et al. 5-fluorouracil/leucovorin combined with irinotecan and oxaliplatin (FOLFIRINOX) as second-line chemotherapy in patients with advanced pancreatic cancer who have progressed on gemcitabine-based therapy. *Chemotherapy* (2013) 59:273–9. doi: 10.1159/000356158

6. Wild AT, Hiniker SM, Chang DT, Tran PT, Khashab MA, Limaye MR. Re-irradiation with stereotactic body radiation therapy as a novel treatment option for isolated local recurrence of pancreatic cancer after multimodality therapy: experience from two institutions. *J Gastrointest Oncol* (2013) 4:343–51. doi: 10.3978/j.issn.2078-6891.2013.044

7. Lominska CE, Unger K, Nasr NM, Haddad N, Gagnon G. Stereotactic body radiation therapy for reirradiation of localized adenocarcinoma of the pancreas. *Radiat Oncol* (2012) 7:74. doi: 10.1186/1748-717X-7-74

8. Dagoglu N, Callery M, Moser J, Tseng J, Kent T, Bullock A, et al. Stereotactic body radiotherapy (SBRT) reirradiation for recurrent pancreas cancer. *J Cancer.* (2016) 7:283–8. doi: 10.7150/jca.13295

9. Reddy AV, Hill CS, Sehgal S, He J, Zheng L, Herman JM, et al. Efficacy and safety of reirradiation with stereotactic body radiation therapy for locally recurrent pancreatic adenocarcinoma. *Clin Oncol (R Coll Radiol).* (2022) 34:386–94. doi: 10.1016/j.clon.2021.12.014

10. Parisi S, Ferini G, Cacciola A, Lillo S, Tamburella C, Santacaterina A, et al. A non-surgical COMBO-therapy approach for locally advanced unresectable pancreatic adenocarcinoma: preliminary results of a prospective study. *Radiol Med* (2022) 127:214–9. doi: 10.1007/s11547-021-01441-w

11. Jones L, Hoban P, Metcalfe P. The use of the linear quadratic model in radiotherapy: a review. *Australas Phys Eng Sci Med* (2001) 24:132–46. doi: 10.1007/BF03178355

12. Oh S, Kim S. Deformable image registration in radiation therapy. *Radiat Oncol J* (2017) 35:101–11. doi: 10.3857/roj.2017.00325

13. Jaffray DA, Lindsay PE, Brock KK, Deasy JO, Tomé WA. Accurate accumulation of dose for improved understanding of radiation effects in normal tissue. *Int J Radiat Oncol Biol Phys* (2010) 76:S135–9. doi: 10.1016/j.ijrobp.2009.06.093

14. Velec M, Moseley JL, Eccles CL, Craig T, Sharpe MB, Dawson LA, et al. Effect of breathing motion on radiotherapy dose accumulation in the abdomen using deformable registration. *Int J Radiat Oncol Biol Phys* (2011) 80:265–72. doi: 10.1016/j.ijrobp.2010.05.023

15. Chang JY, Zhang X, Knopf A, Li H, Mori S, Dong L, et al. Consensus guidelines for implementing pencil-beam scanning proton therapy for thoracic malignancies on behalf of the PTCOG thoracic and lymphoma subcommittee. *Int J Radiat Oncol Biol Phys* (2017) 99:41–50. doi: 10.1016/j.ijrobp.2017.05.014

16. Sutera P, Bernard ME, Wang H, Bahary N, Burton S, Zeh H, et al. Stereotactic body radiation therapy for locally progressive and recurrent pancreatic cancer after prior radiation. *Front Oncol* (2018) 8:52. doi: 10.3389/fonc.2018.00052

17. Koong AJ, Toesca DAS, von Eyben R, Pollom EL, Chang DT. Reirradiation with stereotactic body radiation therapy after prior conventional fractionation radiation for locally recurrent pancreatic adenocarcinoma. *Adv Radiat Oncol* (2017) 2:27–36. doi: 10.1016/j.adro.2017.01.003

18. Benedict SH, Yenice KM, Followill D, Galvin JM, Hinson W, Kavanagh B, et al. Stereotactic body radiation therapy: the report of AAPM task group 101. *Med Phys* (2010) 37:4078–101. doi: 10.1118/1.3438081

19. Abusaris H, Storchi PR, Brandwijk RP, Nuyttens JJ. Second re-irradiation: efficacy, dose and toxicity in patients who received three courses of radiotherapy with overlapping fields. *Radiother Oncol* (2011) 99:235–9. doi: 10.1016/j.radonc.2011.03.010

20. Zhu X, Li F, Ju X, Shen Y, Cao Y, Cao F, et al. Prediction of overall survival after re-irradiation with stereotactic body radiation therapy for pancreatic cancer with a novel prognostic model (the SCAD score). *Radiother Oncol* (2018) 129:313–8. doi: 10.1016/j.radonc.2018.08.012

21. Zhu X, Li F, Liu W, Shi D, Ju X, Cao Y, et al. Stereotactic body radiation therapy plus induction or adjuvant chemotherapy for early stage but medically inoperable pancreatic cancer: A propensity score-matched analysis of a prospectively collected database. *Cancer Manag Res* (2018) 10:1295–304. doi: 10.2147/CMAR.S163655

22. Zhu X, Shi D, Li F, Ju X, Cao Y, Shen Y, et al. Prospective analysis of different combined regimens of stereotactic body radiation therapy and chemotherapy for locally advanced pancreatic cancer. *Cancer Med* (2018) 7(7):2913–24. doi: 10.1002/cam4.1553

23. Bondar L, Hoogeman MS, Vasquez Osorio EM, Heijmen BJ. A symmetric nonrigid registration method to handle large organ deformations in cervical cancer patients. *Med Phys* (2010) 37:3760–72. doi: 10.1118/1.3443436

24. Vasquez Osorio EM, Hoogeman MS, Bondar L, Levendag PC, Heijmen BJ. A novel flexible framework with automatic feature correspondence optimization for nonrigid registration in radiotherapy. *Med Phys* (2009) 36:2848–59. doi: 10.1118/1.3134242

25. Vasquez Osorio EM, Hoogeman MS, Teguh DN, Al-Mamgani A, Kolkman-Deurloo IK, Bondar L, et al. Three-dimensional dose addition of external beam radiotherapy and brachytherapy for oropharyngeal patients using nonrigid registration. *Int J Radiat Oncol Biol Phys* (2011) 80:1268–77. doi: 10.1016/j.ijrobp.2010.10.006

26. Cox JD, Stetz J, Pajak TF. Toxicity criteria of the radiation therapy oncology group (RTOG) and the European organization for research and treatment of cancer (EORTC). *Int J Radiat Oncol Biol Phys* (1995) 31:1341–6. doi: 10.1016/0360-3016(95)00060-C

27. Nobnop W, Chitapanarux I, Neamin H, Wanwilairat S, Lorvidhaya V, Sanghangthum T. Evaluation of deformable image registration (DIR) methods for dose accumulation in nasopharyngeal cancer patients during radiotherapy. *Radiol Oncol* (2017) 51:438–46. doi: 10.1515/raon-2017-0033

28. Rigaud B, Simon A, Castelli J, Gobeli M, Ospina Arango JD, Cazoulat G, et al. Evaluation of deformable image registration methods for dose monitoring in head and neck radiotherapy. *BioMed Res Int* (2015) 2015:726268. doi: 10.1155/2015/726268

29. Sarrut D, Baudier T, Ayadi M, Tanguy R, Rit S. Deformable image registration applied to lung SBRT: Usefulness and limitations. *Phys Med* (2017) 44:108–12. doi: 10.1016/j.ejmp.2017.09.121

30. Samavati N, Velec M, Brock KK. Effect of deformable registration uncertainty on lung SBRT dose accumulation. *Med Phys* (2016) 43:233. doi: 10.1118/1.4938412

31. Flower E, Do V, Sykes J, Dempsey C, Holloway L, Summerhayes K, et al. Deformable image registration for cervical cancer brachytherapy dose accumulation: Organ at risk dose-volume histogram parameter reproducibility and anatomic position stability. *Brachytherapy*. (2017) 16:387–92. doi: 10.1016/j.brachy.2016.12.006

32. Yu J, Hardcastle N, Jeong K, Bender ET, Ritter MA, Tomé WA. On voxel-by-voxel accumulated dose for prostate radiation therapy using deformable image registration. *Technol Cancer Res Treat* (2015) 14:37–47. doi: 10.7785/tcrt.2012.500397

33. Thörnqvist S, Petersen JB, Høyer M, Bentzen LN, Muren LP. Propagation of target and organ at risk contours in radiotherapy of prostate cancer using deformable image registration. *Acta Oncol* (2010) 49:1023–32. doi: 10.3109/0284186X.2010.503662

34. Nithiananthan S, Schafer S, Mirota DJ, Stayman JW, Zbijewski W, Reh DD, et al. Extra-dimensional demons: a method for incorporating missing tissue in deformable image registration. *Med Phys* (2012) 39:5718–31. doi: 10.1118/1.4747270

35. Risholm P, Samsett E, Talos IF, Wells W. A non-rigid registration framework that accommodates resection and retraction. *Inf Process Med Imaging*. (2009) 21:447–58. doi: 10.1007/978-3-642-02498-6_37

36. Milano MT, Mihai A, Kong FS. Review of thoracic reirradiation with stereotactic body radiation therapy: A focus on toxicity risks. *Pract Radiat Oncol* (2018) 8:251–65. doi: 10.1016/j.prro.2018.01.008

37. Meijneke TR, Petit SF, Wentzler D, Hoogeman M, Nuyttens JJ. Reirradiation and stereotactic radiotherapy for tumors in the lung: dose summation and toxicity. *Radiother Oncol* (2013) 107:423–7. doi: 10.1016/j.radonc.2013.03.015

Frontiers in Oncology

Advances knowledge of carcinogenesis and tumor progression for better treatment and management

The third most-cited oncology journal, which highlights research in carcinogenesis and tumor progression, bridging the gap between basic research and applications to imrpove diagnosis, therapeutics and management strategies.

Discover the latest Research Topics

See more →

Frontiers

Avenue du Tribunal-Fédéral 34
1005 Lausanne, Switzerland
frontiersin.org

Contact us

+41 (0)21 510 17 00
frontiersin.org/about/contact